Reconstruction of the Pleistocene Landscape of Southern KwaZulu-Natal, South Africa

by means of GIS, Remote Sensing and Geomorphological Techniques

Dissertation

der Mathematisch-Naturwissenschaftlichen Fakultät
der Eberhard Karls Universität Tübingen
zur Erlangung des Grades eines
Doktors der Naturwissenschaften
(Dr. rer. nat.)

vorgelegt von
M.Sc. Christian Sommer
aus Heidenheim a. d. Brenz

Tübingen

2021

Table of Contents

Inhalt

Zusammenfassung

Das östliche Südafrika und besonders die Region um *Sibudu Cave* spielt in der Geschichte des *Homo sapiens* eine wichtige Rolle. Das Middle Stone Age ist geprägt von technologischer Innovation, Bevölkerungsdynamik und komplexem symbolischem und sozialem Verhalten, aber auch von räumlicher und zeitlicher Variabilität (Will et al., 2019a). Diese werden durch diverse Hypothesen zu erklären versucht, von denen die meisten die spätpleistozänen Umweltveränderungen berücksichtigen. Aus diesem Grund liefert die Paläoumweltforschung einen wichtigen Beitrag um sich ein Bild der Lebensweise der frühen Menschen zu machen. So wurde in Sibudu Cave seit Jahrzehnten, neben der archäologischen Forschung, hoch anerkannte Erkenntnisse zum Paläoklima, -vegetation und -fauna gewonnen.

Die vorliegende Dissertation liefert einen Beitrag zur geomorphologischen Entwicklung der Region, der darin enthaltenen Landschaftsformen und -prozesse. Dazu wurden mehrere Landschaftselemente in zwei Untersuchungsgebieten untersucht: Das Tongati Valley, das die direkte Umgebung der Urmenschen darstellt und der Obere Umkomazi am Fuße der Drakensberge, wo überregional zusammenhängende Umwelteinflüsse betrachtet werden. Methodisch ist die Arbeit breit aufgestellt und umfasst Themen aus der GIS Analyse, Fernerkundung und der geomorphologischen Geländearbeit. Dabei wurden jeweils maßgeschneiderte Lösungen für die Fragestellungen entwickelt, wie 3D Modellierung, Object Based Image Analysis, Simulation, Geomorphometrie, usw. Auch die Analyse der Masotcheni Formation mittels elektromagnetischer Spektroskopie kann als innovativ bezeichnet werden. Die Ergebnisse zeigen, dass das Tal des Tongati durch die African, Post-African I und Post-African II Landschaftszyklen entstand, und somit das Ergebnis tektonischer Hebung und Kippung ist, wie sich aufgrund von Einebnungsflächen rekonstruieren lässt. Durch die komplexe Geologie lief die Evolution des Abflusssystems differenziert ab, sodass sich der Mittellauf stromaufwärts von Sibudu Cave kontinuierlich in die harte Lithologie eintieft, aber kein hydrologisches Gleichgewicht erreicht, während sich der Unterlauf dynamisch an Pleistozäne Meeresspiegeltiefstände anpasst, wie mehrere Terrassengenerationen und ein alluvial verfüllter Mündungsbereich bezeugen. Die spätpleistozänen Meeresspiegelfluktuationen hatten auch eine Expansion der Küstenebene um bis zu 5500 km^2 und eine Küstenregression zur Folge, sodass Sibudu Cave bis über 30 km im Landesinneren lag. Dies hat Bedeutung für die Interpretation der Beschaffung mariner Ressourcen und der Raumnutzung der früheren Bewohner Sibudus.

Die Masotcheni Formation in den Drakensbergen weist auf spätpleistozäne Landschaftsstabilitätszyklen hin, die mit den von Botha (1996) formulierten weitgehend übereinstimmen. Demnach Entwickelten sich im späten MIS4 / frühen MIS 3 Böden unter humiden Einflüssen, während die Böden nach dem mittleren MIS 3 unter semi-ariden Bedingungen entstanden. Diese Phasen sind von Phasen erhöhter Erosion und Deposition unterbrochen. Die Untersuchung der rezenten Gullyerosion ergab, dass die Entstehung dieser Erosionsform in den Masotcheni Sedimenten zeitlich mit der kleinen Eiszeit und gleichzeitiger Bevölkerungs- und Landnutzungsveränderungen im mittleren 17. Jahrhundert geschätzt werden können. Die hohen Erosionsraten unter modernen Klimabedingungen erklären, warum Sedimente sehr selten sind, die vor dem MIS 5e deponiert wurden, welches ein ähnliches Klima aufweist. Es lässt sich zusammenfassen, dass die Region starker landschaftlicher Veränderungen

im Spätpleistozän unterworfen war, und die Auseinandersetzung mit dieser variablen Umwelt ein hohes Maß an sozialen und kognitiven Fähigkeiten voraussetzt.

Abstract

Eastern South Africa, and particularly the region around Sibudu Cave, plays an important role in the history of *Homo sapiens*. The Middle Stone Age is characterized by technological innovation, population dynamics, and complex symbolic and social behavior, but also by spatial and temporal variability (Will et al., 2019). These are attempted to be explained by diverse hypotheses, most of which consider Late Pleistocene environmental change. For this reason, paleoenvironmental research provides an important contribution to building a picture of the lifestyle of early humans. Thus, in addition to archaeological research, highly recognized knowledge of paleoclimate, vegetation, and fauna has been obtained at Sibudu Cave for decades. This dissertation provides a contribution to the geomorphological evolution of the region, the landscape forms and processes contained therein. For this purpose, several landscape elements were studied in two study areas: The Tongati Valley, representing the immediate environment of the prehistoric people, and the Upper Umkomazi Valley at the foot of the Drakensberg, where supra-regional environmental influences were assessed. Methodologically, the work covers a wide range and includes topics from GIS analysis, remote sensing, and geomorphological field work. In each case, tailored solutions to the issues have been developed, such as 3D modeling, object-based image analysis, simulation, geomorphometry, etc. The analysis of the Masotcheni Formation using electromagnetic spectroscopy can also be considered innovative.

The results show that the Tongati River valley was formed by the African, Post-African I, and Post-African II landscape cycles, and thus is the result of tectonic uplift and tilting, as can be reconstructed based on planation surfaces. Due to the complex geology, the evolution of the drainage system proceeded in a differentiated manner such that the middle reaches upstream of Sibudu Cave continuously deepened into the resistant lithology but did not reach hydrologic equilibrium, while the lower reaches dynamically adapted to Pleistocene sea level lowstands, as evidenced by several terrace generations and an alluvially filled estuary. Late Pleistocene sea level fluctuations also resulted in coastal plain expansion of up to 5500 km^2 and coastal regression, such that Sibudu Cave was located up to over 30 km inland. This has relevance for the interpretation of procurement of marine resources and the use of space by Sibudu's earlier occupants.

The Masotcheni Formation in the Drakensberg indicates late Pleistocene landscape stability cycles that are largely consistent with those formulated by Botha (1996). According to this, one type of soils developed under humid influences in the late MIS4 / early MIS 3, while another type of soils developed under semi-arid conditions after the middle MIS 3. These phases are interrupted by periods of increased erosion and deposition. Analyses of recent gully erosion revealed that the origin of this erosional form in the Masotcheni sediments can be approximated to have initiated around the Little Ice Age and concurrent population and land use changes in the mid-17th century. The high erosion rates under modern climatic conditions explain why sediments deposited prior to MIS 5e, which has a similar climate, are very rare.

It can be summarized that the region was subject to strong landscape changes in the late Pleistocene, and the ability to sustain in this variable environment requires a high level of social and cognitive skills.

List of Figures

List of Tables

List of Abbreviations

AAO	Antarctic Oscillation
DEM	Digital Elevation Model
D-GPS	Differential Global Positioning System
ENC	Electronic Navigation Chart
ENSO	El Niño–Southern Oscillation
ERI	Electric Resistivity Imaging
HP	Howiesons Poort
IOD	Indian Ocean Dipole
ITCZ	Inner Tropical Convergence Zone
ka	1,000 years
KZN	KwaZulu-Natal
LGM	Last Glacial Maximum, i.e. MIS 2
LIA	Little Ice Age
LIDAR	Light Detection and Ranging
LIG	Last Interglacial, i.e. MIS 5e
LSA	Later Stone Age
Ma	1,000,000 years
MSA	Middle Stone Age
MIS	Marine isotope stage
NIR	Near Infrared
OBIA	Object Based Image Analysis
OSL	Optically Stimulated Luminescence
RSL	Relative Sea Level
RU	Rock Unit
SB	Still Bay
SfM	Structure from Motion
SRZ	Summer Rainfall Zone
SST	Sea Surface Temperatures
SWR	Shortwave Infrared
TI	Topographic Index
TPI	Topographic Position Index
TTT	Tropical-Temperate Throughs
UAV	Unpiloted Aerial Vehicle
WRZ	Winter Rainfall Zone
VIS	Visual part of the electromagnetic spectrum

Acknowledgements

Chapter 1: Introduction

1.1 Motivation

The modern landscape of southern KwaZulu-Natal is rich in geomorphic landforms formed in several cycles during the Cenozoic (66–0 Ma). The Pleistocene (2.58–0.012 Ma) is particularly characterized by high climate and sea level fluctuations, which are still evident in the landscape's archives of the region, and the research by luminaries such as Danie G. Krige and Lester C. King enriched geomorphological science.

Especially in the climatically varied phase of the Late (Upper) Pleistocene (127–11.7 ka) the region was intensively populated by hunter-gatherers, which is expressed in the dataset of the ROCEEH Out Of Africa Database (Haidle et al., 2010) by a higher number of sites and increased artefact density (fig. 1.1). Due to their attraction for past humans and their function as sediment traps, an imbalance in favor of sheltered sites over open-air sites is recognized by Will et al. (2019a). Two motivations result from this observation: On the one hand, to understand the geomorphological development of such a rock shelter and its valley using the example of the Tongati River; On the other hand, to investigate a possible open-air site, exemplified by the Masotcheni Formation (Fm.) at KwaThunzi, which, despite its exposed location, contains a stratified late Pleistocene sedimentary archive that includes climate indicators and artefact-bearing layers.
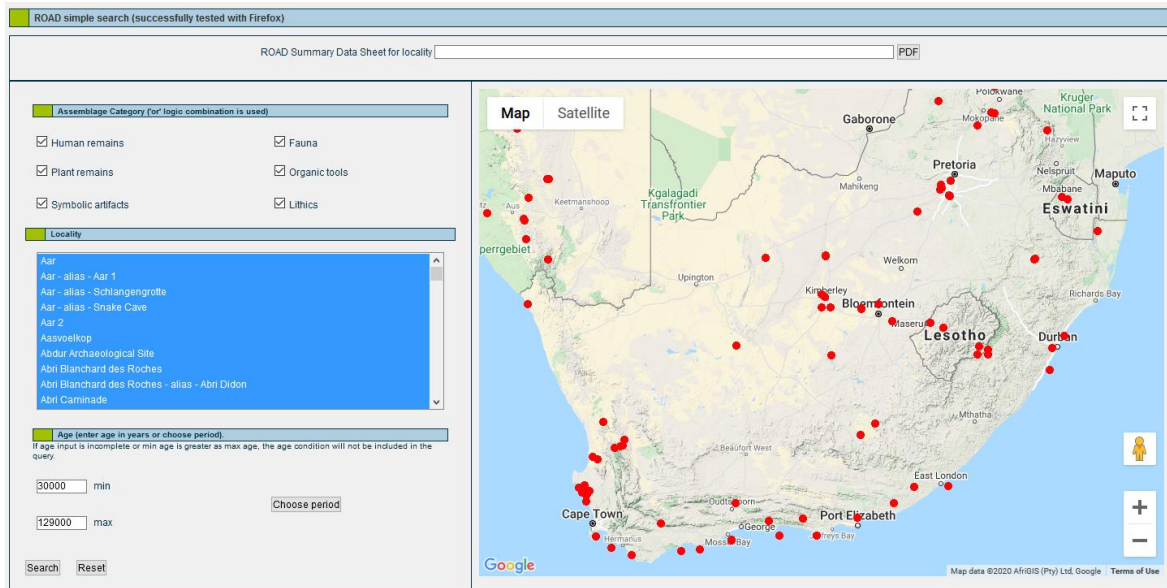
Fig. 1.1: Relevant archaeological sites from South Africa in the Late MSA. Screenshots from the ROAD database on 2020-12-15.

The Southern African Middle Stone Age (MSA, ~300–30 ka) is characterized by behavioral innovations and cultural complexity, which results in a supra-regional subdivision of the archaeological record to technocomplexes, such as the Still Bay (SB) and Howiesons Poort (HP) technologies, that peak in MIS 4 (Lombard, 2012, Kandel et al., 2016). What led to these cultural changes in the MSA is still subject of debate. One theory favors abiotic environmental forcing as primary driver, that induces selection pressure and causes hominins to change their behavior (Ziegler et al., 2013, McCall, 2007), however it is criticized that the interpretations often rely on conceptual climate models rather than high resolution scientific datasets (Chase, 2010). Another

popular theory involves different modes of cultural transmission, in which the social transfer of information, e.g. about the production of lithic tools, is actively selected or follows random traits (Eerkens and Lipo, 2005, Conard and Will, 2015). Furthermore, population dynamics, in terms of e.g. population size, mobility and connectivity, are also held responsible for explaining cultural variability (Powell et al., 2009). These hypotheses are to be tested against high resolution environmental data. While research in Sibudu Cave has already yielded much acclaimed findings on vegetation, fauna and climate during the occupation phases (Wadley, 2004, Plug, 2004, Plug, 2006, Wadley et al., 2008, Goldberg et al., 2009, Wadley et al., 2011, Bruch et al., 2012, Clark, 2017), there are still gaps in the research on the area surrounding the rock shelter. This leads to the motivation to complement to this "greater picture" with new findings related to the aspects of fluvial landforms in the Tongati Valley and the development of the coastal region, which addresses important issues such as hominin use of space or the exploitation of marine resources. Concerning the regional context, the study of the Masotcheni Fm. is intended to contribute to an understanding of the cycles of landscape stability and climate influences on the still little studied hinterland.

In relation to the Masotcheni Fm. it can be observed that these landscape cycles are still continuing and the geomorphic processes are still at work. Therefore, another concern is to study past processes on recent examples, such as gully erosion in KwaThunzi. This is to provide insights into the erosion rates and the age of the gully in order to assess the vulnerability of the colluvia as an object of paleo research, but also more practically as endangered agricultural land.

To address these questions, the methodological approach of landscape reconstruction was chosen. The present thesis is based on a series of works that assess past processes and landforms by means of GIS, modelling, remote sensing and geomorphological fieldwork, e.g. Vogel and Märker (2010), Vogel et al. (2016), Bachofer (2016), Quénéhervé (2018).

1.2 Research Questions

This chapter is intended to provide an overview of the research questions of this thesis, which will be answered in the following chapters. This aims to the understanding of the landscape with its diverse forms and processes, which can be achieved with a methodological mix of GIS, remote sensing and geomorphological field work. These results are meant to support archaeological research and provide new insights into landscape changes and their significance for early humans. This thesis is spatially and logically divided into two study areas with different research interests.

The Tongati Valley plays an important role in the study of human evolution in the MSA. The reconstruction of landscape elements and processes is intended to complement the existing environmental reconstructions from the strata of Sibudu Cave in order to gain further insights about humans as integrated beings in their environment.

The landforms of the valley are the result of several landscape cycles, ranging from the Early Cretaceous to the Holocene. Some parts, such as the African Surface, are extremely long-lasting phenomena, while others, such as the recent river valleys, are highly dynamic. One question therefore relates to a classification of the different landforms in the study area and their chronological order. This is addressed by a spatial downscaling approach of the seminal work by Partridge and Maud (1987) through GIS analyses with a high-resolution Digital Elevation Model (DEM).

> **Q1**: Which landscape elements are found in the study area, what are their ages and which landscape evolutionary phases can be derived from this?

Sea level fluctuations with a range of over 100 m are a major feature of the Pleistocene. Studies from the Southern Coast imply large extensions of the now submerged landmass at sea level lowstands with effects on early human foraging (Marean et al., 2020). Since Sibudu Cave is located on the Natal Bight, which is also affected by coastline shift, this creates new contexts for the procurement of marine resources by the site's occupants (d'Errico et al., 2008, Vanhaeren et al., 2019). A simulation of the coastal distance of Sibudu Cave was performed to show the extensions of the coastal plain during settlement with high temporal resolution, by using a bathymetric model (Weatherall et al., 2015) and a paleo sea level reconstruction (Waelbroeck et al., 2002).

> **Q2**: How has paleo sea level affected the proximity of Sibudu Cave to the coast and what does this mean for the exploitation of marine resources?

One of the most important and intense processes of Pleistocene landscape evolution is the incision of rivers and the resulting landforms, which have already occupied authorities such as Danie G. Krige (1932) and Lester C. King (1964). The Tongati is an excellent study object, as several factors like uplift, lithology and sea level response interact in a small area, yet produce different stages of river maturity. This also concerns the question of the age of the cliff, that hosts the archaeological site. Distinct geomorphic regions of the channel are identified using hydromorphometric analysis of a DEM (Schwanghart and Scherler, 2014). The use of Object-Based Image Analysis (OBIA) in landform classification allows to predict the spatial distribution

of fluvial terraces and the geomorphological toolkit comprises a number of methods to asses these in field, such as geomorphological mapping, Electric Resistivity Imaging (ERI) and Optically Stimulated Luminescence (OSL) dating.

> **Q3**: What are the drivers of fluvial incision and what does this imply for the age of the valley and Sibudu Cave?

Besides the Tongati Valley, the present thesis deals with another crucial region, the Upper Umkomazi catchment in the Drakensberg foothills. There, the Masotcheni Fm. offers the opportunity to investigate the paleoenvironment as well as past human occupations in an open-air setting. The study area in KwaThunzi was selected because of the intensive previous research work and availability of data (Märker, 2001, Märker and Sidorchuk, 2003, Hochschild et al., 2003).

The stratified colluvial sediments of the Masotcheni Fm. testify to phases of soil formation and erosion due to cycles of landscape stability and instability in the Late Pleistocene (Botha, 1996, Bosino et al., 2020). Botha (1996) has also shown that these phenomena can be observed over wide regions in northern KZN and Eswatini. In the southern part of KwaZulu-Natal, however, these have been studied much less intensively, so that the question arises to what extent the deposits in the study area can be correlated with those in the north and what conclusions can be drawn about landscape stability at the regional level. Further, this raises the question of how these landscape cycles relate to environmental change, and what connections might exist with human occupation phases. To address these questions, a wide range of geomorphological methods were applied, including, for the first time, analysis using ERI and electromagnetic field spectroscopy.

> **Q4**: What conclusions about past landscape cycles can be drawn from the Masotcheni Fm. exposed at KwaThunzi and which inferences on paleoenvironment and human occupation of the coastal hinterland can be drawn from this?

The last research question addresses the current landscape cycle of the Masotcheni Fm. and associated gully and sheet erosion. The question deals with the estimation of erosion rates by comparing historical air- and UAV-borne imagery obtained by Structure-from-Motion (SfM) 3D modeling. This narrows down the age of the gully and discusses its origin in the context of known hypotheses.

> **Q5**: How intensive is the historical gully erosion and what conclusions can be drawn about the origin of these erosion landforms.

Thus, the research questions of the present thesis cover a broad spectrum of the geomorphological forms and processes of the region. The focus lies on the (Late) Pleistocene, as Q2, Q3 and Q4 make evident. Q1 with the question of the oldest landforms and Q5, which deals with the most recent processes, form a temporal frame.

Chapter 2: Study Area

This chapter gives an introduction about the study area and an overview over important cycles and long-term datasets, that are relevant for a general understanding of temporal variations of the of the South African environment.

2.1 Study area

2.1.1 Tongati catchment

One of the two study areas of this thesis is the catchment of the Sibudu River, which lies on the Indian Ocean 20 km north of Durban.
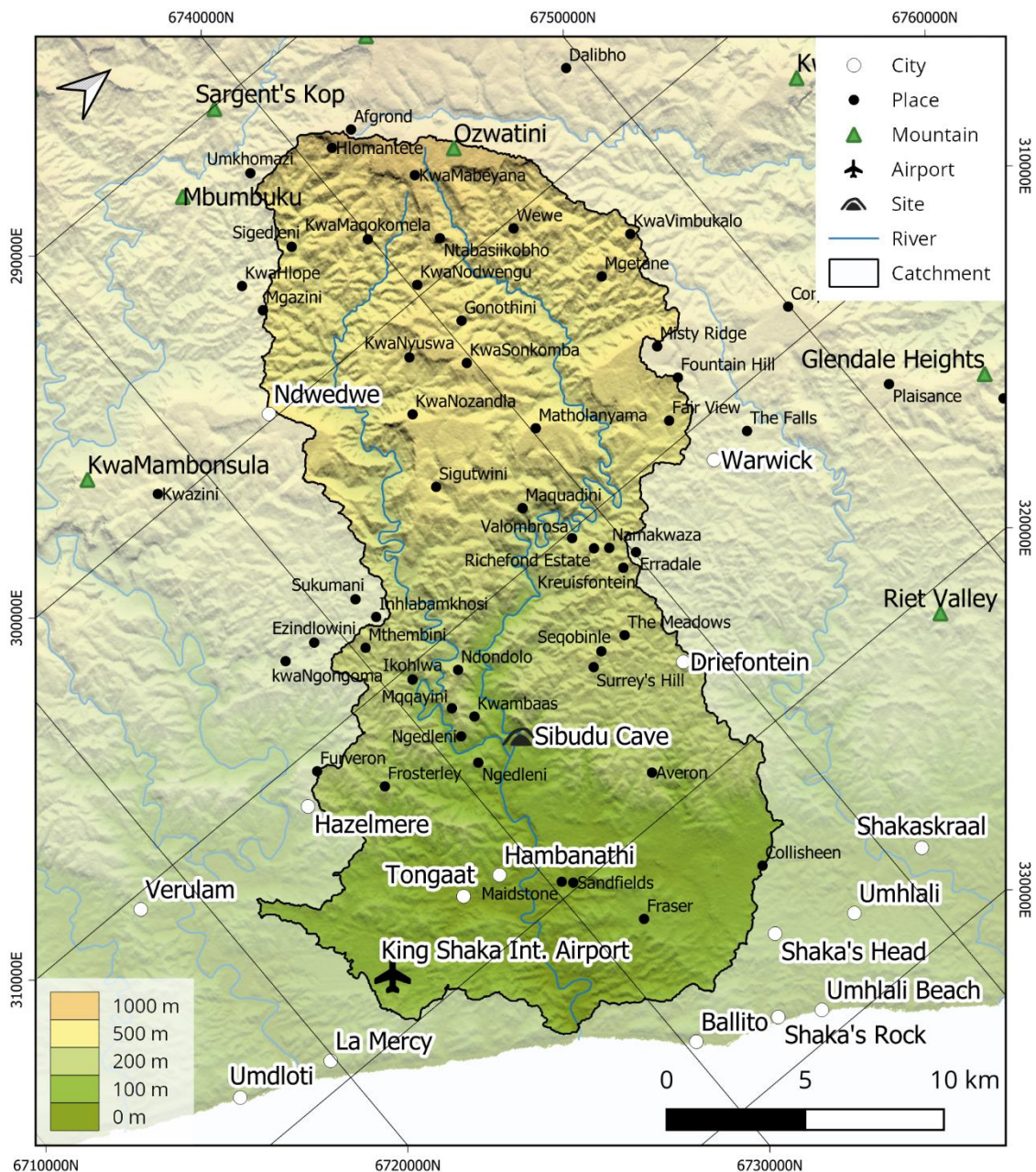
Fig. 2.1: Map of the Tongati catchment.

It was chosen because of its relevance for the archaeological research at Sibudu Cave and the coexistence of a wide range of geomorphic landforms within small space.

The catchment has a size of 408 km² with a maximal length of 32 km and a maximal width of 18 km. It ranges between elevations of over 900 m a.s.l. on the Ozwatini Plateau, and 0 m a.s.l at the estuary. Its climate can be described by the Koeppen-Geiger climate class "Cwa", which stands for warm temperate climate with dry winters and hot summers (Conradie, 2012). The climate station of Ballito has a mean annual temperature of 20.7° and an annual precipitation sum of 985 mm. It is part of the Summer Rainfall Zone (SRZ), which is associated with high seasonality of the hydroclimate, but the proximity to the coast is responsible for high precipitation even in the driest months. March is the month with highest precipitation sum of 121 mm and the dry season peaks in July, when precipitation sum lies around 33 mm.

The catchment is situated in the Eastern Coastal Belt ecoregion (Kleynhans et al., 2005), whose morphology comprises primarily closed hills and mountains with a moderate to high relief. The main vegetation types are Thicket, Grassland and Bushveld.

The lithology comprises Oribi Gorge Granite in the upper catchment, Natal Group Sandstone in the middle catchment and Karroo lithology in the lower catchment. The latter are Dwyka Group diamictites and belonging to the Ecca Group, shalestones of the Pietermaritzburg Fm. and the mud- and siltstones of the Vryheid Formation. Jurassic dolerite is spread all over the catchment in form of dikes, sills and intrusions. Two major fault directions, one trending north-northeast to northeast and another east-northeast, are the result of Gondwana-breakup-related segmentation.

The catchment can be divided into two geomorphic provinces: the Southeastern Coastal Platform that affects the coastline and reaches 10 km inland and intersects with the Karroo lithologies, followed by the Southeastern Coastal Hinterland, which can be found in the more mountainous parts of the Natal Group and Oribi Gorge Fm. lithologies in the middle and upper catchment (Partridge et al., 2010).

2.1.2 Gully KwaThunzi in the Upper Umkomazi catchment

The second study area lies in the Drakensberg Foothills of KwaZulu-Natal (fig. 2.2). It was selected for its good preservation of the Masotcheni Fm. and the high availability of data from its intense research history.

Gully KwaThunzi (Lat -29.6164°, Lon 29.6480°) is situated at ~1200 m a.s.l. on a north-east facing slope in the south of the river Umkomazi. The area is vegetated with moist grassland of the Sub-Escarpment Grassland Bioregion and is situated in the geomorphic province of the Eastern Coastal Hinterland (Partridge et al., 2010).

The region is characterized by warm temperate climate with dry winters and warm summers (Koeppen-Geiger class "Cwb") (Conradie, 2012). Figure 2.3 shows the Walter-Lieth climate diagram of the settlement Stoffelton, situated ~5 km upstream of KwaThunzi on the Upper Umkomazi. The diagram was calculated from monthly averages of climate data provided by the CRU-TS v4.03 database (Harris et al., 2014). Mean temperatures range between a monthly minimum of 8.7°C in June and a maximum of 19.7°C in January with an annual mean temperature of 14.9°C. Average monthly precipitation is highest in January with 137 mm and lowest in July with 8 mm, while annual precipitation sums up to 788 mm. The overall moisture distribution is typical for the Eastern mountainous region and the Summer Rainfall Zone (SRZ) in general. Austral summer moths are strongly humid, whereas the winter months from May to

August are classified as arid. Therefore, the vegetation period is restricted to the months from September to April, due to water availability. This is at least true for the modern climate, but as chapter 2.2 shows, climate has been subject to severe changes through the Late Pleistocene.
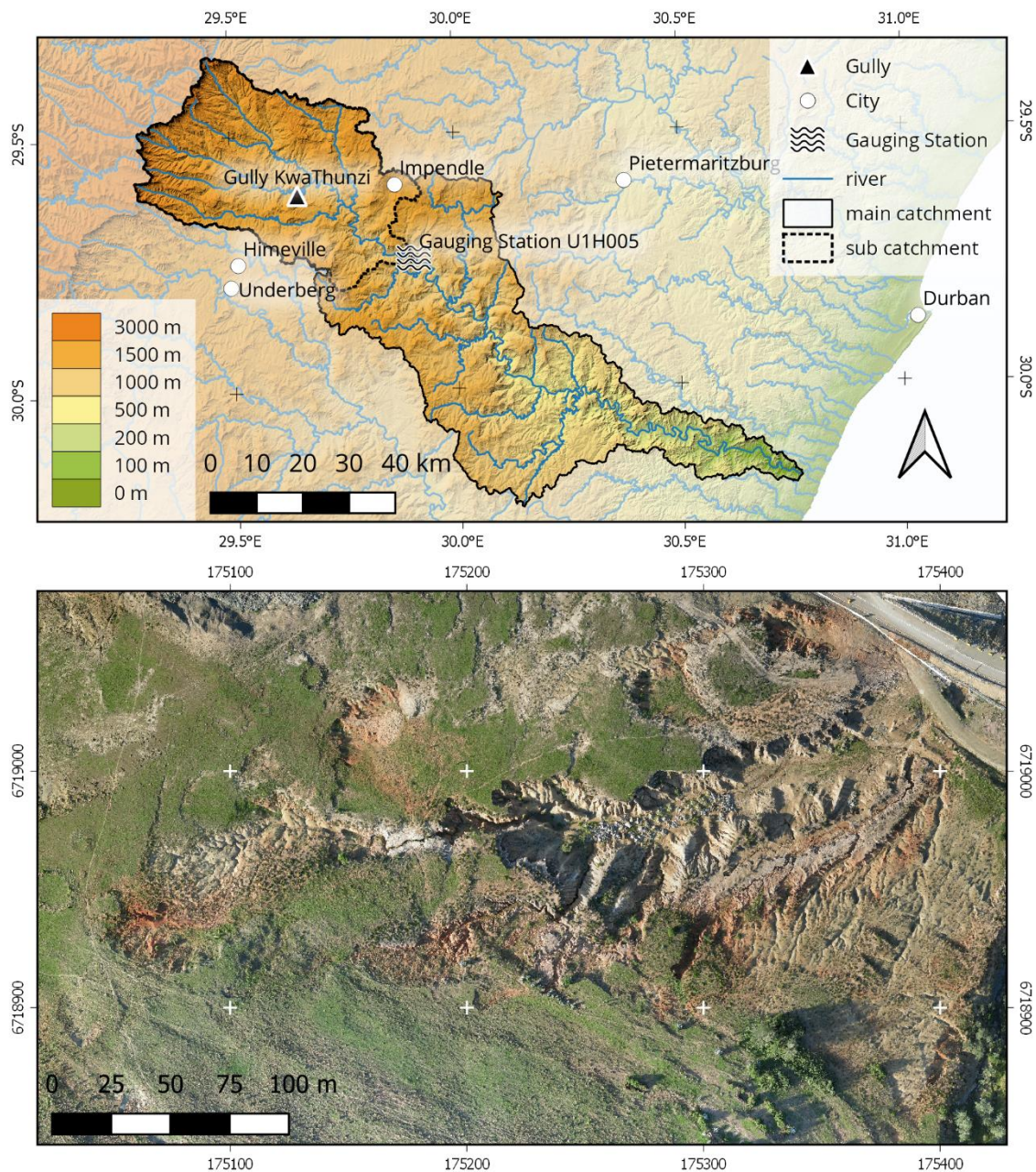
Fig. 2.2: Position of Gully KwaThunzi in the Umkomazi catchment (upper) with elevation data from TanDEM-X. Gully KwaThunzi (lower) as True-Color Orthophoto generated from UAV-Images (2018) and SfM-Modelling.

The lithology of the region comprises sandstones of the Beaufort Group, Late Cretaceous dolerites, Late Pleistocene colluvial sediments of the Masotcheni Formation (Fm.) and Holocene alluvial sediments. The focus of this study is the Masotcheni Fm. because of its function as an archive of Late Pleistocene landscape processes and their relevance for human occupation.
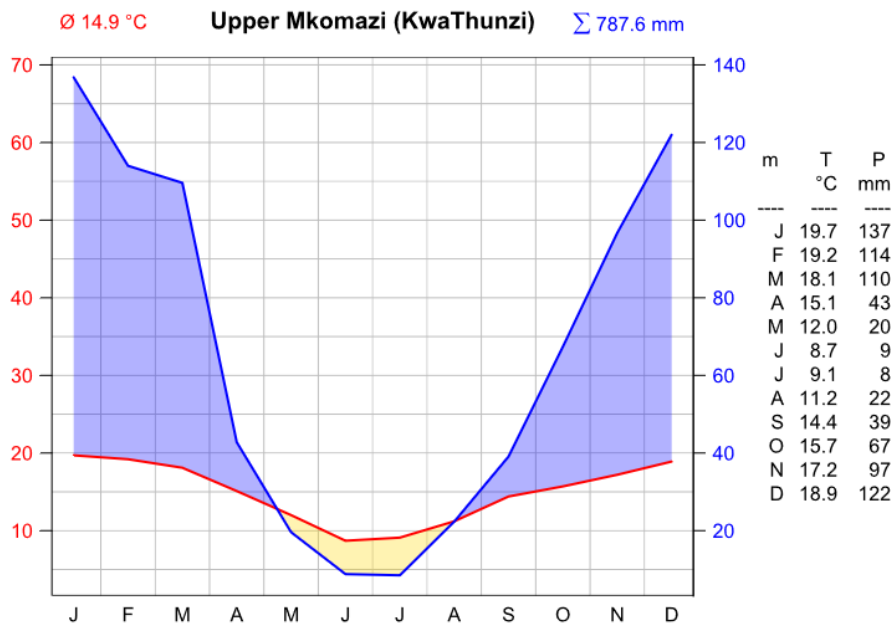
Figure 2.3: Walter-Lieth diagram of KwaThunzi between of 1960–2018. Calculated from data provided by CRU-TS v4.03.

2.2 Climate

The climate of KZN is strongly affected by the proximity to the Indian Ocean and the Agulhas current, as well as orographic effects. Today as in the past, eastern SA lies in the subtropical climate zone and is generally characterized by a strong inter-annual rainfall variability with high austral summer rainfall and winter dryness. This climate is generated from local factors, such as latitude, ocean currents and topography, as well as remote controls like ENSO (El Niño–Southern Oscillation), the Indian Ocean Dipole and the Antarctic Oscillation (Lennard, 2019).

2.2.1 Modern climate

The latitudes of Southern Africa divide the climate into regions with tropical control in the north of 23.5°S, subtropical control south of this latitude and a temperate climate in the mid latitudes north of 66.5°S. The orbital movement of the earth and the resulting migration of the ITCZ (Inner Tropical Convergence Zone) is responsible for the high seasonality of temperatures and precipitation. Furthermore, the warm Agulhas current brings moisture to the East Coast and the cold Benguela current is responsible for dryness on the West. Topography divides Eastern Southern Africa into moist Coastal Plains, the Escarpment with pronounced orographic climatic effects and a dryer interior. In addition, it plays an important role as climatic barrier, such as the Drakensberg Escarpment or as a climatic corridor, such as the Limpopo basin.

Apart from these local conditions, the Southern African climate has three major tele-connective influences. ENSO is a global phenomenon, which describes the Sea Surface Temperature (SST) oscillations over periods of 3–6 years. In Southern Africa, the El Niño years are generally drier than average, while La Niña are marked by increased moisture. ENSO events show their peak impact in austral summer months and therefore affect the important rainfall season in the SRZ (Reason and Rouault, 2005, Lindesay, 1988, Van Heerden et al., 1988).

Another remote connection, which influences especially the Eastern Coast is the Indian Ocean Dipole (IOD). Like ENSO, it is also related to SST variations and in positive phases, the Agulhas current is warmer, stimulating increased evaporation and subsequent precipitation on land. Negative phases consequently show lower SSTs and decreased precipitation in these years. The Antarctic Oscillation (AAO) is the third remote control, however it is not related to SSTs but rather to height anomalies of the mid-latitude zonal band over the Southern Ocean. In positive phases, mid-latitude storm tracks are pushed towards the Antarctic, which results in lower precipitation. Northern migration in contrast strengthens the rainfall, especially in the Winter Rainfall Zone (WRZ) (Reason and Rouault, 2005, Thompson and Wallace, 2000). These teleconnections influence climate at different cycles and amplitudes, so that their effect may overlay and thus weaken or strengthen the predominant local effects (Pohl et al., 2010, Lennard, 2019).

Most substantial rainfall in the SRZ is assigned to a low-pressure band between the tropics and the temperate mid-latitudes, called the Tropical-Temperate Throughs (TTT). It appears as a cloud ribbon spanning from the northwest to southeast and is made responsible for 30-60% of the precipitation in the November–March rain season (Hart et al., 2013, Lennard, 2019).

Mid-latitude cyclones pass south of the landmass in form of cold fronts from west to east. When these low-pressure systems are shifted towards the equator during winter, they cause strong northwesterly winds, storms and strong rainfall in the south and southwest of SA, but also snow

in the Drakensberg mountains. However, when a closed low pressure system diverts from the northern side of a mid-latitudinal cyclone, it is called a Cut-Off Low. These can occur all year round, but have a maximum in the spring and autumn months (Singleton and Reason, 2007, Favre et al., 2013). As they move in northeasterly direction, they contribute to rainfall in the Southern and Eastern Coast. When these become stationary, the may lead to severe floods, like 1987 in KZN (Lennard, 2019).

Subtropical anticyclones form at the descending part of the Hadley Cell. During winter these high pressure systems are often responsible for sunny days, cloudless nights and nightly low temperatures, especially in the interior (Lennard, 2019). During summer, the anticyclones become prevalent on the Western and Southern Coast. South Atlantic high-pressure systems cause the Southeasterlies. These may migrate in eastern direction and result in onshore flow of moist air. Moving towards the escarpment, the latter is subject to adiabatic cooling and condensation, promoting increased orographic precipitation on the South and South East Coast (Simon et al., 2015, Weldon and Reason, 2014).

Tropical cyclones are more short-termed phenomena with life times of few days, but potentially high impact. They form in the equatorial region of the West Indian Ocean or the Mozambique Channel and move along the Eastern Coast, delivering strong winds and severe rainfall to the coastal region. In KZN, cyclones like Domoina (1984) or Dineo (2017) caused heavy floods. Long time series have also revealed a positive relationship of cyclones with ENSO events (Fitchett and Grab, 2014, Reason et al., 2000)

2.2.2 Orbital forcing and paleo climate proxies

The global Pleistocene climate is characterized by the alternation of glacials and stadials with a frequency of ~100 ka (Huybers, 2011). The most prevalent theory makes the periodic oscillation of solar insolation responsible for this phenomenon and was described by Milankovic (1941). Thereafter, the long-term amount of solar insolation is a function of three main orbital parameters, which describe the orbital circulation and position in the solar system. The parameters displayed in figures 2.4a-d and 2.5 and 2.6a were calculated from the equations of Berger (1978), developed at the NASA Goddard Institute for Space Studies and are valid for the last 1000 ka.

The eccentricity (fig. 2.4a) describes the difference of the orbital shape and varies in a ~100 ka period between a rather circular and a more elliptic shape. This results in slightly different distances between earth and sun. The obliquity (fig. 2.4b) is defined as the axial tilt of the earth's rotational axis in relation to the orbital plane. This inclination varies between 21.5° and 24.5° in a ~41 ka period. During times of lower tilting, the polar regions receive reduced amounts of solar radiation. This tilted rotational axis furthermore rotates around the perpendicular line of the orbital plane, a process which is called axial precession (fig. 2.4c). This takes ~23 ka to complete a full rotation. The precession affects predominantly the inter-annual seasonality of climate and especially temperatures. Northern and southern hemisphere are in an antiphase relationship to precessional forcing, which means that a strengthening of seasonality on one hemisphere comes along with a weakening thereof on the other hemisphere. These orbital factors are in a close relation with other climate factors, such as greenhouse gases (e.g. CO_2, CH_4, etc.)
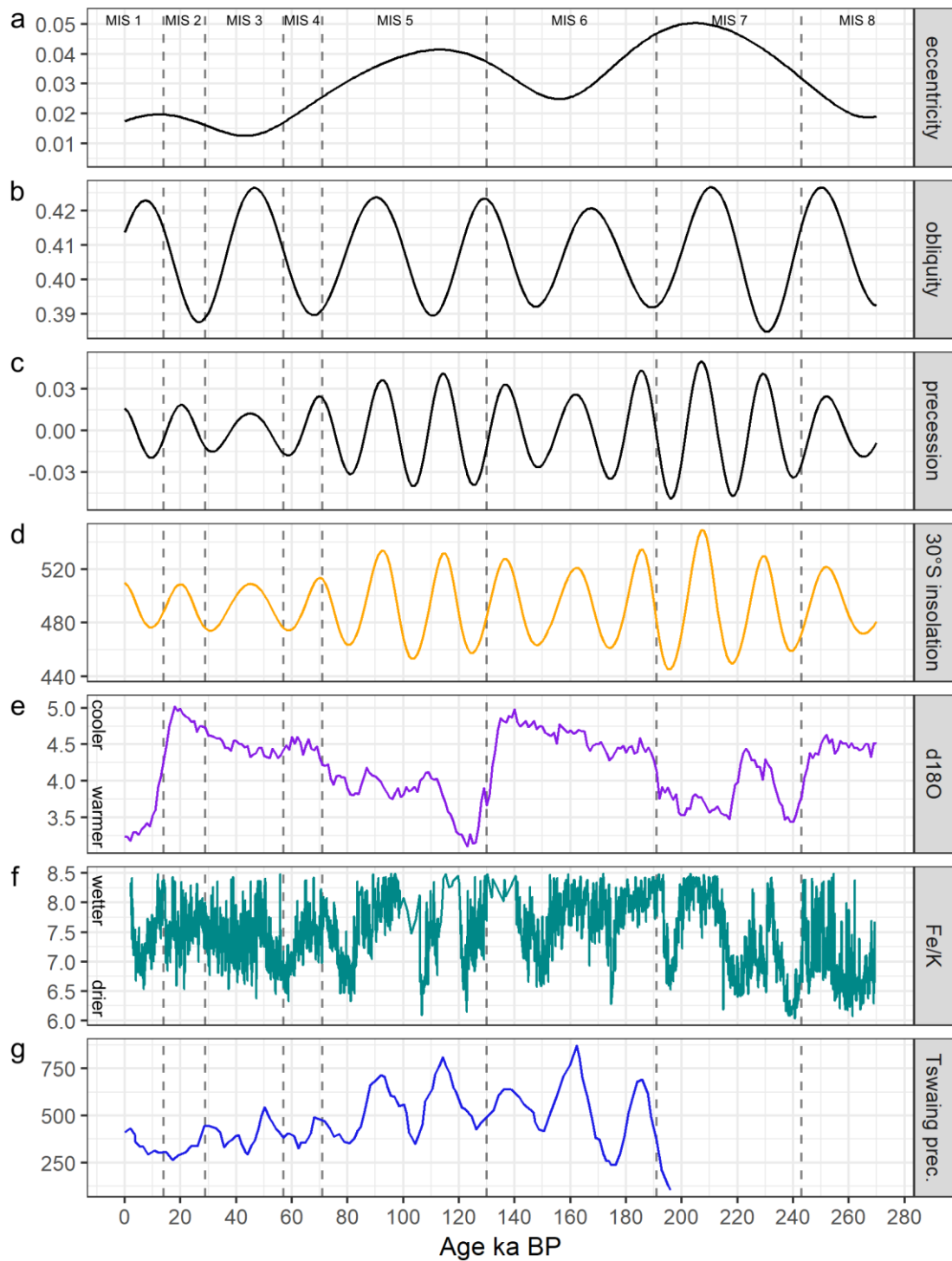
Fig. 2.4: Comparison of global climate drivers and local climate archives. a-d: orbital parameters after Berger (1978)Berger et al. 1987, d: daily insolation in W/m² on Dec 21st at 30°S after Berger et al. 1987, e: benthic oxygen isotope record from Lisiecki and Raymo (2005), f: Fe/K ratio from CD154-10-06P sediment core from Simon et al. (2015), g: precipitation in mm from Tswaing sediment core after (Partridge et al., 1997).

While global climate is dominated by eccentricity and obliquity, the climatic conditions in the lower latitudes, such as KZN, are strongly impacted by the forcing of orbital precession (Wang et al., 2008, Cruz et al., 2005, Collins et al., 2014, Meckler et al., 2012). Figure 2.4c-d displays the close dependency of the rainy season (Dec 21st) insolation at KZN on orbital precession.

Accordingly, positive precession values are linked with increased daily December insolation at 30°S. In MIS 7, variability is highest and fluctuates by almost 100 W/m² within one period, whereas the amplitude decreased strongly at the end of MIS 5 and remained low (~50 W/m²) until the end of the Pleistocene. In addition, figure 2.5 shows the inter-annual insolation variability. When the eccentricity is positive, insolation is strong in summer and low in winter, resulting in a high annual spread, which indicates more seasonal conditions. Negative precession is associated with lower summer insolation and higher winter insolation. These differences between strong and weak seasonality become less significant after MIS 5, when the variability of solar radiation remains lower.
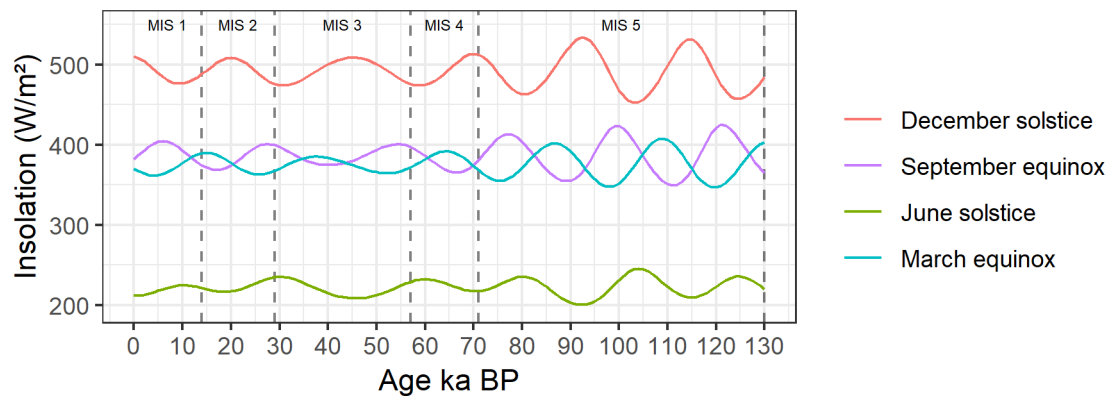
Fig. 2.5: Variation of solar insolation at 30°S calculated after Berger 1987.

Benthic stable oxygen isotope records are derived from the $^{18}O/^{16}O$ ratio in foraminifera calcium carbonate shells and are used as proxy for past climate. Ocean temperature, evaporation, salinity and the amount of water stored in ice determine the proportions of the isotopes, where higher ^{18}O indicate globally cooler conditions (Epstein et al., 1953, Schmidt, 1999). The LR04 stack from Lisiecki and Raymo (2005), assembled from 57 deep sea cores, is presented in figure 2.4e. It displays the global cooling trend since MIS 5e towards the last glacial maximum in MIS 2 and the subsequent termination towards the Holocene. Furthermore, the widely used Marine Isotope Stages (MIS), were derived from this dataset. Uneven stage numbers were chosen for warmer phases, stadials and interglacials, whereas the even numbers stand for cooler glacials and interstadials.

Local long and continuous climate archives, like the terrestrial core from the Tswaing impact Crater (fig. 2.4g) and marine sediment cores (CD154-10-06P, CD154-17-17K) off the Eastern Coast show a positive relation between 30°S summer insolation and precipitation (or moisture, respectively) (Partridge et al., 1997, Simon et al., 2015, Ziegler et al., 2013).

The deep sea core CD154-10-06P in the southwestern Indian Ocean is situated ~160 km off the KZN coast and serves as a marine archive of the region's terrestrial discharge (Simon et al., 2015). Humid climate leads to increased tropical bedrock weathering, enhanced erosion of iron-rich soils and transport of suspended material into the Indian Ocean. Chemical weathering alters the structure of clay minerals through replacement of silica with iron oxides (Govin et al., 2012). Therefore, the Fe/K ratio in sediments is interpreted as a proxy for water related processes, such as chemical weathering, erosion and runoff, where high values represent more humid conditions than low values. The Fe/K ratio curve from CD154-10-06P is presented in figure 2.4f and figure 2.6b. The link between precession summer insolation and this humidity indicator is

apparent until the early MIS 3. At high precession, strong summer insolation strengthens the monsoonal influence and local convection, while the lower winter insolation keeps the dry season desiccation at a low level. From MIS 3 on, the link between precession and humidity becomes less apparent, possibly because the amplitude of precession becomes weaker or other factors become more influential.
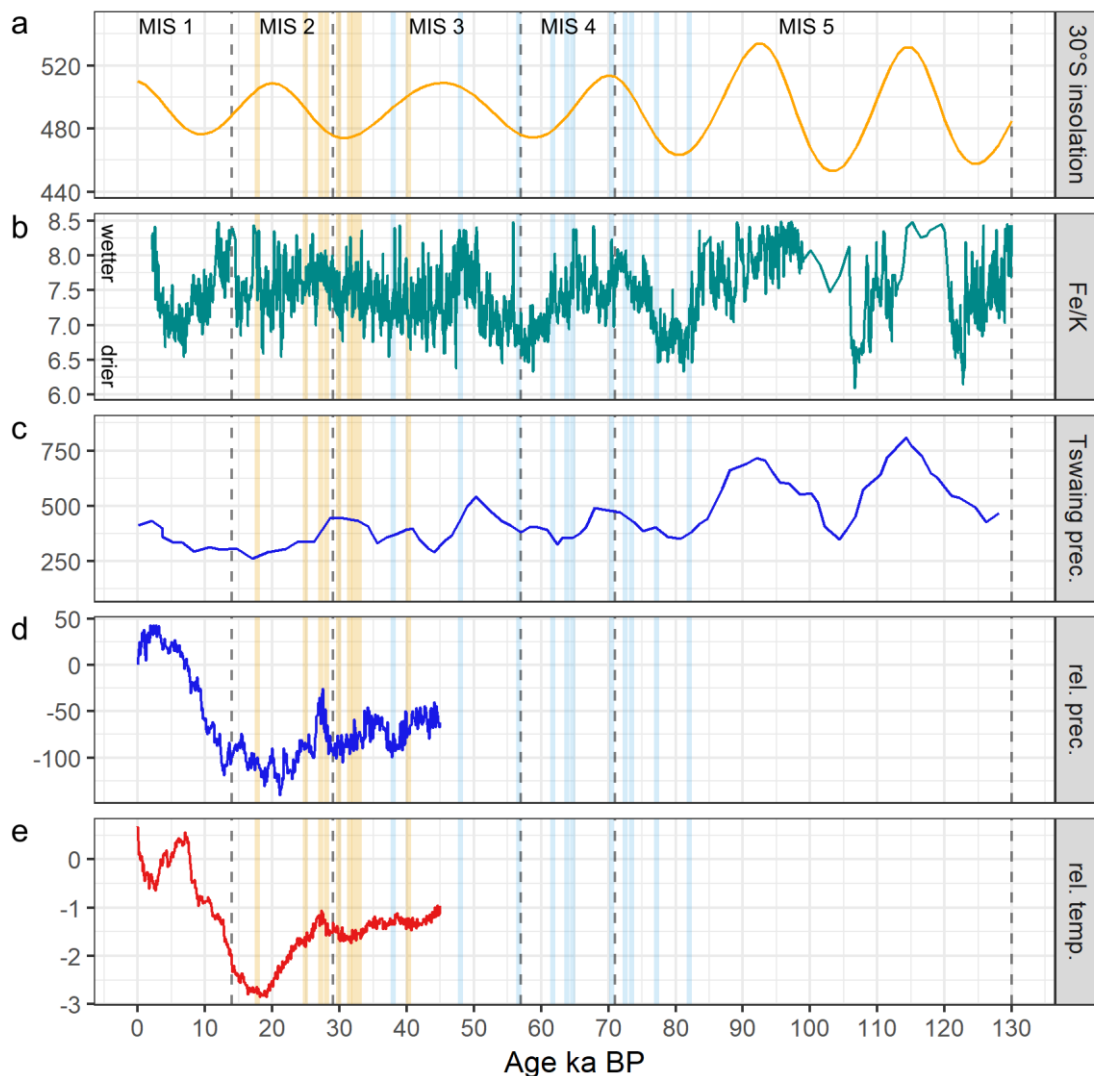
Fig. 2.6: Comparison of local climate datasets with human occupation at Sibudu Cave and Umbeli Belli. a: daily insolation in W/m² on Dec 21st at 30°S after Berger Berger (1978), **b**: Fe/K ratio from CD154-10-06P sediment core from Simon Simon et al. (2015) et al. 2015, c: precipitation in mm from Tswaing sediment core after Partridge et al. (1997), d-e: summer precipitation in mm and annual temperature in °C of the SRZ reconstruction from Chevalier and Chase (2015)Chevalier & Chase 2015, dates from Sibudu (blue vertical lines) and Umbeli Belli (yellow vertical lines).

A paleo precipitation dataset from the interior plateau by Partridge et al. (1997) is presented in figure 2.4g and 2.6c. A lacustrine depression, called Tswaing or Pretoria Saltpan in scientific literature, developed in an impact crater, whose formation event is dated to 220±52 ka (Partridge et al., 1993). The borehole sequence of alternating micritic (carbonate rich) layers and terrigenous sediment layers allowed the authors to reconstruct the proportion of precipitation and evaporation in this area over a time-span of 200 ka. The modelled results suggest a close relationship of precipitation and precession. Just like the data from Simon et al.

(2015), orbital forcing is made responsible for increased austral summer precipitation. Furthermore, the data suggest, that the amplitude of cyclical precipitation changes decreases after MIS 5 in response to local insolation.

Pollen derived reconstructions for southeast Africa (fig. 2.6d-e) from Chevalier and Chase (2015) display stable relative temperatures of -1°C below modern temperatures between 45 ka and 25 ka and a subsequent decrease towards the Last Glacial Maximum with a minimum relative temperature of nearly -3°C. The related precipitation stack proposes stable relative rainfall around -75 mm between 40 ka and 30 ka followed by a reduction to below -100 mm during the LGM. With the termination of the LGM and subsequent Holocene, both temperatures and precipitation increased.

2.2.3 Drivers of paleo climate

2.2.3.1 Inner Tropical Convergence Zone

Southward latitudinal shift of the ITCZ is associated with northern hemisphere cooling events (Johnson et al., 2002, Castañeda et al., 2007, Simon et al., 2015, Schefuß et al., 2011, Broccoli et al., 2006). Thereafter, northern cooling induces a northward energy flux from the southern hemisphere by rearrangement of the Hadley Cell circulation and oceanic overturning (Broccoli et al., 2006). This results in a southward migration of the ITCZ, exceeding its modern-day margins. This goes along with a migration of the ITCZ related rain belts, but also a southward shift of the subtropical anticyclones, that are influential for KZN climate (Simon et al., 2015, Reason and Mulenga, 1999).

For a deeper understanding of the influence of precession on climate processes, Simon et al. (2015) conducted a climate model experiment for South Eastern Africa. They applied a model to simulate past climate during maximal and minimal precession. Their results indicate, that higher land temperatures during precession maxima in the Southern hemisphere come along with low atmospheric pressure over land. This promotes a pressure gradient and consequent strengthened north-easterly winds from the ocean off Mozambique. Assuming that the Southern hemisphere warming also increased Indian Ocean and Agulhas Current SSTs, greater amounts of moisture could be transported onshore. Furthermore, local evapotranspiration was reinforced through higher temperatures, thus resulting in increased precipitation.

2.2.3.2 Sea surface temperature

Around the LGM several authors indicate, that the periodical climate-insolation relationship was superimposed by the influence of the Sea Surface Temperatures (SST) in the Mozambique Channel (Chevalier and Chase, 2015, Truc et al., 2013, Dupont et al., 2011). Although the summer insolation was at a peak during the LGM, the upper layers of the tropical western Indian Ocean were considerably cool and in phase with northern hemisphere ocean circulation (Bard et al., 1997, Sonzogni et al., 1998). A climate model experiment by Otto-Bliesner et al. (2014) makes alterations in the Mediterranean-Arabian anticyclone responsible for coastal upwelling off Somalia and the Arabian peninsula, which in turn cools the Western Indian Ocean. In most studies investigating the resulting LGM temperature depression, these values are centered around a relative SST of -5 – -6°C (Holmgren et al., 2003, Kulongoski et al., 2004, Scott, 1982), while Chase et al. (2015) point out, that there is gradient of temperature depression from coastal to inland areas, so that their reconstruction of a relative SST of -3°C appears plausible for the

Eastern Coast of SA. An influence of SSTs on precipitation can be inferred from pollen records of marine sediment cores (Dupont et al., 2011) or terrestrial sources (fig. Cd). The record presented by Chase et al. (2015) constitutes a decrease of precipitation by more than 100 mm. The underlying hypothesis constitutes, that lower SSTs reduce convection. Together with cool land temperatures, this weakening the pressure gradient between sea and land and leads to reduced transport of moist air onshore. According to correlations of SSTs with the temperature and precipitation stack by Chase et al. (2015), the influence of SSTs on climate is already present in MIS 3 and becomes most dominant in MIS 2. After the glacial termination however, precession is made responsible primarily for warming and an increase of precipitation.

Apart from the Mozambique Channel, also the SSTs at higher latitudes are expected to impact Southern African climate. An expansion of southern sea ice during glacial maxima is expected to have shifted the prevailing westerlies towards a more equatorward position. Therefore, areas in the Western Cape, the Southern Coast and also the interior would be affected by these wind belts and thus increased winter precipitation. This effect has been described by several authors and was affirmed by multiple climate simulations (Chase and Meadows, 2007, Miller et al., 2019, Stuut et al., 2004, Govin et al., 2009, Mills et al., 2009, S.C. et al., 2009, Mills et al., 2012)

Furthermore, short timed strongly humid phases are mentioned in Ziegler et al. (2013) and brought into relationship with temporary Northern Hemisphere cooling events (e.g. Heinrich events).

Chapter 3: Cenozoic Planation Surfaces

This chapter addresses Q1 and the question of the age, evolution and landforms of the Tongati Valley. Planation surfaces play an important role in the development of the valley, which owes its mountainous character of the middle and upper catchment to long-lasting landscape cycles. Therefore, this tackles the question, how different levels of the landscape scenery can be correlated and what this tells about their age, but it also deals with the issue, how the catchment got its modern shape.

3.1 State of research

3.1.1 Gondwana breakup

The breakup of Gondwana started with the split up between Africa and Antarctica in the Jurassic. West Gondwana started to separate during the Cretaceous. Lithospheric movements between 135 and 115 Ma created weaknesses "along pre-existing Pan-African welts" (Partridge, 1998), which had forged the cratons and terranes of Gondwana together (Knight, 2019). The Tugela fault is the most extensive example of such a weakness in KZN. On the East Coast, the stretching of the margin between Africa and Antarctica led to tilted block faulting in a seaward direction (Maud, 2012). This tilting produced a gradient from the high elevations in the Interior towards the low-lying coast and led to a change from a depositional basin towards an erosional regime. An earlier stage of the Escarpment, within ~50 up to 200 km from the coast, commenced to retreat. This was supported by the humid tropical climate during the early Cretaceous (Maud, 2012). By the end of the Cretaceous, the Proto-Escarpment receded as close as 20 km to its modern-day position, which is indicated by remnants surfaces all over eastern SA (Brown et al., 2002).
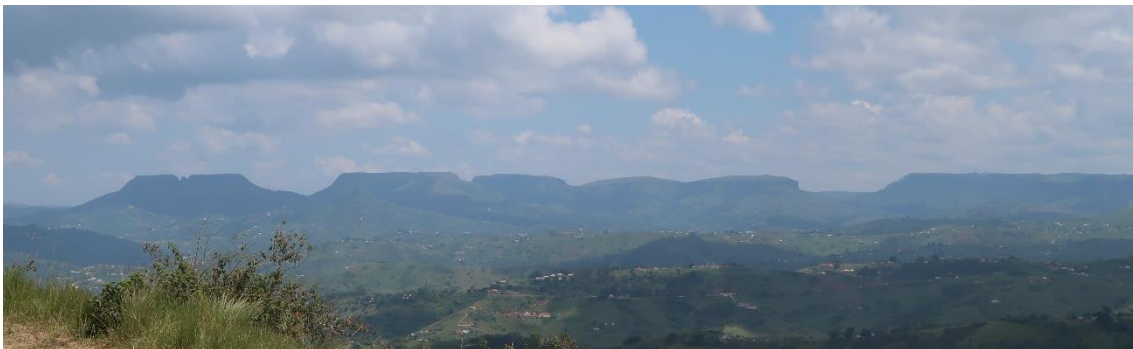
Fig. 3.1: Image of the African Surface in the Tongati Valley. View from the Ozwatini Plateau to the west illustrates the accordance of summits, which is related to the African Surface. Photo: Sommer.

Today, mesa-like flat surfaces at different elevations and degrees of weathering can be noticed in the landscape. Different explanations for the genesis of these features have been presented and heavily debated, including peneplains, pediplains and etchplains (Twidale, 1988). The role of this region in the development of geomorphological theory is not at last the result of the work of King (1948), who developed his theories of pediplanation, in which a pediplain is formed through deposits on footslopes of retreating scarps. Most argue however, that the planation surfaces in KZN were formed through peneplanation, the process of extensive widening of valley bottoms leaving behind eroded, flat surfaces as the final state of W.M. Davis' Cyclic Theory (Burke and Gunnell, 2008, Burke and Wilkinson, 2016, King, 1948, Du Toit, 1954). Therefore, the

multiple levels of planed surfaces would represent multiple cycles of uplift and hence rejuvenated phases of erosion (Knight, 2019). Other authors see a more complex relationship of regional drainage patterns and drainage divides, which change in response to uplift (Partridge and Maud, 2000) or the migration of mantle swells (Moore et al., 2012, Moore and Larkin, 2001). Furthermore, Knight and Grab (2018) make climate change driven alterations in drainage density responsible.

3.1.2 African Surface

The *African Surface*, which is the oldest known planation surface, is expected to have lasted 70 Ma and is older than the end of the Cretaceous (66 Ma) (Maud, 2012) or 85–54 Ma (Knight, 2019). Remnants spread all over SA indicate, that a complex co-action of processes was indeed involved. The simplified assumption states, that different elevation levels of planation surfaces represent different times of creation and appears to be valid for the general understanding of the landscape. However, this statement is too imprecise in detail. The African Surface rather consists of two simultaneously developed planation surfaces (Partridge and Maud, 1987). The lower one comprises a well-developed erosion platform sloping gently towards the coast, which in turn embodies the erosional base level. The presence of marine abrasion benches onshore testifies for at least two major ocean transgressions between the Upper Cretaceous and the Eocene (Maud, 2012). Diatremes from kimberlite remains in the coastal hinterland allowed the reconstruction and dating of this low-lying planation surface (Partridge, 1998, Hanson et al., 2009). The higher part of African Surface lies above and inland of the continuously retreating Escarpment. This planation surface developed in fluvial networks, that drained the elevated platform. Therefore, outlets and waterfalls that lay above steep slopes along the edge of the Escarpment were base levels of this high-lying African surface. Some mountain massifs, like the Cape Fold Mountains, but also areas above the Great Escarpment in Lesotho, Mpumalanga and Limpopo were unaffected by the planation process (Maud, 2012).

The warm and humid conditions during the Cretaceous not only created efficient erosion networks, but also deep, chemically weathered crusts, where altered bedrock was not removed. Partridge and Maud (1989) describe kaolinized saprolite profiles with a depth of over 50 m, which attest the tropical-like conditions of weathering. In the Late and Post-Cretaceous, climatic conditions changed towards higher aridity and even desiccation, especially in the central and western regions of Southern Africa. This fostered the development of resistant duricrusts on the weathered surfaces, protecting the African Surface from erosion until today (Botha, 2000, Nash, 2012). The majority of African Surface remains are covered by silcretes, however the remains in KwaZulu-Natal were conserved under laterite and ferricrete cappings. The cementation of silcretes allows to make estimations on the past environmental conditions. Pedogenic silcretes are formed under a climate with variable humid and arid seasons or periods (Nash, 2012). Furthermore, drainage line silcretes, groundwater silcretes and pan silcretes allow conclusions about topography, drainage pattern and groundwater table of the planation topography (Nash and Ullyott, 2007). Laterites however are formed under more humid and tropical conditions with warm temperatures and high seasonal precipitation (Widdowson, 2007). Therefore, KwaZulu-Natal, in contrast to other regions of the sub-continent, appears to have been less affected by Late Cretaceous desiccation (Maud, 2012, Nash, 2012). In KwaZulu-Natal, remains of the African Surface are very prominent in area halfway between Pietermaritzburg and Durban, extending to the north. Further remains of the high-lying African Surface are found above the

Great Escarpment, the Highveld (Free State Province) and the Mpumalanga Province (Maud, 2012).

3.1.3 Post-African I

In the Oligocene / Early Miocene, the South African sub-continent was subject to an epeirogenic uplift, which raised the entire landmass without any orogenic or volcanic activity. Upheaval was spatially unbalanced, while the Western part was lifted by about 150 m, the Cape region by about 200 m and the Eastern Part is expected to have risen between 250 m and 300 m (Maud, 2012). High terraces, situated 40-50 m above the recent Orange River on the West Coast, indicate fluvial erosion with 100-200 m of depth cut into the African Surface. In the northern part of South Africa, the uplift was accompanied by flexural movements in the lithosphere, cutting southward draining rivers from the north and relocating the main water divide further south towards the Bushveld Basin (Maud, 2012). On the East Coast, where uplift was strongest, the Natal Monocline, already established in the Jurassic, was reactivated once again. Along this axis, situated ~80 km inland parallel to the Indian Ocean coastline and spanning from Port Elizabeth to Eswatini, the surface inclined towards the ocean (Partridge, 1998). The part of the landscape, which formed in response to this uplift, was denominated as Post-African I by King and King (1959). After the removal of major parts of the African Surface, a relative lower lying plane surface was eroded into the subjacent bedrock. This left behind a smooth surface with scattered koppies, i.e. structural resistant hills that withstood degradation. The fluvial terraces of the Orange river, mentioned before, which were lowered in response to the uplift, were dated to 19-17 Ma based on faunal remains in fluvial deposits (Maud, 2012). Pedogenetic skins, which covered the Post-African I and are therefore slightly younger than the surface itself, were estimated to an age of 12-15 Ma (Van Niekerk et al., 1999). Remains of the Post-African I surface can be found on the East Coast parallel to the southern shoreline up to the Tugela Valley. Also the Lowveld in the Mpumalanga province bears large areas covered with these planed surfaces (Partridge, 1998). However, the planation of Post-African I never became as advanced as the African Surface, since another, even heavier uplift interrupted the progress.

3.1.4 Post-African II

By the Early to Middle Pliocene another epeirogenic event shaped the landscape. The premature Post-African I surface development was discontinued by a massive uplift, that centered in the eastern coastal hinterland, proximal to the axis of the Early Miocene events. According to Partridge et al. (2010), the land was raised by up to 600-900 m. Marine fossils in the southernmost Eastern Cape, which date to the Early Pliocene, lie today ~20 km inland and were lifted to an elevation of 400 m a.s.l. (King, 1973). Not far from that, near East London, Partridge and Maud (1987) mention Late Cretaceous and Eocene marine sediments at an elevation of 350-400 m above modern sea level. The uplift on the East Coast was followed by tilting of the landscape towards the ocean. Maud (2012) reports, that the pre-developed and ripe planed surfaces in the stable area, west of the tilting axis, have an average gradient of 1-3 m/km. In the inclined area however, their counterparts' gradient is distinctly higher with up to 40 m/km. In other regions of South Africa, total uplift was considerably lower, with 200 m in the Cape region and only 100 m on the West Coast, while the flexural movements around the Bushveld Basin, which were already active in the Miocene, intensified and resulted in a subsidence of up to 400 m. In the Cape region, tilting along the Agulhas-Vredenburg axis led to the subsidence of larger

land masses below the sea level, which re-emerge at sea level lowstands (Partridge and Maud, 1987).

Unlike the previous erosional surfaces, the Post-African II generated only few planed surfaces due to the short lifetime of ~3 Ma. Some of the few examples of planation, which developed in weaker lithologies, as Maud (2012) points out, are preserved in the eastern Lowveld of Mpumalanga, Eswatini and in northern KZN. In contrast, the Post-African II can be characterized by increased valley incision. The steepened gradient between hinterland and coast, resulting from seaward tilting, increased channel gradients. This augmented the erosional capacity of eastward draining rivers on the East Coast. The deep-cut gorges and dissected landscapes in the *Valley of a Thousand Hills*, between Durban and Pietermaritzburg, or the Tugela Valley are attributed to this period. Furthermore, the influence of the uplift event on fluvial morphology in terms on knickpoints can be correlated across many river long profiles (Maud, 2012). Furthermore, the headcut erosion of river systems further displaced the Great Escarpment towards the interior. Martin (1987) studied the increased sedimentation rates in the marine Natal Valley, and retraced the Pliocene erosional activity in the marine deposits.

3.2 Methods

A comprehensive map of paleo surfaces that developed since the Mesozoic was produced by Partridge and Maud (1987). It covers for the whole of South Africa, Eswatini and Lesotho at a mapping scale 1:2.500.000. The aim of this work is to take up the fundamental method by these authors and (i) transform their 2D-profiles to 3D-maps, (ii) provide a GIS-based method to downscale their map to a large-scale map of the study area by using a high-resolution DEM (TanDEM-X 13 m), in order to produce a chronological framework of the large geomorphic cycles of the study area.
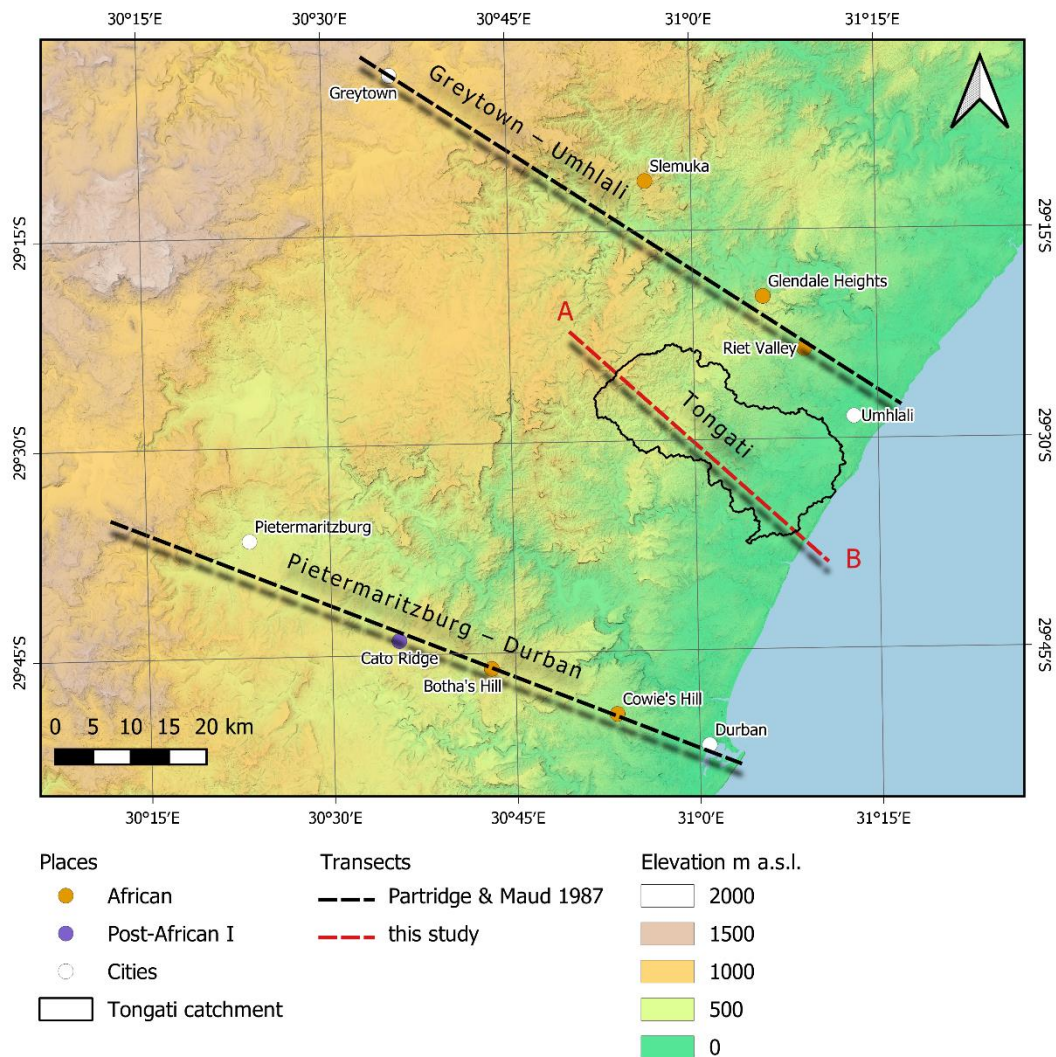
Fig. 3.2: Transects through recent topography and reconstructed paleo-surfaces with relevant locations in Partridge and Maud (1987) and this study.

3.2.1.1 Mapping criteria

The fundamental method by Partridge and Maud (1987) comprises the field mapping of surface remnants along transects and subsequently, the correlation and identification of areas between these sections through interpolation. The authors mapped a total of 21 transects in SA, of which eight are located perpendicular to the East Coast shoreline. Sections Nr.4 (Greytwon–Umhlali) and Nr.5 (Pietermaritzburg–Durban) lie in the vicinity of the Tongati catchment.

21

The authors identified surfaces along intersections, and interpolated missing remnants based on elevation information from topographic maps with scales of 1:250,000 and 1:50,000. These 2D sections were further interpolated and areas that intersected the estimated paleo surface were mapped at a scale of 1:2,500,000.

The survey compiled datable marine deposits and different levels of duricrusts. The oldest surfaces were identified as laterites in eastern SA (or silcretes in other areas of SA) with kaolinized underlying bedrock. Their results from the East Coast show, that kaolinization is prevalent in bedrocks like granite, dolerite, shales, schist, phyllite and Karoo sedimentary rocks, while morphologically hard bedrocks, like the Natal Sandstone, are less prone to this process. Younger profiles (i.e. Post-African I and II) are typically marked by ferricretes and deep weathering, and differ from the African surface by the lack of kaolinization. They also included areas, where laterite cappings or weathering profiles were removed by erosion, but the presence of remnants was apparent and tectonic origin could be excluded. In addition, broad flat areas were used as indicator, and traces of erosional or structural alteration within the remnants were taken as evidence for imperfect planation in the subsequent cycles. Furthermore they included paleo-drainages, such as "defunct channel systems, dismembered drainage, pans [..] and gravel lags of old channels"(Partridge and Maud, 1987).

3.2.1.2 GIS based downscaling

The procedure to increase resolution and map paleo surfaces at a finer scale in the study area incorporates three steps: (i) collection of interpolation points, (ii) spatial interpolation of hypothetical paleo surfaces between those points, (iii) calculation of the intersection of modern-day topography with the estimated elevation of paleo surfaces. An optional additional step (iv) includes the derivation of flat areas from the DEM, to facilitate the mapping of typical planation surfaces.

The outer boundary of the interpolation points was collected along the section Nr.4 (Greytown–Umhlali) and Nr.5 (Pietermaritzburg–Durban) in Partridge and Maud (1987). Their findings were digitized based on topographic maps with a scale of 1:50,000 and 1:250,000 (fig. 3.2). These were combined with observations from field survey in the Tongati Valley, as well as information provided by the explanations of the geological map 2931CA Verulam (Clarke et al., 2007).

Elevation information was sampled from the TanDEM-X elevation model and attached to the interpolation points. The sampled points were assigned to either African or Post-African I surface. Post-African II was omitted, since it produced few well-developed surfaces in this area and is rather represented by incised valleys than broad planations. The points were interpolated to create an artificial surface, which represents a hypothetical planation surface. This virtual surface implies completed surface lowering and a topography that is cleared to the erosional base-level of the respective erosion cycle. The Natural Neighbor (NN) method was found to be most suitable for this purpose, as the method is beneficial for small point datasets (Boissonnat and Cazals, 2002). NN belongs to the group of deterministic, local and exact interpolators (Sibson, 1981, Watson, 1999, Boissonnat and Cazals, 2002, Ledoux and Gold, 2005).Therefore it shows many commonalities with other weight averaging methods, such as the Inverse-Distance-Weighted (IDW) interpolation. Furthermore, the uneven distribution of samples, even centered along the linear sections, hinder the application of geostatistical methods, such as Kriging

techniques. Especially the observed spatial clustering of paleo surface remnants is likely to produce artefacts in the calculation of semi-variograms, which are fundamental for the latter. While this makes NN an adequate technique for this study, limitations are the improper ability to extrapolate beyond sampling extent (spatial as well as elevation dimension) and incapacities to handle boundary conditions. This means practically, that this method does not allow to estimate (i) values outside of the sampling area (here the rectangle between Pietermaritzburg, Durban, Umhlali and Greytown), (ii) values that are higher (or lower) than the highest (or lowest) sampling point, and that (iii) natural breaks in the surface, such as tectonic dislocations that would have succeeded the planation cycle, would cause distortions in the interpolation. In areas, where these subjects apply, methods like Global Polynomial Interpolation (for i & ii) or kernel interpolation with barriers (iii) should be favored. In the Tongati Valley, this was not necessary.

As a result, raster datasets with the potential elevation of paleo surfaces in each pixel were constructed. Differential paleo surfaces were then calculated through basic raster arithmetic from the artificial paleo surfaces and modern elevation data. Ergo, the differential surfaces represent the vertical difference between the potential planation surface and recent topography. The differential surfaces are presented in figure 3.3.

Furthermore, masks were created from the differential DEM, where slopes were lower than 5°. This mask could not be calculated from the modern DEM, since modern slopes represent a sum of paleo landscape slope and the subsequent tilting. Finally, flat areas were vectorized and assigned to their respective planation surface based on the vertical distance to the differential surfaces. In other words, flat areas were intersected with areas, that lie within a vertical margin above or below the potential planation surfaces.

3.2.1.3 Landform classification

The topographic position index (TPI) is a topographic index that describes the terrain position quantitatively from height information. The relative elevation of a central terrain point is compared to the average elevation of the surrounding. This results in a value of

- TPI>0, if the terrain position is higher compared to its surrounding, for example a mountain peak or ridge
- TPI=0 if the terrain point has a similar height as the average of the surrounding area. Thus, this value can stand for a middle slope, a flat surface or a saddle.
- TPI<0, if the terrain position is lower than the average of the surroundings, which is the case for example in a valley or a gorge.

By choosing a multi-resolution approach, which combines the results of different kernel sizes, the terrain position can be further specified. Since the TPI is scale-dependent, the results of different kernels must first be normalized to allow a direct comparison of the values. This combination allows to classify geomorphic features, such as high valleys or meander spurs in river valleys.

In a GIS environment this approach is solved by combining a DEM with a spatial kernel window that defines the environment. Thus, the value of the TPI is largely determined by the raster properties (i.e. cell size of the DEM) as well as kernel radius and a weighting function. The method proposed by Guisan et al. (1999) and Wilson and Gallant (2000) is available in the "Terrain Analysis Toolbox" of "SagaGIS" v.7.3.0 (Conrad et al., 2015).

a) African surface
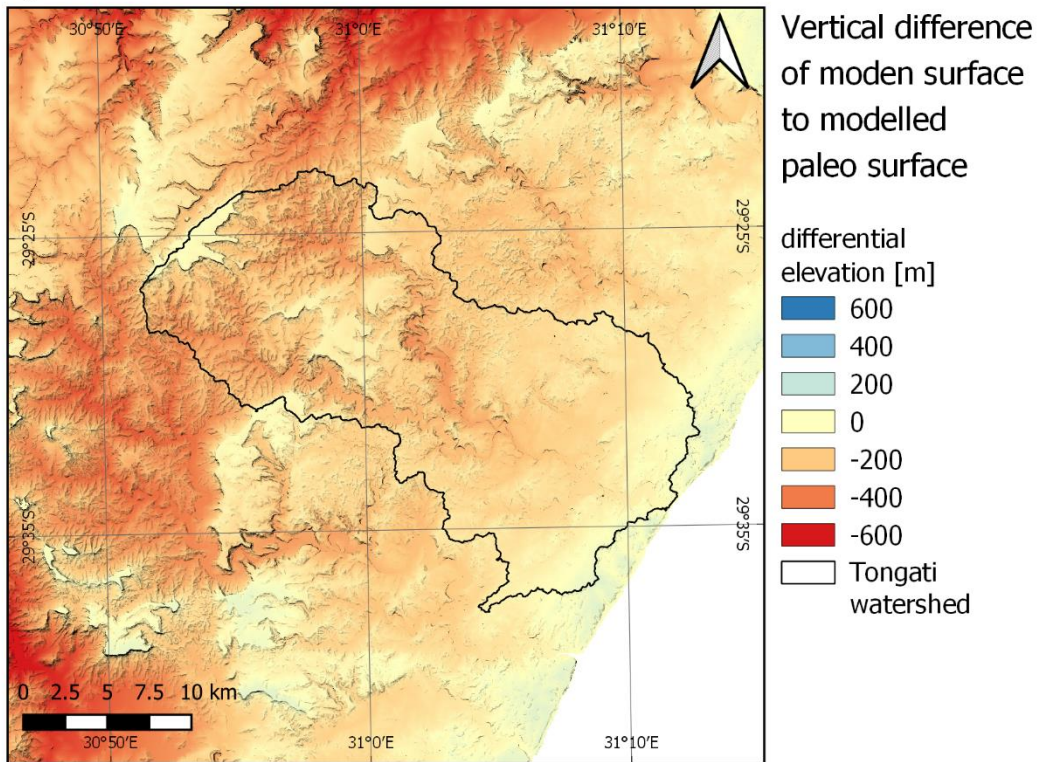
b) Post-African I surface
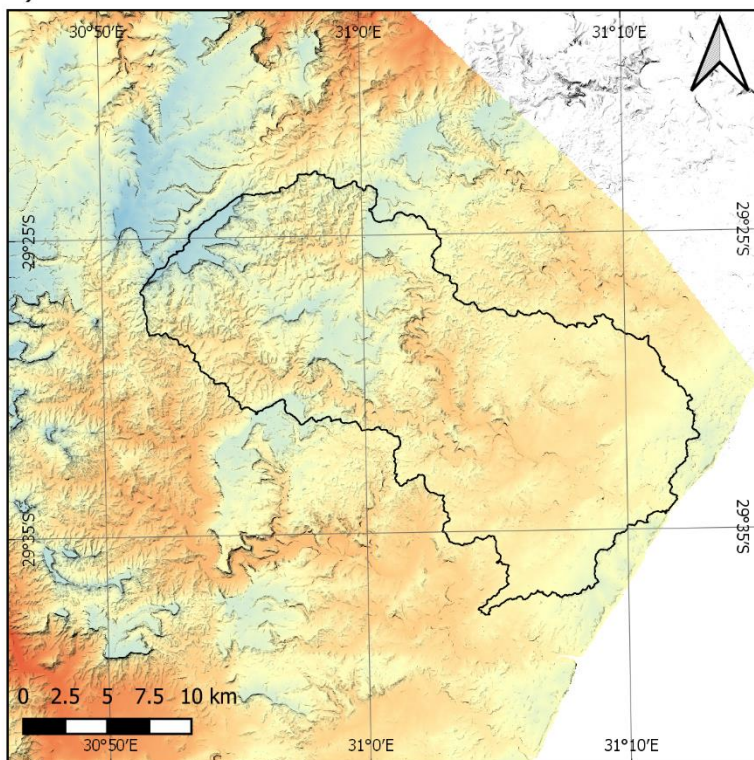
Fig. 3.3: Differential DEMs show the vertical distance of the modern elevations to the estimated paleo surfaces.

Several combinations of kernel size (100 m–2000 m) and weighting functions (no weighting, inverse distance, exponential, gaussian) were tested in this study. The optimal configuration to reproduce the conditions observed in the field with TanDEM-X data was achieved with an inner radius of 200 m, outer radius of 1000 m, and a gaussian weighting. The landform classification of the Tongati Valley is presented in figure 3.4.

The results of the TPI analysis for flat areas was combined with the classification described in chapter 3.2.1.2 in order to produce a dataset with these landforms. The final classification was validated by literature studies, visual interpretation of the topography according to the criteria named in chapter 3.2.1.1 and field observations in 2018 and 2019. The map is presented in figure 3.5.
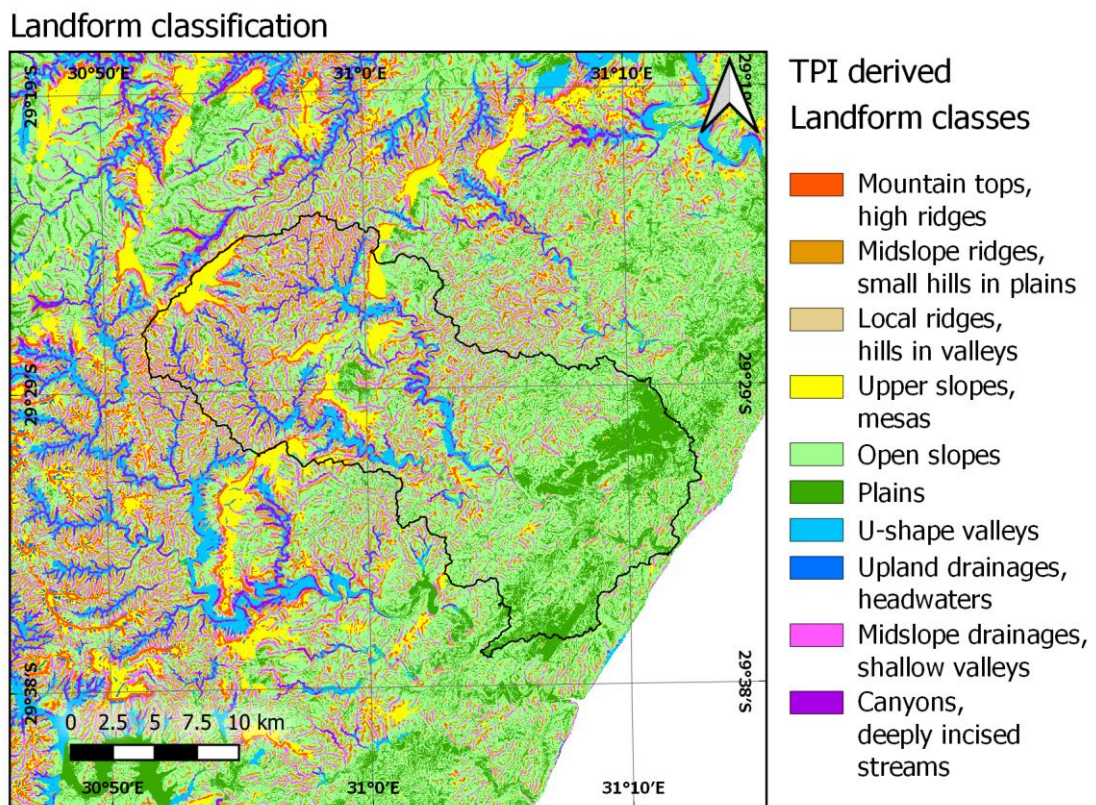
Fig. 3.4: The landscape classes of the Tongati catchment derived from the DEM.

3.3 Results

The map displayed in figure 3.5 shows the remnants of the planation surfaces in the Tongati catchment. A cross-section through the study area is presented in figure 3.7.
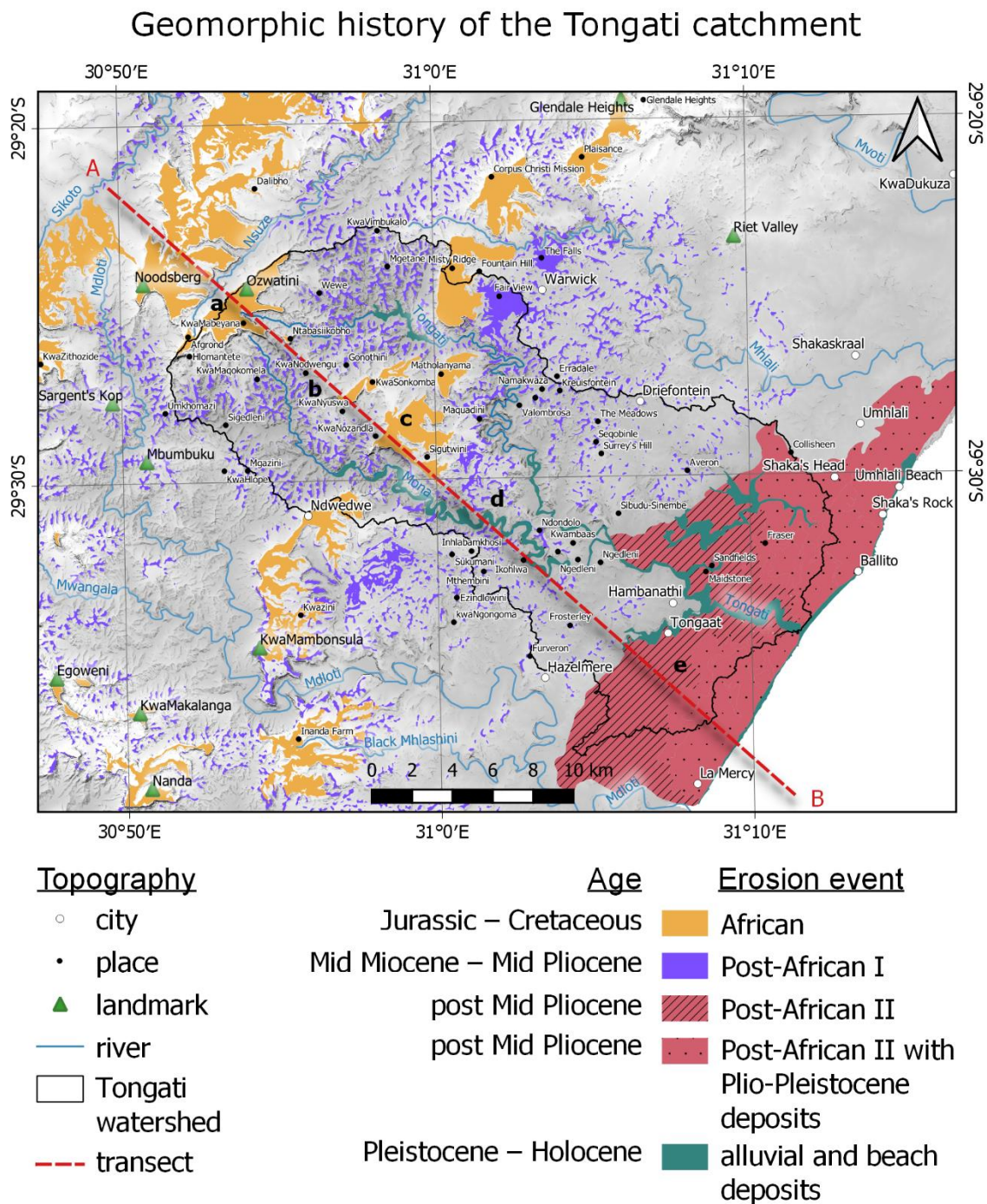
Fig. 3.5: Geomorphic history of the Tongati catchment.

The remains of the African surface are located in the headwaters and the middle part of the catchment. A distinct planation was identified in the uppermost catchment, the Ozwatini Plateau. Althogh clearly identified as an African surface, It contains several high and shallow dry valleys, which are reactivated nowadays during heavy precipitation runoff. To the northwest, the plateau is bordered by the Nsuze Valley, which separates the Ozwatini Plateau from the leveled surfaces around Noodsberg. This valley is also the northwestern boundary of the Tongati

catchment area. As displayed in figure 3.7, the Nsuze runs on the elevation of the expected base level of the Post-African I surface. Accordingly, the Tongati catchment was likely part of a larger catchment during the African erosion cycle, when Noodsberg and Ozwatini Plateau were still connected. During the Post-African I cycle, the Nsuze dissected this plateau and produced the upper catchment boundary of the modern Tongati. The steep slope of the plateau, exposed to the southeast into the Upper Tongati and Mona Valley, is strongly dissected by the heads of present-day rivers while spurs indicate the former extent of the planation surface prior to edge retreat.

Besides the Ozwatini Plateau, remains of the African Surface can also be found in the middle reaches of the catchment. These are part of a larger arc of planation surfaces, which spans parallel to the coast from Glendale Heights to Cowie's Hill. These two endpoints have already been mapped in the transects by Partridge and Maud (1987). The Tongati catchment is crossed by this arc along a NE-SW axis. The plateaus are preserved on the left side of the Upper Tongati at Misty Ridge, where it is covered by widespread agricultural use. The planed surfaces at Matholanyama, KwaSonkomba and the area between KwaNozandla, Sigutwini and Maquadini, are drainage divides within the catchment and separate the upper catchment from the middle one. Due to their level surface, they host larger infrastructures like schools, hospitals or the Sonkombo football stadium. On the right side of the Mona River, the Planation surface is populated by the municipality of Ndwedwe. This name means "long, bare table-land or ridge" (Raper et al., 1989) in isiZulu and aptly describes the shape of the African surface.

Fig. 3.6: Profiles of the Post-African I surface. Quarries of dolerite (left) and granite (right) expose the weathering mantles covering the Post-African I surface.

The Post-African I surface, compared to the African, is hardly developed in form of large continuous plains. The largest examples are found at Fair View or outside the catchment area at The Falls (near Warwick), although even those have been more severely affected by subsequent erosion than the African. In the upper catchment area, located between the Ozwatini Plateau and the African remnants of the middle catchment, many areas of flattened mountain ridges but also high-lying dry valleys were identified as Post-African I surfaces. Some are displayed in the transect in figure 3.7, labelled with b. However, today these are dissected by deep valleys, that incised in the later Post-African II cycle. This surface is also found in the middle catchment, in an area situated between the aforementioned arc of the African Surface and the Sibudu-Sinembe

Mountains. Here, the Post-African I is related to the mountain ridges, that lie between the valleys with an extremely dense channel network. The weathering mantle of the Post-African I Surface is exposed in the terrain especially at quarry sites, which are being exploited for sand extraction in the areas of the Oribi Gorge granite or at dolerite intrusions. Two examples from the catchment are presented in figure 3.6.

The Post-African II erosion is not yet complete, as it has so far not been deactivated by another tectonic uplift. Thus, many of the Pleistocene and ongoing processes are actually attributable to this erosion cycle. In terms or larger planed topographies, the Post-African II erosion surface can be found in the study area in the coastal area outside the mountainous hinterland. The landform classification shows large areas in the coastal hinterland mapped as plains and open slopes, that span a coast parallel strip of 5-10 km width and have a maximal elevation of ~115 m. These are the result of an uplifted marine platform. Inland, these consist of horizontally planed lithologies of the Dwyka Group and the Pietermaritzburg Shale and Vryheid Formation, that have been subsequently incised, creating a shallow and wavy topography. Towards the coast, a layer of Plio-Pleistocene sand deposits of the Maputaland Fm. (which should not be confused with the Maputaland Geomorphic Province in Northern KwaZulu-Natal) overlie the Post-African II surface (Botha, 2018). The oldest deposits of the Maputaland Fm., the Uloa Member, are scarce in the catchment. Only two minor remains of the Pliocene marine terraces are mapped in the north of the Tongati river mouth (Geological map 2931CA) and display direct evidence of the raised beaches. The Berea "red sands" Member covers the majority of the Maputaland Fm. and is the undifferentiated residual of reworked aeolian and former marine deposits. In the later Pleistocene, larger areas of the Berea red sands were leached and displaced through fluvial redistribution and sheet wash, and are found today inland of the coastal Berea red sands as well as smaller ocean tributaries that developed in this Member.

The youngest parts of the catchments are the valleys with fluvial terraces of Pleistocene age and the Holocene alluvial infilled valleys. These are described in further detail in chapter 5.
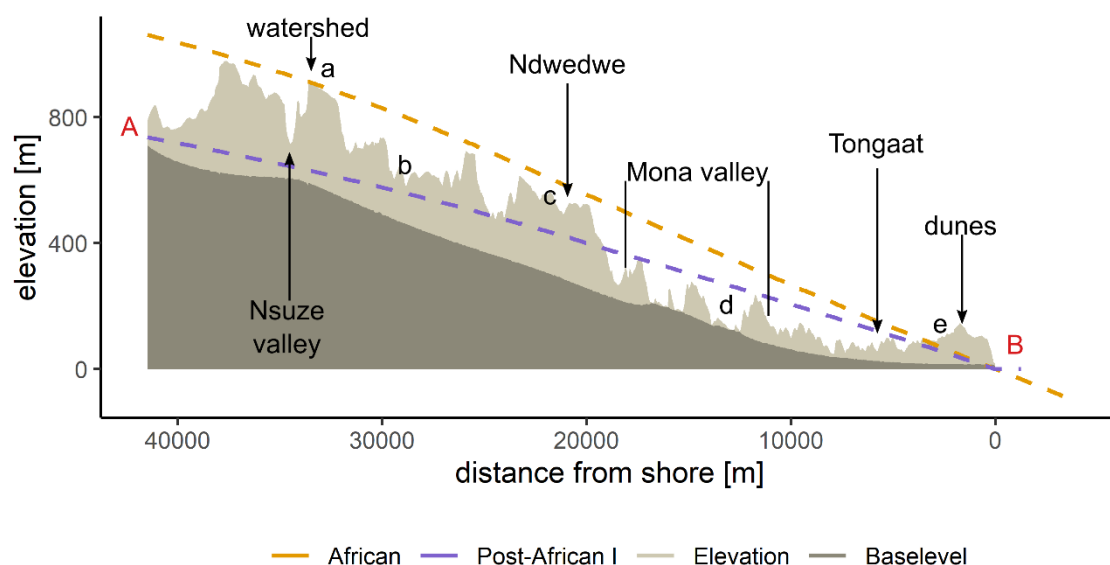
Fig. 3.7: Cross-section of the Tongati Valley and the reconstructed paleosurfaces.

The cross-section (fig. 3.7) of the catchment area visualizes the current topography, the erosion base level as well as the modelled African and Post-African I surfaces in profile. It shows the profile of the modern topography and erosional base level below the modeled African and Post-African I surfaces. The highest part of the landscape, the African Surface, can be identified in the form of correlatable plateaus and Mesas (a + c) in the upper and middle reaches. The Post-African I is found in the upper reaches between the remains of African (b) and in the summit areas of Mona Valley (d). In addition to the valleys, like the Mona Valley shown here, the cross-section displays the flat coastal plain, which is an uplifted marine platform (e) and part of the Post-African II.

3.4 Discussion

An overview of past landscape cycles, their timing and macro-scale geomorphological features compiled by Maud (2012) is presented alongside the local observations from the Tongati Valley in table 3.1.

Tab. 3.1: Summary of the macroscale geomorphic evolution of eastern South Africa and its preservation in local landforms. Adapted and extended from Maud (2012).

Time	Event	Macro-scale geomorphology	Tongati catchment geomorphology
Late Pliocene to Holocene	Climatic fluctuation, glacio-eustatic sea level changes	Marine benches, coastal and interior dunes, river terraces	Raised marine terrace in the coastal hinterland, Berea red sand, fluvial terraces, (see chapter 4)
	Post-African II erosion	Post-African II Surface formed, incision of gorges	
Mid Pliocene (~5Ma)	Major Uplift (up to 900 m)	Asymmetrical uplift and marginal seaward tilting of erosion surfaces	Estimated uplift <200 m and tilting of 14-18 m/km
Mid Miocene (~8 Ma) to Mid Pliocene	Post-African I erosion	Post-African I erosion surface formed (imperfectly planed)	Hill crests, ridgelines, minor plateaus and dry valleys in the upper catchments and the Sibudu-Sinembe Mts.
Mid Miocene (~18 Ma)	Moderate Uplift (200–300 m)	Termination of African Surface erosion and marginal seaward tilting	Estimated uplift of up to 250 m and tilting of 14-18 m/km
Late Jurassic – Early Cretaceous (140 Ma) to Mid Miocene	Multicyclic African erosion	Extensive advanced planation of African Surface, deep weathering and duricrust formation	Larger Plateaus and Mesas (Ozwatini and a coast-parallel arc in the middle catchment)
Late Jurassic – Early Cretaceous (140–125 Ma)	Gondwana Fragmentation	Subcontinent formed by rifting, rapid erosion to new base levels, initiation of Great Escarpment in marginal areas	Dolerite Intrusions

3.4.1 Tectonic history

The inclinations of the paleosurfaces allow to decode the tectonic history of the landscape in terms of uplift and tilting. The vertical difference between the modelled surfaces, i.e. African and Post-African I, lies in the upper catchment at about 250 m and decreases continuously towards the coast. This difference is consistent with the findings of Maud (2012) who estimated an uplift of 200–300 m for this part of the East Coast in the Miocene, that is made responsible for the initiation of the Post-African I erosion cycle.

The vertical difference between the remains of the Post-African I and the present surface, which is considered the product of the ongoing Post-African II erosion cycle, is small in the upper catchment, but increases to 200 m in the middle reaches. The marine terraces at around 100 m a.s.l. in the lower part of the Tongati catchment (Clarke et al., 2007), indicate only a minor net

uplift, especially when taking into account, that sea level was 20–30 m higher in the Plio-Pleistocene (Miller et al., 2005, Dwyer and Chandler, 2009) and uplift is still ongoing with 9.4 ± 2.2 m/Ma (Erlanger et al., 2012).

These results are substantially lower than the values of 600–900 m estimated by Maud (2012) for the Pliocene uplift. The Valley of a Thousand Hills and the Tugela Valley are examples where the Post-African II has produced gorges with depths of 500 m and 1000 m respectively, and thus testify extremely high uplift rates. However, these are closer to the expected main axis of the uplift, the Natal Monocline. Therefore, it can be concluded that the Tongati Catchment has experienced less net uplift due to the general tilting towards the coast. In addition, the Post-African II is described as the incomplete or immature surface, which is supported by the findings in chapter 5 of this thesis. Thereafter, the channel of the middle and upper Tongati has a very steep gradient and the river's long profile is still in the process of adaption to the raised base level, that originates from the Pliocene uplift.

The slope of the modelled paleo surfaces gives information about the tilting, which has influenced the steepening of the landscape east of the principal axis of uplift. King named this axis the Natal Monocline. It extends approximately 80 km inland and parallel to the coast from Port Elizabeth to Eswatini. According to Maud (2012), the slope of an untilted advanced planation ranges between ~1–3 m/km. Today's slope of the reconstructed paleo surfaces compared to the horizontal results in a rise of about 33 m/km for the African Surface and about 17 m/km for the Post-African I. Assuming that the paleosurfaces were well developed before their uplift, and thus deactivation, a subsequent tilting of the African by 30-32 m/km and the Post-African I by 14-16 m/km can be expected. These results are consistent with the macroscale findings of Maud (2012), who estimated the gradient of up to 40 m/km for the African surface, whereas the Post-African I is described as "marginally less steep". Considering that the African I is a double lifted and tilted surface (by both Miocene and Mid-Pliocene events), the observed gradient is the sum of both events. Thus, the tilting of the Mid-Miocene event can be estimated to roughly 14-18 m/km and the Mid-Pliocene event, as already mentioned, to a gradient of about 14-16 m/km.

Consequently, it can be assumed that the two events in the study area had approximately the same magnitude and these are conformal with literature. However, the expected heavy uplift of the Pliocene could not be confirmed, which is possibly due to the distance to the axis of uplift.

While the planation surfaces represent the oldest landforms in the study area, the Pleistocene and Holocene landforms are mainly found in the valleys. These comprise river cut terraces that lie up to 35 m above the modern floodplain and alluvial valley fills. Chapter 5 goes into detail, how and where fluvial processes were and are still affected by the Plio-Pleistocene uplift, but also by Pleistocene sea level fluctuations. Chapter 4 examines, how the sea level lowstands shifted the coastline and how this might have affected the availability of marine resources for early humans.

Chapter 4: Sea Level and Coastline Variations

This chapter addresses research question Q2 and examines the variations of the coastline in response to Late Pleistocene sea level fluctuations. First, regional and global proxies for sea level fluctuations and the geography of the now submerged Natal Shelf is described. A simulation using bathymetric data and a paleo sea level reconstruction is used to analyze the change of the coastal distance of Sibudu Cave and Umbeli Belli (chapter 4.2 and 4.3). Finally, hypothetical environmental conditions on the exposed shelf and the relevance for the archaeological record is discussed.

4.1 State of research

4.1.1 Sea level

Pre-Quaternary sea levels were controlled dominantly by tecto-eustatic crustal changes, related to processes of epeirogenic uplift and global basin deformation (Worsley et al., 1984). During the Quaternary however, glacio-eustasy became the dominant driver for sea level variations, with the terrestrial glacier volume mainly in the northern hemisphere being the determining factor. Considering the notable tectonic stability in South Africa in this period (Erlanger et al., 2012), it can be assumed that local sea level was affected to the largest possible extent by the global sea level dynamics (Tankard et al., 1982a, Pillans and Naish, 2004). The following overview combines global sea level reconstructions from Bintanja et al. (2005) and Waelbroeck et al. (2002) with regional sea level indicators, as presented in figure 4.1.

A Middle Pleistocene relative sea level (RSL) highstand of +13 m is reconstructed from aeolianite at the Southern Coast (Roberts et al., 2012) and dated with OSL to MIS 11 with ages of 391±16 ka, 370±14 ka and 388±14ka (Jacobs et al., 2011). Possible remains thereof, rounded boulders and laminated sands covering these, were discovered in the seaward exposed archaeological site of Pinnacle Point 13B (Jacobs, 2010, Karkanas and Goldberg, 2010). Another Middle Pleistocene sea level is preserved in form of a high coastal dune facies at Isipingo in the south of Durban. The cemented beach rock was U-series-dated to the MIS 7a interglacial or early MIS 6 (Pta-U430: 182±18ka) and indicates a RSL of -3 m (Cooper and Flores, 1991, Ramsay and Cooper, 2002).

For the early Late Pleistocene, a sea level highstand of 6-8 m was described by multiple authors at the Southern Coast (Tankard, 1976, Marker, 1987, Ramsay and Cooper, 2002, Carr et al., 2016). This range is consistent with global RSL reconstructions of the MIS 5e (Rovere et al., 2016). The latest OSL dates by Jacobs and Roberts (2009) on aeolianites bearing fossilized human footsteps yielded an age of 127±6 ka and 116±9 ka and was therefore likely deposited in the MIS 5e interglacial. Aeolianite samples from the Durban Bluff with an estimated age of 132 ka predate the MIS 5e only slightly (Cawthra et al., 2012b).

After the interglacial highstand, both modelled sea levels as well as a local evidence indicate a regression beneath a RSL of -40 m. At Sodwana Bay, northern KZN between St. Lucia and Lake Sibaya, Ramsay and (1990) discovered beachrock of a submerged shoreline at a RSL of -44 m with an estimated U-series age of 117±7 ka (Pta-U487). According to the modelled curves, RSLs undulated between -40m and -20m until ~80 ka. Both sea level curves are in phase and proposes slightly lower levels. While one sample of beachrock (Pta-U435: 84±0.3 ka) by Ramsay (1994) at Sodwana Bay generally supports the modelled curves, three other observations between 115 ka and 95 ka indicate highstands between a RSL of 0 m and +4 m that seem to

contradict the modelled curves. The oldest of these (Pta-U415: 112±23 ka, 0 m) was a date from elephant tusk excavated from a pothole, which was in turn cut into the MIS 7 dunes near Reunion (south of Durban). Based on the interpretation of Ramsay et al. (1993) and the possible deposition of the tusk inside the pothole after the regression, this mammalian artefact likely confirms the MIS 5e highstand (Ramsay and Cooper, 2002). Two other dates (Pta-U568: 104.9±9 ka, +4.5 m; Pta-U565: 95.7±4 ka, +4 m) were calculated from samples of oyster shells from Coffee Bay (southern KZN) and the Munywana Valley (northern KZN). They indicate higher than modern sea level, in contrast to the modelled lower levels.
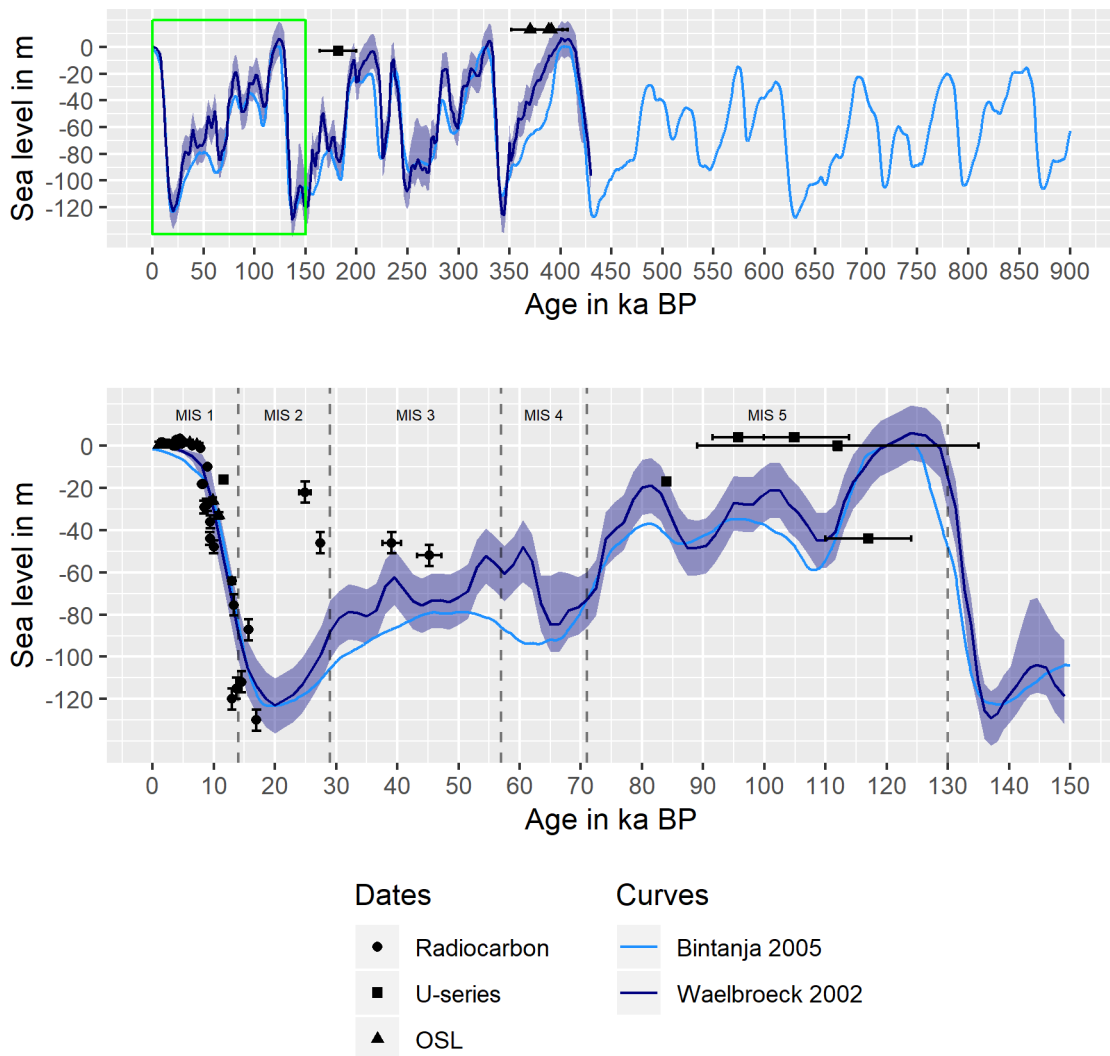
Fig. 4.1: Sea level reconstructions and regional sea level indicators.

The modelled sea levels by Bintanja et al. (2005) and Waelbroeck et al. (2002) predict a strong regression of about 60 m starting after MIS 5a (82 ka), reaching an intermittent lowstand RSL of -85 m (or -92 m respectively) in MIS 4 (~60-65 ka). Thereafter the models predict undulating RSL between -45 m and -80 m (-80 m and -100 respectively) until the end of MIS 3. Ramsay and Cooper (2002) note, that dated local evidence from this timeframe is sparse. Three radiocarbon dates from Richards Bay and Durban Bay predate the LGM and lie consistently higher than the modelled values (Pta-4140, Pta-4142, GaK-1390). However this has to be treated with caution,

as the authors assume that the wetland peats were formed in back-barrier estuaries proximal to, but not directly at, the seashore. Maud (2000) however points out, that the dated peats were formed under freshwater conditions, which might imply they originated under non-marine conditions.

The inland glacier volumes and decreased sea temperatures associated with the LGM caused sea level lowstands, globally as well as in Southern Africa. Dates of calcareous algae from Cape St. Francis, east of Port Elizabeth indicate local sea level regressions to a minimum RSL of -130±5 m and -120±5 m during the LGM (Vogel and Visser, 1981, Ramsay and Cooper, 2002). This is conformal with the modelled global estimates. Also, the subsequent Flandrian Transgression with a rise of ~120 m between 18 ka and 9 ka can be matched to the abundant local Radiocarbon dates. Evidence from the East Coast is reported from the Mfolozi and Umkomazi Estuary, the Mgeni Estuary and Sondwana Bay (Ramsay, 1991, Ramsay and Cooper, 2002). The high transgression rates stabilized between 7 and 6 ka, until a Middle Holocene sea level highstand of +3.5 m was reached (Pta-6252: 4480±80 ka)(Ramsay, 1997). Afterwards, sea levels converged towards the recent level (Ramsay and Cooper, 2002).

4.1.2 Marine and coastal landscape development

This chapter addresses the geography, geology and geomorphology of the Natal Bight. The text refers to the map in figure 4.2. The continental shelf of the southern East Coast is a narrow, roughly 15 km wide protrusion parallel to the modern-day coastline. It is a well marked-off borderline between continental and oceanic crust, called the Agulhas-Falkland Fracture Zone (AFFZ), which was initiated by the breakup of Gondwana in the Middle to Late Jurassic (175–166 Ma). The Transkei Swell spans from Port Elizabeth to 30°S off the Durban coast, and forms a ledge on the western boundary of the AFFZ, while the submarine Natal Valley lies adjacent (Tankard et al., 1982b). Broad et al. (2012) argue, that sediment cover on the Transkei Swell is comparably low, because the Agulhas Boundary currently relocated deposits into the Natal Valley.

Higher sediment accumulations, and therefore extended marine benches can be found north of the AFFZ, which ceases close to Port Shepstone into a northwest-southeast direction strike-slip fault. North of this zone lies the Durban Rift Basin, which comprises a basement of Natal Sandstone and Karoo Supergroup lithology that extends from the inland and is bounded to the Indian Ocean by the -2500 m isobaths (Broad et al., 2012). The Zululand basin follows up to the North of the Durban basin and is bounded by the Lebombo Mountain Range in the west and the 1500 m isobaths in the east. The basal layer of this basin is composed of Lebombo Group volcanic deposits of 180-140 Ma age (De Wet, 2013). These two basins build the foundation of the modern day Natal Bight between Durban and Richards Bay (Lutjeharms et al., 2000). During the Early Cretaceous, non-marine (Hobday, 1982) and marine sediments were accumulated in several interrupted episodes (McMillan, 2003). These deposits are combined in the Zululand Group and are exposed particularly in coast-parallel strip north of St. Lucia.

By the Final Cretaceous / Early Cenozoic inset of the African Surface erosion cycle, major amounts of inland eroded material were transported and deposited on the continental shelf. Between Durban and Richards Bay, the sediment load of the Tugela River, which was initially formed during the Late Cretaceous, created a subaquatic delta. The delta grew throughout the Early and Middle Cenozoic, from the mouth of the Tugela River towards the shelf edge and consequently buried the Early Cretaceous deposits (Broad et al., 2012). De Wet (2013) notes,

that the Oligocene uplift with contemporaneous sea level lowstand and succeeding Post-African I erosion cycle filled the Durban Basin, whereas the later Miocene / Pliocene events, leading to the Post-African II cycle, were responsible for the construction of major parts of the Tugela Cone. The development of the fan of the Limpopo River further North seems to have occurred similarly (Hobday, 1982). South of the Durban Basin, no larger fans expanded due to the high slopes towards the abyss along the AFFZ.
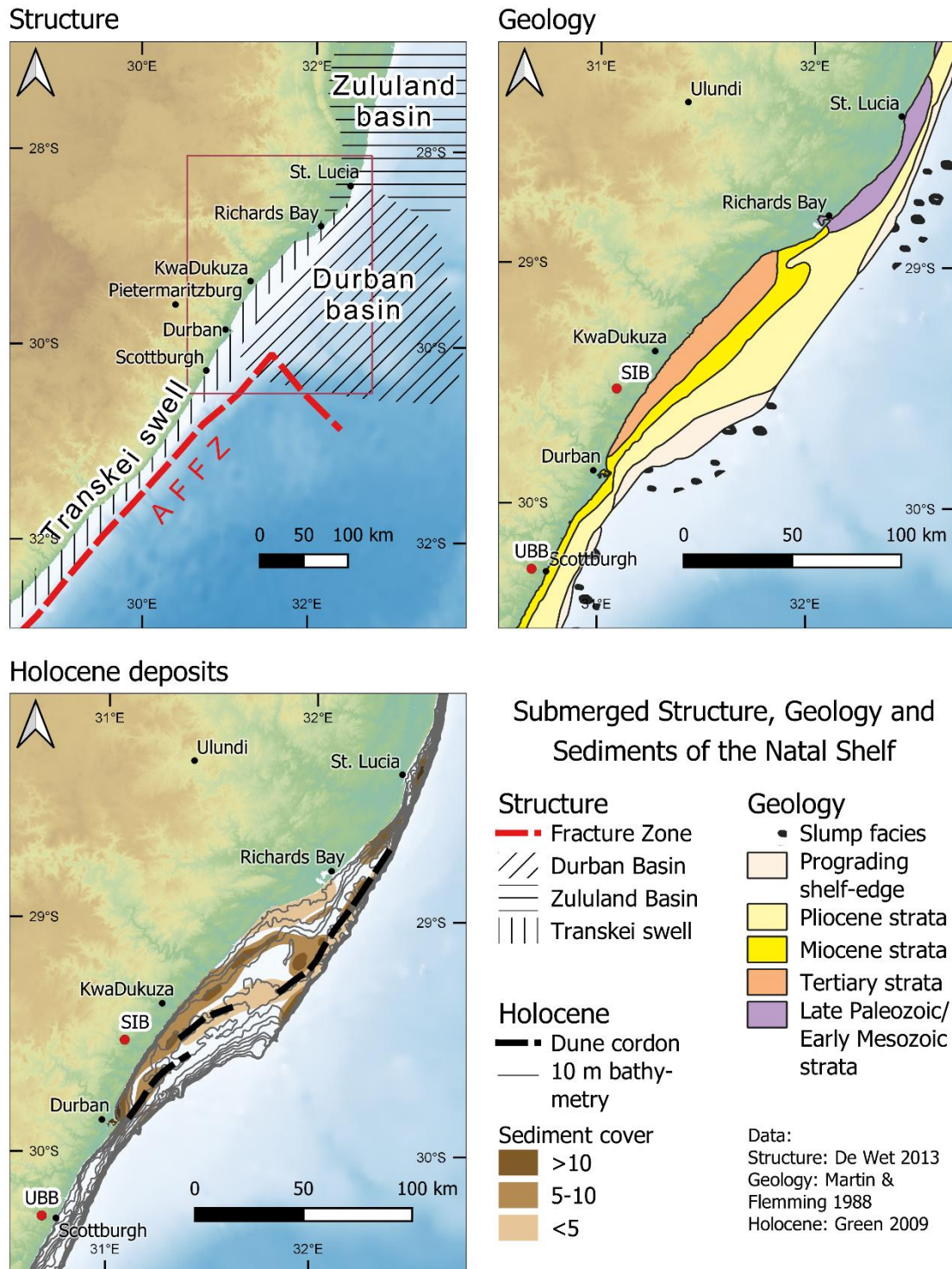
Fig. 4.2: Submerged structure, geology and Holocene sediment of the Natal Bight.

On the coast, the Neogene littoral marine deposits of the Maputaland Group were developed in the KwaZulu-Natal coastal zone and in the Maputaland Coastal Plain, which extends even further north into the Mozambique Coastal Plain (Botha, 2018). The Group was accumulated under coastal conditions and comprises unconsolidated as well as calcite-cemented sediments. These are found in the Tongati catchment as a raised marine platform, that makes up large parts of the lower catchment (chapter 3.3, fig. 3.5).

Today, most of the continental shelf is covered by Quaternary sediments. Martin and Flemming (1986) describe, how these overlay the Neogene strata unconformably with a relatively flat boundary including knickpoints at elevations of -40 m, -50 to -55 m, -75 to -80 m and -100 to -105 m. These are interpreted as several sea-level still-stands, that are explained through paused Late Cenozoic sea level fluctuations. While the outer shelf is dominated by unconsolidated material from the Early Pleistocene, the middle to outer shelf regions display aeolianite dune cordons at water depths between -20 m and -70 m, which are related to the whole Pleistocene (Martin and Flemming, 1988, Flemming, 1980, Birch, 1982, Ramsay, 1991). Davies (1976) reports as much as six parallel dune cordons between -65 m and -100 m, that are preserved close to the Zululand coastline. North and South of the Natal Bight, close to Durban and near St. Lucia, expansions of these dunes are presented inland, such as the Durban Bluff (Cawthra et al., 2012b, McCarthy, 1967). Decalcified and rubified weathering products of several Neogene to Late Pleistocene aeolian sands are described by multiple authors as the Berea "red sand" Formation (Krige, 1932, McCarthy, 1967, Botha and Porat, 2007). One marine dune system comprises the Aliwal Shoal off Scottburgh and the Protea Banks near Port Shepstone and is situated at a RSL of -68 m on a wave-cut bench. This is expected to originate from the latest persistent sea level low stand in the Late Pleistocene (Tankard et al., 1982b, Bosman et al., 2005, Flemming, 1981).

The Pleistocene layers are coated in most of the inner and middle shelf, especially on the Tugela cone, by Holocene unconsolidated material. Green (2009a) mapped up to five depocenters of Holocene shelf sediments with thicknesses of up to 20 m based on the works of Flemming and Hay (1988) and Sydow (1988). Estuaries and lake systems developed inland with infilled paleo channels, that were previously incised into bedrock during multiple cut-and-fill cycles. The most extensive examples are the St. Lucia and Lake Sibaya on the Zululand coastal plain, but also smaller estuaries in the Durban area, like those of the Mvoti or Mgeni (Cooper, 1986, Cooper, 1993, Green, 2009b, Cooper, 1994). There is evidence, that the larger estuaries are formed in pre-existing canyons, e.g. St. Lucia in the Leven Canyon and Lake Sibaya in the Wright Canyon (De Wet, 2013).

These canyons align on the continental slope. Few, like the Tugela canyon, developed early and incised into the Late Cretaceous basement of the Natal Bight (Goodlad, 1986) and were thereafter reactivated during the Cenozoic uplift events (De Wet, 2013, Green and Garlick, 2011). Green (2009a) associates the initiation of the majority of the marine canyons with the Late Cenozoic uplift. Besides the canyon incision, also extensive mass movements transfer shelf material into the adjacent Natal Valley. Continuous accumulation of loose material destabilized the continental slope, resulting in slope failures and slumping (Green, 2009a). Martin and Flemming (1988) mapped large areas of slump facies at the bottom of the continental margin.

4.2 Methods

4.2.1 Data

The shelf area reconstruction is based on the General Bathymetric Chart of the Oceans (GEBCO) provided by Weatherall et al. (2015). The GEBCO raster dataset has a global seamless coverage of sea depth, relative to current mean sea level, with a spatial resolution of 500 m. The entire dataset is composed of a variety of 11 depth measuring techniques, ranging from coarse satellite-derived gravity data to precise bathymetric lidar (light detection and ranging) and the spatial interpolation of data-scarce areas. The regional chart of the Natal shelf merges bathymetric information from the Electronic Navigation Chart (ENC) of the South African Navy Hydrographic Office with seabed elevations collected from shipborne multibeam echo sounding.

The relative sea level curve was reconstructed by Waelbroeck et al. (2002) from oxygen isotope ratios and covers a timespan that reaches back to 430 ka. It has a high temporal resolution of 1.5 ka with a temporal error 0.5–0.8 ka after 40 ka and 1–4 ka before. The vertical error of the RSL curve lies around ±13 m for the whole dataset, however the younger data are more precise (fig. 4.1). The specification of the temporal and vertical errors for each reconstructed time step was a decisive reason why this model was preferred to others. In this way, inaccuracies in the model can be offensively handled (see error margins in figure 4.4).

4.2.2 Shelf area reconstruction

This method is inspired by the "paleoscape model" presented in Fisher et al. (2010), who used a similar approach to simulate the shelf exposure of the Agulhas Plain. The presented model however is a new application and shows further developments e.g. in the form of a dynamic calculation of the shortest Euclidean distance. The flowchart of the model of the program is presented in figure 4.3.

Isobaths with a vertical interval of 1 m were derived from the GEBCO 2019 dataset using the contour tools of the GIS-Software "QGIS" v.3.8.0 (QGIS Development Team, 2020). The derived isobaths dataset has a vertical range of 0 to -140 m a.s.l. and spans from the St. Lucia Outlet in the north to the Isipingo Beach River Mouth in the south of Durban. This spatial and bathymetric extent covers the whole part of the Durban Basin and the Tugela Fan, which is exposed during Pleistocene sea level lowstands.

Two adjoining isobaths were merged to polygons, iteratively for the whole dataset. Areas of the polygons were calculated in UTM Zone 36S (EPSG:32736). Each of these polygons represents the land area (km^2) that is exposed by 1 m regression of relative sea level, or the other way around, the land which is submerged by 1m of transgression. Furthermore, a cumulative land area (km^2) was calculated, representing the total exposed landmass at any given sea-level.

Based on this relation between sea level to exposed area, a temporal shelf exposure model was developed in the statistical software "R" v.3.5.2 (R Core Team, 2019). Using the sea level reconstruction, the area of exposed shelf was approximated for each timestep using a linear interpolation. The result describes the modelled area of the exposed shelf in timesteps of 1.5 ka between 0 and 150 ka.

4.2.3 Shoreline distance reconstruction

The creation of isobaths, which represent the paleo-shoreline at a specific RSL is described in the previous chapter. For each isobath, hence paleoshoreline, the closest distance to the location of Sibudu Cave and Umbeli Belli was constructed using the trigonometric package 'geosphere' v.1.10 by Hijmans (2019) within the software "R" v.3.5.2. The module calculates the shortest Euclidean distance between the location point feature and the nearest segment of the linear shoreline feature. A geodesic factor based on the WGS 84 ellipsoid was incorporated. The model output comprises isobaths, corresponding distances to the archaeological sites and the coordinates of the closest paleo shoreline position for each timestep.
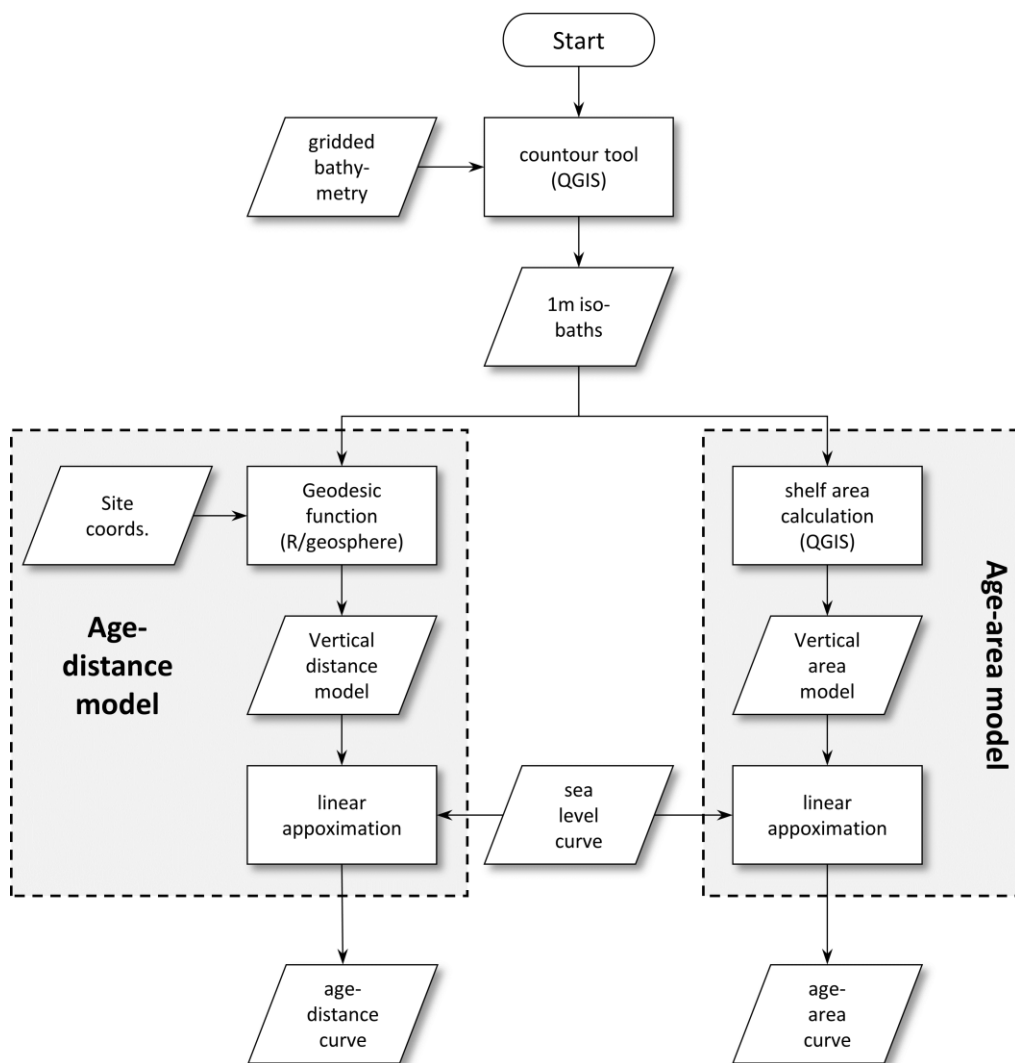
Fig. 4.3: Flowchart of the models to estimate shoreline distances and area of the exposed shelf.

4.3 Results

4.3.1 Sea level and shelf exposure

The exposed shelf surface at different sea levels and ages was reconstructed for the area between Isipingo Beach in the South of Durban and the outlet of St. Lucia. This circumscribes the Tugela Delta and the Durban Basin. As presented in fig. 4.4, the exposed shelf area increases linearly with sea level regression between a RSL of 0 and -40 m. In this section, every 1 m of sea level decrease releases ~40 km² of land. A clear breakpoint at a RSL of -45 m indicates that the section between this level and a RSL of -52 m contains larger flat submerged plains, which are highly sensitive to sea level fluctuations, since 1 m of variation may result in land loss or gain ranging between 100–400 km². The lower lying parts have again a steeper gradient, which continuously decreases from rates around ~60 km²/m to less than 10 km²/m at -130 m. However another, yet smaller planed surface can be expected at relative sea levels around -70 m, where variations of ~100 km²/m are predicted by the model.
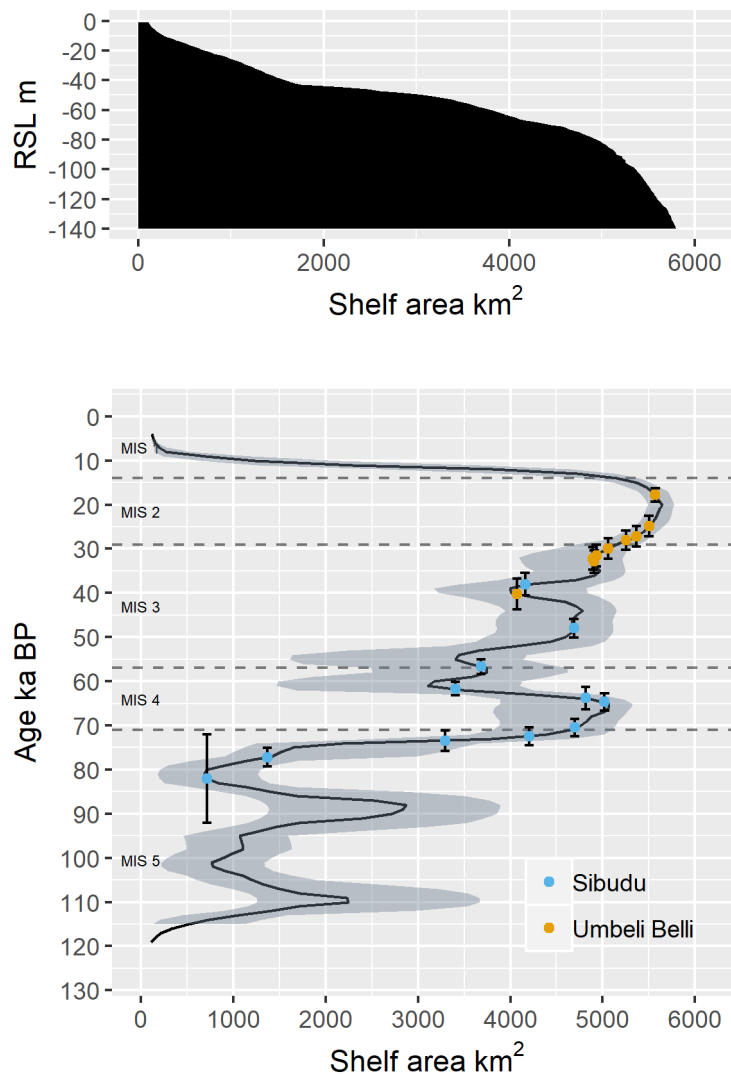
Fig. 4.4: The exposed shelf area during the Late Pleistocene. The upper part shows the exposed shelf area at different relative sea levels. The lower part shows the temporal development of shelf exposure and includes dates of human occupation from Sibudu Cave and Umbeli Belli.
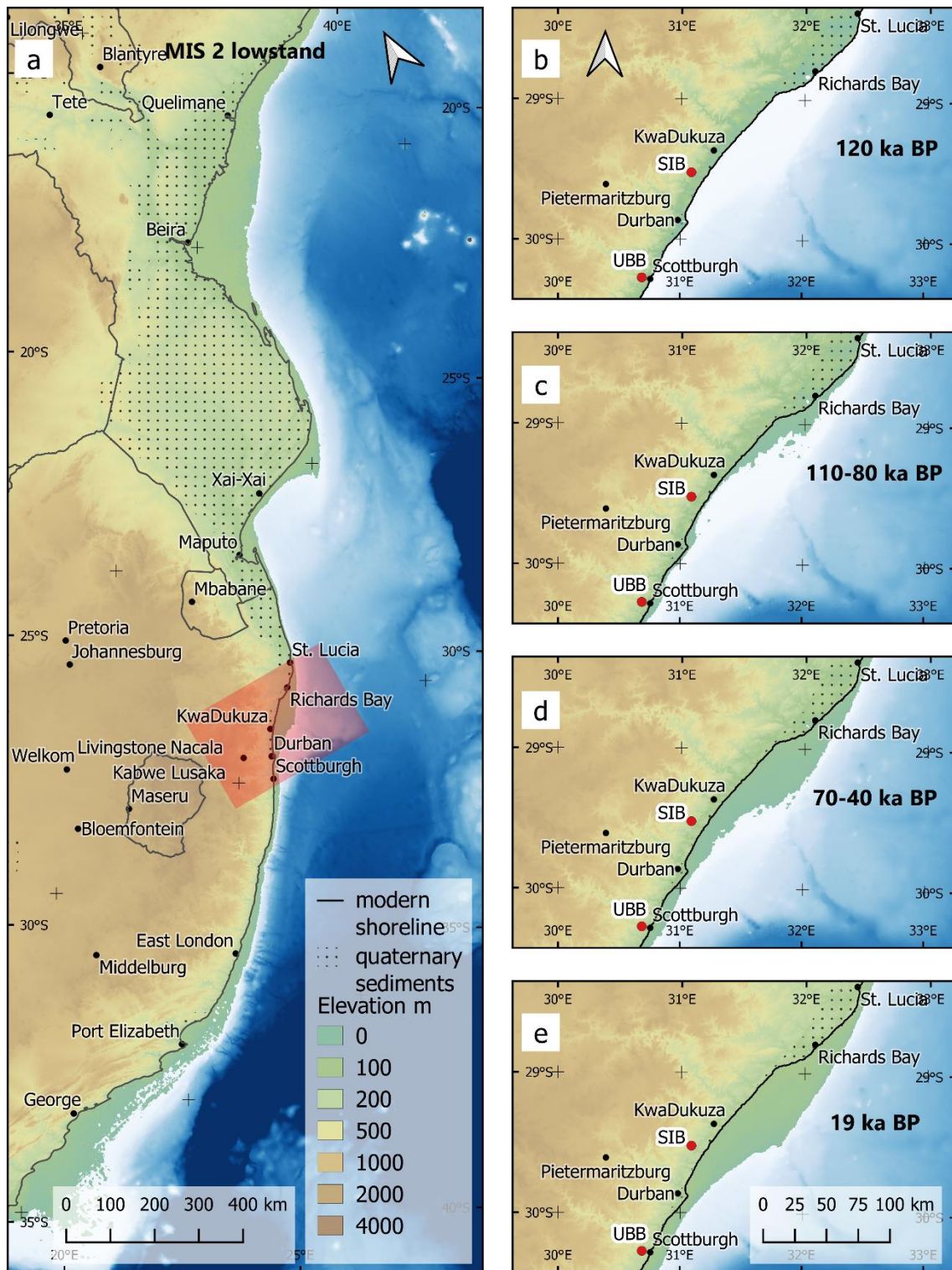
Fig. 4.5: Map of the stages of shelf exposure through the Late Pleistocene.

The temporal development of the exposed shelf area is displayed in figures 4.4 and 4.5. Thereafter, the MIS 5e exposure was comparable to modern day conditions. Between 110–80 ka, RSLs between -20 m and -50 m caused comparably strong shelf area variations between 800 km² and 2800 km². Two partial lowstands at ~110 ka and ~88 ka reached depths, that lie in the sensitive zone below -45 m, resulting in major but short-lived, land expansions. However, uncertainty estimates are quite high in this section. As depicted in map 4.5c. the exposure located on a coast parallel strip between St. Lucia and KwaDukuza with a mean width of ~10 km

and maximal extent south of Richards Bay. North of the Durban harbor is another minor, more isolated piece.

The timespan between 80–70 ka is characterized by another regression reaching an RSL below -80 m and associated shelf exposition of more than 5000 km^2. The following period between 70–40 ka is marked by a mean RSL of -70 m and variations of ±20 m. As fig. 4.5d shows, this results in a well-developed shelf exposure of 3000–5000 km^2, which almost attained the maximal extent of the Late Pleistocene at several times during this period. Map 4.d displays a mean RSL of -70 m. According to this, the northern part of the shelf, namely the region of the Tugela Cone, was widely developed with parts where shoreline shifted up 30 km from its modern position. South of KwaDukuza, the paleo-shoreline ran parallel and ~20 km seaward to the modern shoreline and was connected to the narrow shelf that proceeded South of Durban.

The subsequent regression to a RSL lowstand of -120 m related to the LGM had minor impact on the shelf area in the Natal Bight. By 20 ka, only ~500 km^2 of additional land was released compared to the preceding period. This is explained by the comparably steep topography below a depth of -70 m. While the northern part of the shelf stayed stable in its extent, especially the central and southern coastline migrated further seawards to a mean distance of ~30 km from its modern position and a maximum width of almost 50 km off KwaDukuza (map 4.5a,e).

Following the Flandrian Transgression, largest parts of the ~5500 km^2 of exposed shelf of the Natal Bight were flooded within a timespan of ~10 ka.

4.3.2 Shoreline distance reconstruction

The closest Euclidean shore distance was reconstructed for the archaeological sites of Sibudu and Umbeli Belli. The shelf offshore Umbeli Belli is bordered by the Agulhas-Falkland Fracture Zone (AFFZ) and therefore rather narrow compared to the extensive Durban Basin, that forms the shelf related to Sibudu. This general setting, together with the local bathymetric conditions produces a diverging response of the shoreline to sea level variations. The relationship between relative sea level and shore distance is depicted in fig. 4.6.

At present mean sea level, Sibudu is situated 11.3 km (Umbeli Belli 7.2 km) inland from the shore. Between 0 and -27 m, the shore retreat rate is equal low for both sites at 50 m/m (~50 m horizontal retreat per 1 m vertical sea level decrease). At the Sibudu shore, this rate continues to depths of -45 m. At the Umbeli Belli shore in contrast, a submarine upper platform widens at depths between -27 m and -35 m, causing a shoreline shift of 3.8 km in that area. The shore off Sibudu flattens below the elevation -50 m and a broader platform expands between -65 m and -80 m, where a coastal distance of 30 km is predicted by the model. At roughly the same elevation (-70 – -80 m), another smaller subsea plateau in the South causes the Umbeli Belli shoreline to retreat to a distance of ~17 km. Below RSLs of -80 m, a steeper shelf gradient can be found at both sites, which induces weaker shoreline migration as reaction to sea level variation.

Between 120 and 75 ka, shore migration was low in general, although the upper platform offshore Umbeli Belli was exposed at ~110 ka, ~90 ka and ~75 ka, so that both sites had the same distance to the ocean (~12.5 km). The subsequent regression left the shore near Umbeli Belli at a quite stable distance of 13–17 km between 75 ka and 30 ka. In the same period, the shelf in the Durban Basin showed major expansions and contractions, varying Sibudu shore distance between 15 km and over 30 km. However, this comes along with predicted high

uncertainty of the shore distance model. At both sites, the LGM shows the largest Euclidean distances (Sibudu: 34km, Umbeli Belli: 18.8 km). With the Flandrian transgression, the shoreline approached quickly towards its modern position.
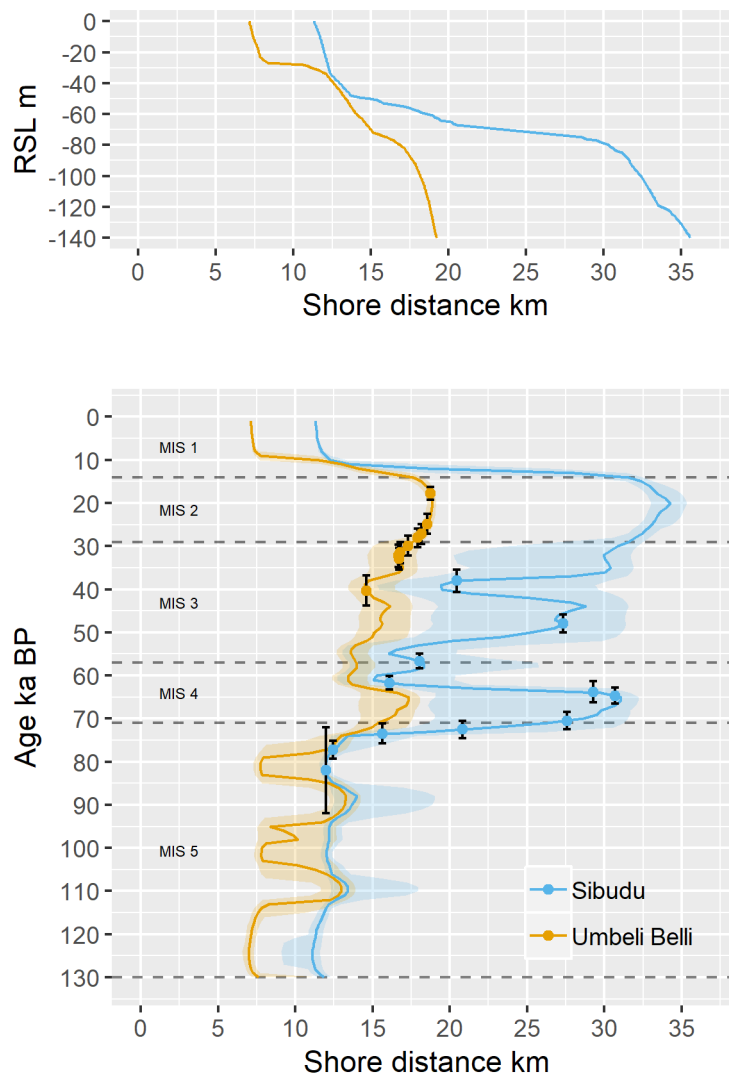
Fig. 4.6: The displacement of the shoreline during the Late Pleistocene relative to Sibudu Cave and Umbeli Belli. The upper part shows the coastal distances at different relative sea levels. The lower part shows the temporal development of coastal distances and includes dates of human occupation from Sibudu Cave and Umbeli Belli.

4.3.3 Sea level and human occupation

The age of the oldest known layers of Sibudu (D-A) is estimated between 92–72 ka. Despite the comparably wide temporal range, the model predicts low difference to modern sea level at that time and therefore neglectable shelf exposure offshore Sibudu due to the strong upper slope.

The pre-SB layers of Sibudu are dated between 77.2±2.1 ka and 72.5±2 ka, when both the bare shelf and the shore distance expanded rapidly in response to a regression after 80ka. Shelf area grew by ~3000 km² and the shoreline retreated by ~8,5 km during in this period.

When the sea level came to a short-timed lowstand around 66 ka with a RSL below -80m, up to 5000 km² of shelf were laid dry and the distance from Sibudu to the shore had grown to ~30 km,

which corresponds to almost three times the modern-day distance. The SB deposits of Sibudu, dating to 70.5±2 ka and the beginning of the HP assemblages, dated 64±1.9 ka, fall in this environmental setting. The subsequent HP occupation at Sibudu is marked by a short-termed MIS-4 transgression, during which water level rose by ~40 m and ~15 km of previously exposed land seaward off Sibudu was flooded. The HP occupation (61±1.5 ka) ended simultaneously with this transgression.

The layers of the Sibudan occupation date to 56.7±1.7 ka. This is associated with a short phase of relative stability, which lasted ~8 ka and showed lower sea level variations of ~10m. Sequentially, the shoreline is much closer and stable, with variations of only ~2.5 km. During this phase, the exposed shelf near the site was reduced to a strip with a width of 2.5-5 km.

MIS 3 sea levels are again highly variable. The Late MSA from Sibudu Cave has a date of 48±2.1 ka and coincides with a partial lowstand, which increased the shore distance to 25 km and extended the width of shelf strip to 15 km. The ensuing MIS 3 transgression is interesting, because it shows contemporaneously the last Stone Age occupation of Sibudu (38±2.6 ka) and the so-far first occupation of Umbeli Belli (40.3±3.5 ka), both displaying Final MSA technology.

The oldest date of Umbeli Belli concurs with a shoreline distance of ~15 km, while shelf was exposed with a width of ~7.5 km. The whole occupation of Umbeli Belli occurred in a phase of strong sea level regression towards the LGM in MIS 2. During both Final MSA and LSA, the shoreline dislocated continuously to a maximal distance of ~18.5 km, thus indicating a widening of the exposed shelf to a width of more than 10 km. Just before the inset of the Flandrian transgression, the last LSA occupation of Umbeli Belli is dated to 17.8±1.5 ka.

Except for the D-A and earliest pre-SB layers of Sibudu, all occupations of the investigated sites are associated with regressed sea levels and increased shore distances. At a sea level below -60 m, the shelf off both Sibudu and Umbeli Belli appears to become wider and flatter, however this feature is much stronger pronounced in the Natal Bight. Simultaneously, the deposition of SB, the majority of HP, Late MSA and Final MSA at Sibudu, as well as the whole Umbeli Belli sequence, occurs in this setting. Mean sea levels above -60 m are characterized by a higher gradient of the shelf and display therefore lower shore distance expansions. The pre-SB, last HP and the Sibudan sediments were accumulated in this environment.

4.4 Discussion

4.4.1 Geomorphic properties of the resurfaced coastal plain

This chapter deals with what the exposed shelf might have looked like. Since data on important factors such as climate and vegetation are scarce, this discussion focuses on the geological and geomorphological setting. Hereby two neighboring geomorphic provinces, as defined by Partridge et al. (2010), are brought into the discussion as potential modern analogs.

Based on scientific studies of the geomorphological features of the submerged shelf of the Natal Bight, these geomorphic provinces can be considered: the Southeastern Coastal Platform and the Zululand Coastal Plain (fig. 4.7). Both are located between Indian Ocean and Southeastern Coastal Hinterland. The provinces are narrow with a width of only 5–30 km, but the Zululand Coastal Plain becomes much wider further to the north (not depicted in fig. 4.7).
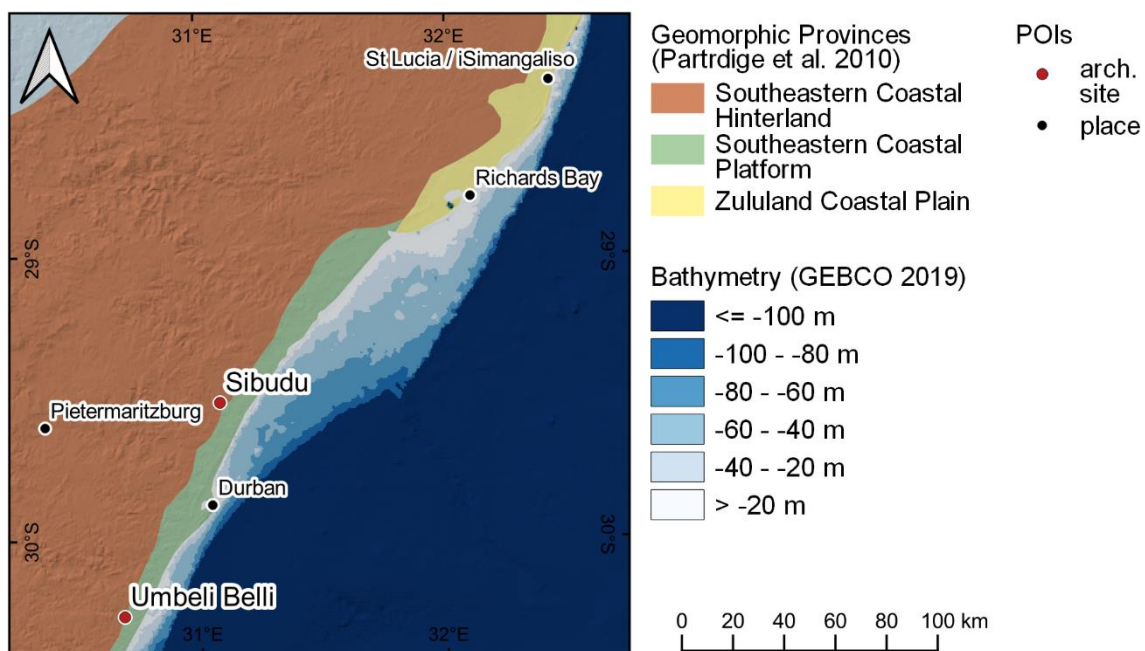
Fig. 4.7: Geomorphic Provinces bordering the Natal Bight. Data by Partridge et al. (2010) and Weatherall et al. (2015).

A distinguishing feature is the lithology. The Southeastern Coastal Platform is based on bedrock from the Karoo Supergroup, but also Natal Group sandstone and Jurassic dolerites. The Zululand Coastal Plain is hosted on younger rocks from Cretaceous to Miocene marine sediments (Partridge et al., 2010). Therefore, the submerged shelf, which has Tertiary to Pliocene bedrocks (Martin & Flemming 1988), is more comparable to the northern Zululand Coastal Plain from a geological perspective.

As far as geomorphic history is concerned, the two provinces are similar in that both are wave-cut platforms covered with quaternary aeolian deposits and unconsolidated beach sediments that were subsequently lithified and weathered. This has resulted in a rich collection of geomorphological forms that include 5-7 different dune types (Ramsay, 1991, Jackson et al., 2014), raised shorelines (Porat and Botha, 2008), aeolianites and beach rocks (Cawthra et al., 2012b) and wetlands developed in the river mouths and proximal to the coast (Cooper, 2001, de Lecea et al., 2016).

Dune systems have been identified and mapped intensively on the submerged Natal Bight, the adjacent Transkei Swell and the Zululand Basin (Flemming, 1978, Flemming, 1980, Flemming, 1981, Flemming and Hay, 1988, Martin and Flemming, 1988, Ramsay and 1990, Ramsay et al., 1993, Bosman et al., 2005, Bosman et al., 2007, Porat and Botha, 2008, Cawthra et al., 2012b, Cawthra et al., 2012a, Salzman, 2013, Salzman et al., 2013, Green et al., 2017). The dune cordons can generally be associated with a temporary sea level standstill, but they do not necessarily indicate coastlines, but are mobile at sea level and above, which makes the correlation of age and sea level difficult. Many dune systems are not yet clearly dated and do not necessarily belong to the last glacial cycle. However, if erosion forms, such as notches, terraces or biogenetic erosion are visible on the sea side of the fossil dunes, the deposits contained therein can at least relatively safely be assigned to the last (Flandrian) transgression (Lambeck et al., 2010).

Estuaries are the most common wetland phenomenon on the modern East Coast north of Durban and noteworthy examples comprise Durban Bay, Thukela Estuary, Richards Bay, Lake Eteza, St. Lucia Estuary, Lake Sibaya and Kosi Bay. These have also been subject to intensive studies of the paleoenvironment (de Lecea et al., 2016). Cooper (2001) has divided the South African estuaries into 6 classes, where the majority of the East Coast estuaries showed to have similar characteristics: They are usually located in bedrock incised valleys, which were filled during the last transgression. Furthermore, they are indirectly influenced by the comparatively flat tide, but usually not directly connected to the ocean due to a barrier system. In some cases, this extends to a back barrier wetland system, which runs parallel to the coast behind a barrier dune (de Lecea et al., 2016). At earlier sea level highstands, such as MIS 5e, these have combined to form larger lagoons, as it is still the case e.g. at St Lucia. With sea level lowering, however, the estuaries have shifted with the coastline towards the shelf edge during the LGM (Green et al., 2013a). There, deltas have partly formed from the sediment transported over the edge (Green et al., 2013b, Green, 2011). Seismic investigations allowed to reconstruct back barrier lagoons that formed on the shelf during times of stable sea levels (Green et al., 2013a, Green and Garlick, 2011). Thus it can be summarized that (i) the modern geomorphic provinces hardly differ from each other in terms of geomorphological features, however, there is (ii) an internal differentiation into coastal and hinterland regions. Accordingly, the Pleistocene sea level changes are likely less pronounced in the Zululand Basin (i.e. in the area of Zululand Geomorphic Province) and the Transkei Swell (southern Southeastern Coastal Platform), as these have always been proximal to the shelf edge. In the area of the broad shelf of the Durban Basin (northern Southeastern Coastal Platform), however, sea level fluctuations caused substantial shifts of coastal areas and associated wetlands.

In modern geomorphic provinces, Partridge et al. (2010) have classified the river morphology in terms of sediment balance. According to this, the Southeastern Coastal Hinterland is characterized by shallow to moderately inclined longitudinal profiles and narrow confined valleys, while the Zululand Coastal Plain, according to its name, is characterized by wide flat plains where the rivers meander freely and form wide flat valleys. In general, the topography of the continental shelf is comparable to the Zululand Coastal Plain due to its flat relief and low gradient. The regional seismic surveys of (Green and Garlick, 2011, Cawthra et al., 2012a, Green, 2011, Dladla, 2013, Green, 2009b) provide further insights into the properties of the shelf's currently filled drainage network. In the area of the modern coast, the rivers are cut into 30 m deep infilled valleys (Clarke et al., 2007). This is comparable to the shelf, where a complex drainage system has developed, partly since the Cretaceous period (Dingle 1983, Stevenson and

McMillan, 2004; Green et al., 2013a), which is characterized by wide meanders and cut-off channels (Dladla 2013). In the later Pleistocene, these paleochannels were reactivated and partly deepened further in several cut-and-fill cycles. Also compound valley systems with narrow but shallow valleys are reported (de Lecea et al., 2016, Green et al., 2013b, Green and Garlick, 2011). Compared to the geomorphic classification by Partridge et al. (2010), the river gradients of the shelf are relatable to the flatter Zululand Coastal Plain. However, seismic river cross-sections imply characteristics that are more common on the Southeastern Coastal Platform.

It can be summarized that the exposed continental shelf in Natal Bight combines many features of the two adjacent geomorphic provinces, as far as can be reconstructed from the different sources. Consequently, conditions like in the lower Tongati Valley, especially the coastal regions covered by the Maputaland Fm. can be expected on the exposed shelf. Wetlands at the river mouth were probably larger, as the modern Tongati Estuary is confined in a narrow valley. Here, a back-barrier lagoon system, like the iSimangaliso Wetland Park around Lake St Lucia, might serve as modern analog.

Fig. 4.8: The iSimangaliso Wetland Park, a part of the Zululand Coastal Plain. Photo: Thomas Spiess.

4.4.2 Shoreline variations in context of the archaeological record

The relationship between the occupation of Sibudu and the coast is expressed in the archaeological record mainly by the presence of marine gastropods (d'Errico et al., 2005, d'Errico et al., 2008, Vanhaeren et al., 2019). The collection contains 23 remains of the 3 species *Nassarius kraussianus*, *Afrolittorina africana* and *Mancinella capensis*. These assigned to the layers of the SB (70.5 ± 2.0 ka), HP (64.7 ± 1.9 ka) and late MSA (46.6 ± 2.3 ka) occupation (Vanhaeren et al., 2019). All described species still have natural occurrences on the modern Dolphin Coast, but they represent only a fraction of the total present taxa. While a natural

accumulation is described as rather unlikely due to the distance to the coast, Vanhaeren et al. (2019) take human activities into account for the apparent selection. As some bivalve shells show traces of heat treatment, it would initially seem reasonable to estimate their use for food. However, their tiny size and low caloric energy of the edible components argue against this interpretation (d'Errico et al., 2005, d'Errico et al., 2008). Furthermore, Plug (2006) argues that the small amounts of the bivalves *Perna perna* and few gastropods indicate rare or no seafood consumption at site. It is also discussed if the finds of *N. kraussianus* were introduced into the assemblages as unintentional "by-catch" of loggerhead sea turtles (*Caretta Caretta*), which were discovered in the MSA layers of Sibudu (Hughes, 1974, Plug, 2006).

However, the treatment of parts of the shells with heat, perforation but also pigment suggests other motives. Vanhaeren et al. (2019) argue for a use as shell beads or raw material with the same purpose as those discovered at Blombos Cave (Henshilwood et al., 2004) and Border Cave (d'Errico et al., 2012) in the MSA and early LSA. The results of chapters 4.3.2 and 4.3.3 support this argumentation. Calculations by d'Errico et al. (2008), demonstrated the caloric inefficiency of gastropods as a long transported food source. These estimates were based on a modern coastal distance of only 15 km. The presented model results however show, that these finds are associated with a far more distal coastline, which ranged among the largest Pre-LGM extensions of over 27 km. This reinforces the interpretation that the nutritional value of shells is disproportionate to the physical effort required to transport them to the cave. Moreover, their presence indicates that early occupants of Sibudu placed a certain value on shells, apart from nutrition, that made it plausible for them to transport these over distances beyond the daily foraging distance.

Furthermore, the shells show that the exposed continental shelf was at least travelled through by earlier inhabitants, which points at increased mobility and range expansion of these populations. But it may also imply that this temporally and spatially variable landscape was integrated into their self-constructed niche. As demonstrated in chapter 4.3.1 and chapter 4.4.1, a landscape comparable to the modern coastal geomorphic provinces emerged, with an area that equals a third of the size of Eswatini, during the sea level lowstand of MIS 4 to MIS 2. This came with an ecosystem that is nowadays confined to a few kilometers between the hinterland and the ocean, but offered an open landscape with the opportunities of resource exploitation and demographic expansion for earlier populations. This corresponds to findings by Will et al. (2019b), who assessed that "coastal adaptations were a helpful 'add-on' to previous subsistence and adaptive strategies, not only broadening the diet, but also increasing options for occupation and range expansion".

Finally, it is evident that this landscape has undergone several expansions and contractions throughout the Late Pleistocene, but the fact that human occupation was present in all phases of fluctuation is witness to behavioral flexibility that allowed to sustain in a changing environment.

Chapter 5: Fluvial Morphology of the Tongati Catchment

This chapter addresses Q3 with the question, how fluvial erosion has affected the Tongati catchment and what drivers are made responsible for the different landforms. This comprises the analysis of the morphometry of the channel, the prediction of terraces, geomorphological mapping with classic methods, ERI and OSL dating. The results are discussed with regard to differential impact of primary drivers (i.e. sea level fluctuations and erosion), and the age of Sibudu Cave.

5.1 State of research

5.1.1 Fluvial morphology

The relationship between river morphology and its underlying drivers, tectonics and climate, are a classic of geomorphological research and, at the latest since the works of Davis (1899), the characteristics of fluvial landforms have been regarded as archives of landscape genesis. The variation of the base level of a channel, which is compensated by erosion or deposition, is regarded as a fundamental process. These variations can be global (e.g. sea level as the base level of ocean-tributary rivers), regional (e.g. uplift of mountain ranges) or local (e.g. displacements along faults and knickpoints). Through a series of interactions (e.g. climate, lithology), feedback mechanisms (e.g. isostatic uplift) and boundary conditions (precipitation, petrovariance, rates and duration of events, availability of sediment) this system becomes complex.

Current research is investigating river morphology in response to currently active tectonic and climatic processes, which allows the estimation of important variables, such as response times and knickpoint retreat rates through the study of modern analogues (Schumm et al., 2002, Whipple, 2001, Kirby and Whipple, 2012, Whittaker and Boulton, 2012). Another approach uses the description of the characteristics of today's rivers as a diagnostic tool to draw conclusions about the evolutionary processes of the landscape. For example, tectonic uplift rates and deformation processes can be quantified and dated, climatic divers can be reconstructed and changes in the fluvial patterns can be derived from the observed landforms (Westaway et al., 2002, Westaway, 2007, Bridgland and Westaway, 2008, Schildgen et al., 2009, Kirby and Ouimet, 2011, Evenstar et al., 2020, Lauer et al., 2020). Roberts and White (2010), for example, used this approach to estimate the African uplift history and incorporated rivers from KwaZulu-Natal in their study.

Of course, the emergence of GIS and digital remote sensing and the associated possibilities of quantitative analysis have also greatly enhanced the study of fluvial morphology. Among the first common applications were analyses of catchment areas, longitudinal profiles, channel slopes and knickpoints by Hack (1957). Thereupon, he developed various indices to extend the quantitative description of these (Hack, 1973). Many of modern analytical tools are still based on these principles, although their performance is constantly being enhanced by more robust algorithms, better usability and more accurate data, especially in form of high resolution digital elevation models. Consequently, these numerical analyses of river form developed into a number of digital tools for the derivation of geomorphic indicators from river geometries (Holbrook and Schumm, 1999, Dollar et al., 2006, Demoulin et al., 2007, Schwanghart and Kuhn, 2010, Cook et al., 2013, Finnegan, 2013, Cook et al., 2014, Schwanghart and Scherler, 2014, Campforts et al., 2017, Demoulin et al., 2017, Demoulin et al., 2018). These are increasingly applied in case

studies for the reconstruction of past geomorphic processes and their tectonic and climatic drivers from the fluvial archives (Snyder et al., 2000, Berlin and Anderson, 2007, Bridgland and Westaway, 2008, Pérez-Peña et al., 2009, Pérez-Peña et al., 2010, Bridgland and Westaway, 2014, Demoulin et al., 2015, Geach et al., 2015, Shi et al., 2020, Lauer et al., 2020, Evenstar et al., 2020), and are also part of this work. This method has an enormous practical range and can be used to analyze processes with extremely young (decades) to very old ages (millions of years) on the one hand, but also processes with very fast (e.g. lava dam) or slow rates (e.g. uplift) of change, on the other hand (Demoulin et al., 2017).

5.1.2 River long profile

The river long profile is the gradient of the water level between source and mouth. In general, river profiles strive to achieve an ideal shape under constant conditions, where the elevation of the river grades continuously from the high-lying source with high slopes to the low-lying mouth, associated with nearly flat slopes. Mackin (1948) states, that such an idealized graded river accomplishes a dynamic equilibrium between the properties profile slope, geometry, discharge and sediment load. In simple terms, this means that due to the increasing flow accumulation on the way to the outlet, and the resulting increasing discharge, the transport capacity is maintained even in flatter gradient. In more recent research, such a steady state is more precisely divided into four subtypes, namely a steady state of (i) erosional flux, (ii) topography, (iii) thermal conditions and (iv) exhumation (Willett and Brandon, 2002). Therefore, the methods described here refer to the topographic subtype. In an equilibrium, the elevation of each point in the profile is preserved through the balance of uplift U (or actually movement of the base level) and erosion (Demoulin et al., 2017). With erosion being a function of the channel slope S, the upslope contributing catchment area A and the erodibility coefficients k, m and n, the equilibrium can be expressed with equation 5.1:

$$U = kA^n S^m$$ eq. 5.1

with
U = uplift [m]
A = upslope area [m^2]
k,m,n = coefficients

There is agreement on the concave shape of the terminal graded river profile, but there are different views on its actual function. Hack (1957) was among the first to speak out for a logarithmic decrease of the elevation with the distance to the source, but there are also advocates of a decrease rate according to the power law (Flint, 1974, Whipple and Tucker, 1999, Goldrick and Bishop, 2007), and under specific circumstances, exponential function or a quadratic expression (Demoulin et al., 2017). Others, such as (Blight, 1994), move away from the idea of describing the profile as a function and suggest to describe the longitudinal profile by the area under curve.

Regardless of the preferred mathematical description of the steady state curve, all authors agree that the base level has a substantial influence on the river profile. It represents the lower limit of the possible bed erosion of a river and thus also determines the development of the upstream river course. It also controls the development of morphological forms in the entire catchment area since the products of weathering and denudation are transported by the fluvial system. The main base level determines the erosion base for an entire fluvial system and can be, for example, the sea level or a higher situated inland lake with no outflow. In addition, there are regional or

local base levels, e.g. the confluence to the main stream for a tributary, a step caused by lithology or a fault, or man-made infrastructures, e.g. a dam.

Therefore, a change in the height of the base levels affects the processes in the entire catchment area. These include long-term and continuous sea level variation (including eustasy and isostasy), crustal uplift and subsidence, infilling of basins of endorheic rivers, changes in main stream affecting the tributaries and river capture. When the base level is lowered, at first the local slope directly upstream to the base level is steepened, which causes erosion to intensify and consequently leads to lowering of this section. In the long run, this erosional impulse is propagated upstream throughout the stream network and defined as headcut or headward erosion. Lowering of the riverbed eventually leads to the valley slopes being steepened, so that headcut erosion can ultimately also lead to increased denudation or the emergence of linear erosion (e.g. rill, gully erosion). On the other hand, the raise of the base level leads to a reduction of the river gradient, which in turn results in reduced flow energy, lower sediment load capacity and finally sedimentation.

Sections in the river long profile, where stream gradient is lower or higher than expected from its position on the long profile are called knickpoints. These can be convex or concave and are studied as diagnostic features of the river's relief evolution. A summary of these forms of appearance and their genesis is explained by Ahnert (2015). Thereafter, typical examples for origins of concave knickpoints are

- the confluence of a major tributary, which substantially increases the outflow of the main stream, which in turn has an impact on discharge depth and potential debris load
- a change in the erodibility of the bedrock, where a river flows from a resistant into a more erodible lithological regime, which more susceptible to lowering or
- the transition from a mountain range to a flatter environment, such as a tectonic depression, which over a longer period of time turns into an alluvial cone to compensate for the knickpoint.

In the field, convex knickpoints can be identified through the presence of step-pool sequences, sections with resistance against bed erosion and rapids and waterfalls.

A convex knickpoint, in turn, indicates that erosion is too low and thus incapable to produce a long profile that fits the demands of a steady state equilibrium line, or that the knickpoint is still young and the adjusting process of headward erosion is still in action. Possible reasons for such a convex knickpoint comprise, among others,

- the tectonic movement of a fault. The distance of the knickpoint from the fault is therefore an indicator for the timespan since the inset of its activity
- the presence of resistant lithology. If this bedrock is layered near-horizontally, the knickpoint can erode backwards through this layer. However, if such a bedrock barrier is layered upright or has the form of a dike, the knickpoint persists until the barrier is removed.
- the confluence of a minor tributary, which is due to its low discharge, incapable to hold pace with the lowering of the main stream.

5.1.3 Terraces

Terraces can be identified in the field as planed landscape elements along valley slopes, which are delimited by steeper gradients up- and downslope. A distinction is made between river and denudation terraces. The first are former valley bottoms left behind by further depth erosion, and thus the result of a fluvial erosion process. The second are the result of petrovariance in the bedrock, so that resistant layers are preserved without fluvial processes. In addition, anthropogenic agricultural terraces, which were abandoned also take on the appearance of natural terraces after some time. In order to distinguish a river terrace from other types, they must (i) be correlated along the river profile, and (ii) be examined for evidence of residues of the former river bed in the field (Goudie, 1998).

Due to their genesis and their physiognomy, fluvial terraces can be further differentiated into cut-and-fill terraces and strath terraces. Strath terraces are nearly flat landforms with a bedrock floor, which is occasionally covered with a thin veneer of alluvium, a remainder of the former valley floor. This is however not a diagnostic feature, because especially older terraces can be subject to ongoing landscape processes altering their initial appearance. Strath terraces are created in three steps. In the first, a bedrock eroding river incisions downwards, which is paused in the second step, when the river widens its valley through lateral erosion. In the third step, the channel lowering through fluvial downcutting is reactivated, thus abandoning the former riverbed. Due to its formation in solid bedrock, the strath terrace is notedly durable (Ahnert, 2015).

Cut-and-fill terraces, also termed alluvial terraces or accumulation terraces are the second type of fluvial terraces. These are composed of thick deposits of unconsolidated sediments, that make up the whole riser of the terrace. In its simplest form, this type is created in three steps as well. In the first, the downcutting river erodes in the manner of a bedrock river. The resulting valley is infilled in the second step with loose sediment, which forms a nearly flat valley bottom on top of the accumulation. In the third step, this sediment body is excavated through the reactivated incising river, leaving behind a terrace body composed of the former channel fill. The cut-and-fill type can be more complicated, when this succession of infill and erosion repeats, so that complex system of nested terraces is produced. In this case, the age of the landform is younger than the age of the sediment, which imposes further challenges on the chronological correlation methods, such as OSL dating.

The main reasons for terrace formation are related to the drivers of changes in the long profile, but not limited to those. Conversely, the presence of terraces bears information of the landscape's history (Merritts et al., 1994, Vandenberghe, 2015, Mather et al., 2017, Demoulin et al., 2017). Most important drivers are:

- Crustal deformation is a common driver especially for strath terraces. A temporarily paused uplift creates the typical pattern of incision, lateral erosion and again incision, which generates this landform.
- Eustatic sea level change, as the base level of exorheic drainage systems, not only conducts phases of headward erosion and accumulation through sea level lowering and rise, which are relevant for cut-and-fill terraces. Phases of relative sea level stability can also cause valley widening, which favors the generation of strath terraces (Merritts et al., 1994, Finnegan, 2013).

- Climate change related terraces are well-known in the middle to higher latitudes of the northern hemisphere, where these glacial-interglacial cycles formed major cut-and-fill terrace landscapes (Bridgland and Westaway, 2008, Bridgland and Westaway, 2014, Vandenberghe, 2015, Olszak, 2017). These cycles are less pronounced in Southeastern Africa, where the shorter precession cycles prevail, which are known to alter humid and arid phases rather than glacial-interglacial phases. However, the former can affect a cascade of geomorphic processes, such as weathering of bedrock (e.g. kaolinization in the granite landscapes of KZN), thus controlling the sediment load of rivers, which in turn influences their ability to erode (Grenfell et al., 2009).
- Stream capture is a special type, which acts local and produces a single terrace level. This type is formed, when a channel with high lying erosional base level is captured by a stream with lower base level, so that the high-lying tributary adjusts to the new base level. The terrace marks the elevation of pre-capture base level conditions.

The interpretation of terrace formation is a complex subject, where these external drivers co-occur and superimpose each other, or where terraces are the result of discrete external factors (Soria-Jáuregui et al., 2016, Olszak, 2017). Autogenic factors can obstruct the exogenic drivers, even on local reach level (Erkens et al., 2009, Fryirs et al., 2007). Examples from KZN show an intrinsic geological control, often related to dolerite dikes and sandstones, which intermit the connectivity of geomorphic processes (Tooth et al., 2007, Keen-Zebert et al., 2013, Grenfell et al., 2008, Grenfell et al., 2014, Oldknow and Hooke, 2017, Larkin et al., 2017, Fryirs et al., 2007).

Examples from South Africa, where river terraces have been mapped and dated with the luminescence method comprise Grenfell et al. (2014), Keen-Zebert et al. (2013), Lyons et al. (2013) and Tooth et al. (2013).

5.1.4 Terrace modelling

Semi-automated methods for the detection of terraces from DEMs were developed to support geomorphological fieldwork. Demoulin et al. (2007) propose a method to delineate terrace levels from river cross-sections of DEMs. This method was applied to a mid-resolution DEM on catchment scale. While this is useful to detect terrace heights along the long profile, it does not actually map geographic position and size of the terraces. Stout and Belmont (2014) developed the "TerEx Toolbox" to derive spatially explicit terrace features from high resolution DEMs, e.g. derived from ground based or airborne lidar data. A more local approach to map terraces was conducted by Li et al. (2019) using a Structure-from-Motion approach based on UAV photogrammetry.

Summarizing, this shows a coexistence of tools using high resolution DEMs with reasonable computing times on reach level on the one side, and mid-resolution DEMs at catchment level, which lack the functionality to map the spatial distribution of terraces on the other. The TanDEM-X unifies a high vertical accuracy with a middle horizontal resolution, which makes it potentially capable to derive terraces on catchment scale with high integrity. In this work, this objective is addressed through a novel approach using Object Based Image Analysis (OBIA).

OBIA is a method that is particularly common in multispectral remote sensing. The advantage of this method compared to pixel-based approaches is, that besides spectral information and image processing also GIS-typical analyses such as topological relations, shapes, context, can be integrated (Blaschke, 2010). In this approach, high-resolution satellite imagery is decomposed by a segmentation algorithm into homogeneous and semantically significant entities called

'object candidates', each consisting of several pixels. These are agglomerated into meaningful objects through further processing, often through a procedural or automatic statistical classification.

In addition to the classical application with spectral channels, the method is also used to determine landscape objects, whereby DEMs and Topographic Indices replace the remote sensing imagery as base data. Drăguţ and Blaschke (2006) have developed an object-oriented landscape classification that provides a similar result to the Topographic Position Index (TPI). However, a specific method for the detection of objects like river terraces is missing. Therefore, a method was developed to classify terraces in a semi-automated way from selected topographic indices and expert knowledge.

5.2 Methods

The tools described in this chapter (chapter 5.2.1-5.2-4) were used to distinguish different modes and magnitudes of fluvial erosion in the catchment with the software "TopoToolbox" for hydromorphometric analyses provided by Schwanghart and Kuhn (2010) and Schwanghart and Scherler (2014) in "Matlab" (MATLAB, 2019).

Fluvial terraces as indicators for past fluvial activity were predicted with a custom-made Object Based Image Analysis (OBIA) model (chapter 5.2.5). Furthermore, the procedure to detect buried terraces with the non-invasive method of Electric Resistivity Imaging (ERI) is described in chapter 5.2.6, as well as Optically Stimulated Luminescence (OSL) to derive ages from alluvial and colluvial sediments (chapter 5.2.7).

5.2.1 Concavity index from Slope-Area plots

The concavity index θ is a measure of the upstream elevation gain of a river profile, and commonly calculated to describe the shape of the whole stream or single reaches (Demoulin, 1998, Kirby and Whipple, 2012, Demoulin et al., 2017). According to Flint (1974), it is an important indicator of erosion, alongside local slope, steepness and catchment area, which is used as a proxy for runoff. The index can be derived from a Slope-Area (or S-A) plot (Snyder et al., 2000, Kirby and Whipple, 2001). When both variables slope S and area A of a channel network are visualized in logarithmic scales, the concavity index θ and the channel steepness k_s can be derived by fitting a linear relationship based on equation 5.2 to the profile points (Mudd et al., 2018):

$$log(S) = -\theta \cdot log(A) + log(k_s)$$
<div align="right">eq. 5.2</div>

with
S = local slope [m m-1]
A = catchment area
θ = concavity index
ks = channel steepness

Accordingly, θ equals the slope of this function, while k_s is its intercept. In general, the function of such an S-A plot is linear and has a negative slope, (i.e. a positive θ) in a mature river system (Demoulin et al., 2017).

5.2.2 Normalized profile steepness k_sn

The profile steepness k_s was found to be positively correlated to the rate of erosion (Ouimet et al., 2009, DiBiase et al., 2010, Harel et al., 2016, Mudd et al., 2018). However, k_s values may differ widely between channels. Therefore, it is appropriate to estimate a normalized profile steepness k_{sn}, in order to derive deviations of single reaches or segments of the stream from the overall steepness to identify parts of increased or decreased erosion.

Based on equation 5.1, which describes the equilibrium of uplift U and erosion, the equilibrium slope S can be derived through equations 5.3 and 5.4:

$$S^n = \frac{U}{kA^m}$$
<div align="right">eq. 5.3</div>

$$S = \left(\frac{U}{k}\right)^{1/n} \cdot A^{-n/m}$$
<div align="right">eq. 5.4</div>

These include the erosivity coefficient k, the slope exponent n and the exponent of the catchment area m from equation 5.1. The factor k comprises a wide range of environmental properties such as sediment load, bedrock erodibility, climate, hydraulic and discharge (Demoulin et al., 2017). The first term of equation 5.4 is also known as the profile steepness k_s (eq. 5.5) and the exponent of the second term in equation 5.4 describes the concavity index θ, as in equation 5.6.

$$k_s = \left(\frac{U}{k}\right)^{1/n} \qquad\qquad \text{eq. 5.5}$$

$$\theta = \frac{m}{n} \qquad\qquad \text{eq. 5.6}$$

According to Flint (1974), the channel slope S can be expressed as a function of profile steepness k_{sn}, the catchment area A and the concavity index θ, as expressed in equation 5.7.

$$S = k_{sn} \cdot A^{-\theta} \qquad\qquad \text{eq. 5.7}$$

Consequently, the normalized channel profile steepness k_{sn} can be calculated with equation 5.8:

$$k_{sn} = \frac{S}{A^{-\theta}} \qquad\qquad \text{eq. 5.8}$$

5.2.3 Knickpoint analysis

Knickpoints are sections in a river network, where the graded concave river profile is disturbed. The knickpoint function in the "TopoToolbox" library is designed to find such deviations by fitting a hypothetical strictly graded profile to the observed profile (Schwanghart and Kuhn, 2010, Schwanghart and Scherler, 2014). Thus, a knickpoint is represented by a vertical offset of the convex profile from the expected concave profile. The initial concave profile is iteratively adjusted to the observed profile, where the convex offset is maximal. Consequently, the upstream profile is modelled to readjust to the knickpoint related base level. These specific points are identified as knickpoints by the algorithm and assigned with a magnitude related to the offset.

Uncertainties in the river profile, primarily caused by inaccuracies of the DEM, from which the long profile was derived, produce a small-scale pattern of high and low offsets from the modelled profile, so that the number of iterations and consequently the number of identified knickpoints exceeds reasonable levels. Therefore, a tolerance threshold is introduced to compensate this effect and avoid over-adjustment of the model.

The result of this method is displayed in figure 5.1, with the whole long profile on the left and a detailed view of one pronounced knickpoint on the right. Here, the function was evaluated by approximating the main channel of the Tongati with three threshold values: 1 m, 10 m and 100 m offset constraint. The TanDEM-X model has a vertical accuracy of ~3 m. Therefore, the model with 1 m tolerance overfits to the channel profile and predicts a large number of false positive knickpoints (n=181 knickpoints for the whole channel). The model with threshold 10 m finds less (n=7), but more valid knickpoints (see fig. 5.1 detail plot). The most relaxed model with a tolerance of 100 m omits relevant knickpoints, so this model underestimates the actual number.

After a number of tests, an offset tolerance value of 5 m of has shown results, that best represent the field observations.
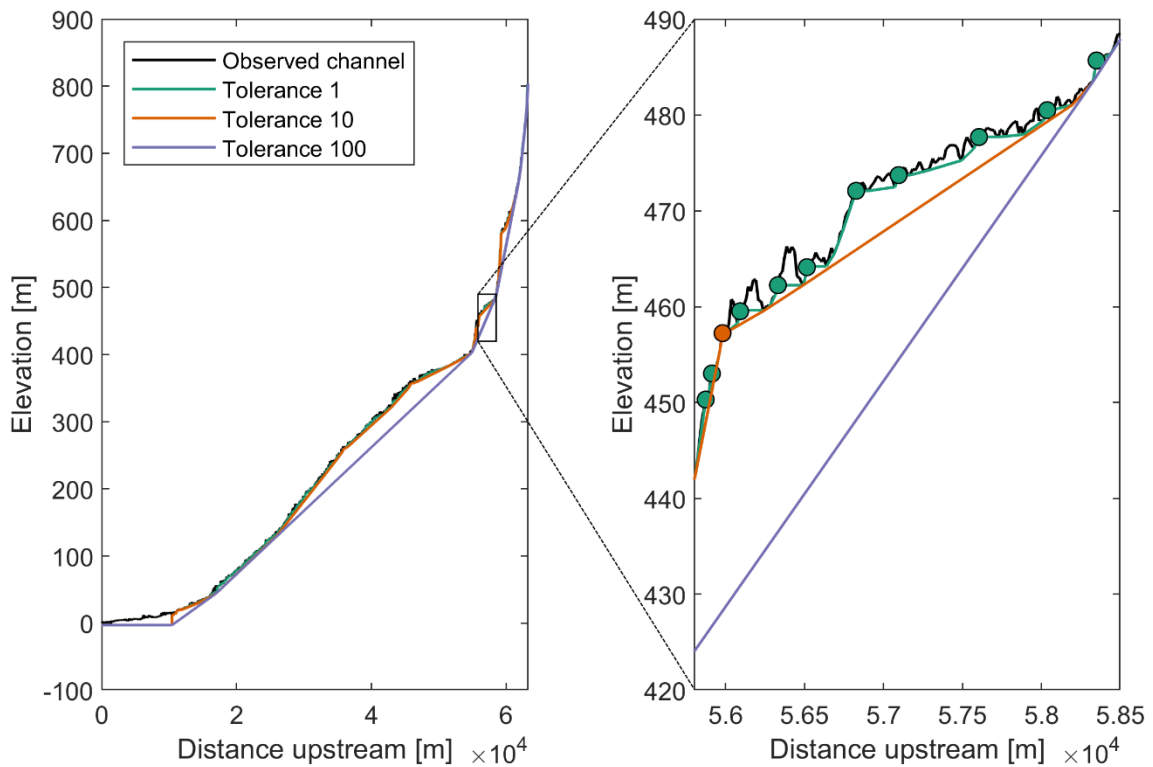
Fig. 5.1: Full long profile (left) and detailed subset (right) of the Tongati main stream (black line) with three different tolerance threshold models (green, orange and purple lines) and their respective knickpoints (colored points).

5.2.4 Planform sinuosity

Sinuosity is a measure of the windings of a fluvial channel. The sinuosity index (SI) is commonly calculated by the division of the curvilinear channel length L_c of a reach by the Euclidean distance between start and endpoint of this reach. The sinuosity function of the "TopoToolbox" software applies this principle to the planform vector geometries of the channel using equation 5.9.

$$SI = \frac{L_c}{L_e}$$

eq. 5.9

With
SI = sinuosity index
L_c = curvilinear length along windings
L_e = Euclidean distance between start and end point

Therefore, this metric is sensitive to the length of the reaches. A segment that is chosen too short may appear nearly straight, although it is actually part of an extended meander. A rule of thumb by Rosgen and Silvey (1996) suggests a minimum segment length, which equals 20-40 times the channel's bankfull width.

According to Schumm (1985) and Brierley and Fryirs (2005) the SI can be used to classify three degrees of sinuosity: straight, low sinuosity and sinuous or meandering. Further measures, which can be extracted with channel mapping are the number of channels, the types of sinuosity as well as its lateral stability.

57

5.2.5 Object-based terrace classification

The terraces in the area are various and can be found at different terrain levels, but also barely visible specimens exist buried under colluvial deposits. This analysis refers to the detection of fill or strath terraces, but also meander cutoffs exposed on the surface. These were predicted with an OBIA approach and later confirmed through field work. All Topographic Indices (TI) were calculated with the "Terrain Analysis Toolbox" of "SagaGIS" 7.3.0 and segmentation was performed with the "Grid Toolbox" of this software (Conrad et al., 2015).

For this purpose, TIs describing the landscape in a quantitative and qualitative manner were selected with great care. In general, object-based geomorphic landscape classification is focused on the differentiation of landscape elements, so that TIs, such as elevation, slope and plan and profile curvature provide good results for the distinction of slope areas (Drăguţ and Blaschke, 2006, Dikau, 1989). However, terraces are a hierarchically subordinate landscape form that is not considered in these classifications. Consequently, a customized set of TIs was selected to predict this specific landform, comprising the Topographic Position Index (TPI), the slope relative to the stream gradient (S_{rel}), as well as the elevation above stream level (E_{rel}).

The TPI (Weiss, 2001) comprises 10 landform classes and is described in more detail in chapter 3.2.1.3. It was selected, because it is suitable for masking landscape forms, that are not related to terraces, such as mountain tops, mesas and local ridges, and for highlighting particularly suitable landscape forms, such as U-shaped valleys, mid-slope drainages and canyons. The TPI landform classification is depicted in figure 5.2.
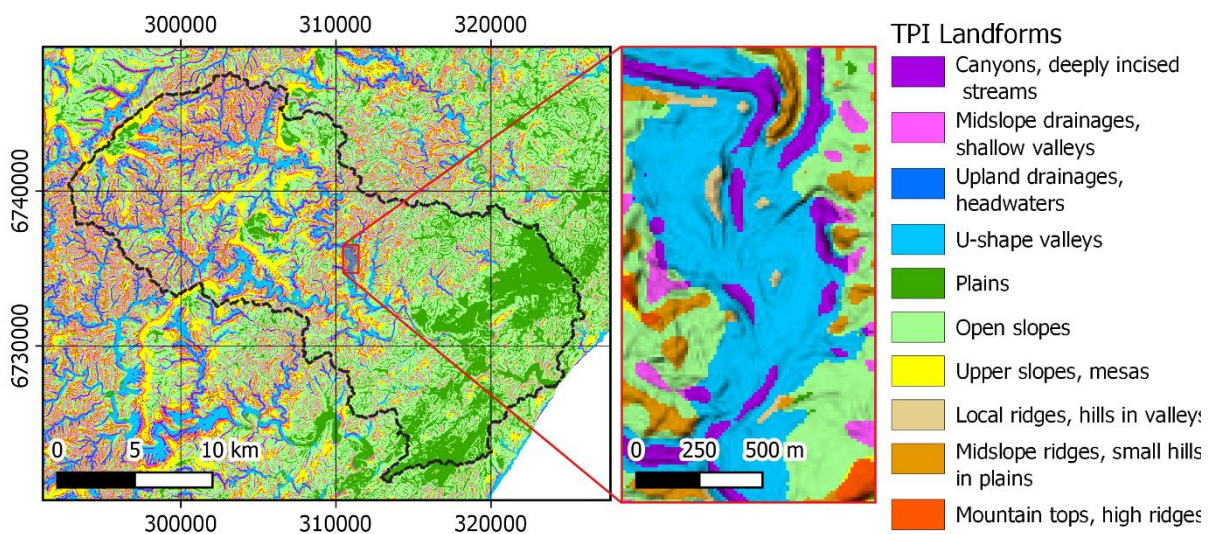
Fig. 5.2: Landforms classified by the Topographic Position Index (TPI) by Weiss (2001).

Because terraces can potentially occur at all altitudes where a river does geomorphic work, the elevation above mean sea level, as delivered by the DEM, is per se unsuitable for their detection. However, since terraces can be correlated by their height above the recent river course, the TI "Vertical Distance to Channel Network", which refers to the main channel, is the variable of choice (fig. 5.3). E_{rel}, as it is denoted here, serves as a relative height measure. Furthermore, Clarke et al. (2007) note that terraces in the region reach heights of up to 50 m above the river. This information serves as a selection criterion to filter relevant landscape units.
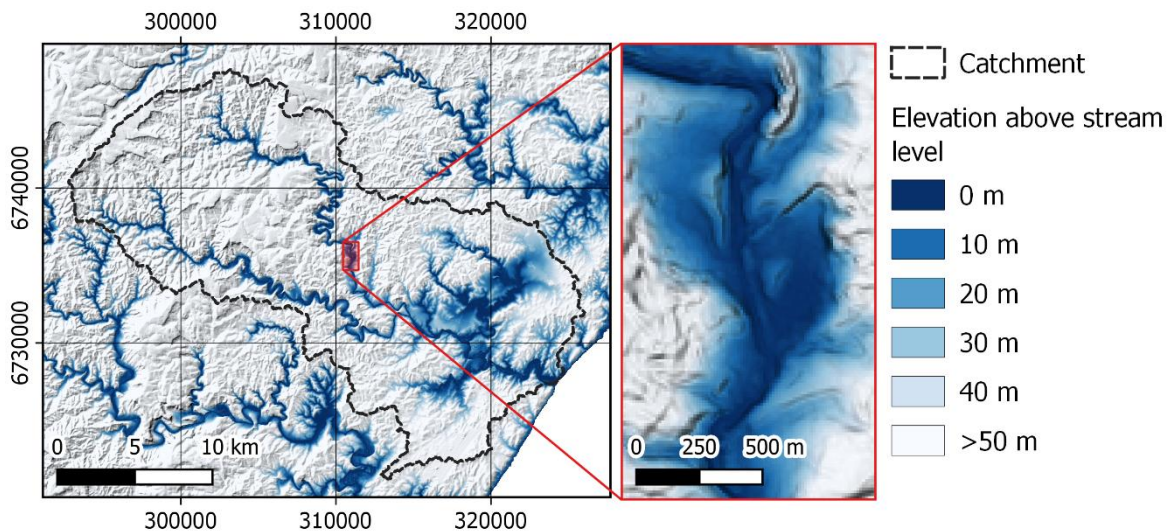
Fig. 5.3: The relative elevation above stream level (E_{rel}), where values associated with terraces are indicated in blues.

Furthermore, a nearly flat surface is a distinct characteristic of a river terrace, which can be quantified by the TI "Slope". This was not computed directly from the DEM, but from the "Vertical Distance to Channel Network" index, so that the estimated values of are compensated for the channel slope of the longitudinal profile (fig. 5.4). Consequently, S_{rel} represents the inclination of a surface, relative to the channel gradient. This also helps to distinguish fluvial terraces from the other flat areas of the African (mesas) and Post-African II (coastal plains) geomorphic provinces, which originate from earlier geomorphic phases.
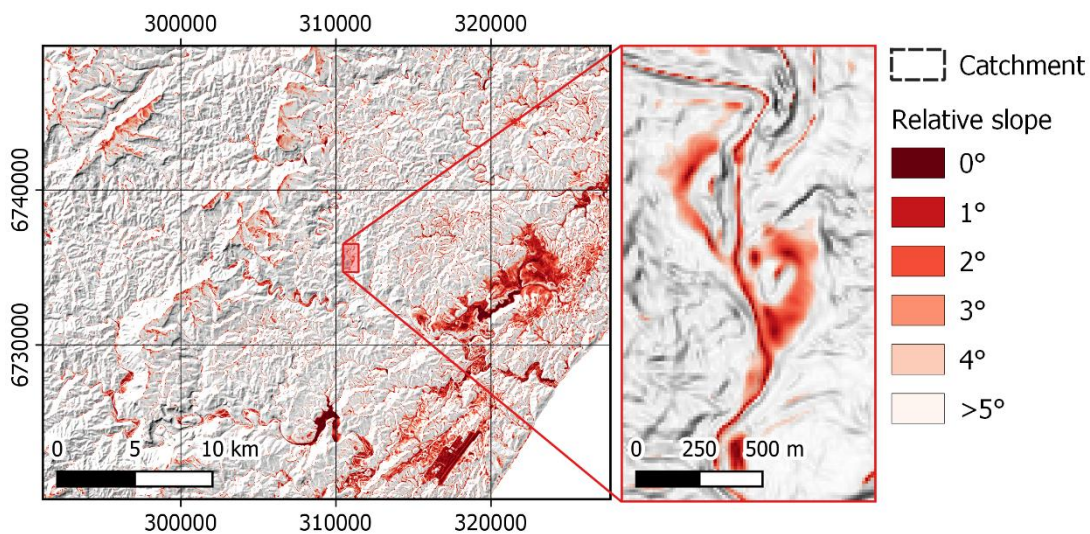
Fig. 5.4: The slope relative to the river gradient (S_{rel}) and flat areas indicated in reds.

With the landscape being quantified by these three indices, a decomposition was subsequently carried out to extract distinct, spatially continuous and homogeneous landscape units (Blaschke et al., 2014). An unsupervised k-means classification after Forgy (1965) and Rubin (1967) was chosen for segmentation, which is available as the tool "K-Means Clustering for Grids" within the "Imagery Processing Toolbox" in SagaGIS (v.7.2.0). With 40 possible target classes, the algorithm was given enough flexibility to differentiate the values of the 3 input variables sufficiently. The results of the segmentation is presented in figure 5.5. Afterwards, each of the segmented polygons was attributed with the majority of TPI and the means of E_{rel} and S_{rel} of the pixels it

circumscribes. The distribution of these attributes can be visualized in a feature space, as depicted in figure 5.6. In this example, likely candidates for terrace landforms, described by low E_{rel} and low S_{rel}, can be expected in the lower left corner.
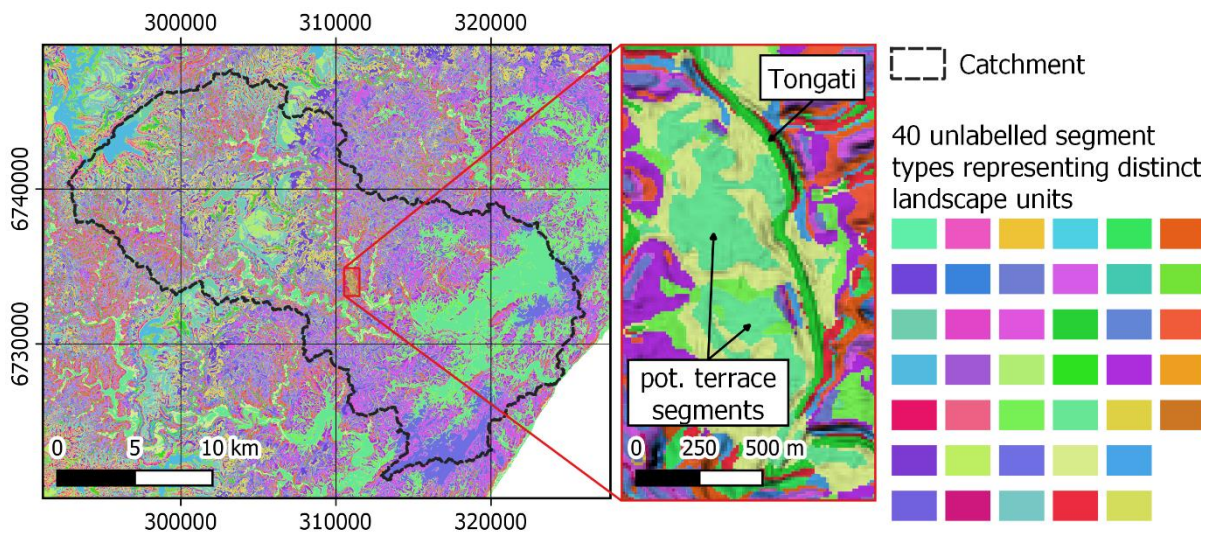
Fig. 5.5: Distinct landscape units generated by image segmentation.
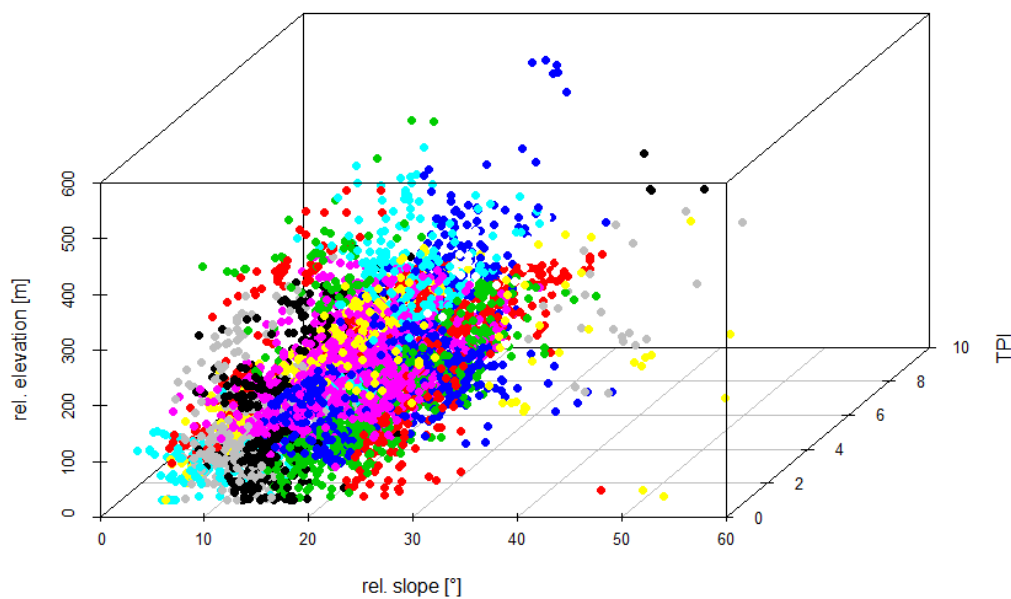
Fig. 5.6: Feature space of a random subset (n=5000) of the ~450.000 segments. Each segment is attributed with the mean relative slope in degrees (x-axis), the majority of the TPI (y-axis) and the elevation above stream level in meters (z-axis). Colors indicate the distinct and unspecified landscape unit classes.

A selection from the total of 474,530 segments was classified as 'potential terrace' based on the derived object attributes. By filtering the mean relative height above the riverbed by a value of $E_{rel} \leq 50$ m, as derived from observations by Clarke et al. (2007), the number of object candidates could be reduced to 93,232 (19.6% of total). A selection of segments whose mean slope does not exceed $S_{rel} \leq 5\%$ allows the number of object candidates to be further reduced to 11,194 (2.4%). Due to these conditions, land form classes TPI=3 (upland drainage, headwaters), TPI=7 (upper slopes, mesas) and TPI=10 (mountain tops, high ridges) were already eliminated from the

60

remaining segments. Subsequently, the segments with the following TPIs were selected as potential terraces based on their valley-related position: TPI=1 (canyons, deeply incised streams), TPI=2 (midslope drainages, shallows valleys) and TPI=4 (U-shape valleys). Objects of class TPI=8 (local ridges, hills in valleys) were included in this context, since these segments are often part of meander spurs. Class TPI=5 (plains) covers the largest area of the remaining segments, but is problematic, since it includes both terraces and the raised marine platform from the post-African II phase. Here, further differentiation at site is necessary. Altogether, the number of object candidates could be reduced to 3,806 (0.8 % of total, excluding class 5) or 10,239 (2.2 %, including class 5) by selecting suitable TPI classes. Of course, this should not be interpreted as a number of 3,806 individual terraces (or 10,239 respectively). The applied classification filter is expressed by the Boolean equation 5.10.

$$\text{pot. terrace} = E_{rel} \leq 50 \text{ m} \wedge S_{rel} \leq 5° \wedge \text{TPI in } (1,2,4,5,8) \qquad \text{eq. 5.10}$$

Figure 5.7 shows the result of the landform classification using equation 5.10. More detail is provided in the results section (chapter 5.3.6).
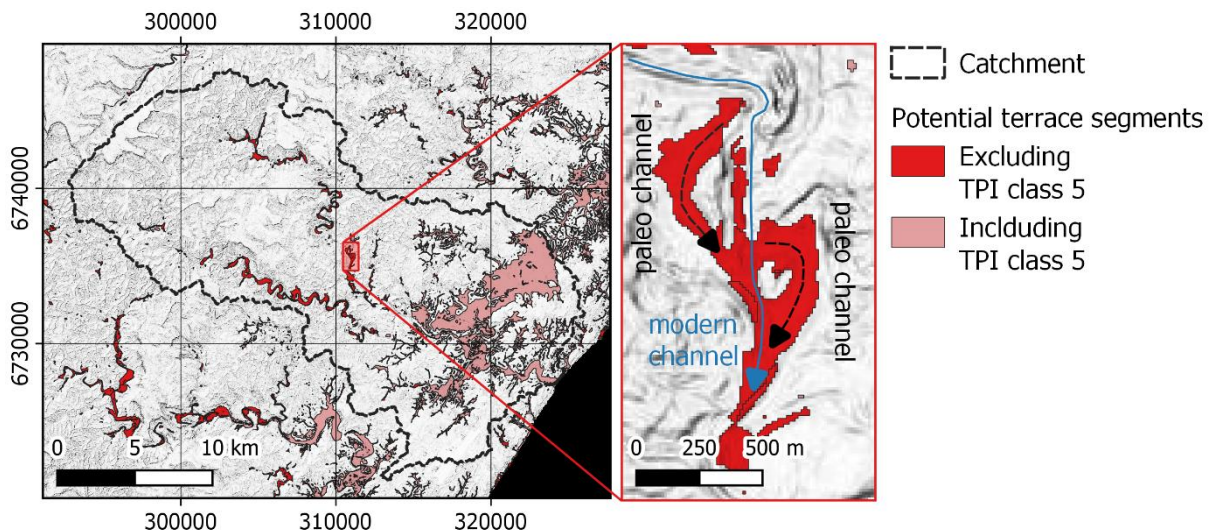
Fig. 5.7: Predicted terraces produced with OBIA landform classification. Note that the scale of this map is the same as figures 5.3-6 to ensure comparability between individual factors and outcome. A more detailed version is shown in figure 5.23.

5.2.6 Electric resistivity imaging

5.2.6.1 Theoretical background

A constant electric current is applied to the ground over two current electrodes (c), which creates the electric potential field. The resulting voltage is measured with two potential electrodes (p), which allows to estimate the bulk electrical resistivities of the materials around the current electrodes. The voltage V measured at the potential electrodes is the result of the applied current I, the material electrical resistivity ρ and the distance a on a uniform half-space from the potential electrode (eq. 5.11).

$$V = \frac{\rho I}{2\pi a}$$
eq. 5.11

with
V = Electric potential at given point (e.g. the potential electrode)
I = Electric current applied at current electrode
ρ = resistivity of the material
a = distance on the half-space

In a geoelectric measurement array, the distance a on the half-space is a function of the geometric factor K, which varies with the distribution of electrodes within arrays. In general, the apparent resistivity ρ_a is calculated with equation 5.12.

$$\rho_a = 2\pi K \frac{V}{I}$$
eq. 5.12

with
ρ_a = apparent resistivity
K = geometric factor

Wenner mode, displayed in figure 5.8a, is referred to as the standard array for vertical electrical sounding (Milsom and Asger, 2011). This array excels with its simple arrangement, where all electrodes are spaced equally. This configuration allows two measurement methods: The electrode spacing is increased to perform a depth sounding, whereas a horizontal movement of the configuration allows the profiling at a fixed depth (Kearey et al., 2002). Its results are characterized by low noise influence on the signal and it performs well in identifying horizontal layering of material in a depth sounding investigation (Schrott et al., 2013). In the Wenner configuration, the apparent resistivity ρ_a involves the equal spacing distance, so that equation 5.13 can be applied.

$$\rho_a = 2\pi a \frac{V}{I}$$
eq. 5.13

with
a = distance between the equally spaced electrodes

The Schlumberger array (fig. 5.8b) is an appropriate method for depth sounding, just like Wenner, however it is known to have a higher resolution when identifying inhomogeneous material in the succession (Schrott et al., 2013). In contrast to Wenner, the electrodes do not have to be spaced equally. Here, the distance between the outer current electrodes is expressed

in relation to the spacing between the inner potential electrodes. Here, the apparent resistivity ρ_a is derived from equation 5.14.

$$\rho_a = \pi \frac{L^2 - l^2}{2l} \frac{V}{I}$$

eq. 5.14

with
l = distance between potential electrodes
L = distance between current electrodes

The major advantage of the Dipole-Dipole array lies in the avoidance of inductive noise, which is achieved by the separation of current and potential electrodes. The pair of current, or potential electrodes respectively, is placed with the inter-dipole distance *a*, whereas these dipoles are separated by *n* multiples of the inter-dipole distance (fig. 5.8). The depth penetration is therefore a function of *n*. Milsom and Asger (2011) stress, that the distance between dipoles should exceed 7 times the inter-dipole distance. Schrott et al. (2013) describe this method as suitable for the detection of objects predominantly in the shallow subsurface. In this array, the calculation of apparent resistivity ρ_a involves the spacing within and between the dipoles (eq. 5.15)

$$\rho_a = \pi n(n+1)(n+2)a \frac{V}{I}$$

eq. 5.15

with
a = distance between the electrodes of a dipole (current or potential)
n = distance between the dipoles as multiples of a
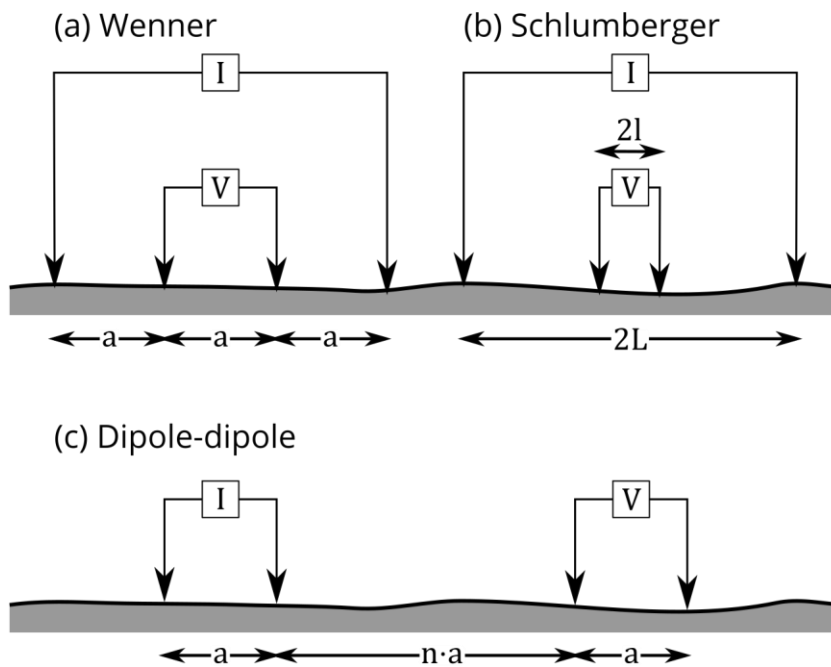
Fig 5.8: Electrode arrays used in this study with current electrodes (indicated by *I*) and potential electrodes (indicated by *V*). Redrawn after Kearey et al. (2002) and Milsom and Asger (2011).

5.2.6.2 Setup and model inversion

Electric resistivity Imaging (ERI) produces depth-cross-sections of the resistivity distribution of the subsurface material. Therefore, electrodes are placed along a traverse and measured in the three array configurations described in the last chapter.

A multielectrode setup consists of number of electrodes, which are connected to a chain. When the electrodes are spaced equally, this allows to perform depth and profile measurements with a single setup (Barker, 1997). In this study, configurations of up to 4 chains with 20 electrodes each were concatenated. Spacing ranged between 1 and 3 meters, depending on desired profile length, depth and resolution. This allows a maximal depth sounding of <20 m (Milsom and Asger, 2011). The electrode chains were attached to the resistivity meter "4point light 10W" by "Lippmann Messgeräte", which was in turn connected to a laptop computer (fig. 5.9). Measurements were acquired with the software "GeoTest" version 2.47 (fig. 5.10). The software was used for profiling and sounding along the transect with Wenner / Schlumberger / Dipole-Dipole configuration to generate a vertical 2-D grid. The measurements were saved in the *.Res2DInv format.

Fig. 5.9. Electric resistivity imaging setup at a paleo meander spur of the Tongati.

The positions of electrodes were measured with a differential GPS (D-GPS) to ensure high accuracy in latitude, longitude and height dimension. Altitude was measured above sea level, or as an alternative baseline, relative to stream level, where this was beneficial for the interpretation (e.g. river terraces).

Model inversion was carried out with the software "RES2DINV" (Loke, 2017) in order to create a high resolution scaled image of the subsurface. It is based on the Gauss-Newton least squares inversion technique (Sasaki, 1992) and applied to the measured apparent resistivity data. The D-GPS-localized electrode positions were considered in the topographic modelling technique after Loke (2000). An example of the model inversion over 4 steps is displayed in fig. 5.11. Where the apparent resistivity pseudo-section (fig. 5.11a) is rather difficult to interpret, the subsequent model inversions reveal successively new underground features while simultaneously increasing model accuracy. The first (fig. 5.11b) and second (fig. 5.11c) iteration contain higher absolute errors (28.0 Ωm, 11.3 Ωm) and fail to illustrate the buried paleochannel situated between 88 and 100 m of the section. In iteration 3 (fig. 5.11d) and 4 (fig. 5.11e) the error is decreased to 8.3 Ωm, and 6.9 Ωm respectively, which allows a proper identification of the feature. The use of elevation above stream level as altitudinal reference base for topographic modelling supports furthermore the interpretation of groundwater influence on the resistivities.
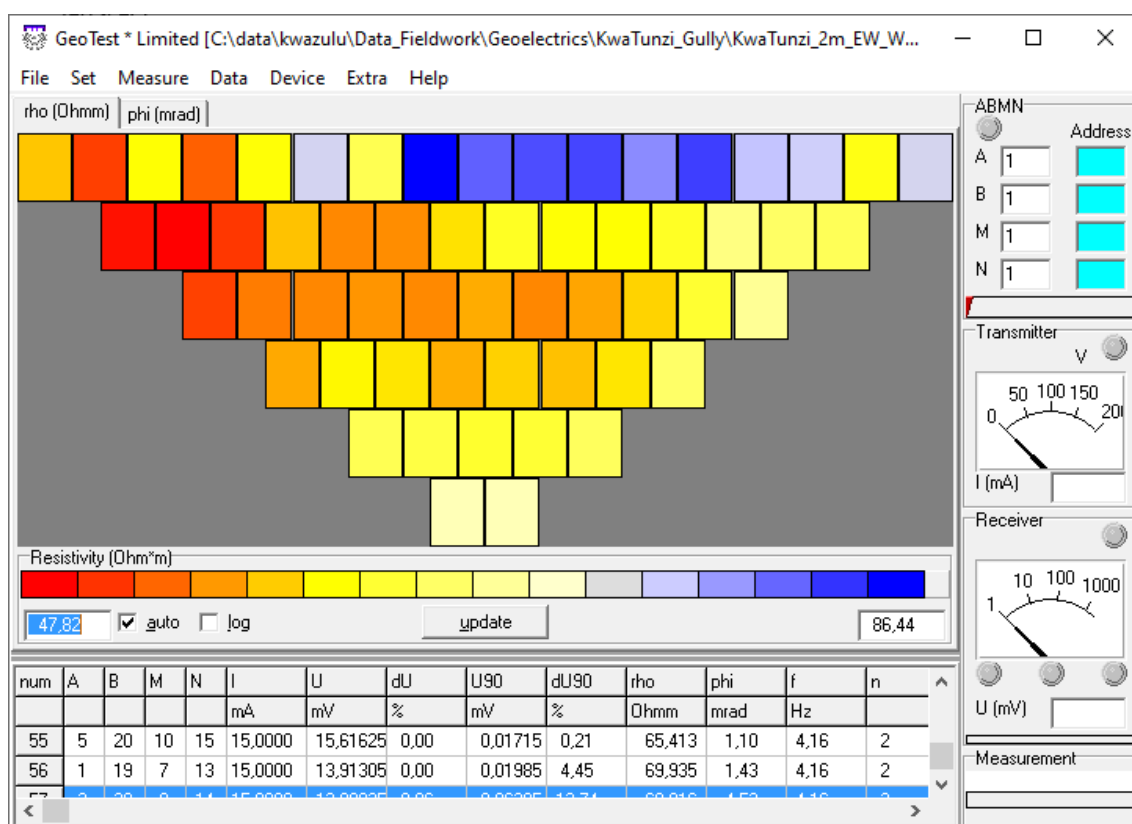
Fig. 5.10: Measurement of subsurface resistivity in GeoTest. Example of a Wenner configuration at KwaThunzi.

Silicate minerals, which are a dominant component of most rocks, are insulators and therefore have a low conductivity. Hence, conductivity of soils is strongly influenced by porosity, moisture content, hydraulic permeability, dissolved electrolytes, pore fluids, and colloidal content. The ranges of typical resistivity values of the most dominant materials of the earth's (sub-) surface are presented in table 5.1. Further effects of rock properties are documented, which help to understand electric resistivity observed in the study area:

- Igneous and metamorphic rocks, which are unaffected by weathering have high resistivities due to their density, little pore volume and little water content. (Yoshino, 2011). Among the weathered products, duricrusts have highest resistivities, which are comparable to unweathered metamorphic rocks (>1000s of Ωm), in contrast to

65

saprolites, which can be as low as 10 Ωm (McNeill, 1980). This may result in a heterogeneous pattern of high and low resistivities, where e.g. core stone weathering occurs.

- In fracture zones, the resistivity is altered compared to unaffected bedrock. This effect can be explained by the increased porosity in the material. Depending on water saturation of the pore volume, this induces higher or lower resistivities (Loke, 2011).

- As conductivity is predominantly a function of porosity, the characterization of soils is difficult. Porosity of unconsolidated material ranges between 20–70%, depending on its texture. Gravels and sands have highest resistivities, followed by loam, whereas clays stand out with a very low resistivity. Since clay has an excellent surface to size ratio, this has a positive effect on its cation exchange capacity, rendering it a good electric conductor (McNeill, 1980).

Tab. 5.1: Typical electric resistivities (Ωm) of sedimentary rocks after Palacky (1988).

Unconsolidated		Consolidated	
Material	Range	Material	Range
Clay	5–150	Argillite	74–840
Gravel	480–900	Conglomerate	2,000–13,000
Loam	20–160	Dolomite	700–2,500
Loess	25–40	Greywacke	400–1,200
Marl	12–70	Limestone	350–6,000
Sand (valley)	360–1,500	Sandstone	1000–4,000
Sand (dunes)	6,200–7,700	Shale	20–2,000
Glacial silt	13–20	Slate	340–1,600
		Coal	1–200,000
		Igneous and Metamorphic rock	1 000–100,000
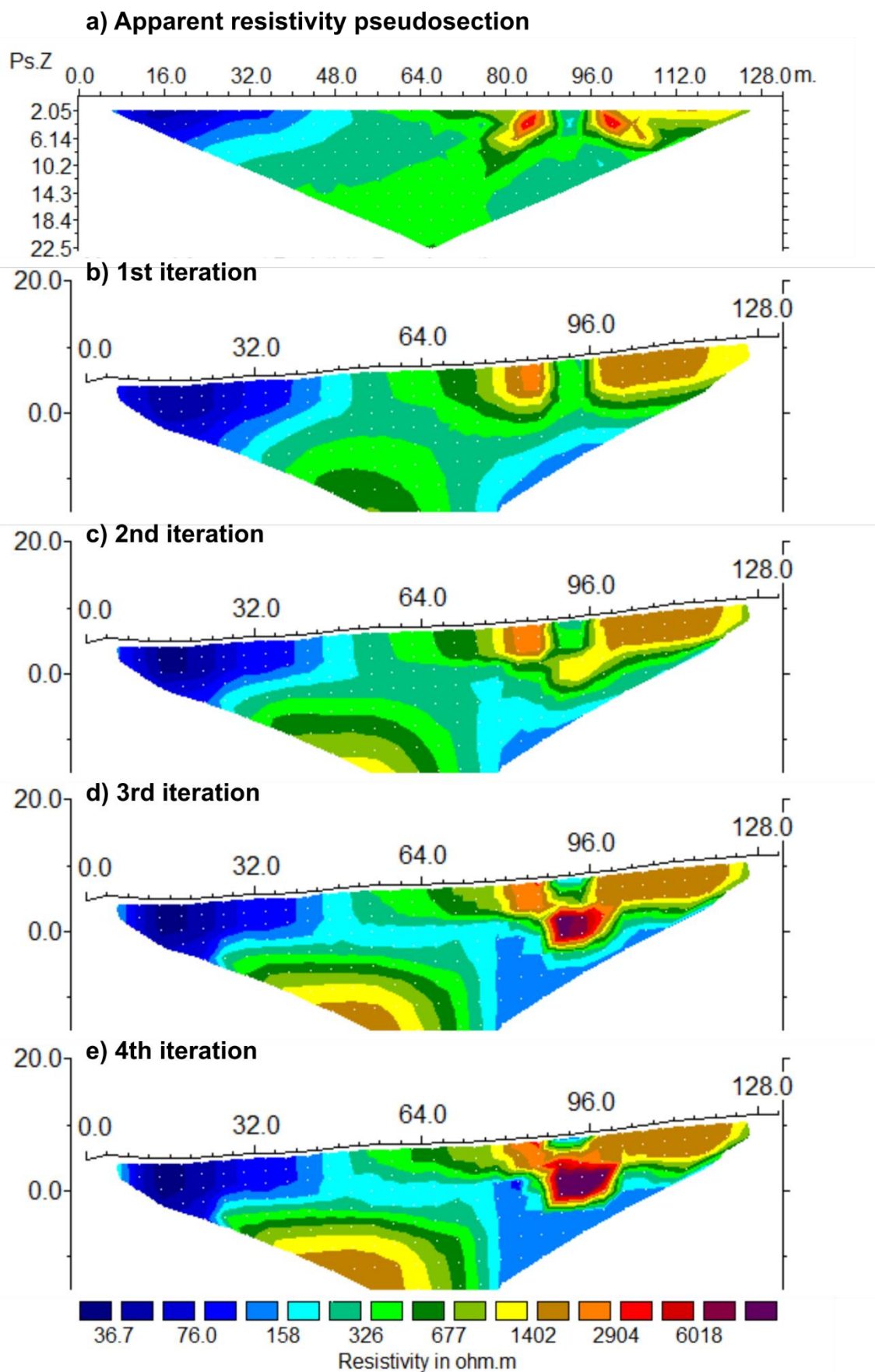
Fig. 5.11: Development of an ERI model over 4 iteration steps from Wenner measurements at a buried channel cross-section. The profile elevations (y-axis) are related to modern stream level.

5.2.7 Luminescence Dating

Optically Stimulated Luminescence (OSL) is a method to estimate the burial ages of sediments (Adamiec et al., 2008). When a mineral, commonly a quartz grain, is exposed to an external source of light or heat, it is stimulated to emit an amount of light, which in turn is determined by the amount of radiation previously absorbed in electron traps since the last zeroing event. Given the fact, that these electron traps can be saturated, the conventional OSL method is restricted to burial ages younger than ~200 ka (Duller, 2004). The equivalent dose (D_e) of a sample is estimated from measurements of the OSL signal in comparison with an artificial OSL response curve generated from a calibrated radiation source induced in the laboratory. Hence, D_e represents the amount of input radiation, that produces an OSL signal equal to the measured signal. In other words, the amount of radiation absorbed since its last exposition. The dose rate (D_r) is the estimated rate of ionizing radiation, which is emanated from the sample itself and the surrounding sediment since the burial. Therefore, the radioactivity of the sediment within ~20-40 cm around the sample determines the amount of absorbed radiation trapped in the sample (Bøtter-Jensen et al., 2003). In bulky, homogeneous sediment beds, like the colluvial and alluvial beds investigated in this study, the D_r can be estimated from a subset of the sample itself, based on the assumption that the appearance of radioelements in the sample is representative for this sediment body. However, for samples taken from a finely laminated profile, which would be typical for archaeological sites, additional radiation measurements are compulsory, since neighboring layers may vary in radioactivity. The timespan since the last complete reset of the OSL clock can then be estimated from the division of D_e and D_r. The overdispersion is a measure of the spread of D_e values as well as measurement errors. In this context, it can be interpreted as the result of sediment mixing of completely reset and incompletely reset quartz grains at the burial event, which is likely to occur e.g. in colluvial deposits, or as the result of exposition and bleaching after the core sampling. Where overdispersion lies below 20 –22%, one can assume, that all grains were homogeneously bleached and a Centralized Age Model (CAM) can be applied (Galbraith et al., 1999). Where overdispersion exceeds 22%, it is appropriate to report the Minimum Age Model (MAM), which relies on the proportion of grains in the mixed population, that were fully bleached at deposition (Evans, 2019, pers. comm.).

The sampling of geomorphological deposits in this study was carried out according to the OSL Sampling Strategy Guidelines of the Geo-Luminescence Laboratory of the University of the Witwatersrand, Johannesburg. All samples in this study naturally contain a high amount of quartz sand, due to its ubiquitous presence in colluvial and alluvial deposits, which guarantees a sufficient amount of dateable material. All sediment bodies exceed 40 cm of thickness, so that samples taken from the center of the layer are not contaminated from neighboring stratigraphic units' radioactivity. The first 5 cm of a sample face were cleared to remove bleached surface grains. Then, a steel tube with 5 cm diameter and 20 cm length was hammered into the sediment and both ends sealed with black, opaque tape, when filled with sediment. The sample tubes were labelled with sample ID and orientation and recorded alongside auxiliary information, including GPS coordinates and altitude, profile depth and stratigraphic information. The sites are described in table 5.2.

Tab. 5.2: OSL sampling sites and description.

ID	GPS (Lat/Lon)	Altitude (m a.s.l.)	Profile position (cm)	Description
CSA1	-29.53591 31.09104	93	30	Lower Tongati, cross section of alluvial sediments at a level T2 terrace (+15 m); fig. 5.12a.
CSA2	-29.53032 31.10737	56	50	Lower Tongati floodplain, level T1 alluvial sands; fig. 5.12b.
CSA3	-29.49200 31.04822	180	120	Upper Tongati, paleo meander spur, level T2 colluvial fill (+15m); fig. 5.12c.
CSA4	-29.52273 31.07407	120	150	Upper Tongati, soil profile with alluvial clasts in the lower part and burried by colluvial sediments; fig. 5.12d.
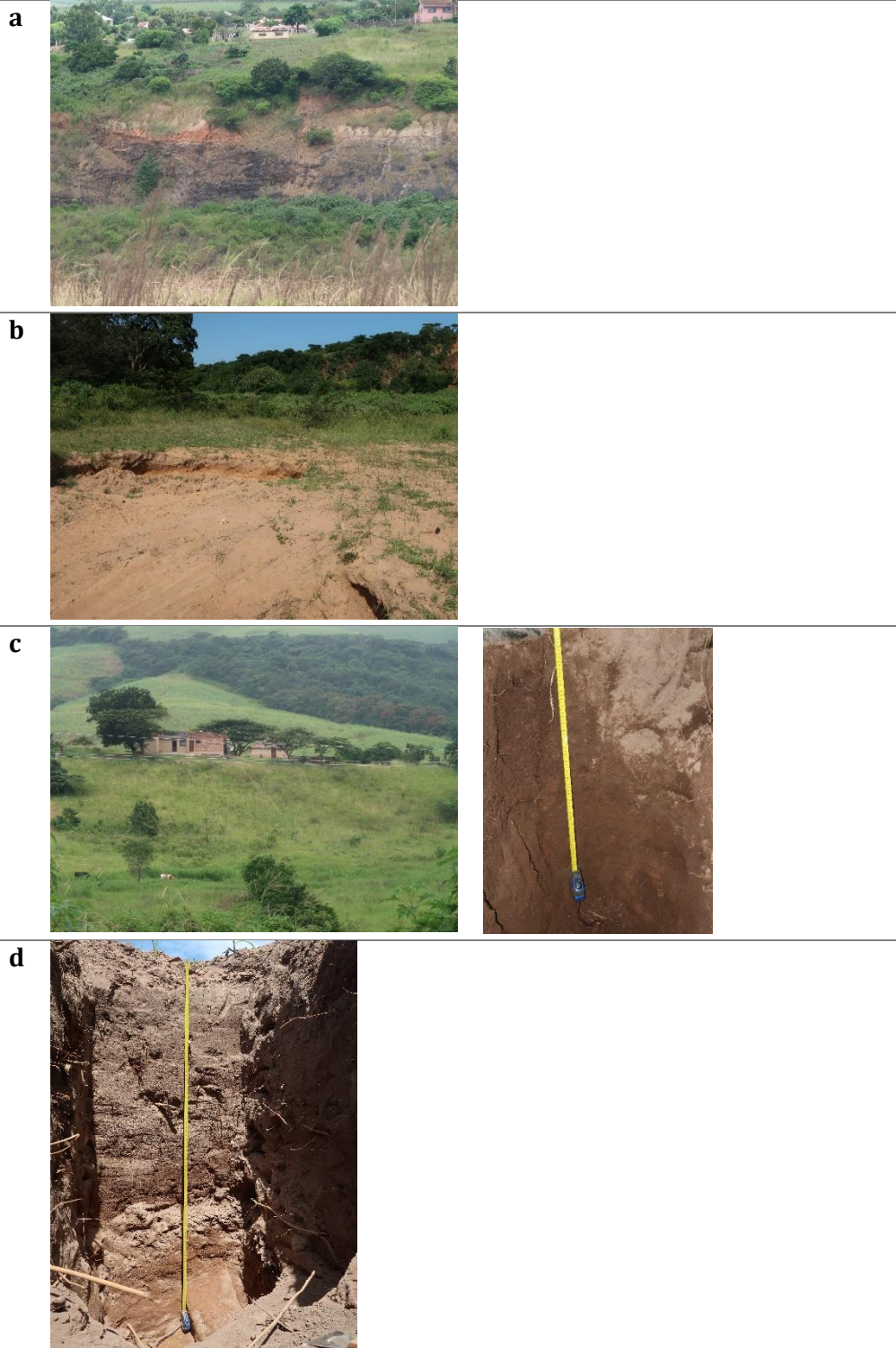
Fig. 5.12: Origins of the OSL samples. Details on sites a-d are listed in table 5.2.

5.3. Results

5.3.1 Stream network

Catchment area and stream network models are typical GIS applications, which allow to derive fluvio-morphological parameters for the description of water-related properties and processes from the DEM. To derive such a network, it must be analyzed, how large a sub-catchment area must be to generate perennial surface runoff. This threshold can vary from catchment to catchment due to diverse general conditions regarding soil, geology, climate, vegetation, etc. In this study, the initiation of perennial surface runoff was quantified based on official topographic maps at the scale of 1:50,000, where ephemeral and perennial streams are mapped. The map sheets 2930DB, 2930BD, 2931CA and 2931AC show 15 such points where water-bearing tributaries of the Tongati River constitute themselves all year round. These form the side streams Wewe, KwaManzaduma, KwaNgqakala, Dwaleni, Ngobhoza, Mona, KwaSonkombe, KwaBopa, KwaManamnyama and Mtebeni. The points were digitized and the related values of flow accumulation (i.e. the contributing catchment area) derived with the "D8" algorithm, were sampled.

Figure 5.13 displays a violin plot, where the horizontal width of the violin represents the relative abundance of the flow accumulation values, which are indicated on the y-axis. The left feature shows, that 95% of all pixels in the catchment have a flow accumulation lower than 10^4 m^2, but few pixels situated at the Tongati outlet, have values almost as high as 10^9 m^2. As indicated through the right feature, the threshold, at which perennial flow is initiated, lies roughly between 10^5 and 10^7 m^2, with a mean value of 2,214,787 m^2 and a median value of 715,340 m^2. Therefore, a threshold value of 10^6 m^2 was chosen as a suitable estimate.
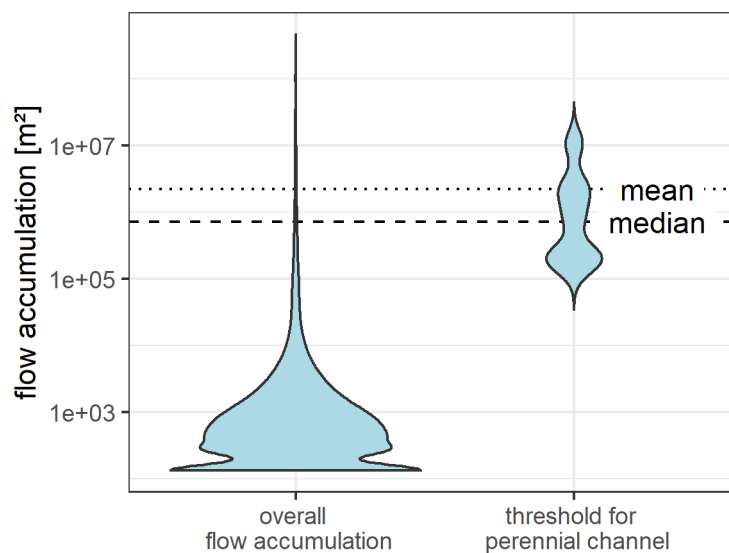
Fig. 5.13: Distribution of flow accumulation values in the whole catchment and the thresholds for the initiation of perennial runoff.

The calculation of the channel network from the DEM results in the drainage pattern shown in figure 5.14. The generated stream network correctly reproduces the Tongati main stream and all the tributaries mentioned above and thus provides a valid representation of the actual discharge system. Therefore, it is suitable to derive further fluvio-morphological properties and to detect characteristic deviations from the stable system. The factors gradient S, steepness k_{sn}, and

71

sinuosity were included in this figure for quick comparison, but are presented in more detail in their respective chapter.
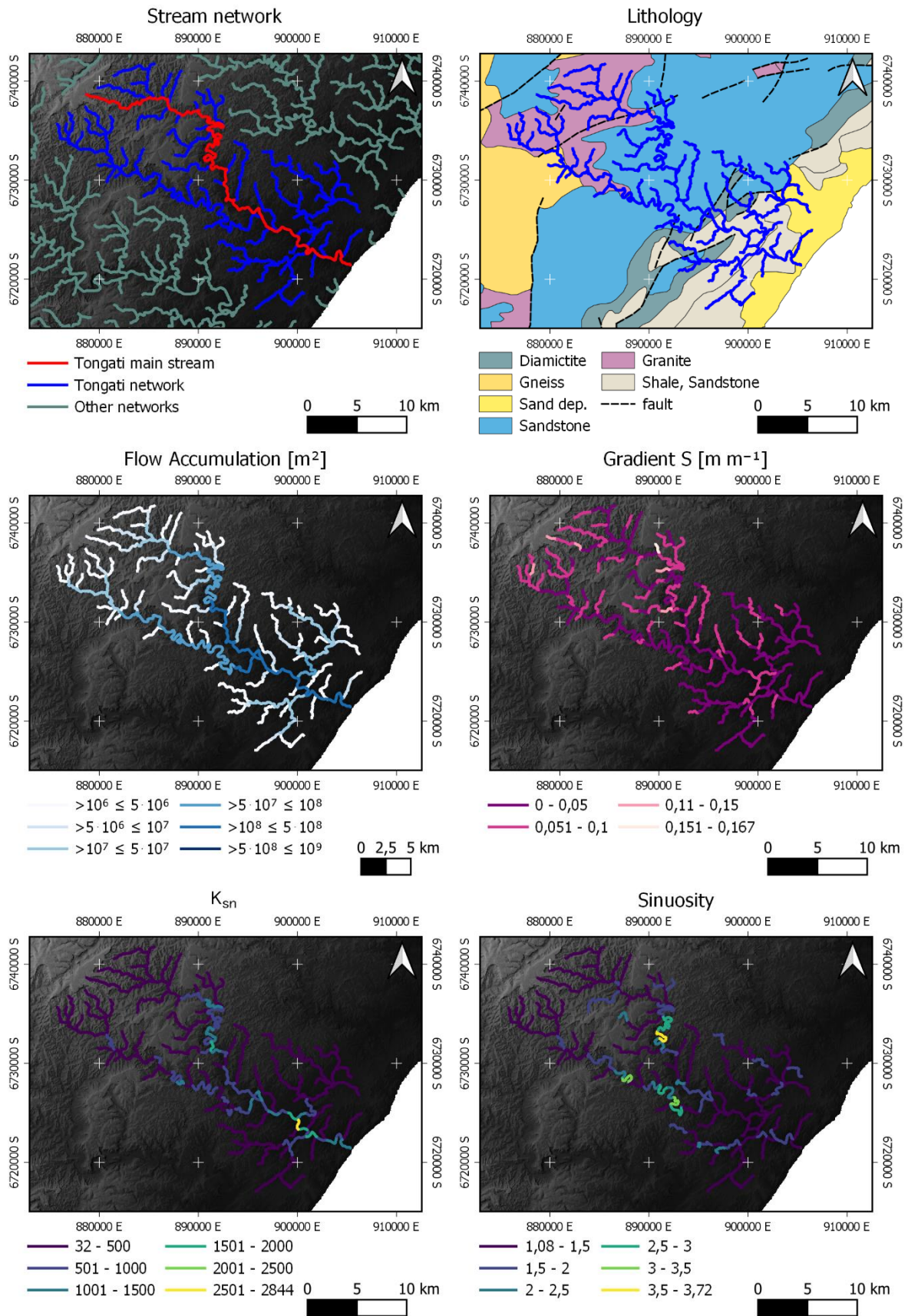
Fig. 5.14: Comparison of the channel network and fluvio-morphological metrics of the long profile as derived from TanDEM-X with TopoToolbox.

72

5.3.2 Longitudinal profile

The longitudinal profile of the Tongati, shown in figure 5.15, shows the height of the main channel in relation to the distance to the outlet, which allows the discovery of the following characteristics. First of all, it can be stated that the Tongati is not a steady-state hydromorphic system. Looking at the main channel (in red), three major zones along the longitudinal profile can be identified. In the upper reaches, at upstream distances of more than 55 km to the outlet, there is a zone that is in general concave, but also has two distinct convex knickpoints. These knickpoints can also be identified in the tributaries (in blue) flowing down from the Ozark plateau parallel to the main channel. A more detailed analysis of knickpoints is given in chapter 5.3.5.

The second zone is located between 28 km and 55 km from the source and shows an elongated convex profile of the main channel of the Tongati and its parallel flowing tributary, the Mona River. This deviates from the expected steady-state profile and indicates continuous erosion in the section, likely associated with the hard Natal Group sandstone. In the smaller tributaries, which flow into Tongati and Mona, there are some knickpoints at higher altitudes (>100 m) above the confluence to the main valley.
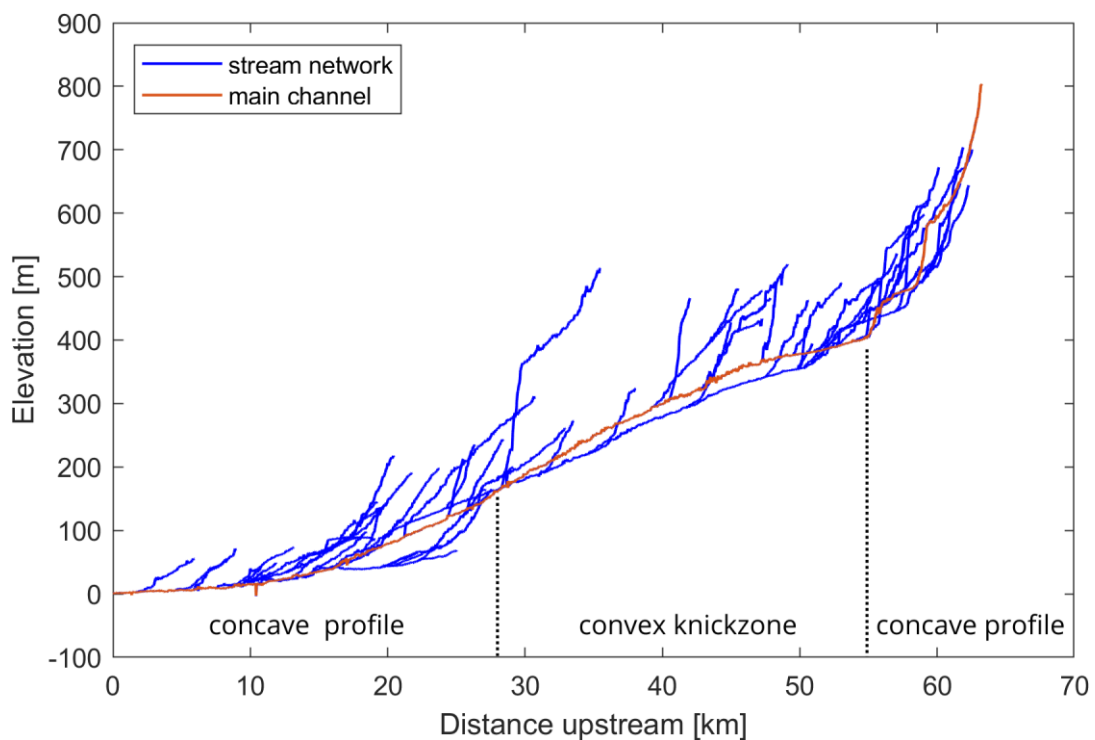
Fig. 5.15: Longitudinal profile of the Tongati river.

In the third and lowest zone, between the outlet and 28 km upstream, the stream has the concave shape that resembles the expected ideal profile of steady-state system. Later, it will be confirmed by the analysis of the S-A plot and the k_s values that this is not the case (chapter 5.3.3 and 5.3.4) because there is a concave knickpoint at a upstream distance of ~15 km. Furthermore, the Mona river, the largest tributary in this zone, flows into the Tongati. At 15 km upstream distance another tributary with a rather flat long profile flows into the Tongati. This is the Wewe, which, in contrast to the main stream, is not perpendicular but parallel to the coastline and therefore not as strongly exposed to the general coastward gradient. This shallow river course is nowadays used as reservoirs of the Dudley Pringle Dam and the Siphon Dam. A

lot of the tributaries in the concave profile of the lower Tongati have knickpoints at low elevations (<50 m) above the modern valley floor. These are likely the result of side streams trying to hold pace with the lowering of the main valley. More detail on these and other convex knickpoints is provided in chapter 5.3.5.

5.3.3 Slope-Area plot and concavity index

The connection between the channel slope S and flow accumulation has already been explained in detail in chapter 5.2.1, but it can be summarized that according to Hack (1972) the ideal longitudinal profile becomes logarithmically lower, and thus flatter, the greater the flow accumulation of the stream becomes. The relation between these metrics, the S-A plot, is displayed in figure 5.16. For this purpose, the channel network was segmented to reaches, with each reach being an uninterrupted stretch of flow between points of initiation, confluence or outlet. When these reaches are longer than 1 km, they are subdivided to maintain a high resolution of the analysis. The figure confirms the assumption derived from the long profile, that the Tongati is not a river in a steady-state, because in a such all points would lie on a straight line with a negative slope. Such a line cannot be constructed by the present distribution. Instead, three straight lines can be approximated to the points by subdividing them into three sections. It should be noted that these sections do not correspond to the zones calculated in the long profile. The positions of these sections are mapped in figure 5.17.
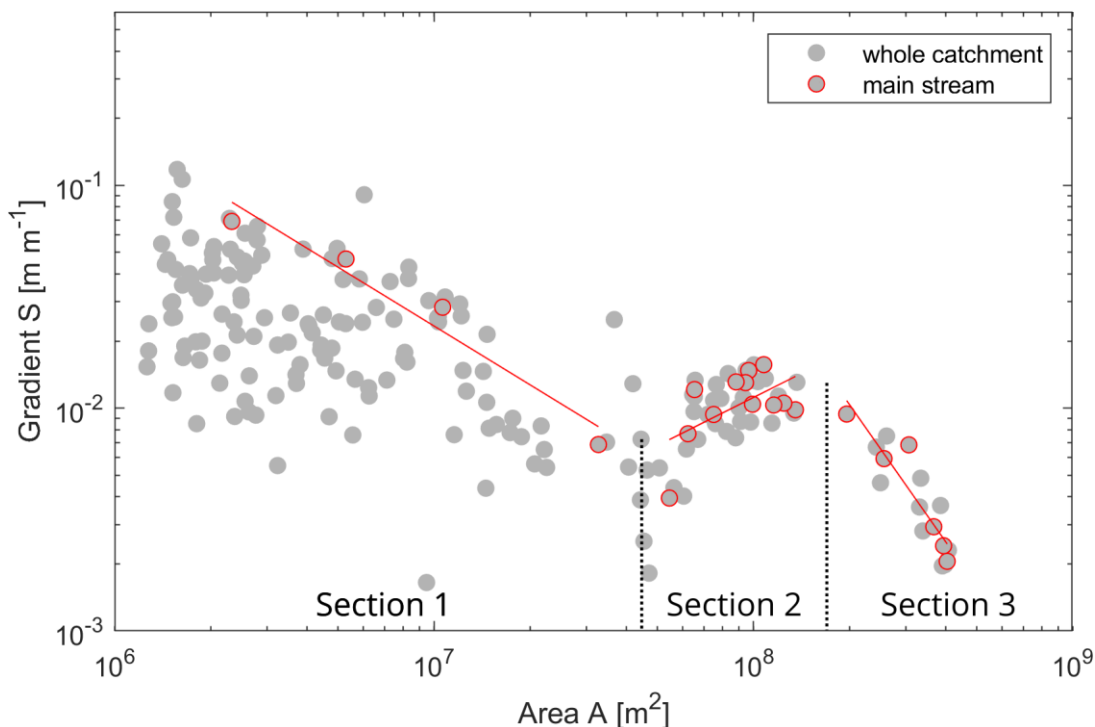
Fig. 5.16: Slope-Area (or S-A) plot of the Tongati.

Section 1 comprises the reaches with the lowest flow accumulation, between the initiation of perennial flow at and a flow accumulation of 35 km². In this section, a general decrease of the slope with the drainage area can be observed, but the variance is very high, especially with reaches of small discharges. This is because the smaller tributaries occur in all parts of the catchment area, which is very heterogeneous. Some branches originate in the steep slopes of the mountainous headwaters and show high slopes, others, such as branches of the Wewe River, originate in the flat coastal area and show correspondingly lower slopes. Additional complexity

74

is added by tributaries, which originate on the rather flat plateaus of the African surface in the upper and middle reaches, but then plunge down into the valley after a certain distance, thus inverting the commonly expected succession of a channel. Therefore, the diversity of the landscape and its genesis is reflected in the high variance of the gradient S of this section. Regarding the main stream alone, however, a linear relationship with negative slope can be constructed. The mean concavity $\theta=0.88$ and the profile steepness $k_s=4.51$ can be estimated (tab. 5.3) with this function.
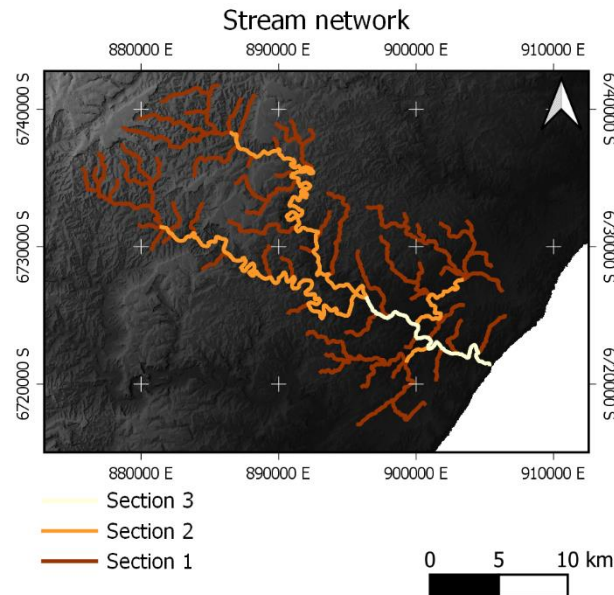
Fig. 5.17: Stream network with sections derived from the S-A Plot.

Section 2 contains the reaches with higher flow accumulations than section 1 (>35 km²), and up to values of ~175 km². These include the middle and upper reaches of the Tongati, the Mona, that runs parallel to the main stream before it confluences, and the main branches of the Wewe and Hlawe, which flow into the lower reaches of the Tongati at Maidstone and Tongaat respectively. In this section a positive correlation between gradient S and the catchment area A can be observed. In other words, the more discharge accumulates in the channels of this section, the higher their gradient S becomes. The fitted function yields a negative concavity of $\theta=-0.71$, i.e. a convex profile, and a steepness value of $k_s=-7.7$. These observations cannot occur in a mature steady state system, because the increased erosive potential would compensate for this excess by headward erosion, and consequently a lowering of the channel. Therefore, it indicates a disturbance of the channel network in this section. It can be assumed that the flow in this section is in a transient state.

Section 3 is initiated at the confluence of the Mona and Tongati rivers with a joint catchment area of 195 km², which increases to just over 400 km² by the end of the section, the river mouth towards the Indian Ocean. With the estimated concavity of $\theta=2.04$ and a steepness of $k_s=15.00$, the negative slope of the fitted function is pronouncedly high. This concavity θ deviates from the typical "narrow range centered on 0.5", as observed by Demoulin et al. (2017). Also Mudd et al. (2018) derived values not higher than 1.0. Ergo, observations of this section indicate that the channel profile slope becomes extraordinarily flat, thus creating a pronounced concave shape.

As the results of the deviations from the normalized k_{sn} analysis show, this change from normal steepness towards flat steepness occurs in a rather short segment.

Tab. 5.3: The Sections of the S-A Plot and the derived coefficients from the loglog-linear fitted functions.

Section	Min A [m^2]	Max A [m^2]	Concavity θ	Steepness k_s
1	10^6	$3.50 \cdot 10^7$	0.8778	4.5129
2	$3.5 \cdot 10^7$	$3.75 \cdot 10^8$	-0.7191	-7.7051
3	$3.75 \cdot 10^8$	$4.04 \cdot 10^8$	2.0445	14.9863
All together	10^6	$4.04 \cdot 10^8$	0.5350	2.2196

5.3.4 Profile steepness and sinuosity

The channel morphological properties flow accumulation A, channel gradient S and the channel steepness k_{sn} are presented in the overview figure 5.15. While A and S follow the expected pattern, i.e. logarithmic descrease of S related to the growth of A, the k_{sn} value of the single reaches reveals deviations from the expected normalized channel steepness. It was calculated with equation 5.8 using the segments' flow accumulation, its gradient S and the overall channel concavity θ=0.5350. A detailed overview of the segments and their k_{sn} and sinuosity values are presented in figure 5.18. Thereafter, five sections of the channel stand out for their characteristic deviations from the expected profile and planform shape.

In general, few to none disturbances are to be found in the upper reaches of the Tongati, Mona and the side streams. Most deviations exist in the middle and lower reaches of the Tongati as well as the middle parts of the Mona.

The highest deviation from normalized steepness was detected in the lower course (section 1) between the confluences of the Wewe and Hlawe tributaries, where channel gradient decreases remarkably. Although a certain decrease in slope would be expected due to the additional runoff from the confluences of these side branches, such a high k_{sn} value indicates the presence of further processes that flatten the channel gradient. The sinuosity of this part is unremarkably low. This section is associated with the change to a depositional regime with a wider, sediment aggrading floodplain.

Another set of deviations was found near Sibudu Cave, the lowermost reach of the Mona and the confluence of both (section 2). This phenomenon is linked to the New Glasgow / Hazelmere fault complex, which forces the Mona to perform a perpendicular bend to the left-hand side and subsequently follow the fault system till the confluence into the Tongati. These faults are also a boundary between the different lithologies and erodibilities of the harder upstream Natal sandstone and the weaker Dwyka shales downstream. Accordingly, this inactive tectonic displacement fosters a slight increase in gradient and sinuosity.

A third reach (section 3), situated in the Mona, is related to a crossing fault. There, sinuosity increases strongly, whereas no deviations in gradient were detected. Here, the tectonic movement provoked a displacement of the geological beds of the Natal sandstone, which is an obstacle in the river channel. It deflects the river's course and induces meandering, which is propagated up- and downstream of the fault.
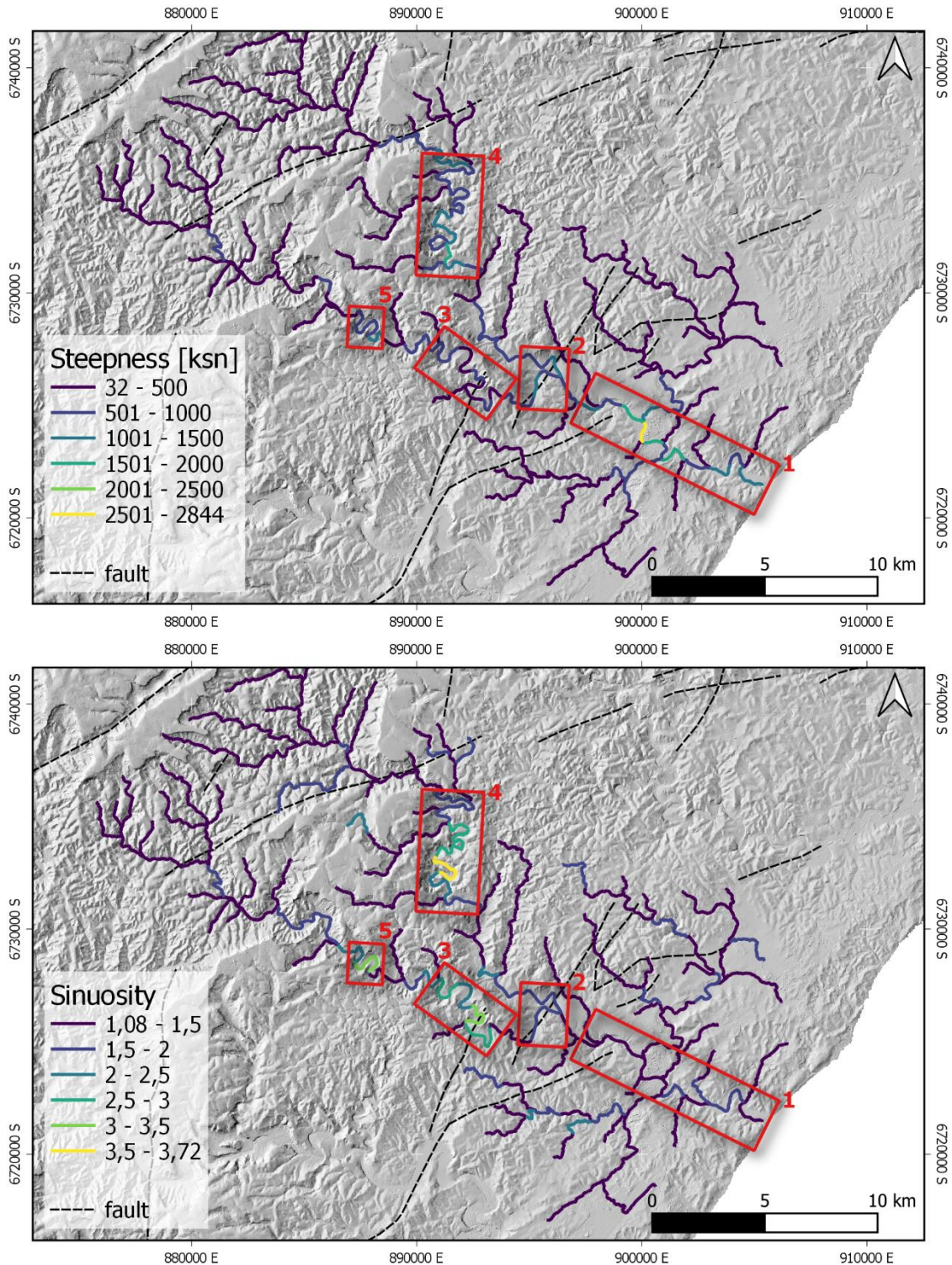
Fig. 5.18: Steepness and Sinuosity of the Tongati channel network and 5 sections with characteristic deviations.

Section four, situated in the Middle to Upper Tongati, is characterized by the highest sinuosity in the network and the highest gradient apart from section 1. It is hosted in the convex knickzone, which was already identified in the long profile and the S-A plot (chapter 5.3.2 and 5.3.3). Furthermore, it is developed in Natal sandstone, which is fractured and strongly intruded by dolerite in this section. Therefore, two processes can be deducted. On the one hand, the increased gradient of the convex profile, which does not allow the channel to incise due to the resistant lithology, but rather strives for an energy balance through lateral erosion, causing

increased meandering. On the other hand, the presence of dolerite barriers forces the channel to bypass.

A fifth section in the Mona valley is characterized by high sinuosity, which is neither associated with increased gradient nor the presence of major faults. The upper boundary of this section is marked by the change of the lithological regime from the Oribi Gorge Granite to the Natal sandstone, which is more resistant to vertical erosion. Consequently, increased lateral erosion promotes higher sinuosity in this section.

In summary, the hydromorphometric inventory of the Tongati comprises channel deformations induced through lithological, tectonic and sedimentological control.

5.3.5 Knickpoints

This analysis of the Tongati catchment area revealed a total of 93 knickpoints, whose magnitudes were determined from the vertical distance from the expected concave-up model. It is the vertical displacement from a potential steady-state channel. Figure 5.19 shows the knickpoints along the long profile of the catchment, whereas their spatial distribution is mapped in figure 5.20. 59% (n=46) of all knickpoints are minor with less than 10 m deviation from the expected profile, while one knickpoint has an extremely high value of 130 m. The remaining knickpoints vary within a range from 10 to 62 m (n=47). A more precise classification allows to differentiate the anthropogenic, tectonic, lithological and morphological drivers of the derived knickpoints.
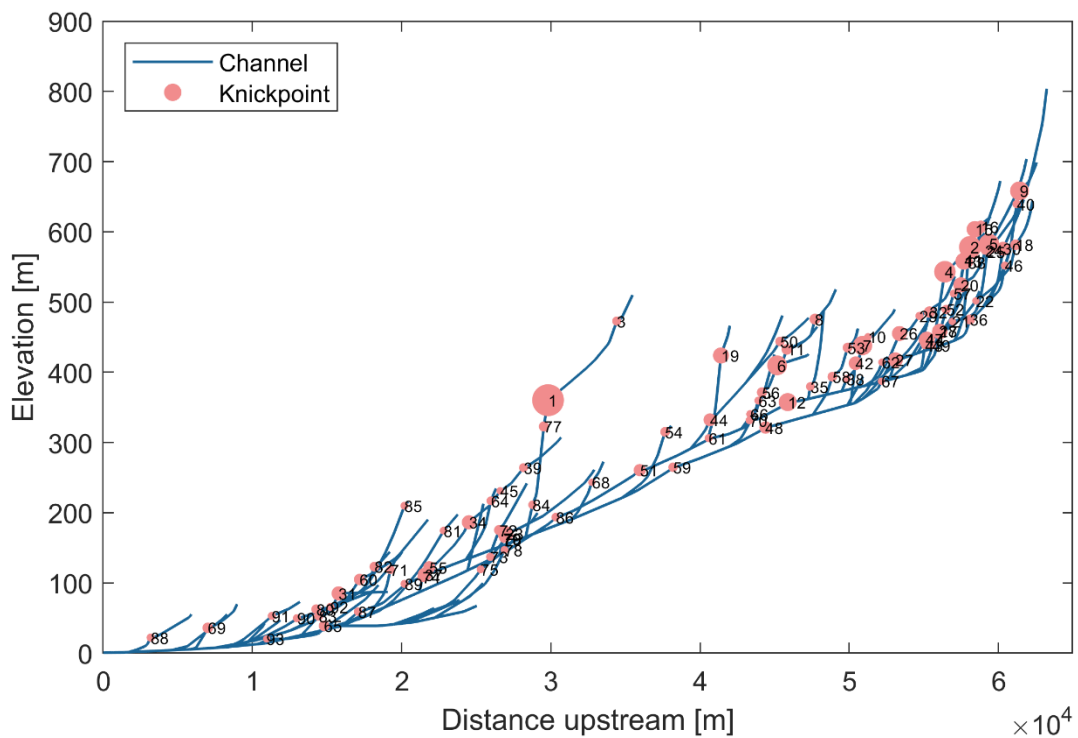
Fig. 5.19: Long profile of the channel network with knickpoints.

Three knickpoints are related to anthropogenic influence on the modern drainage system. These are related to man-made structures on the King-Shaka Airport (Number 31) in the southernmost catchment, as well as the retaining walls of the Dudley-Pringle Dam (65) and the Siphon Dam (93) in Maidstone.

The knickpoint with the highest magnitude (1) is a vertical step, where the stream drops by 130 m within few hundred meters of distance. It is an example of the knickpoints, that are related to the paleo surfaces building larger planations in the catchment, i.e. the African and Post-African I surface. The difference between the channels on the planed surface and the steep decline off their margins create pronounced knickpoints in the middle reaches of the Tongati. These comprise knickpoints 1, 77, 3, 19, 50, 6 and 8. No knickpoints were detected on the African surface of the Ozwatini plateau, which is the highest part of the catchment, because low flow accumulation does not form perennial flow in this landscape feature.

At least two regions were identified, where knickpoints are associated with major faults. In the Upper Tongati, the main channel follows a fault, which is also crossed by side streams. This induces variability in the bedrock erodibility responsible for the knickpoints 11, 35 and 38.
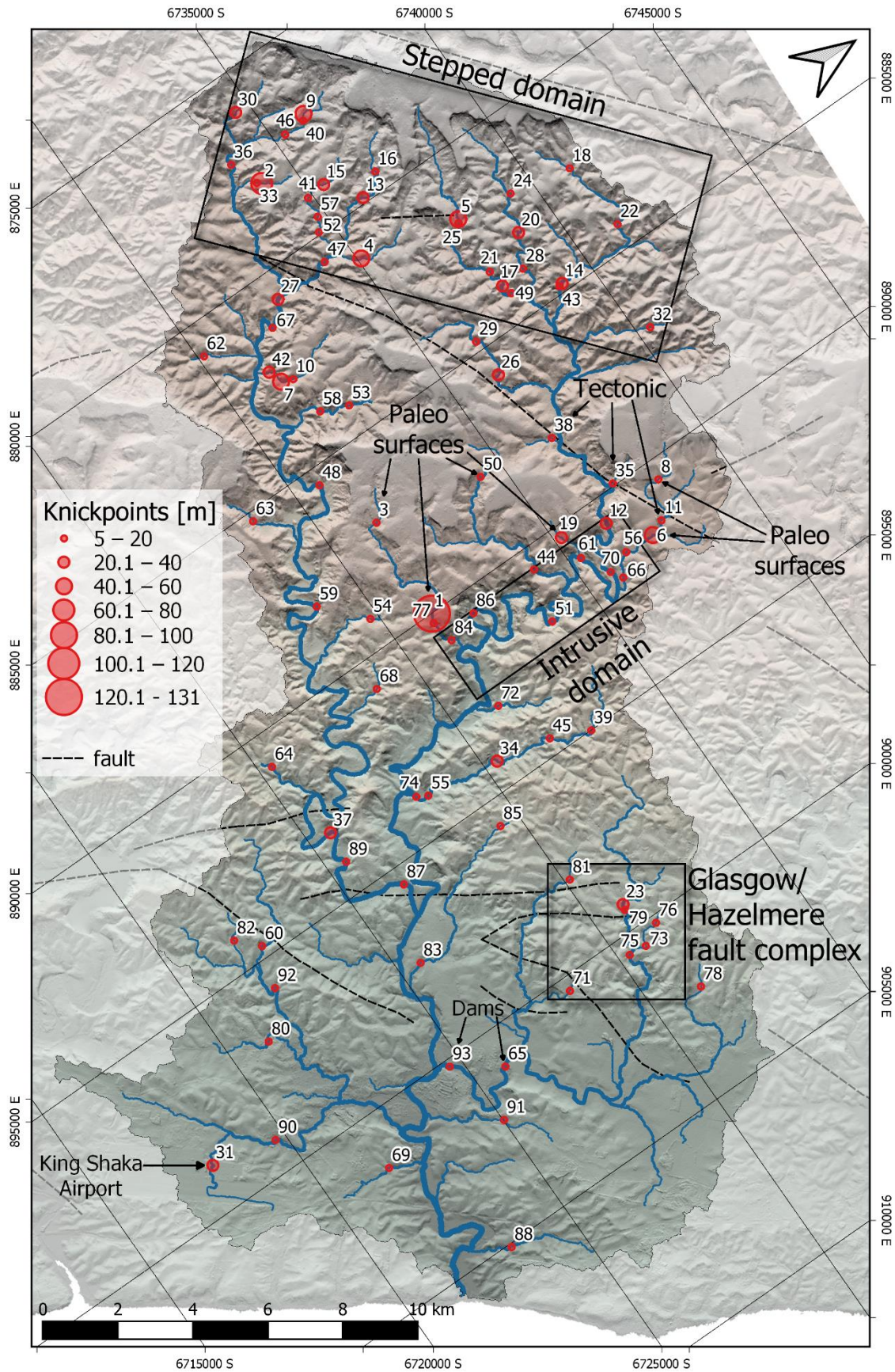
Fig. 5.20: Spatial distribution of the long profile knickpoints in the Tongati catchment.

Tectonic related knickpoints can also be detected in the lower catchment where the largest left hand tributary Wewe crosses the Glasgow / Hazelmere fault complex.

While the Ozwatini plateau itself does not have any knickpoints due to the lack of perennial flow, a large number of knickpoints occur on its slopes, draining into the Upper Tongati and Mona. These can be correlated to two vertical steps, where all knickpoints appear on the same elevations of 450 m and just below 600 m (fig. 5.21). These are likely to be major knickpoints related to the two uplift phases of Post-African I and Post-African II cycles, which rejuvenated the then active streams and initiated further channel lowering. Consequently, these knickpoints are the remains of the backward migrating erosion induced by these uplift events and are still preserved due to the low erosive power of these headwaters. Another possible explanation of this phenomenon would be the potential presence of a fault scarp geology. However, the alignment of the upper step with the reconstructed Post-African I (chapter 3.3), which continues in the neighboring geological testifies for an uplift related generation.
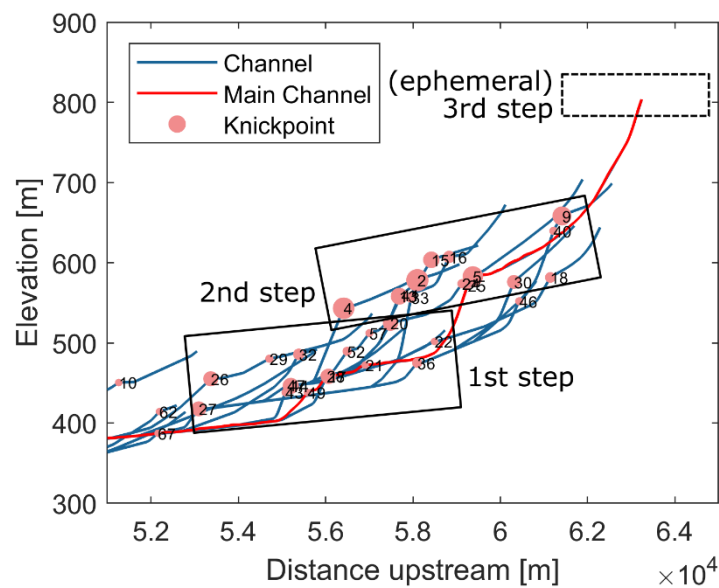
Fig. 5.21: Knickpoints in the upper Tongati Valley. Two steps of parallel knickpoints in the upper reaches of Tongati and Mona. The expected third step, associated only with ephemeral streams from the Ozwatini Plateau, is indicated.

In the steep intrusive domain, which the Middle Tongati crosses with a heavy meandering course, several minor knickpoints can be found in the tributaries. The small-scale dolerite intrusions form small steps, due to their resistance to fluvial erosion. Since the dikes are predominantly upright, the knickpoint does not erode backwards, but persist until the barrier is eliminated.

The main channels of the Middle Tongati and the Mona are particularly free from punctual knickpoints. These are rather characterized by an elongated knickzone, which is best expressed in the channel long profile (fig. 5.15). In the field, these can be identified as bedrock rivers, with sporadic minor cascades or step-pool sequences smaller than 2 m in height.

In the lower Tongati (fig. 5.22), a parallel series of knickpoints can be correlated along all side streams, excluding the left hand tributary Wewe, where two dams conceal potential non-anthropogenic knickpoints. Although the knickpoints are dispersed over several minor left- and right-hand tributaries (69,83, 88,91) and branches of the Hlawe side stream (80, 90, 92) at distances of up to 20 km from the outlet, their heights can be corelated along a 3-dimensional plane grading towards the ocean. This feature follows the former marine and coastal platform known to have been raised and tilted during the Middle Pliocene uplift (Clarke et al., 2007).

Maud 1968 describes this platform to elevations of up to 115 m in widespread areas around Verulam and Tongaat, in the center of the lower catchment. Consequently, the reaches upstream of the knickpoints can be interpreted as older channels, which are still adjusted to the former base level, which existed at the end of the Post-African I circle. Rejuvenated through the uplift event and periodical sea-level fluctuations throughout the Pleistocene, the base level was lowered and headward erosion deepened the younger channels downstream of the knickpoints. The knickpoints retreat radially from the catchment outlet and larger catchment areas reinforce knickpoint migration speed.
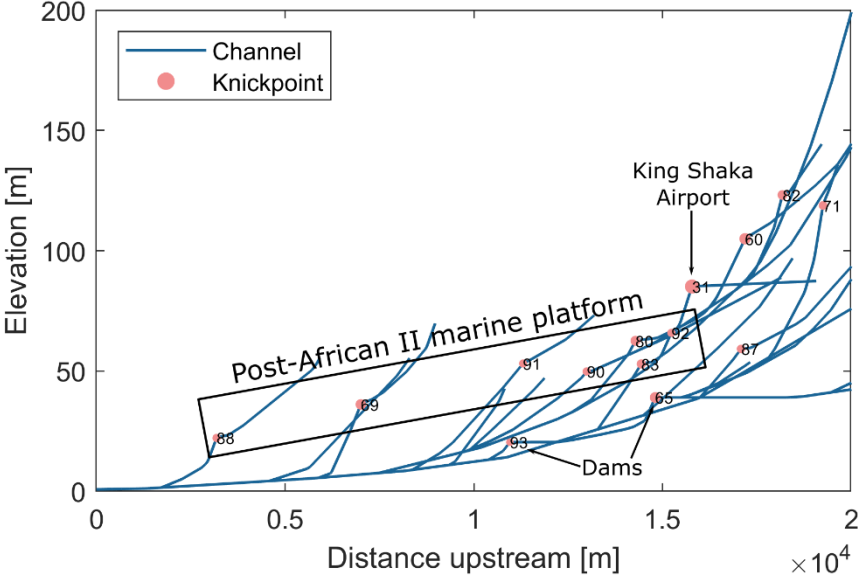
Fig. 5.22: Knickpoints in the lower Tongati Valley.

5.3.6 Object-based terrace classification

The presented method for object-based terrace detection yields two types of terraces, which are distinct by the integration of the landform "Plains" (TPI 5). All potential terraces, no matter of which origin, are presented in figure 5.23.
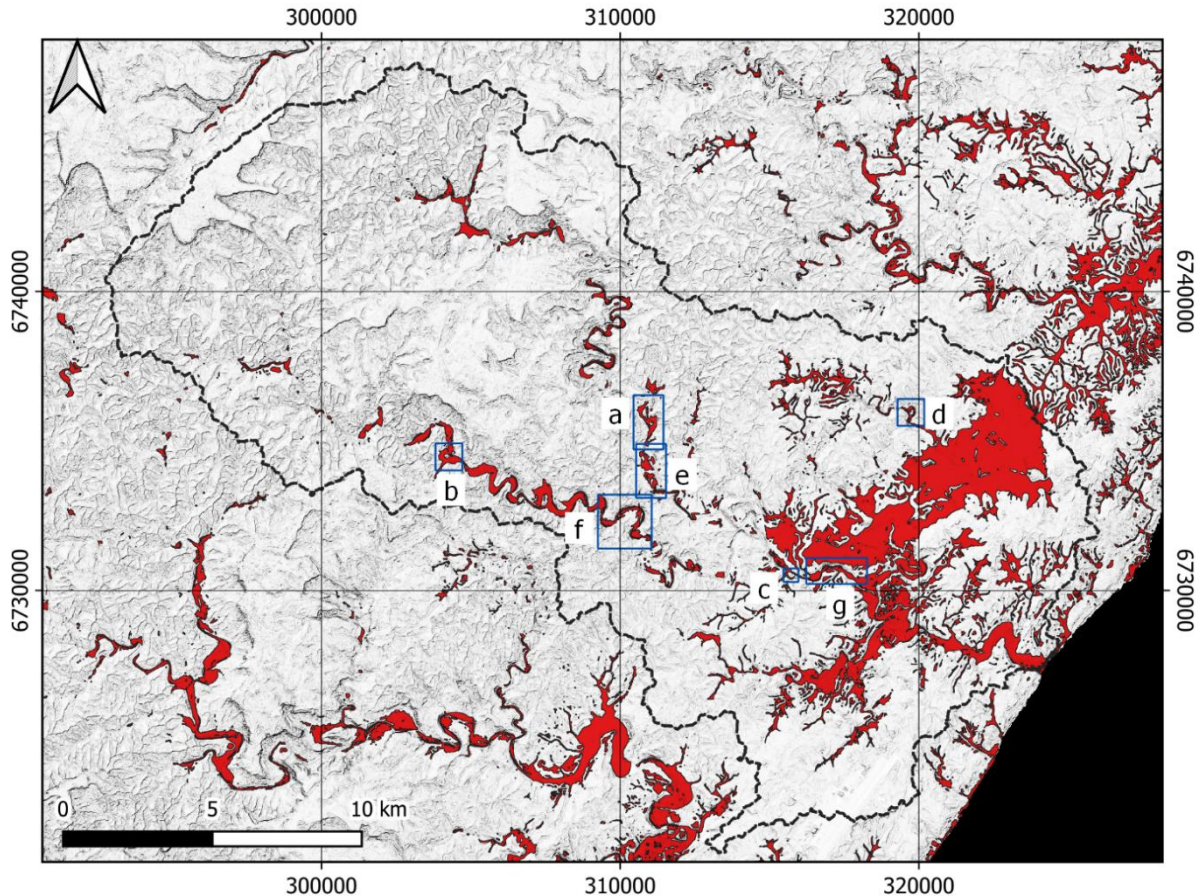
Fig 5.23: Results of the terrace classification. The distribution of objects identified as terraces (Type I and II combined), including the large uplifted marine terrace, ~5 km inland, and the fluvial terraces along the river course. The details a-d highlight avulsed paleo-meanders and e-f larger bank terrace systems.

Type I comprises rather linear and narrow features, which are typical for lateral terrace bars on the sides of recent river courses or abandoned paleochannels. Figures 5.24a-d show a selection of paleo channels, that were once cut-off, possibly formed oxbow-lakes before running dry and are now used for agriculture. Often, they contain a resistant spur between paleo- and modern channel. The detailed maps in figure 5.25e-f show fluvial terraces. An extensive terrace system is shown in 5.25, which includes a stepped relief with several generations of terraces, nowadays hosting a settlement. Figure 5.25f shows several remnant point bars above the Mona River.

Type II incorporates plain landforms in the classification and consequently predicts the marine terrace and the wider alluvial plains and valley fills in the lowermost reaches of the catchment, often several hundreds of meters wide. Accordingly, also non-fluvial landforms are labelled as Type II terraces, like the raised marine terraces in the coastal hinterland, ~5km off the coast. Figure 5.25g indicates the complex situation at the lower Tongati, where marine and fluvial terraces meet. While the marine terrace lies in the north, the river has incised into this plain,

forming a visible scar, which now separates these landforms. In the valley, there are several generations of terraces to be found.
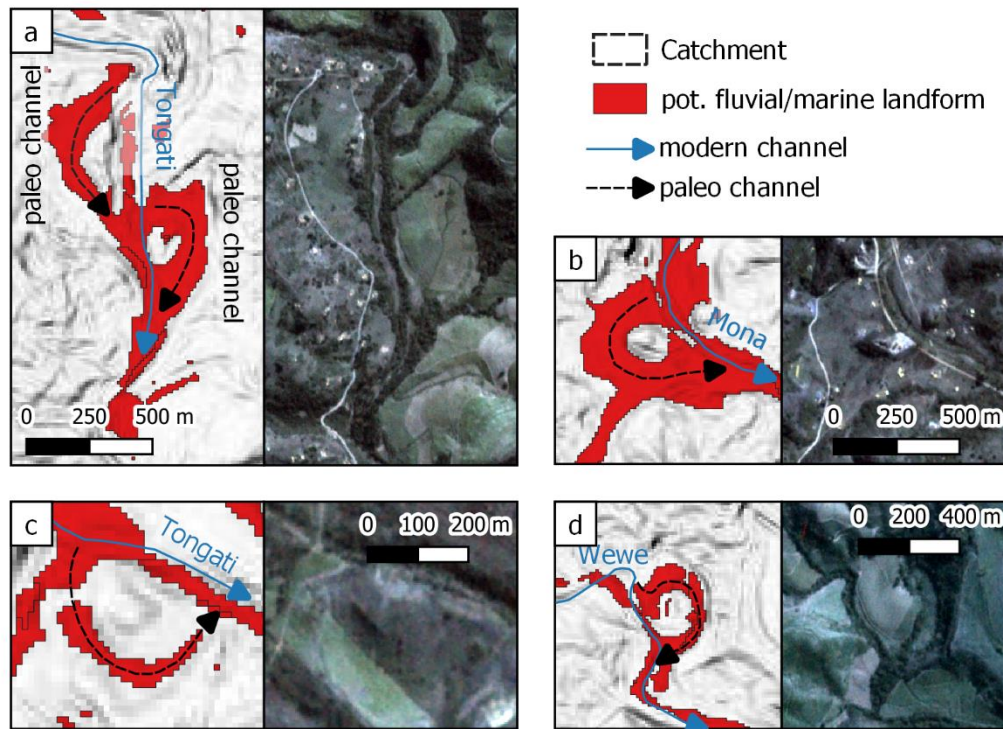
Fig. 5.24: Details of paleo channels of the Tongati (a, c), Mona (b) and Wewe (d). Satellite imagery from PlanetScope provided by Planet Team (2017) for scientific purposes.
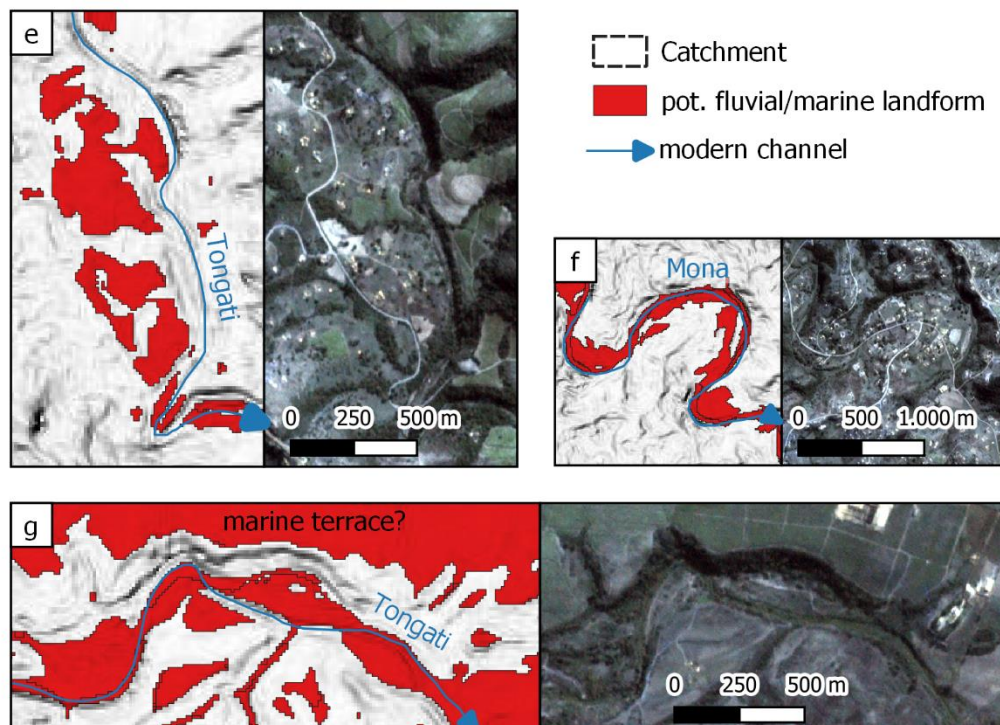
Fig. 5.25: Details of major terraces along the (a) Upper Tongati, (b) Mona and (c) Lower Tongati. Satellite imagery from PlanetScope provided by Planet Team (2017) for scientific purposes.

Despite their differences in genesis, an automated distinction between these landforms, based solely on their surface characteristics, appears to be not feasible with this method and at this scale. Especially in the lower reaches, where the Tongati crosses the lithological domain of the Karoo Supergroup, the differentiation is complex, as the river carves its terraces directly into the initial marine surface. Accordingly, it is essential to verify the predicted potential terraces using classical fieldwork methods, as is described in chapter 5.3.7 and 5.3.8.

5.3.7 Field description of terraces

The predicted potential terraces of chapter 5.3.6 were validated through field campaigns in 2018 and 2019. Figure 5.26 shows the resulting map of three levels paleo-fluvial features (besides other planed surfaces), that were compiled through geomorphological mapping, soil profiles and ER imaging.
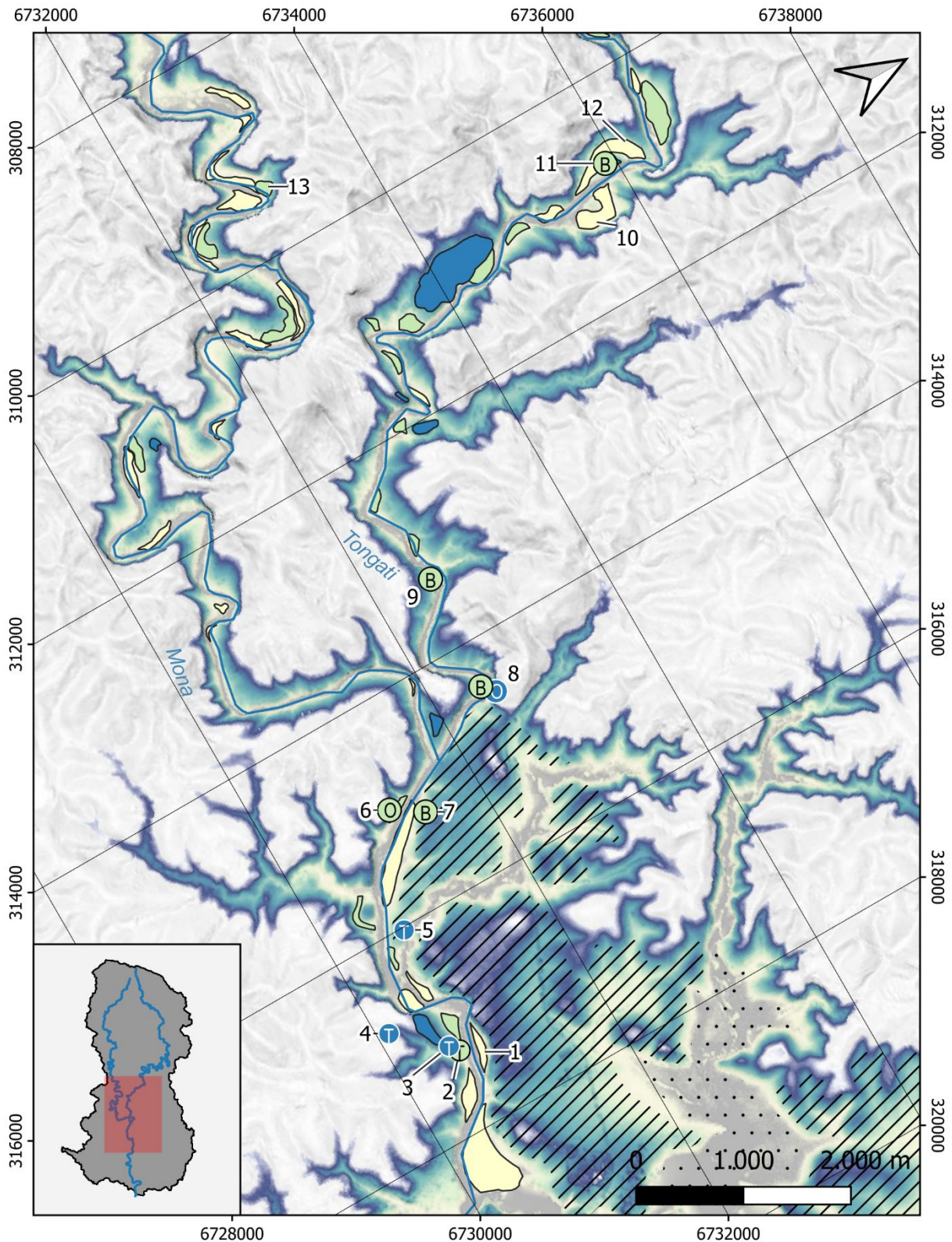
Fig 5.26: Correlated fluvial terraces of the Middle Tongati and Mona. Numbers indicate POIs mentioned in the text. Legend in fig. 5.26-2.
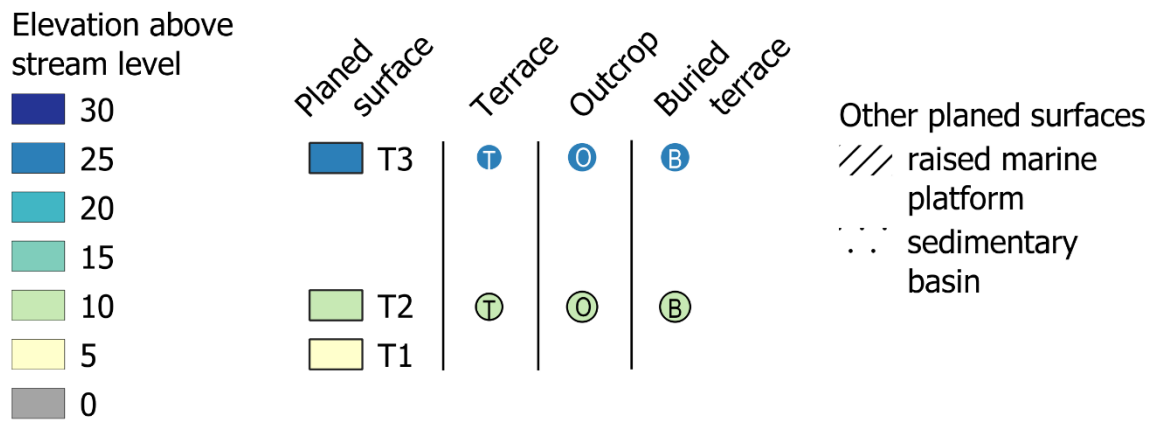
Fig 5.26-2: Key to the terrace levels and elevations, as well as other planed landforms mapped in fig. 5.2.6.

5.3.7.1 Level T1

Three terrace levels could be mapped and correlated in the Tongati Valley. T1 is the lowest and thus youngest generation of terraces and lies about 2-4 m above the stream level of the river. Especially in the Lower Tongati, where the valley widens, larger contiguous areas are covered with this terrace. In the upper reaches of Tongati and Mona it occurs frequently at the point bar or as a raised lateral gravel bar above the floodplain. This terrace occurs only as alluvium composed of red-colored sands from the headwater's granite. In some places, they also contain layers of chaotic bedding (fig. 5.27b) that comprise cobble- and boulder-sized subrounded fragments of Natal Group quartz arenite and Pietermaritzurg Fm. shalestones, which indicates episodes of turbulent flow and deposition. At POIs 1 and 13, it is evident that this alluvial terrace is slowly eroded, but today's freestanding remains (such as figure 5.27a from POI 1 and figure 5.27c,d from POI 13) bear witness to the former terrace height. An OSL date sampled at POI 1, close to the basement of the depicted remnant, revealed a Holocene age of 9.05±0.92 ka (Lab No. CSA2). Ergo, the top of the terrace must be younger than this date.

On the Upper Tongati, this terrace level is also preserved at POI 10 as an infilled paleo meander that flows around a spur, as shown in figure 5.27e. At POI 12, just 0.5 km upstream, a similar but larger paleo meander was screened with ERI (chapter 5.3.8). Thereafter, the modern meander bottom lies on sandy alluvium of up to 8 m of thickness, with a buried paleo channel at the level of the modern Tongati.

5.3.7.2 Level T2

The next terrace level T2 was observed at 7-15 m, which has a slightly higher span than the terrace level of 7-13 m mentioned in the Geological Map. Two terraces are referred to in the explanation sheet of the Geological Map of the Verulam area. The first could not be registered in the field due to lack of coordinates, but is described as a gravel terrace on the north bank of the Mona River, where "the base of the terrace is undulating and occupies elevations between 7 and 10 m above current level of the Mona River, resting on a Natal Group substrate. The terrace deposit consist of subrounded cobbles and boulders of Natal Group, ranging in diameter from less than 5 cm to large boulders over 1 m in diameter" (Clarke et al., 2007).

Another terrace of level T2 is mapped in POI 2 and described as follows: "Along the Tongati River south bank, northwest of Hambanati […] this terrace comprises well-rounded boulders

and cobbles of fine-grained Natal Group quartz-arenite. Sorting is poor and the lateral extent of the deposit has probably been exaggerated by extensive cultivation" (Clarke et al., 2007).

POI 6 describes a terrace at ~15 m above the Tongati, which is incised into a bed of Pietermaritzburg Fm. shalestones and covered by 2-4 m of colluvium (fig. 5.28a). This outcrop displays a riverbed cross-section with larger clasts of quartz arenite with a length of up to 0.5 m on the long-axis, which are poorly sorted and show percussion marks (fig. 5.28c). While this is interpreted as the central part of the channel with high flow velocity, the outer margins of the outcrop show laminated and cross-bedded red clayey sand (fig. 5.16b), indicating deposition under calmer flow conditions. The stratified sand deposits were sampled for OSL dating and yielded an age of 83.71±9.29 ka.

POI 7 on the opposing slope, left side of the Tongati, features a buried terrace of the same elevation, that was discovered through ERI investigations. These are described in more detail in chapter 5.3.8.

Another buried terrace was detected with ERI at the slope opposing Sibudu Cave (POI 8). A terrace is assumed there, which is indicated by a flattening on the slope at a height of 11 meters. The ERI measurements showed a fill with a thickness of ~4 m and increased resistance, as was the case with other terraces in the valley. Further details are to be found in chapter 5.3.8.

POI 9 is situated on a break in slope on the right-hand side of the Tongati, ~1 km north east of Sibudu Cave. A soil profile revealed a bed of gravel with a thickness of ~20 cm, underlaid by boulders with ~20 cm length along the long-axis and coarser clasts, whose size lies around 0.5 m (fig. 5.28e,f). These deposits of fluvial origin are overlaid by 1.2 m of colluvium. The OSL age of 4.74±0.76 ka (Lab. No. CSA4) sampled in the gravels, is very unlikely to be the age of the fluvial terrace, but rather an indicator for redistribution of the materials on the slope. Through this interpretation, the high overdispersion of 80% could also be explained by a post-depositional partial bleaching and remixing of the sediments.

POI 11 is a meander spur with a flattened top, that belongs to the paleo meander already mentioned in POI 12 (fig. 5.28f). Its western slope towards the meander bottom was investigated with ERI and revealed two resistant steps, that were interpreted as terraces. The colluvium that filled the upper terrace was dated to an age of 9.05±0.92 ka.

5.3.7.3 Level T3

The highest and thus oldest terrace level is located at a height of 25-35 m above the present course of the river. Three terraces of this group are referred to in the geological map. POI 2 is mentioned to sit on a height of 24 m above the channel, "along the Tongati River south bank northwest of Hambanati" and appears to be affected by extensive cultivation, so that "only a few pebbles and cobbles were observed" (Clarke et al., 2007). Accordingly, "the deposit comprises well-rounded but poorly sorted cobbles and boulders of fine-grained quart arenite of the Natal Group. The lateral extent of the boulder bed is difficult to delineate due to extensive cultivation" (Clarke et al., 2007).

POI 3 is described, where "another exposure in the same area [...] comprises numerous well-rounded clasts. Cobbles and boulders consisting coarse-grained quartz arenite of Natal Group origin comprise this terrace, which is developed on both sides of the stream" (Clarke et al., 2007).

The geological map also mentions POI 5, where "extensive cultivation has probably resulted in an exaggeration of the extent of the terrace exposure […] which comprises well-rounded but poorly sorted cobbles and boulders of the Natal Group".

Another terrace can be found at POI 8, the cliff of Sibudu Cave, on both sides of the Tongati. To the right of the river, at a height of 20-25 m, there is a noticeable flattening of the slope (fig. 5.29a). Today, this provides the basis for a small built-up area with several huts. At the right-hand side of the abris on the left side of the river, an erosion platform is exposed at the same level. In contrast to the typical structure of the arkose beds, which show a dip towards the southeast, this platform is horizontal and therefore likely of fluvial origin (fig. 5.29b).
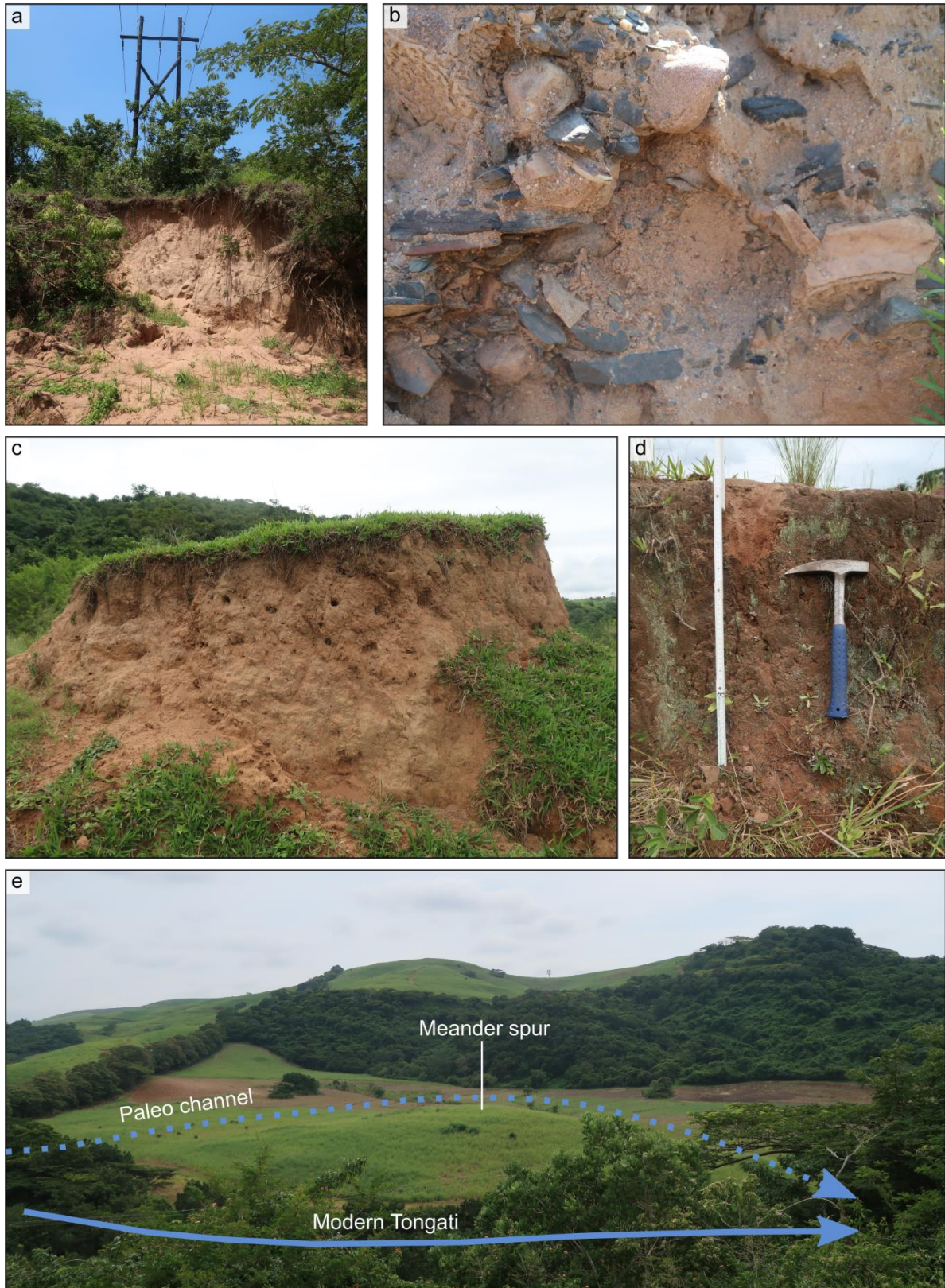
Fig. 5.27: Photographs of features belonging to terrace level T1 mapped in figure 5.26. The images are situated at POI1 (a+b), POI 13 (c+d) and POI 10 (e).
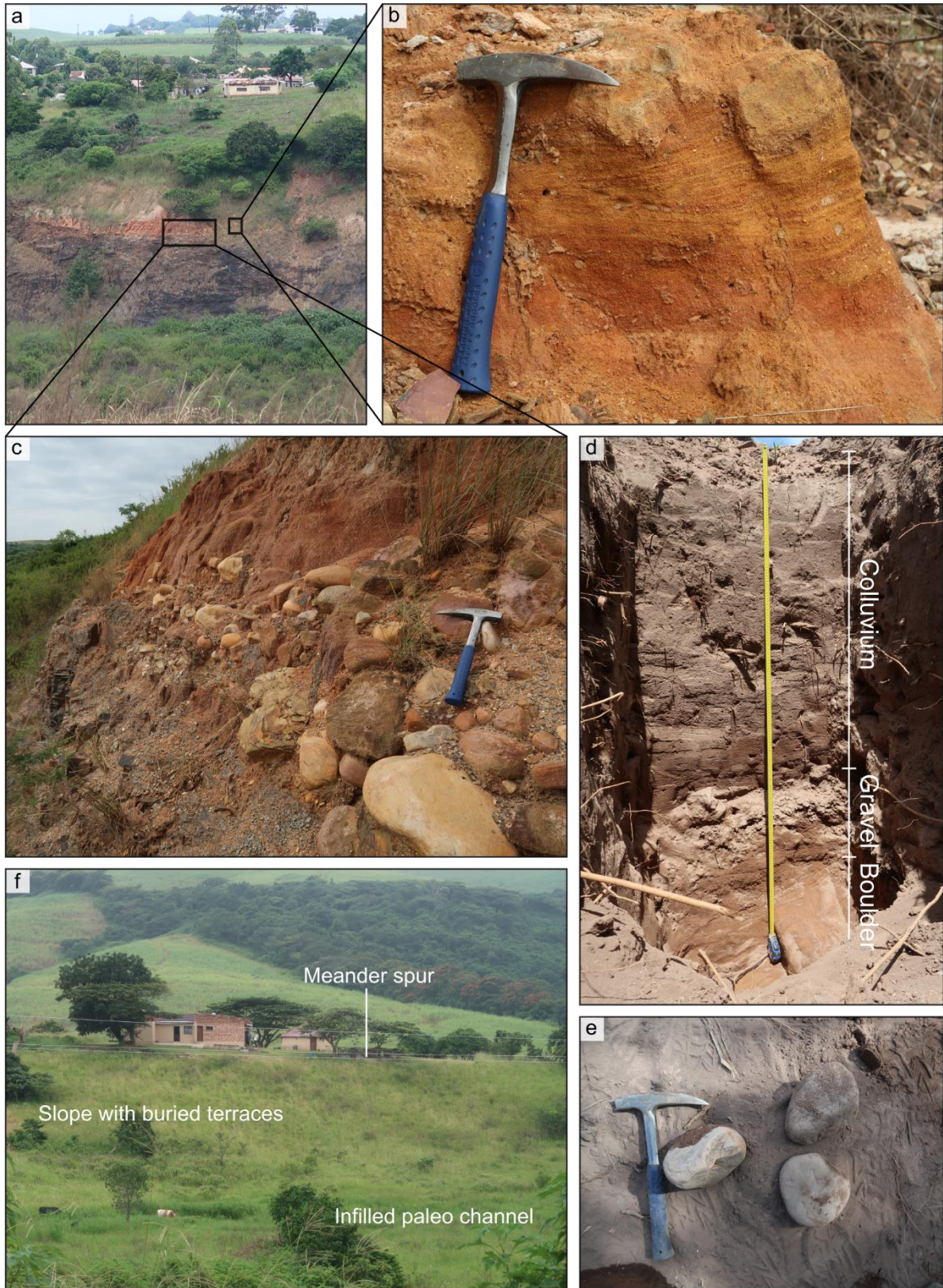
Fig. 5.28: Photographs of features belonging to terrace level T2 mapped in figure 5.26. The images are situated at POI 6 (a-c), POI 9 (d+e) and POI 11 (f).

Fig. 5.29: Photographs of features belonging to terrace level T3 mapped in figure 5.26. The images are situated at POI 8 (Sibudu Cave).

5.3.8 Electric Resistivity Imaging

Electric Resistivity Imaging (ERI) was applied to investigate the subsurface topography and sediment fills related to fluvial erosion in the Tongati catchment. The inverse model results are considered accurate with absolute errors below 10 Ωm. The properties of the transects are presented in table 5.4 and their position can be found in figure 5.30.
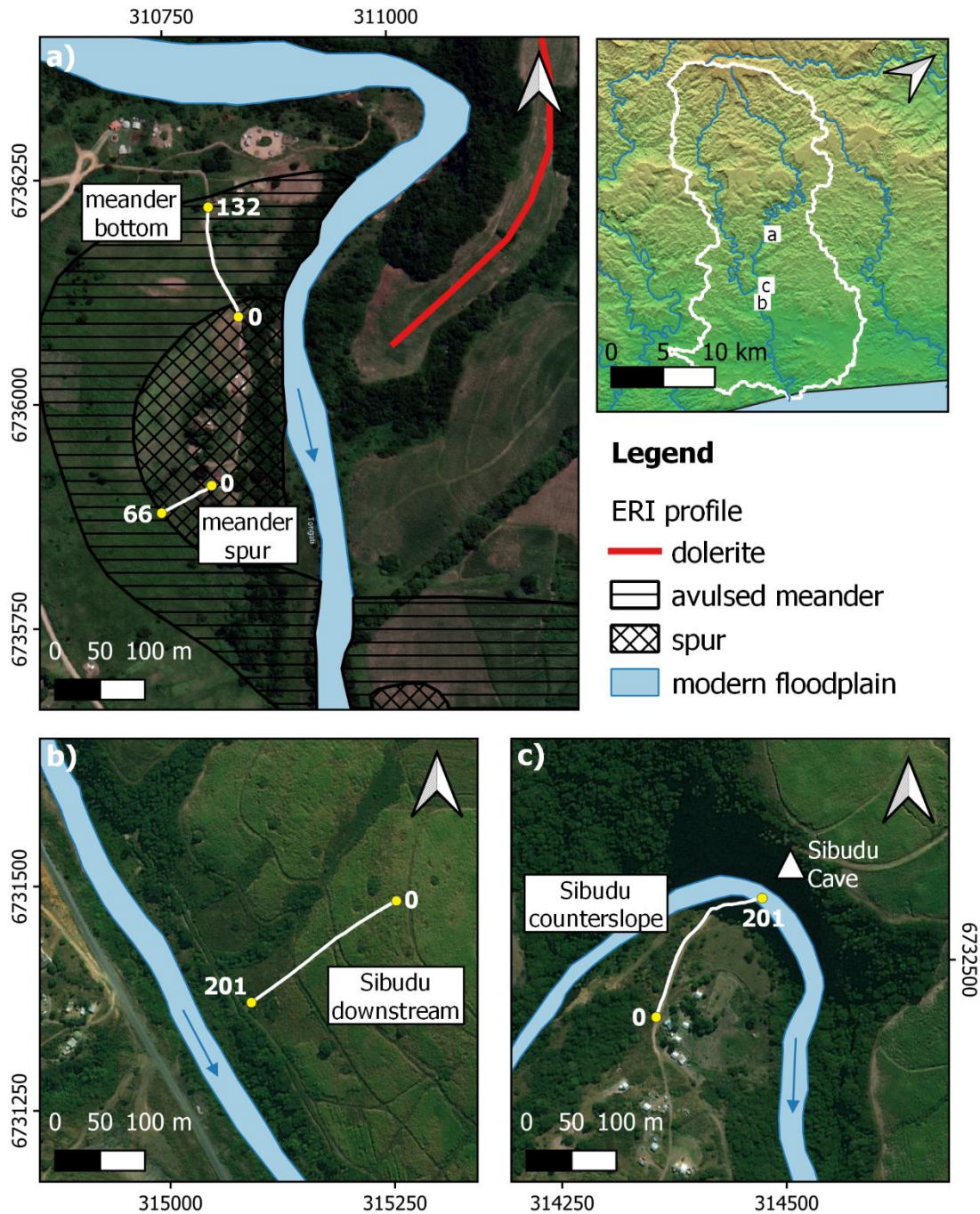
Fig. 5.30: Position of ERI transects in the Tongati valley. a at a paleomeander in the Upper Tongati, b at a slope facing the channel of the Lower Tongati and c at the slope opposing Sibudu Cave. Satellite imagery from PlanetScope provided by Planet Planet Team (2017) for scientific purposes.

Tab. 5.4: Properties of the ERI transects and inverse model accuracy. Length and spacing in meters, Error of model inversion in Ωm.

Cross section	Type	Length	Electrodes	Spacing	Point number	ERROR 1st	ERROR 2nd	ERROR 3rd	ERROR 4th
Meander bottom	Wenner	132	34	4	176	28.04	11.29	8.31	6.92
Meander bottom	Schlumberger	132	34	4	412	29.34	10.04	8.41	7.66
Meander spur	Wenner	66	34	2	176	18.61	9.66	4.75	3.18
Meander spur	Schlumberger	66	34	2	412	19.67	6.77	3.82	2.39
Meander spur	Dipole-dipole	66	34	2	475	28.95	11.55	8.6	7.29
Sibudu downstream	Wenner	201	51	4	408	13.8	10.17	5.58	5.41
Sibudu downstream	Schlumberger	201	51	4	960	14.99	10.42	9.71	9.74
Sibudu counterslope	Wenner	201	68	3	680	8.86	7.51	6.7	6.54

5.3.8.1 Paleomeander

The transect of the cut-off meander bottom (fig. 5.30a, fig. 5.31) has a gentle slope and its surface lies between 5 and 10 m above modern stream level of the Tongati. The subsurface below 0 m shows a distinction between very high resistivities, that occur on the southern part of the transect (26–76 m) and very low resistivities in the northern part (>76 m). With values as low as 100 Ωm, this resistivity falls below the expected values of all consolidated rocks in this area, including the predominant Natal Group sandstone. Considering the local geography, the high resistivity feature between the southern end of the transect and the 76 m electrode must be an underground extension of the dolerite dike, which is exposed on the left bank of modern day Tongati. Accordingly, the low resistivities north (right) of the 76 m electrode are the result of heavy fracturing of the sandstone, originating from the Jurassic intrusions, and the ground water saturation caused by its position below modern stream level. Comparable settings, with equally low resistivities have been described by Rønning et al. (1995), Yadav and Singh (2007) and Sharma and Baranwal (2005).

The most striking object in this transect is a very high resistivity feature between the 88 m and 100 m electrode, based at recent stream level. This can be interpreted as the cross-section of an abandoned channel, likely filled with coarse, blocky material. Furthermore, a succession from low resistivities in the South (left) to the higher ones in the North (right) can be observed, which reflects a transition from clay-rich substrates on the left bank of the paleo channel towards more resistant sandy deposits on the right bank. This pattern allows an interpretation as a northward (right) migrated paleo channel, which deposited fine material on its left-hand point bar, whereas the more turbulent right bank is filled with coarser material. The high resistivity material covering the avulsed channel at the 96 m electrode and higher, was identified as sand deposits in the field, and likely originate from the slopes that border the transect in the North (right side).
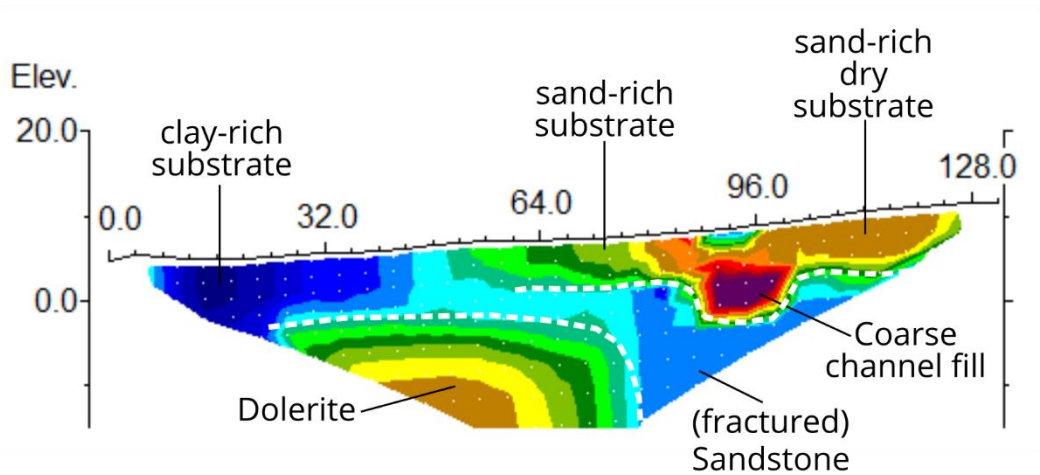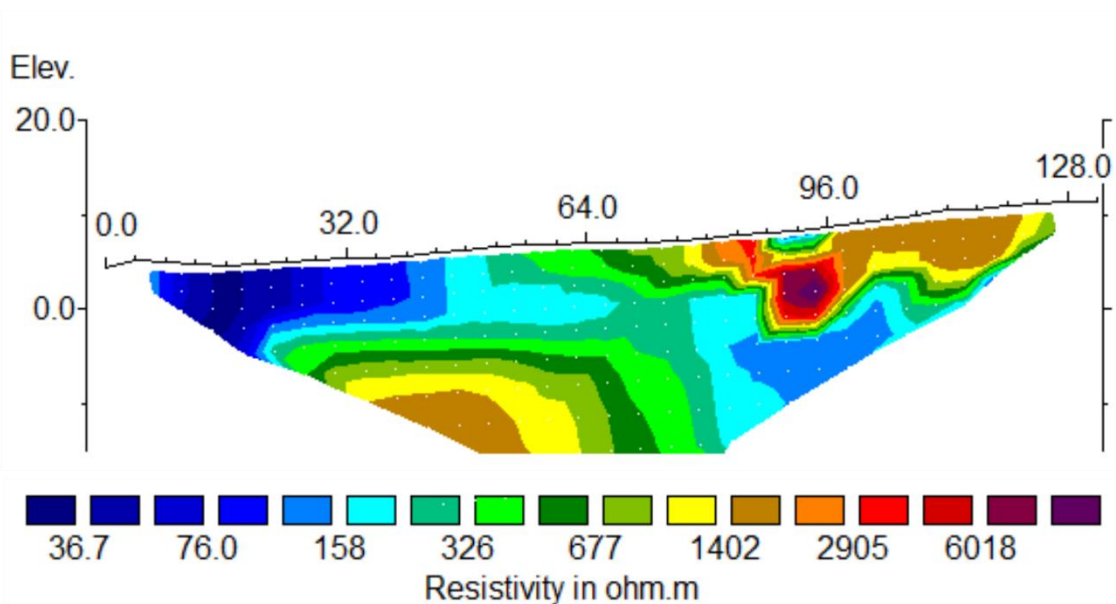
Fig. 5.31: ERI of the bottom of the cut-off paleo meander.

The avulsed paleo meander flowed around a cut-off meander spur, which now separates the infilled valley from the modern stream and rises ~25 m above recent stream level. A transect along the eastern slope of this spur represents the left bank of the paleo channel (fig. 5.30b, fig. 5.32). The basis of this landscape feature has resistivities between 300 and 600 Ωm, which is, comparable to the finding at the meander bottom, an indicator for fractured sandstone. In contrast to the Wenner and Schlumberger arrays, the Dipole-dipole measurements reveal inhomogeneities and higher absolute resistivities. A feature between 26 and 30 m of the transect in an elevation between 5–10 m above stream level, reaches resistivities of ~1400 Ωm and can therefore be interpreted as an unweathered and unfractured sandstone core or dolerite intrusion, which is surrounded by fractured sandstone bedrock. The bedrock is topped by a layer of reduced resistivities (<150 Ωm), which lies between 1–5 m below the modern surface. Observations in the field allow to attribute this layer to strongly weathered Natal Group sandstone, which has low resistivities when soaked with water, e.g. through a precipitation event that preceded the measurements. In the lower parts, from ~40 m to the western (right) end of the transect, the resistivities are lower than in the high lying parts, because the mid slope

devolves to the footslope and stagnant water is dominant. In the midslope between 30–34 m this layer seems to be absent, probably due to erosion through the overlying features.
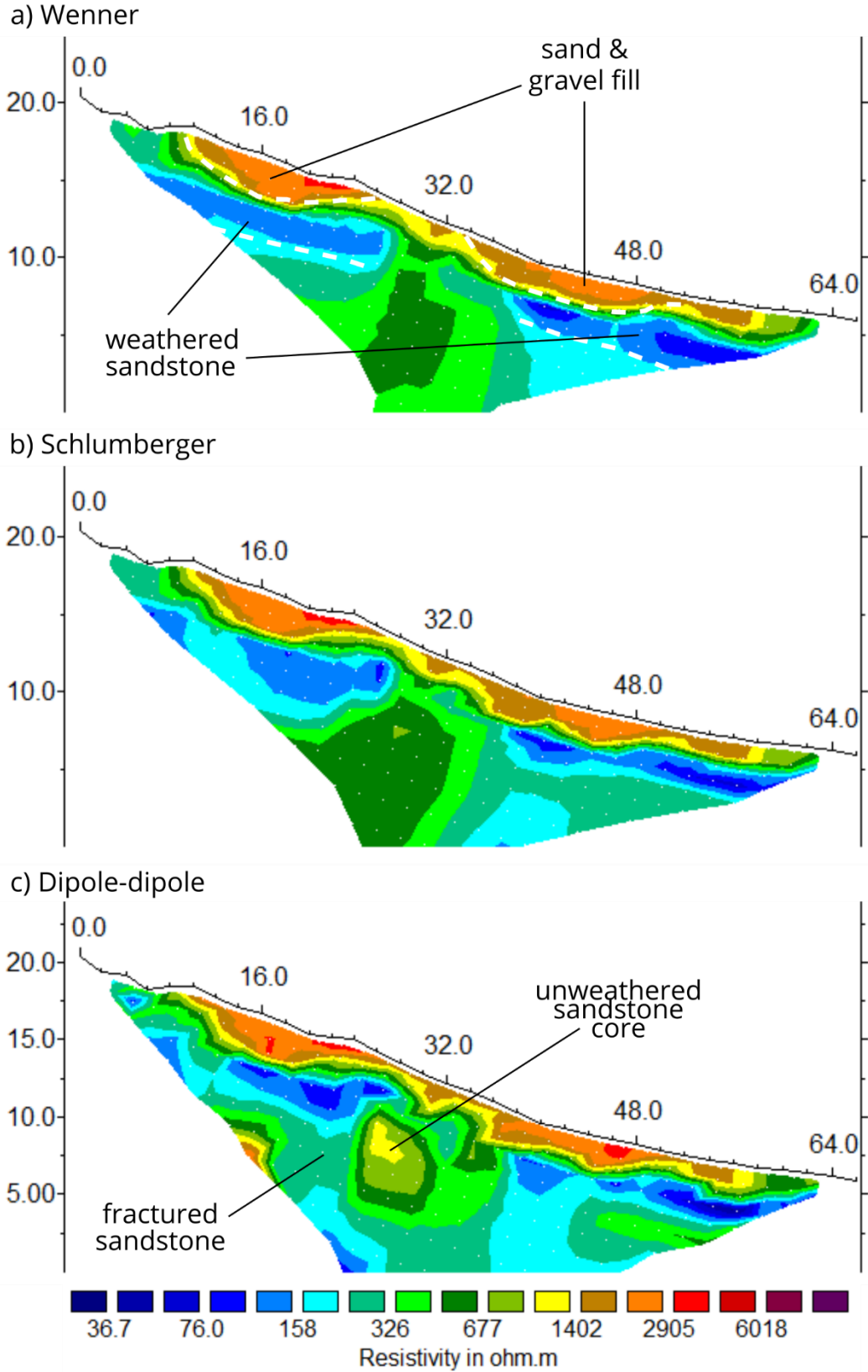
Fig. 5.32: ERI of the spur on the left bank of the cut-off paleo meander.

The demarcation between the weathered sandstone and the overlying layer is sharp. The latter stands out through high resistivities of ~3000 Ωm and higher, and is caused by loose, sandy material. The geometry of the deposits is particularly striking because the sands are deposited in pocket-shaped indentations with nearly horizontal basis. The two main sediment bodies are based on elevations of ~14 m (10–22 m horizontal) and ~7 m above stream level (40–50 m horizontal). But also between 28 and 36 m of the transect, smaller indents can be identified. These characteristic forms can be interpreted as strath terraces, which were carved into the sandstone bedrock through lateral erosion, when stream level was higher than today.

5.3.8.2 Sibudu counterslope

The slope on the right side of the Tongati (fig. 5.30c), opposing the archaeological site of Sibudu Cave, was tested for subsurface traces of past erosional features with a transect depicted in figure 5.33. The bedrock section of transect shows highly diverse resistivities ranging between 200 and >1000 Ωm. The higher values can be attributed to the Natal Group sandstone, which dominates the region, as well as intrusive dolerite, which can be observed, for example close to the rock shelter in a 2.5 m thick sheet dipping to Southeast. Two features with reduced resistivities may be interpreted as fractured bedrock, caused by the many faults in the region (Clarke et al., 2007), with raised moisture content and accordingly higher electric conductivity. A clear assignment of the materials in the bedrock requires further information, such as core drilling.
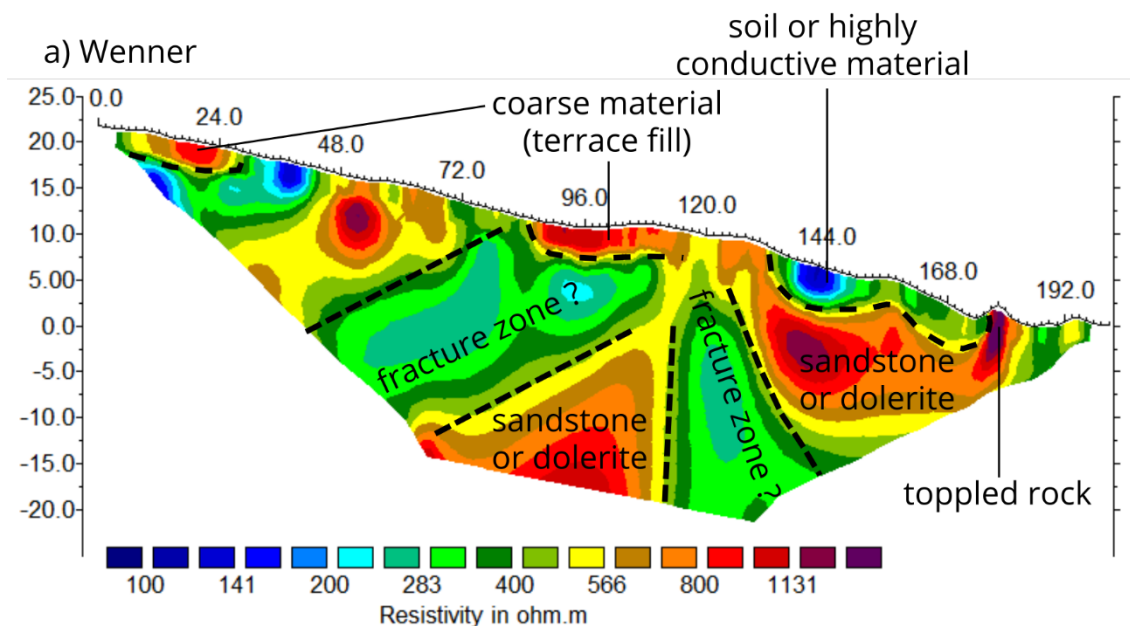
Fig. 5.33: ERI profile of the slope opposing Sibudu rock shelter.

In the shallow subsurface, several features indicate cycles of erosion into the bedrock and subsequent infilling with material. At an elevation above +17 m (0–30 m horizontal) and around +10 m (85–110 m horizontal), two features with resistivities of more than 1000 Ωm are associated with coarse material, which can be interpreted as terrace fills. Especially the second feature is recognizable in the field as a level surface. Two other levels of erosion can be observed through strong resistivity gradients around +5 m (135–155 m horizontal) and 0 m (above 155 m horizontal). Both are characterized by lower resistivities than the surrounding bedrock or

97

coarse gravel fills. The feature around +5 m shows very lows resistivities as low as 100 Ωm, typical for clays, thus indicating (a) point bar deposits of a left migrating stream or (b) overbank deposits of a stream at recent elevation. The lowermost feature around 0 m represents the modern day Tongati erosional level. The resistivities around ~400 Ωm can be explained by moist and sandy riverbank deposits, that were observed in the field. Very high resistivities at 180 m of the transect evoke from a massive and toppled boulder, likely originating from the free face of the rock shelter.

5.3.8.3 Downstream Sibudu

Approximately 1.3 km downstream the cliff of Sibudu Cave and 0.5 km downstream the confluence of the Upper Tongati and the Mona River (fig. 5.30b), the lithology is changed from the sandstones of the upper catchment to silt- and shalestone of the Pietermaritzburg Formation.
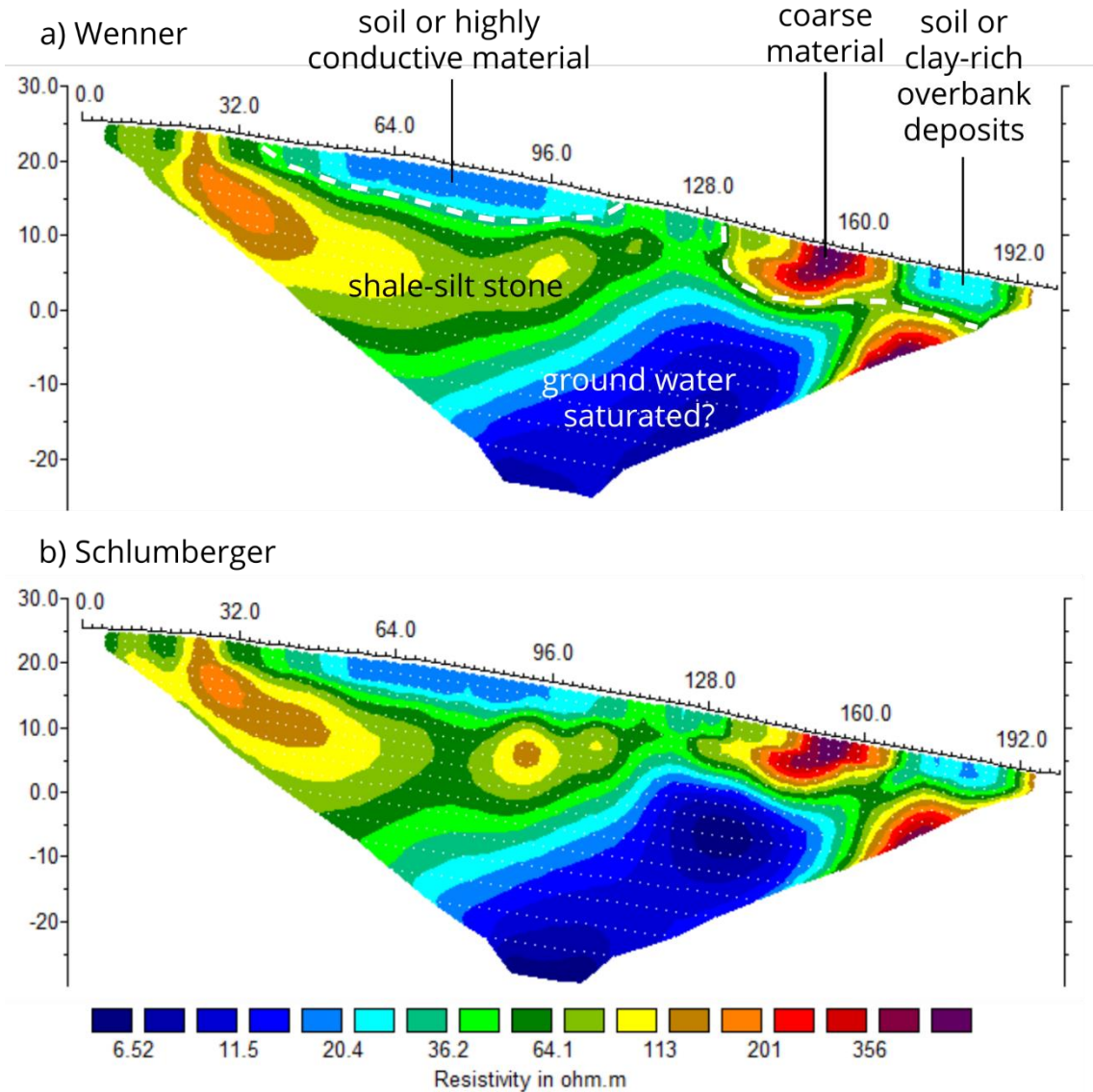
Fig. 5.34: ERI profile of the left bank of Tongati river in Pietermaritzburg Formation shalestone.

In the ERI cross section (fig. 5.34), this is expressed by clearly lower electrical resistivities than in sandstone, which range here between 30–200 Ωm, a typical value according to Palacky

(1988). Even higher conductivities close to recent stream level and below indicate high permeability and the presence of ground water. In the upper slope, highly conductive materials are abundant in the section between 35–110 m of the transect and reach as deep as 5 m below the surface. The low resistivity allows the interpretation of a well-developed, permeable soil cover. Hence, this slope is used for intensive cultivation of sugar cane. A feature with distinctly higher resistivities can be found around +5 m (130–170 m horizontal), whose geometry suggests the interpretation of a terrace infilled with looser sediment, whose electrical properties differ from the surrounding bedrock. The area right of 170 m of the transect reaches the depth of the recent stream and consists of moist, clay-rich deposits, which explains the low resistivities.

5.3.9 Dating results

OSL dating of all samples was conducted by the Geo-Luminescence Laboratory of the University of the Witwatersrand, Johannesburg under the supervision of Dr. Mary Evans. The results are summarized in table 5.5. Two samples (CSA3, CSA4) need to undergo further single grain measurements that are not yet available, so that the results presented in table 2 reflect preliminary results.

Tab. 5.5: Results of luminescence dating including Dose rate (D_r), Equivalent dose (D_e) values and derived optical ages from the Central Age Model (CAM) and Minimum Age Model (MAM). Final age models were selected from overdispersion values and are highlighted in green.

Sample code	Water content	U	Th	K	D_r	Overdis-persion	D_e (CAM)	CAM Age	D_e (MAM)	MAM Age
	(%)	(ppm)	(ppm)	(%)	(Gy ka^{-1})	(%)	(Gy)	(ka)	(Gy)	(ka)
CSA1	3.05	1.78	1.14	2.42	3.01±0.08	20	251.90±9.29	83.71±9.29	210.27±14.62	69.88±5.24
CSA2	2.24	4.95	12.73	2.38	4.52±0.12	54	80.65±7.22	17.83±1.67	40.92±4.01	9.05±0.92
CSA3	5.92	2.72	1.22	2.69	3.36±0.10	65	89.08±8.78	26.53±2.74	34.18±3.44	10.18±1.07
CSA4	6.18	1.71	2.22	2.78	3.28±0.10	80	66.56±8.97	20.56±8.97	15.54±2.43	4.74±0.76
CSA5	19.55	4.45	11.39	2.36	4.15±0.13	43	284.40±27.56	68.51±6.95	163.65±21.30	39.42±5.27
CSA6	4.93	4.07	3.81	1.82	2.67±0.08	29	244.11±16.22	91.60±6.62	177.55±19.85	66.62±7.68

Alluvial deposits (fig. 5.35a, fig. 525, POI 6), exposed +15 m above the lower Tongati were estimated from sample CSA1 to an age of 83.71±9.29 ka. With 20% overdispersion, this sample shows lowest overdispersion of all samples presented in this study and therefore allows the application of the CAM model. The low overdispersion supports the assumption, that the fine curved parallel-bedded alluvial sands were deposited in a brief time range before the channel was lowered and the cross-section preserved. This age correspond well with a short sea-level apex, which is estimated by models from Bintanja et al. (2005) and Waelbroeck et al. (2002) between MIS 5b and MIS 5a.

CSA2 was taken at the lower Tongati, close to Hambanathi, where the valley is widened more than 200 m and the whole floodplain consists of alluvial coarse sands (fig. 5.35b, fig. 5.25, POI 1). It was obtained from ~50 cm below current surface and roughly at recent stream level from an unstratified body of well-sorted coarse quartz sand. This indicates deposition under high energy conditions, and the strong mixing associated with such an event helps to explain the overdispersion of 54%. Accordingly, a MAM model yielded an age estimation of 9.05±0.92 ka, which lies in the early Holocene and coincides with the intense sea level rise of the Flandrian transgression.

Sample CSA3 (fig. 5.35c) is taken from colluvial fill of a fluvial terrace at the paleomeander (fig. 5.25, POI 11) and yields an age of 10.18±1.07 ka.

CSA4 (fig. 5.35d) is fluvial sediment from a gravel bed overlain by colluvium (fig. 5.25, POI8) and its age is estimated to 4.74±0.76 ka.

The latter two (CSA3 and CSA4) show very high overdispersion, so that their age estimates of 10.18±1.07 ka and 4.74±0.76 ka should not be considered for the interpretation without further single grain analysis.

5.4. Discussion

5.4.1 Primary drivers of fluvial incision

The Tongati has a special role to play in the study of fluvial erosion and its possible drivers. Due to its short length and small catchment area, but also due to its location and tectonic history, some potential agents can be neglected, so that the impact of the remaining drivers becomes more obvious.

In a global synthesis of the "considerable and protracted debate in the geological and geomorphological literature about the formation of river terraces", Bridgland and Westaway (2014) state a "general consensus that many have been climatically triggered […], often in synchrony with glacial–interglacial fluctuation". Despite, it is mostly improbable that the Tongati valley was formed by glacial processes, because the small catchment

- does not provide a glacier feeding area due to its warm climate and low altitude,
- has been isolated from a potential larger catchment that extended to the Great Escarpment, since the African surface was dissected by Post-African I surface (see chapter 3.4), and furthermore,
- glaciation during the Quaternary, and especially during the last glacial cycle (Mills et al., 2017), in the Drakensberg Mountains is highly controversial (Hall and Meiklejohn, 2011), where geomorphological evidence suggests smaller niche and cirque glaciers (Mills et al., 2009) rather than widespread glaciation (Grab et al., 2012).

Also uplift, often of epeirogenic nature, is mentioned by Bridgland and Westaway (2014) as a crucial factor for terrace development, and large number of authors used fluvial archives as indicator for crustal deformation, as reviewed by Demoulin et al. (2017). However, this process alone cannot explain the terrace levels observed at the Tongati, since the region is considered stable. Erlanger et al. (2012) derived rock uplift rates from a marine terrace near Durban with a value of 9.4±2.2 m/Ma. If uplift was the primary driver for incision, the terrace level T2 with a relative elevation of 7-15 m (chapter 5.3.7) would be related to an age of ~0.7-1.6 Ma, however, actual OSL results show a much younger age of only 83.71±9.29 ka (chapter 5.3.9). This indicates that the incision rate is higher than the uplift rate by a factor of ten, and consequently, river response to sea level fluctuations should be considered.

Bridgland and Westaway (2008) summarize, that "a small number of detractors […] have sustained debate […] doubting the requirement for uplift […] and/or favoring base-level (sea-level) change as principal driver, […] often through the mechanism of knick-point regression". However, it is clear that such influence is possible in the vicinity of the coast (Schumm, 1993), where the long profile is not affected by knickpoints. Clarke et al. (2007) suspected that the terraces in the geological map of Verulam (including the Tongati) are likely the result sea level fluctuations, however it is critically noted that knickpoints could cancel out this effect. Here, the analysis of the longitudinal profile (chapter 5.3.2) and the knickpoints (chapter 5.3.5) provide clarity. Thereafter, the main stream of the lower Tongati, which crosses the Karroo Supergroup lithologies downstream of Sibudu Cave, is free of knickpoints. The middle Tongati upstream of Sibudu Cave, in contrast, is associated with an elongated convex knickzone, which indicates that the river is in a constant, transient state of erosion into the resistant Natal Group bedrock. Accordingly, from this point on, the river is cut off from the sea level's influence and is still in the process of adapting to the Plio-Pleistocene uplift, which is associated with the Post-African II

surface. This further indicates that the midstream and downstream terraces may have the same level but may not necessarily be correlatable.

Thus, it can be summarized that the incision of the lower Tongati mainly follows the variations of the sea level and shows high erosion rates, while the middle Tongati is affected by uplift and shows much lower incision rates, so that it has not yet reached the long profile equilibrium.

5.4.2 Sea level response

In the classical model of terrace formation under a varying influence of the sea level, a base level standstill corresponds to lateral erosion, which excavates a strath terrace (Merritts et al., 1994, Finnegan, 2013). When sea level falls, the channel incises vertically, so that the former floodplain is abandoned, leaving behind the former riverbed on the strath. When sea level stabilizes again, the cycle is repeated at the bottom of the riser, forming the next generation of terrace. A sea level rise, in contrast, is associated with fill terraces, as a response to the raised base level. This conceptual model is discussed in this section with regard to dating results (chapter 5.3.9) of the terrace levels and the sea level reconstructions by Bintanja et al. (2005) and Waelbroeck et al. (2002). The interpretation is summarized in figure 5.35.

The fluvial terrace at level T2 is well preserved and dated to an age of 83.71±9.29 ka, which coincides with the end of the MIS 5 sea level stability. This is consistent with the conceptual model to the extent that these sediments were deposited at the end of a prolonged phase of lateral erosion and the channel has subsequently been incised in MIS 4 as sea level has dropped.

The dating of terrace level T1 with an age of 10.18±1.07 ka can be reconciled with the conceptual model, since it was sampled from alluvium and is therefore indicates an infilling of the valley in response to the Flandrian transgression after the LGM. This interpretation of T1 also explains the very high concavity observed in the long profile of this part of the river (chapter 5.3.3 and 5.3.4). Accordingly, the river is flatter in the lowermost part than it should be, compared to the idealized longitudinal profile, because the latter estimates a lower base level than the present-day sea level. This finding is supported by an observation of Clarke et al. (2007), who note that "all the rivers of coastal Natal are infilled near their mouths by over 30 m of alluvium. Many rivers in the North Coast region have an average depth to bedrock of between 30 m and 36 m, as reflected by drilling results for bridge formations". Furthermore, a number of estuaries submerged by Holocone sea level rise is presented in de Lecea et al. (2016), Cooper et al. (2018) and Cooper et al. (2018). Summarizing, the lower Tongati is further subdivided into an appropriately steep upper part, which has a long profile in equilibrium, and a shallow lower part, whose paleochannel is now covered with thick sedimentary beds. These are divided by a strong concave knickpoint, which is situated between the confluences of the Wewe and Hlawe tributaries, as findings in chapter 5.3.4 suggest. This is also observable in the field, where the valley widens and the dominant sediment size of the floodplain changes from gravel to sand.

The age of T3 could not be estimated by absolute dating methods, due to its poor conservation (chapter 5.3.7). However, since this terrace is situated above T3, a minimum relative age predating the MIS 5 is likely, for example MIS 6.
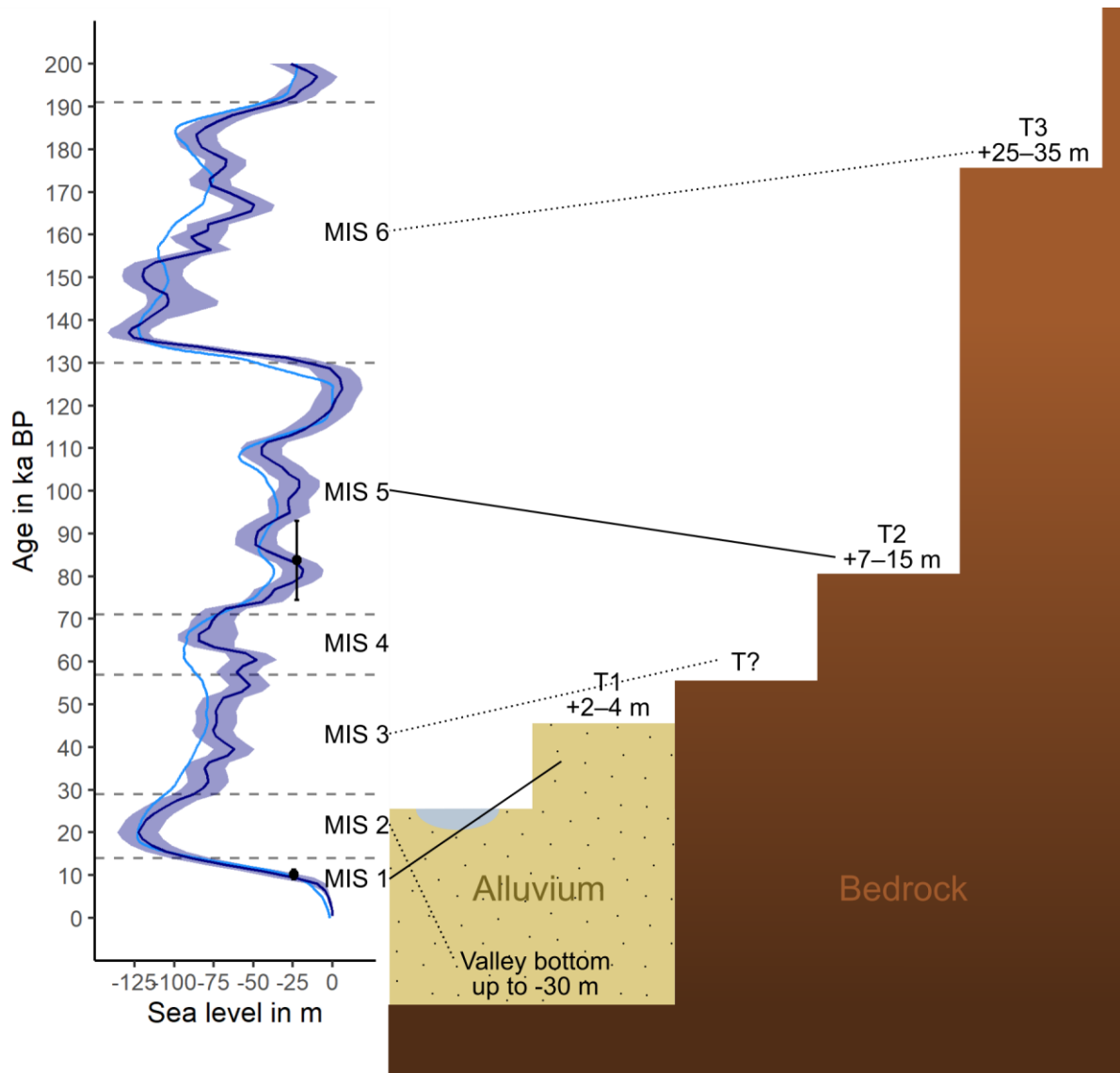
Fig. 5.35: Conceptual cross-section of the terrace levels of the lower Tongati Valley and associated sea levels. Solid lines are confirmed by OSL dating, dotted lines are relative estimates. Sea level curves by Bintanja et al. (2005) in light blue and Waelbroeck et al. (2002) in dark blue.

With T1 and T2 being consistent with the sea level reconstructions and conceptual model, this raises the question, why there is no further strath terrace below T2. MIS 3 is associated with another sea level standstill between MIS 5 (T2) and MIS 1 (T1) and according to the model, one would expect another step of lateral erosion. Terraces of this level are mentioned outside the catchment by two authors, but no corresponding features could be mapped in the Tongati valley for this study. Clarke et al. (2007) describe a gravel terrace of the Mdloti river at +4 m and Maud (1968) mentions two terrace levels at +3 and +6 m, that would fit in this range. However, potential terraces in the lower part of the Tongati are probably buried by the infilling related to the Flandrian transgression, which may explain, why they could not be found in this study. A chronological date ranging within MIS 3, or even the end of this stage, would further confirm the conceptual model. The absence or the weak development of this terrace level can be hypothetically explained by drier climate during the later MIS 3, as suggested by regional climate reconstructions by Chevalier and Chase (2015) and Partridge (1997). Maud and Botha (2000), for instance, make drier conditions at the end of MIS 3 between 45-24.8 ka responsible for the drying out of coastal Lake Sibaya in northern KZN. At the Tongati, lower precipiation and

consequently lower runoff may have reduced the erosion capacity, mitigating lateral erosion, thus producing less pronounced terrace than T2 or T3. Furthermore, potential terraces in the lower part of the Tongati are probably buried by the infilling related to the Flandrian transgression.

5.4.3 Uplift response

The river course upstream of the New Glasgow fault crosses the Natal Group sandstone (mostly Marianhill Fm.) and is associated with a pronounced convex river long profile. This section is decoupled from the sea level baseline and controlled by an uplift controlled baseline. It is however unclear, at which elevation this baseline is, since the river is in a transient state and has not yet reached its equilibrium. It is therefore difficult to estimate the ages of the terraces of this section. Their formation might be related to paused uplift, but also local factors like variance in bedrock hardness or faulting affect the process. A number of examples show, that high sinuosity is related to faults and resistant dikes crossing the valley (chapter 5.3.4), and the terraces upstream are not to be correlated with those downstream (and hence were not investigated in this study). There are also incised meanders in the upper part of the valley, which do not roam freely, but rather follow an ancient channel, that is continuously lowered since the inset of the Post-African II cycle. Furthermore, variations in sediment supply, and thus erosive capacity, may affect this complex system. However, it has to be noted, that the latter is unlikely a limiting factor, given the deep-weathered Oribi Gorge granite in the headwaters of the valley being an excellent source of sediment.

Erlanger et al. (2012) estimated a long-term incision rate of 16.1 ± 1.3 m/Ma at the continentally controlled lower Sundays River in the Eastern Cape, holding pace with local uplift rates. Considering the middle Tongati's convex profile, it becomes clear that the river's incision is not capable to keep up with uplift, and therefore, incision rates must be lower than uplift rates. However, this allows at least to estimate a minimum age of the terraces, with the long-term uplift rate of 9.4±2.2 m/Ma for Durban, provided by Erlanger et al. (2012). Thereafter, a strath terrace T1 at +2– 4 m would correspond to ~0.2– 0.4 Ma, T2 situated at 7– 15 m would be associated with a minimum age of ~0.7– 1.6 Ma and T3 found at +25– 35 m is estimated to an age of ~2.6– 3.7 Ma. These ages indicate, that the terraces of the middle Tongati valley formed throughout the Plio-Pleistocene. Respecting these are only minimum ages, terrace formation likely set in with the Post-African II cycle, postdating the Mid-Pliocene.

5.4.4 The age of Sibudu Cave

Sibudu Cave is the result of left-side outer bank erosion at a stationary right-hand river bend of the Tongati forming a prominent cliff, which hosts an abri that preserves the archaeological sediments. The shelter displays two features of former fluvial erosion, a platform associated with T3 (fig. 5.29.b) and the cave floor associated with T2. The river erosion has excavated weaknesses in the arkose bedding, so that it broadly follows the dip of the lithology.

However, Since Sibudu Cave lies just at the margin between the uplift-controlled middle Tongati and sea level-controlled lower Tongati, the assignment of primary drivers is ambiguous. It is located within the knickzone, but the proximity to the sea-level controlled domain is striking: the position of the exposed terrace (fig. 5.14-1 number 6; fig. 5.16a-c) is only one kilometer away, however considerably lower. Therefore, two alternative hypotheses are discussed here:

- First, the rock shelter was primarily influenced by uplift, and the cliff was carved since the inset of the Post-African II. Thereafter the cave floor (T2) is of Early Pleistocene age.
- Second, the rock shelter formation was influenced by sea level variations and the cave floor is associated with MIS 5 standstill.

The oldest known sediments at a depth ~4.5 m from the Deep Sounding of the archaeological site of Sibudu Cave, are the "D-A layers" (Schmid et al., 2019). With an age of ~92–72 ka these overlap with the expected sea level standstill and river level associated with MIS 5, as proposed in the second hypothesis. Thereafter, the intense human occupation resulting in this layer would have taken place at or little above the paleo-floodplain.

If this were the case, it would be more than surprising that the sediments in Sibudu Cave were mainly of anthropogenic nature or rockfall, but show no traces of fluvial deposits. Furthermore, it may be doubted that the sediments would have withstood the annual or multi-annual floods and the preservation of the fine stratigraphy in its current state would not be possible. Therefore, this hypothesis should be be rejected, if no alluvium is identified in future excavations as direct evidence of this terrace. Instead, it can be assumed that Sibudu Cave was formed in accordance with the first hypothesis and that the abri is considerably older than the site it hosts.

Chapter 6: Late Pleistocene Colluviation

This chapter deals with Q4 by addressing the Masotcheni Formation and the conclusions that can be drawn about the environmental conditions and landscape stability cycles that led to its genesis. This was conducted through classic methods of geomorphological field work, but also ERI and a novel method in this context: electromagnetic field spectroscopy.

6.1. State of research

6.1.1 Spatial distribution of the Masotcheni Formation

Colluvial material has been widespread recorded in Southern Africa. Watson et al. (1984) estimate, that 20% of the land south of the Zambezi River is covered by colluvial sediments. Botha et al. (2016) give a comprehensive overview of their spatial distribution, which ranges from the Mpumalanga Lowveld in the north through Swaziland, KwaZulu-Natal to the Eastern Cape in the south.
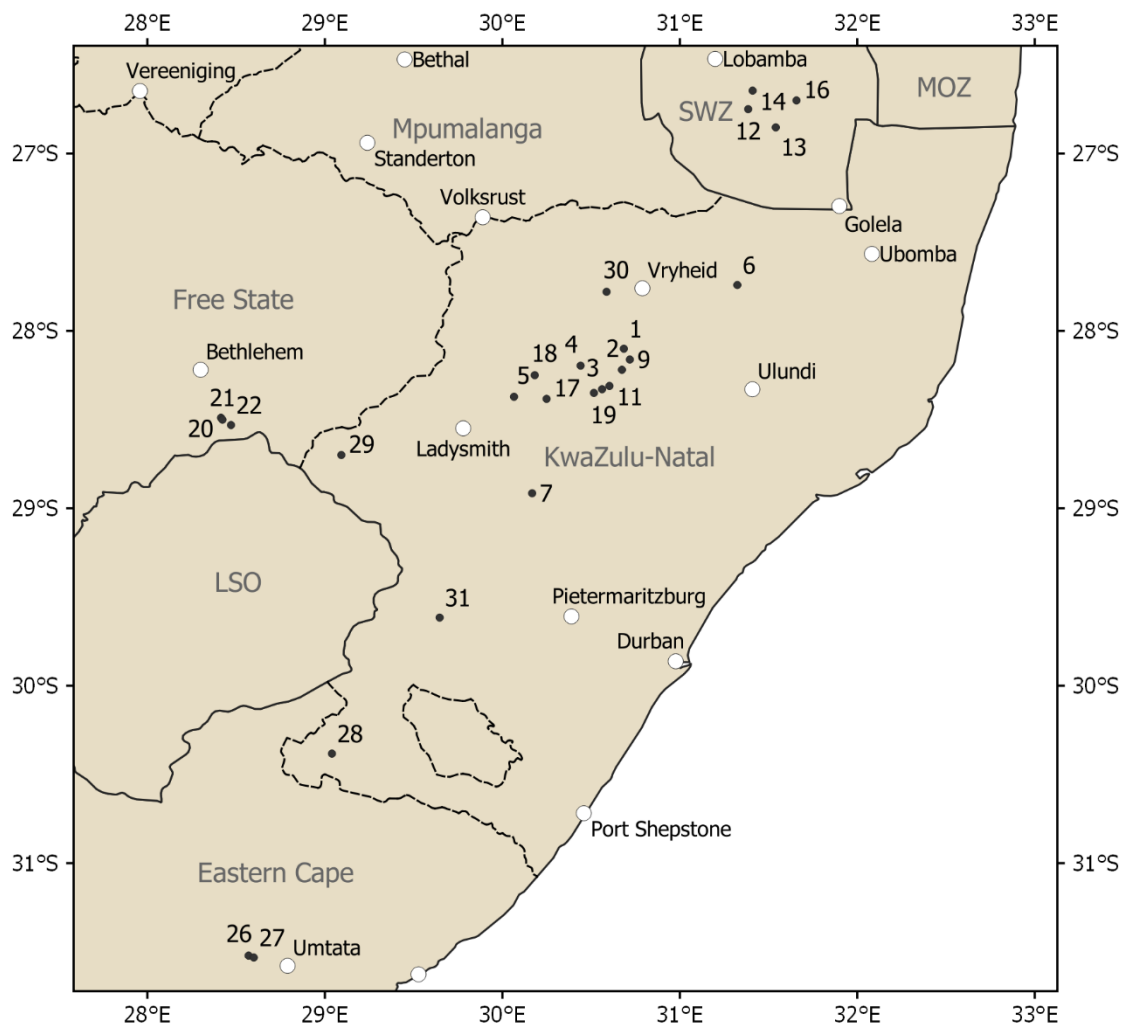
Fig. 6.1: Dated colluvial sediments in eastern Southern Africa. Updated version of Botha (1996) with references in tab. 6.1.

They can be found in high elevated regions, such as the Drakensberg foothills, the eastern Free State and the Maloti mountains of Lesotho (Botha, 1996), as well as in the semi-arid regions of northern South Africa, Zimbabwe and Botswana (Watson et al., 1984). Colluvial sediments in

KwaZulu-Natal of Cenozoic age are referred to as Masotcheni Formation (Partridge et al., 2006). As depicted in fig. 6.1, the investigated site at KwaThunzi (labelled 31) lies in an understudied area in terms of intense studies, which include modern dating methods. It therefore represents a valuable link between the densely studied colluvia in the north of KZN, and the investigations in the south of KZN and the northern Eastern Cape (labelled 26-28).

Tab. 6.1: Locations of intensive studies of the Masotcheni Fm.

ID	Location	Reference
1	St. Paul's	Botha et al. 1990, Wintle et al. 1995
2	Nqutu	Botha et al. 1990, Wintle et al. 1995
3	Masotcheni	Botha et al. 1990, Wintle et al. 1995
4	Hazeldene	Botha et al. 1990, Wintle et al. 1995
5	Matatana	Botha et al. 1990, Wintle et al. 1995
6	Voordrag	Botha et al. 1992, Botha 1996, Clarke et al. 2003
7	The Aloes	Botha & Fedoroff 1995, Botha 1996
8	Malden	Botha & Fedoroff 1995, Botha 1996
9	Jojosi	Botha & Fedoroff 1995, Botha 1996
10	Waterkloof	Botha & Fedoroff 1995, Botha 1996
11	Ngedla	Botha & Fedoroff 1995, Botha 1996
12	Mkohondvo	Price-Williams et al. 1982
13	Ethengethengeni	Price-Williams et al. 1982
14	Sidvokodvo	Price-Williams et al. 1982
15	Mashila	Price-Williams et al. 1982
16	Skoteni	Price-Williams et al. 1982
17	Hlomohlomo	Watson et al. 1984
18	Sikhunyana	Watson et al. 1984
19	Rorke's Drift	Watson et al. 1984
20	Elim	Scott 1989
21	Cornelia	Scott 1989
22	Craigrossie	Scott 1989
23	Bolotwa	Dardis 1988, Dardis & Beckedahl 1988
24	St. Mark's	Dardis 1988, Dardis & Beckedahl 1988
25	Qamata Poort	Dardis 1988, Dardis & Beckedahl 1988
26	Tabase	Dardis 1988, Dardis & Beckedahl 1988
27	Ross Mission	Dardis 1988, Dardis & Beckedahl 1988
28	Cedarville	Dardis 1988, Dardis & Beckedahl 1988
29	Okhombe Valley	Temme et al. 2008
30	Blood River	Lyons et al. 2013
31	KwaThunzi	this study, Bosino et al. 2020

6.1.2 Models of colluviation and pedogenesis

The Masotcheni formation is characterized by alternating layers of colluvial deposits and paleosols. This is the result of episodic hillslope instability, accretion of colluvial deposits at the footslope, and intermediate periods of slope stability, which are associated with the development of soils. The high number of strata, Botha et al. (1992) describe up to 12 pairs of A- and B-Horizons in a composite stratigraphy from northern KZN, implies that "hillslope response

was close to the geomorphic threshold between activity and stability" throughout the Late Pleistocene (Clarke et al., 2003).

This space refers to figure 9.3 in Botha et al. (2016, p.139)

Fig. 6.2: Schematic depiction of colluvial deposits and gully erosion displayed with hillslope elements, as defined by King and Fair (1944) and Conacher and Darlymple (1977). From Botha et al. (2016).

As depicted in fig. 6.2, colluvial sediments are formed by erosion on steep upper slopes and transport of detritus to the shallower footslopes, where the material is eventually deposited. The parent material of the hillslope plays an inferior role in the accretion of colluvia, as the phenomenon appears in a wide range of Karoo lithologies or Jurassic dolerites. Accordingly, the colluvium may consist of medium- or fine-grained sands originating from sandstones or shales in one place, whereas the colluvium in another place may display a coarser texture comprising core-stones, because it was developed from granite. Therefore, the texture of the Masotcheni Fm. varies with the bedrock regolith, from which it is formed, thus rendering it inept for correlation over larger areas with heterogeneous geology (Botha et al., 2016). Therefore, Botha (1996) developed a system that incorporates properties of paleosols to compare the colluvia across wider regions. This system is further described in chapter 6.3.1. Here, the main hypotheses are discussed to explain the genesis of the Masotcheni Fm.

Climate is considered as the most dominant factor of colluviation or soil formation, since its variations make an impact on larger areas and it affects hillslope stability either directly through temperature and precipitation, or indirectly through variations in the vegetation cover. Clarke et al. (2003) point out, that temperature is unlikely to be a controlling factor because the processes of colluviation and soil formation occur both during the cold LGM as well as the warm Holocene. Instead, the dated strata of the Masotcheni formation show a synchrony with the precipitation reconstruction by Partridge et al. (1993), where colluviation is associated with arid climate periods and soil formation is associated with rather humid periods. Clarke et al. (2003) deduced from this observation, that regional precipitation and its seasonality is likely to be a dominant factor.

This space refers to figure 12 in Temme et al. (2008, p.293)

Fig. 6.3: Conceptual landscape response model to changes in rainfall and vegetation by Knox (1972), modified by Botha (1996) and Temme et al. (2008)

Botha (1996) proposed the application of a conceptual landscape response model by Knox (1972) for the understanding of the Masotcheni sequence (fig. 6.3). This model relies on precipitation cyclicity, which is well-known in this region and further discussed in chapter 2.2. Thereafter, alternating shifts towards humid or arid conditions cause a variation towards denser or sparser vegetation over millennia. This response of vegetation patterns is characterized by temporal delay, which eventually results in a situation of high erosive susceptibility after the arid phase and the inset of a humid phase. The increased precipitation coincides with a barely protected soil, thus enabling sheet wash and channel erosion on the upper slopes and deposition of material in the lower slopes or further transport into the draining ditches. When the protecting vegetation cover has densified in response to the more humid conditions, the erosion susceptibility decreases strongly. Also, the depletion of available sediment in the contributing catchment areas can cause a decrease in sediment yield in this part of the cycle. At the end of the humid phase, the resilient vegetation cover is still established for a certain time, and coupled with decreased precipitation, the sediment yield becomes lowest. When vegetation finally adapts to the arid conditions, the proposed erosion cycle returns to the starting point.

Another, less common hypothesis describes the cycles of landscape (in-)stability from the perspective of activated or deactivated response to up-catchment effects of fluvial erosion. Changes in the hydrological system affecting the whole catchment are seen as a possible driver for complex landscape response, thus regulating hillslope activity (Botha et al., 2016). Temme et al. (2008) stress, that "knickpoints on streams or slope breaks can reduce erosive forces or the headcutting retreat rate of gullies, thereby reducing colluviation and promoting pedogenesis on the land surface". Since knickpoints are strongly affected by local lithologies and structures, they are capable of steering colluviation on catchment scale.

6.1.3 Dating the Masotcheni Fm.

Several studies present datings of colluvial materials in KZN with Optically Stimulated Luminescence (OSL) and Radiocarbon dating. Wintle et al. (1995) correlated the stratigraphy of four profiles of the Masotcheni Fm. around St. Paul's Mission in northern KZN and created a chronological framework. A gully at Voordrag has been repeatedly subject of investigations by Botha et al. (1992) and Clarke et al. (2003) and yielded important results for the association of landscape phases with environmental conditions. Several profiles have been correlated and

dated by Temme et al. (2008) in the Okhombe Valley, close to the border between KZN, Free State and Lesotho in the Drakensberg Mountains.

In general, the different dating techniques, OSL and Radiocarbon, allow to discriminate between collvuial accretion and pedogenesis (Botha, 1996). Since OSL measures the latest exposure of quartz grains to (solar) radiation, it can be used to determine the date of colluvial deposition of a stratum. It therefore stands for hillslope instability, erosion of sediment in the upper slope (including exposure to daylight) and the deposition at the lower slope. Fuchs and Lang (2009) reviewed the effect of insufficient exposition before burial, incorporating some of the aforementioned dates, and deduced a possible age overestimation.

Radiocarbon dating instead, is based on the radioactive decay of organic matter in the sediments. The organic matter is enriched in the pedoderm through vegetation. Thus, the radiocarbon date stands for a period of geomorphic stability, in which slopes are stable and pedogenesis is possible. However the analysis by Wintle et al. (1995) showed that radiocarbon dates may be complicated, where roots encroach older layers and post-depositional mobility of organic matter within the profile occurs. Another limitation of this method is its C14 detection threshold equivalent to ~50 ka.

6.2 Methods

This study includes the conventional methods of research of the Masotcheni Fm. such as stratigraphic correlation (chapter 6.3.1), soil analysis and dating (chapter 6.3.2). Furthermore, other non-invasive methods such as Electric Resistivity Imaging (ERI, chapter 5.2.6), and for the first time in this context, spectroscopy (chapter 6.3.4), were applied.

6.2.1 Stratigraphy

The description of the stratigraphy, follows a concept of allostratigraphic and pedostratigraphic systems established by Brewer et al. (1970), which is recommended for Masotcheni-like colluvial deposits by Botha (1996), Botha and Fedoroff (1995). This combination reflects the recurring sequences of sediment deposition (and partial or complete erosion) and subsequent soil formation in these sediments. This configuration reflects the landscape cycles of repeatedly caused sedimentation at foot slopes and subsequent development of soils. This concept is suited to divide a succession based on bounding discontinuities with the concept of pedoderms. The latter are caused by the development of paleosols and post-depositional alterations of the sediment.

Allostratigraphic units, as defined by the North American Commission on Stratigraphic Nomenclature (NACSN), are sedimentary rock bodies, constrained by bounding discontinuities (Oriel et al., 1983). Related to the Masotcheni Fm., this concept can be best applied by identifying the upper discontinuities of a unit through paleosols, which developed within. The pedoderm concept describes these soil units as mantles (superficial or buried), which display the characteristics of soil formation (Brewer et al., 1970, Walker et al., 1984) and thus complement the allostratigraphic approach. Through the combination of both, strata can be described both in terms of rock or soil properties. According to this system, four distinct rock units (RU1-4) could be diagnosed at site.

6.2.2 Spectroscopy

Spectroscopy is a method to sample the spectral reflectance of electromagnetic radiation from materials. These reflectances can be used to derive information about the material's physical or chemical properties from their specific absorption bands.

Samples were collected with the spectrometer device "Spectral Evolution RS-3500", which is equipped with a mobile power source, and thus allows measurements in the field (fig. 6.4). The spectroradiometer measures electromagnetic radiation in the range of the visible (VIS) and near infrared (NIR) region of the spectrum between 350 nm and 2500 nm with a spectral resolution of 1 nm (2151 bands accordingly). The light enters the instrument through a fiber optical input cable equipped with a handheld contact probe, which in turn contains an artificial light source. Paired with a reference white board ("SphereOptics ZenithLite"), this setup allows to measure calibrated reflectance. The single measurements were transferred through a USB connection to a laptop computer equipped with the software "DARWin" and saved in the *.sed format.

Each rock unit, that could be correlated at three gullies, KwaThunzi, KwaGade and Moyeni, was sampled at least three times at each outcrop. At gully Moyeni, additional reference samples were collected from multiple locations within the gully in order to assess within-layer variability at this site. Depending on accessibility, measurements were taken directly on the wall or from larger pieces broken off the wall. In either way, at least the first 10 cm of surface were removed

and a level plane was created. This ensures that the handheld contact probe fits smoothly to the specimen and no external electromagnetic radiation affects the measurement.

Fig. 6.4: Spectroscopic measurement of a prismatic soil feature sampled at gully KwaThunzi by Volker Hochschild. Photo: C. Sommer.

After data collection in the field, the recorded spectral information was further processed. The effect of different brightness baselines, i.e. a vertical offset of the spectra, hinders the direct comparison of signatures. This problem can be mitigated through the normalisation of the reflectance by continuum removal, as depicted in fig. 6.5. This method, described by Clark and Roush (1984), estimates a continuum baseline R_L, which represents the hypothetical background absorption feature. This continuum is compared to the actual absorption values R_0 in order to calculate the continuum removed spectrum R_C, as presented in eq. 6.1:

$$R_C(\lambda) = \frac{R_0(\lambda)}{R_L(\lambda)}$$
eq. 6.1

with
$R_c(\lambda)$ = Continuum removed spectrum
$R_o(\lambda)$ = Measured spectrum
$R_c(\lambda)$ = Baseline spectrum

The continuum is estimated by detecting local maximal reflectances throughout the desired region of the spectrum, which are not affected by absorption features. These maxima are interpolated through linear interpolation or other interpolation methods. As a result, the normalized reflectance emphasizes the absorption features, making it feasible to compare signatures.

Sample analysis, visualization and processing was performed with the R package "spectrolab" v.0.0.8 (Meireles et al., 2018) for hyperspectral data analysis. The continuum removal was conducted with the package "prospectr" v.0.1.3 (Stevens and Ramirez-Lopez, 2014) for physio-chemical analyses in the VIS-NIR spectrum.
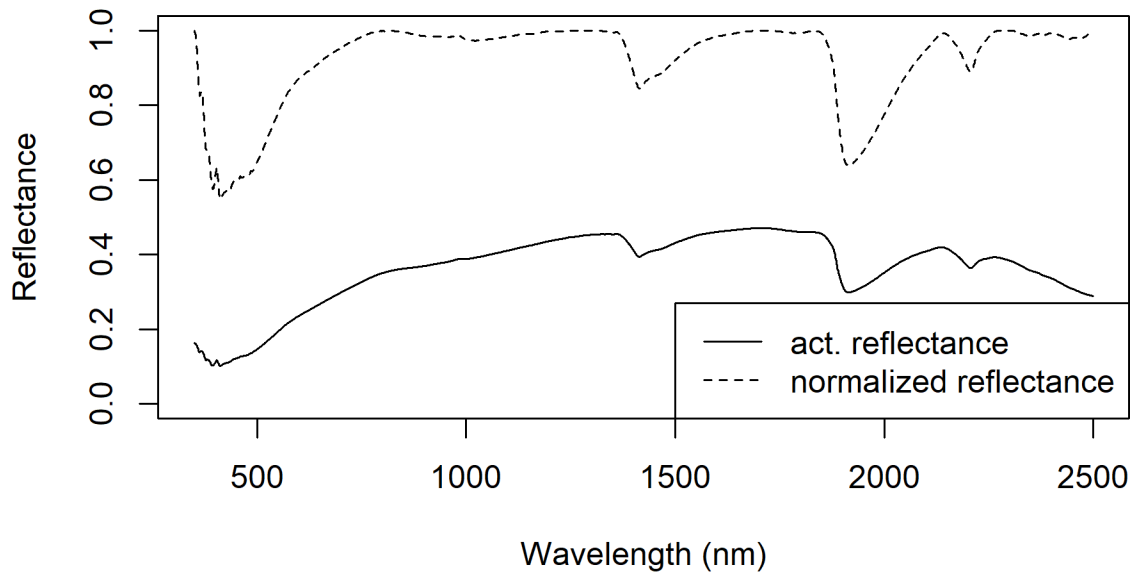
Fig. 6.5: Example of a reflectance curve of a measurement at gully KwaThunzi and the derived continuum-normalized reflectance.

6.3. Results

6.3.1 Stratigraphy of the Masotcheni Formation at KwaThunzi

In this chapter, the stratigraphic profile with distinguishable RUs is described. For a better understanding, RUs have already been assigned to known alloformations and pedoderms from the classification system by Botha (1996). However, this assignment was not made exclusively on basis of the stratigraphic properties, but also requires further information such as dating, correlation with properties of the reference succession and environmental indicators.
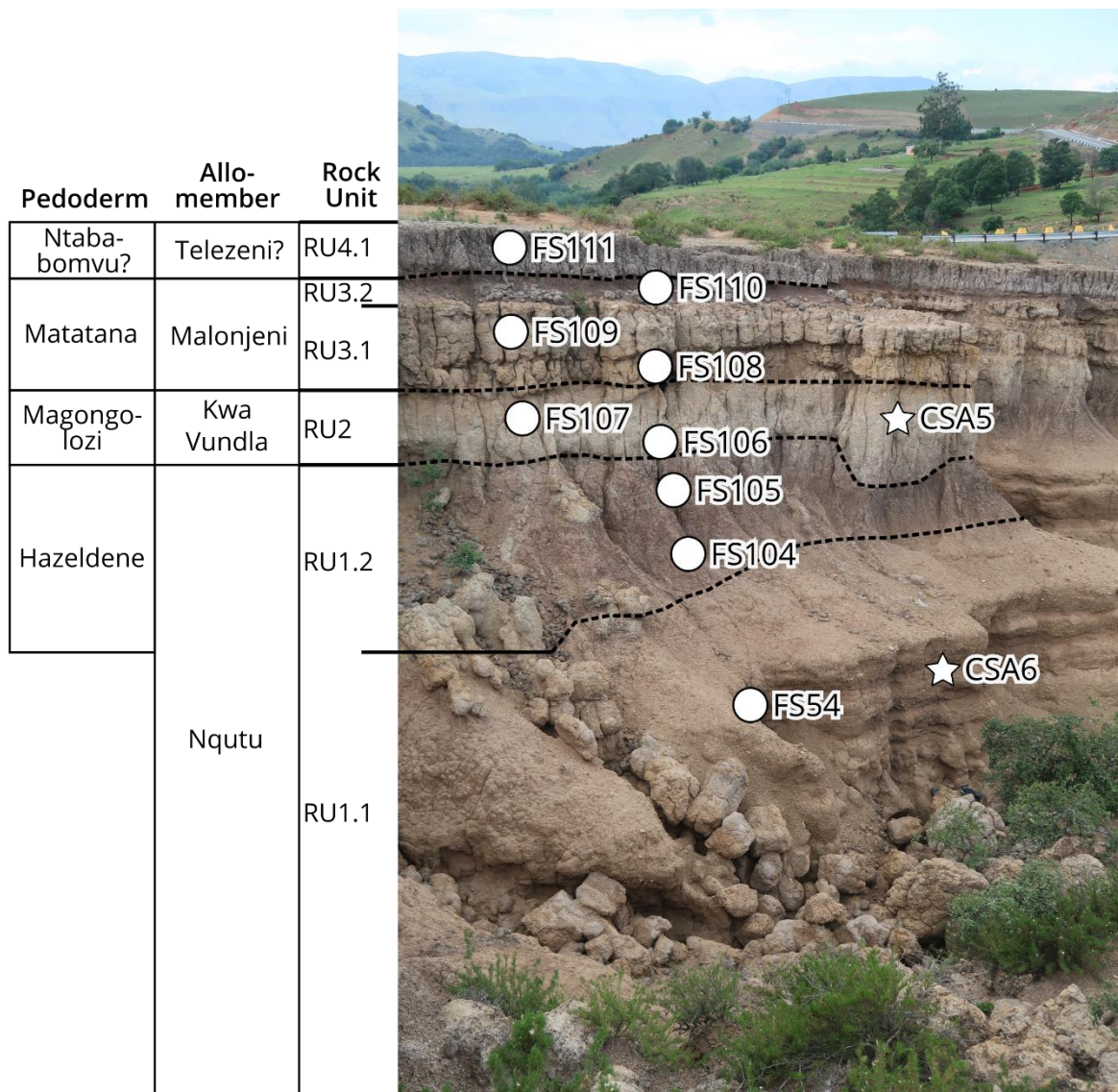
Fig. 6.6: Allo- and pedostratigraphic subdivision of the rock units, exposed on the northern outcrop of the Masotcheni Fm. at Gully KwaThunzi. Soil samples (points) and OSL samples (stars) are labelled with laboratory numbers.

The Masotcheni Fm. exposed at KwaThunzi is underlain by shalestones of the Permian-Triassic Beaufort Group (Adelaide Subgroup). A succession of up to 4 distinct rock units (RU), composed of allomembers and pedoderms can be distinguished on top. The sequence is best pronounced on the northern walls of the gully (fig. 6.6), whereas especially the upper RUs are missing in the southern walls due to erosion.

115

The lowermost layer, RU1.1 is the thickest stratum of the succession. The basis, with an average thickness of 250 cm, is formed of stratified colluvium of yellow-reddish color (10YR7/6), primarily composed of coarse material (FS54: 62% sand and coarse silt) and angular fragments. No indicators of soil formation processes were found in this layer. The transition towards the upper part, RU1.2 with a of thickness 70 cm is visually distinguishable through the darker grey color (2.5Y5/2) and is marked by high clay content (FS104, FS105) and a (coarse) sub-angular structure. This rock unit is interpreted as the Nqutu allomember (RU1.1) with the distinct Hazeldene Pedoderm (RU1.2).
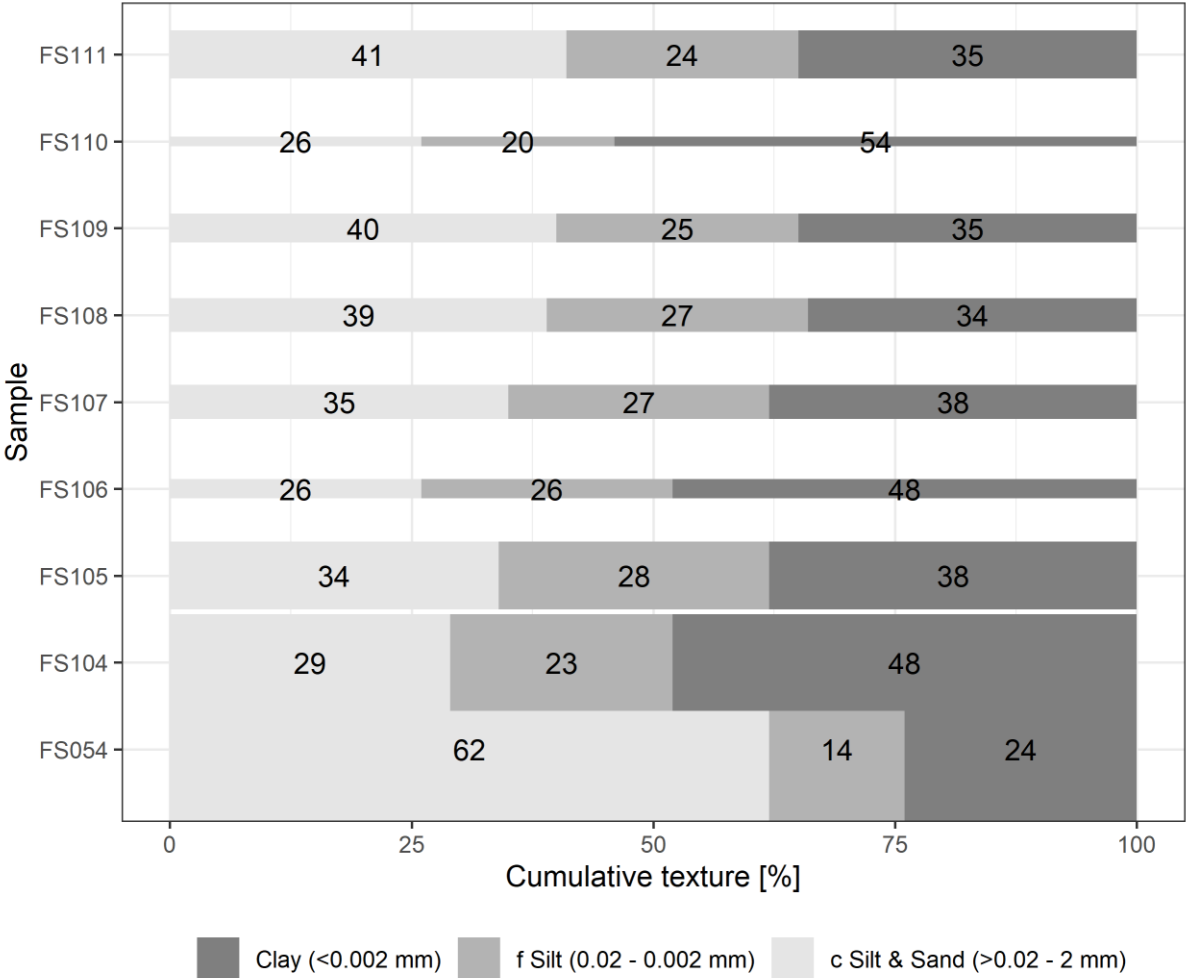
Fig. 6.7: Soil samples from a profile at Gully KwaThunzi. Bar thickness indicates the relative thickness of the layers.

RU2 overlies RU1 and has a mean thickness of 90 cm. The distinction between RU2 and the underlying RU1 is gradual (<15 cm) and the topography smooth to wavy. The layer shows a high concentration of the coarse fraction (sand and coarse silt) and a downward increase of clay content (FS 106, FS 107). The color is greenish grey (5YR8/2). This layer has a prismatic structure, which spans the entire horizon. With a sharp distinction to the overlying RU3, it is interpreted as a superficially eroded subsoil (prismacutanic B horizon) and part of KwaVundla Allomember and Magongolozi Pedoderm.

RU3 overlies RU2 smoothly with a clear to abrupt distinctness. Its absolute thickness lies around 120 cm. The lower horizon (RU3.1) of this rock unit, with 90-100 cm thickness, appears to be

split internally into two parts of varying thickness. However, this distinction cannot be observed in the entire outcrop. Therefore, it was not divided into separate rock units. The texture of this horizon is consistently homogeneous (FS108 & FS109) and color is brown (10YR8/1). Also, this layer shows a clear type of prismatic structure. However, compared to the structure of the underlying RU2, the aggregates are more massive. The upper horizon, RU3.2 is considerably thinner (~20cm), darker (10YR6/1) and rich in clay (FS110). Its structure is generally finer, i.e. medium crumb to subangular blocky. This section is interpreted as a pair of prismacutanic B horizon subsoil (RU3.1) and a A-horizon topsoil (RU3.2), and thus attributed to the Malonjeni Allomember with the Matatana Pedoderm.

The uppermost rock unit (RU4) overlies RU3 with smooth topography and clear distinctness. Apart from its dark color (7.5YR6/1), it resembles some of the features of RU3.1 and RU2: High content of coarse particles (FS111) and a distinct columnar structure. The thickness of this layer lies around 50 cm. It is overlain by the recent topsoil with a thickness of 5-10 cm, where this is not eroded. Consequently, also RU4.1 is classified as a prismacutanic B horizon. The interpretation of this youngest unit is rather unclear, but according to the reference subdivision it is likely part of the Telezeni Alloformation with the Ntababomvu Pedoderm, or Batshe Alloformation with the recent Vumankala soil.

6.3.2 OSL Dating

The two samples from the stratigraphy of gully KwaThunzi were obtained from the basal rock unit RU1.1 (tab. 6.2, CSA6) and the layer RU2.1 overlying the distinctive Hazeldene pedoderm (tab 8.2, CSA5). Overdispersion of 43% and 29% allowed the application of the MAM model to estimate RU1.1 to an age of 66.62±7.68 ka, which overlaps with other colluvium OSL dates from sites at Voordrag (Botha et al., 1992, Botha, 1996, Clarke et al., 2003), St. Paul's and the type locality Masotcheni (Botha et al., 1992, Wintle et al., 1995). The colluvial layer of RU2.1 is dated to 39.42±5.27 ka and is contemporaneous with layers at St. Paul's and Nqutu, the Okhombe Valley (Temme et al., 2008) and radiocarbon dates from Voordrag.

Tab. 6.2: Results of the OSL dates at KwaThunzi.

Rock Unit	2	1.1
Sample code	CSA5	CSA6
Water content [%]	19.55	4.93
U [ppm]	4.45	4.07
Th [pm]	11.39	3.81
K [%]	2.36	1.82
Dr [Gy ka-1]	4.15±0.13	2.67±0.08
Overdispersion [%]	43	29
De (CAM) [Gy]	284.40±27.56	244.11±16.22
CAM Age [ka]	68.51±6.95	91.60±6.62
De MAM [Gy]	163.65±21.30	177.55±19.85
MAM Age	39.42±5.27	66.62±7.68

6.3.3 ERI

An ERI transect with a length of 100 m (fig. 6.8) was recorded in the northern side of the gully to detect the physical properties of the intact colluvium, which is not directly affected by gully erosion. Details about the setup are listed in tab 6.3 and the resulting cross-section is depicted in fig. 6.9.

Tab 6.3: Properties of the ERI transect and inverse model accuracy

Cross section name	KwaThunzi
Type	Wenner
Length [m]	100
Electrodes [number]	51
Spacing [m]	2
Points [number]	408
Error 1st inversion [Ωm]	5.25
Error 2nd inversion [Ωm]	2.67
Error 3rd inversion [Ωm]	2.09
Error 4th inversion [Ωm]	1.71
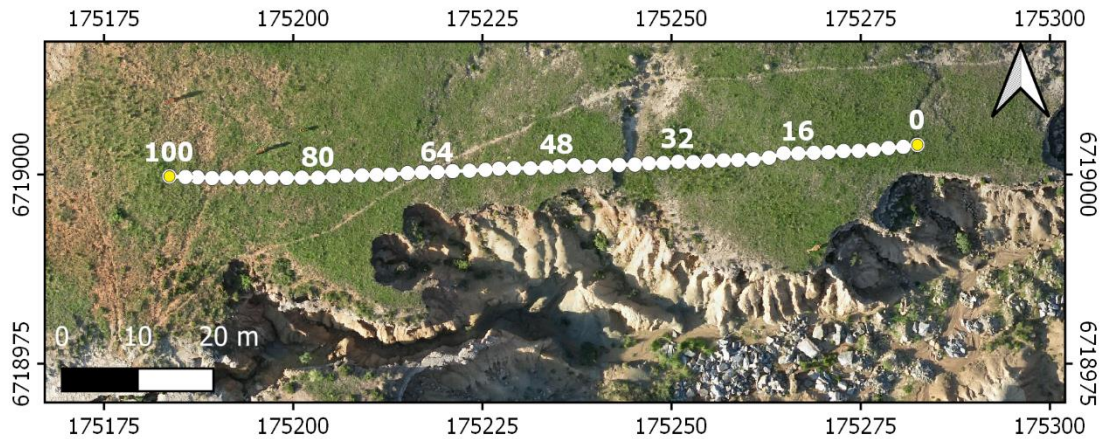
Fig. 6.8: ERI transect of Gully KwaThunzi.

The basal section of the ERI at gully KwaThunzi shows homogeneous high electric resistivities ranging between 100–150 Ωm. This value is typical for impermeable shalestones (after Palacky (1988), tab. 5.1) and coincides with the presence of Beaufort Group (Adelaide Fm.) shales in the field. The non-conformable contact to the overlying sedimentary succession is sharp and the bedrock topography is wavy and undulating. This may be attributed to the effect of erosional processes, caused e.g. by formation of an earlier terrace or gullying, which affected the study area prior to the accumulation of the currently observable sediment body.

The shalestone basement is covered by a succession of material with variable depth, ranging from up to 10 m depth at the long section around 80 m to as low as 4 m of depth at the long section around 60 m. The sediment body shows a horizontal separation into two distinguishable layers, which is marked by a resistivity gradient in ~3m depth and spans the whole profile. This separation has also been observed in the field and the analysis of soil properties, where it separates the Hazeldene Pedoderm (RU1.2) from the overlying prismatic paleosoils (RU2–4). With 25–130 Ωm, the resistance values of both layers lie within the expected range of clay-loam texture (Clay: 5-150 Ωm, Loam: 20-160 Ωm).

The upper layer is generally more resistant, due to its columnar-prismatic structure and the associated clefts. Prismatic structures with a high clay content are typically impermeable, which is why they exhibit low electrical conductivity due to their low water content. Furthermore, the columns are separated by fine air-containing fissures that further impair conductivity.

Additionally, single features, like a carbonate crust in the long section 74–90 m and eroded topsoil in the section 16–30 m reduce surface conductivity.
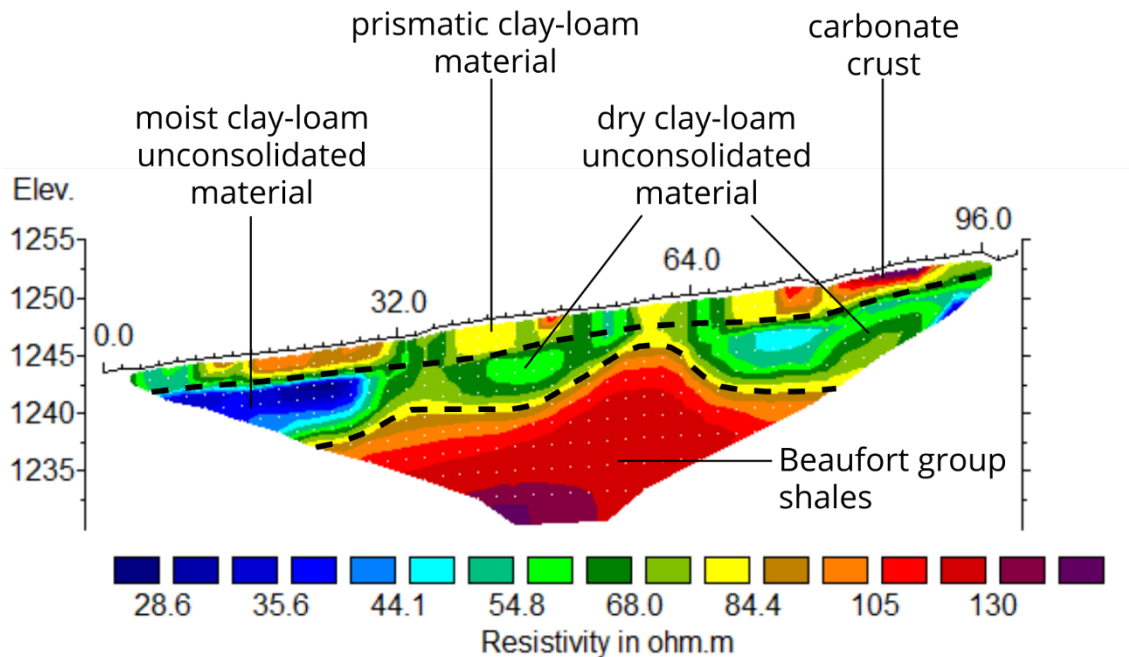
Fig. 6.9: Wenner mode ERI of Gully KwaThunzi.

The differences within the lower layer are less concise, which is due to the fact that it represents RU1, the Nqutu allomember. Especially the lowest part in the section between 0 and 30 m, which lies below 1242 m, hosts the area with the lowest electrical resistivity of the whole transect (<40 Ωm). This is associated with increased soil moisture in the deeper layers. The subsequent long section between 30 and 64 m is close to the erosion edge (fig. 6.8), where these sediments are drained through the free face of the gully wall. This observation indicates increased erosion in this part, where the drainage is accompanied by subrosion processes, which in turn lead to excavation of cavities and piping. These eventually destabilize the gully walls and promote further lateral growth of the gully.

6.3.4 Electromagnetic properties of the Masotcheni Formation

Spectral probes were sampled from three units of the Masotcheni profile at three different locations in the Upper Umkomazi catchment, in order to assess correlations, but also variability (a) between different layers and (b) between different sites. The measurements were obtained as pooled samples from the units RU1.1, RU1.2 and RU3, which are exposed at Gully KwaThunzi (UTM35S: 756313 6720762), Gully KwaGade (UTM35S: 0762735 6719963) and Gully Moyeni (UTM35S: 0760908 6720363). At Gully Moyeni, RU3 could be clearly distinguished into two subunits, so that the sample was split. At KwaGade, the Beaufort Group bedrock was sampled as well.

The spectral signatures of the samples show broad congruence, both within the single strata across the different locations, as well as across the different strata within the single vertical profiles. According to the reflectance curves, all sampled layers of the Masotcheni Fm. represent typical soil spectra, comparable to those discussed in the global spectral library by Viscarra Rossel et al. (2016). Thereafter, the spectral reflectances represent mixtures of different minerals represented in the colluvium, as well as diverse alterations imposed through

119

pedogenesis. This underlines the interpretation of the Masotcheni Fm. as a succession of pedoderms. While the composite soil spectra permit the classification of single minerals through signature matching from mineral databases, the reflectance curves contain valuable information about absorption bands and their associated physio-chemical properties (Gupta, 2018). These diagnostic features are displayed with the averaged signature of gully KwaThunzi in fig. 6.10 and fig. 6.12 and discussed in this section.

KwaThunzi reflectance
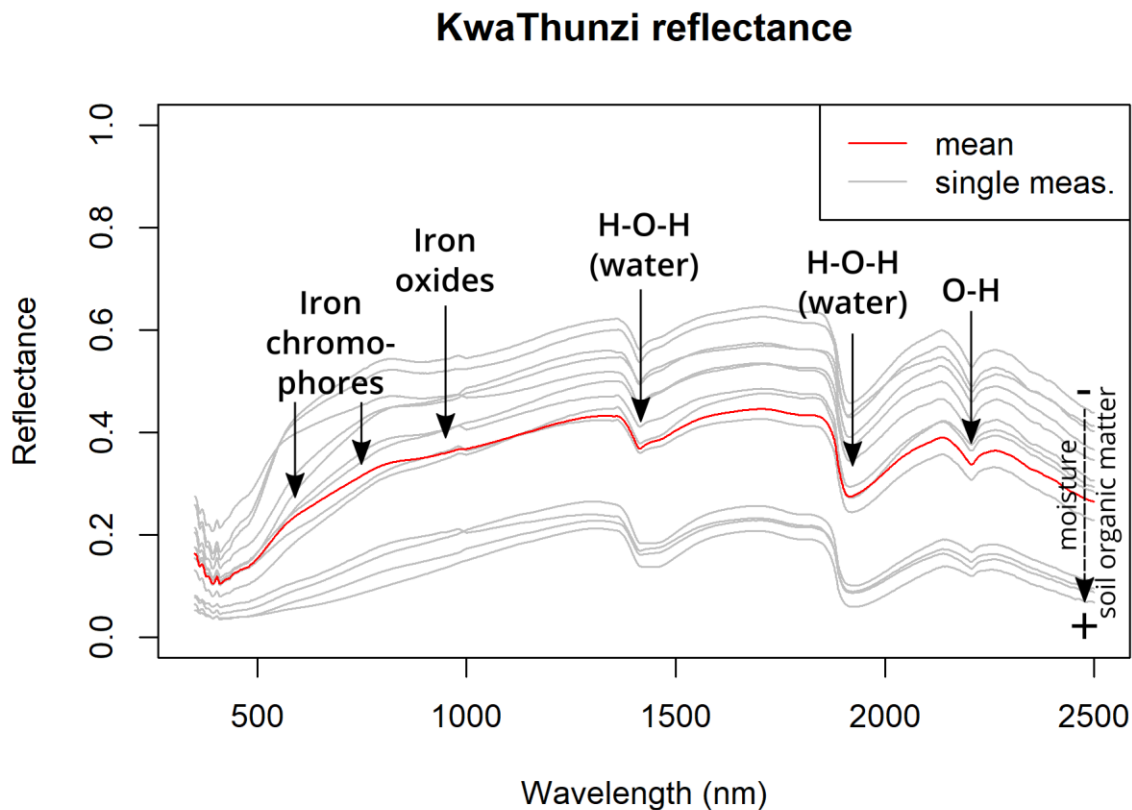
Fig. 6.10: Single and mean observed reflectances (R_0) of samples recorded at Gully KwaThunzi.

Fig. 6.10 shows a vertical offset of the single measurements, that can be attributed to two effects. First, soil organic matter has typically a very low reflectance throughout the VIS and NIR spectrum. Presence thereof in the soil matrix causes absorption and reduces reflectance. The group of four distinctively low ($R_0<0.2$) measurements belongs to the recent, mostly eroded humus-rich topsoil (RU4.2, 3 measurements), as well as the Hazeldene Pedoderm (RU1.2) which supports the interpretation of this layer being a paleosol. Also, one other measurement of RU1.2 was recorded with lower-than-average reflectance, which can be considered as an indicator for increased organic matter in this layer. The second effect to reduce reflectance in the whole VIS-NIR spectrum is the absorption through water (Weidong et al., 2002). Since the measurements were taken under natural conditions from below the surface of the exposed profiles, all curves vary in moisture. The vertical offset of the reflectances of the sedimentary units of gully KwaThunzi are affected by this effect, also because of the visible absorption in water absorption bands.
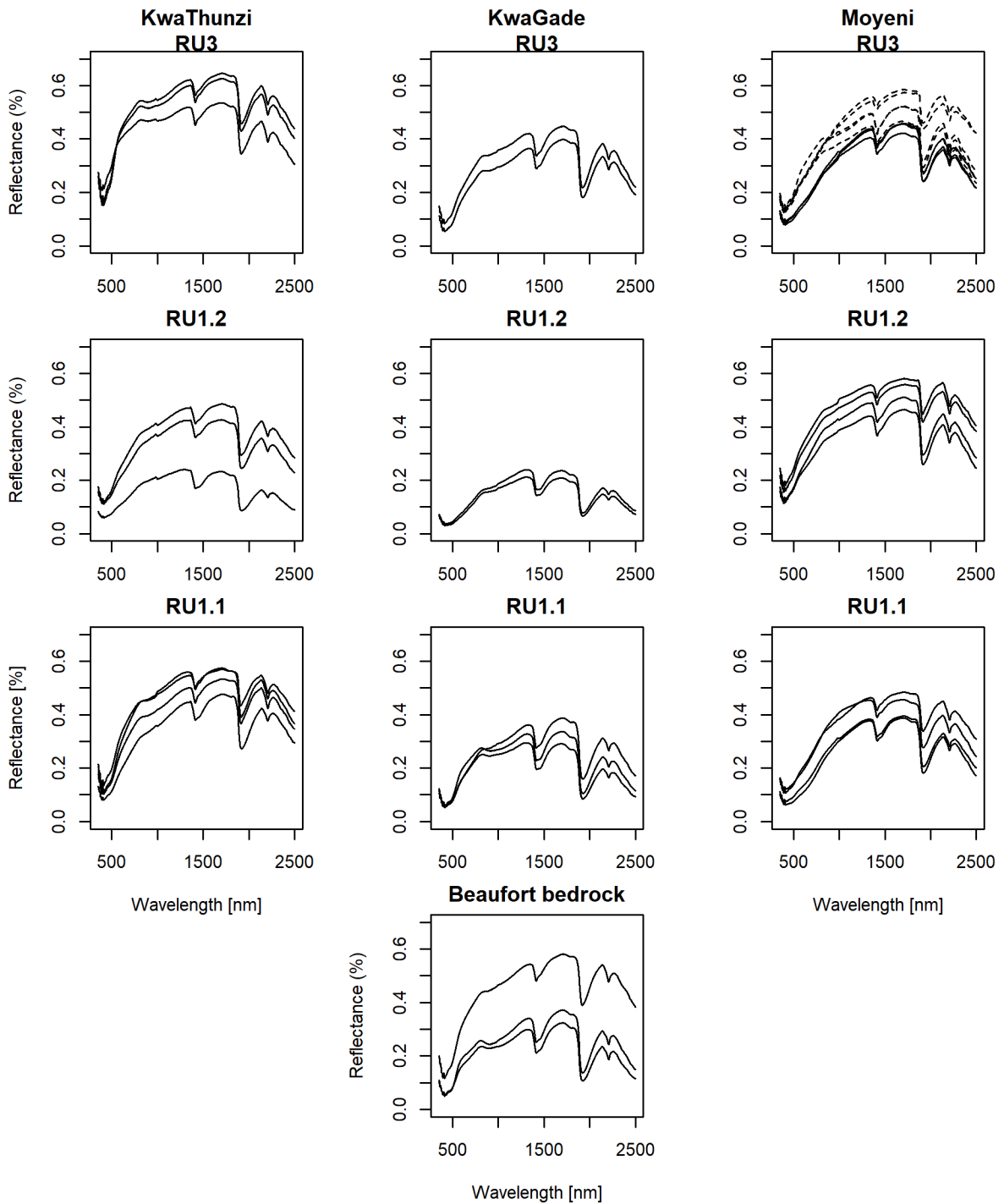
Fig. 6.11: Spectral reflectance of different Masotcheni units in the VIS-NIR region, sampled in three different exposures.

All spectra display three characteristic absorption bands in the NIR, situated at 1440 nm, 1900 nm and 2200 nm (fig. 6.10 and 6.11). The first two are well known as water absorption bands (Bowers and Hanks, 1965, Gupta, 2018). These wavelengths are associated with frequencies that are overtones of the basic frequency of free water molecules. Water molecules absorb electromagnetic radiation at these wavelengths and convert it to physical vibration. The signatures show furthermore, that the amplitude of these absorption bands increases with lower reflectance, and thus, higher moisture content (Weyer and Lo, 2002). Or to put it in other words,

the higher the absorption through moisture affects the whole width of spectrum, the higher is also the absorption in the specific water reflection bands.

The third feature, which is centered around 2200 nm, represents a hydroxyl group absorption band (Hunt, 1979, Workman, 2001). This wavelength is susceptible to stretching of molecular O-H bonds, but also bending of metal O-H bonds, which absorb electromagnetic radiation. In soil samples, these absorption bands are typical, where aluminosilicates, such as Kaolinite, Illite or Smectite are present (Camargo et al., 2018). Consequently, the absorption in this band represents the presence of such clay minerals, which is no surprise, since texture analysis (fig. 6.7) shows a high clay content in all layers (>30% in all layers except RU1.1).

The presence of weaker absorption features can be detected in the normalized reflectance curve R_C, computed through continuum removal after Clark and Roush (1984). Figure 6.12 shows the main absorption features in the continuum removed signatures of Gully KwaThunzi.
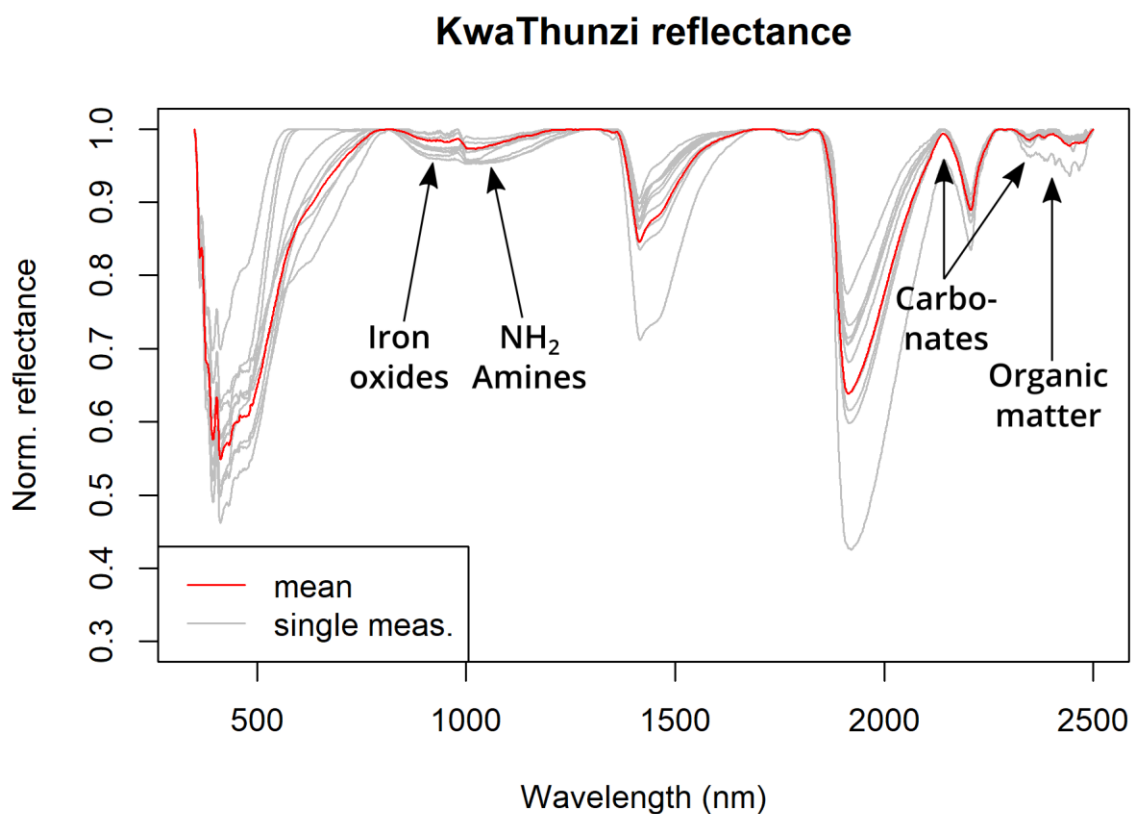
Fig. 6.12: Single and mean continuum-removal normalized reflectances (R_c) of KwaThunzi and the positions of weak absorption bands.

Minor absorption in the areas around R_c(2160 nm) and in the range R_c(2300–2500 nm) can be related to carbonates (Hunt, 1979). However, the latter range of the spectrum R_c(2300-2500 nm) can also be influenced by the presence of soil organic matter, which may lead to misinterpretation (Clark et al., 1990). Typical features of carbonate can be detected in the samples of RU1.2 at Gully KwaThunzi and Gully KwaGade, but also RU1.1 of Gully KwaGade, where absorption affects both carbonate-related wavelength areas. Absorption in the range 2300 –2500 nm is apparent in the other layers of Gully KwaGade, however a clear assignment to carbonate on the one hand and organic material on the other, cannot be made. It is noticeable,

that absorption in the carbonate-sensitive wavelengths is low in all layers of Gully Moyeni. Unlike the other two, it is not in reach of a dolerite dike, and therefore hints at the presence of igneous rock as a possible source of carbonate.

In the visible spectrum, weaker absorption bands can be associated with iron oxides R_c(450–950 nm) in the NIR and iron chromophores related to red hematite or yellow goethite R_c(680–550 nm) (Mortimore et al., 2004, Stenberg and Rossel, 2010). The iron oxide related absorption at R_c(950 nm) can be observed in all samples of Gully KwaThunzi (except for the Hazeldene Pedoderm RU1.2) and all layers of Gully KwaGade (including bedrock), but appears to be weakly developed in the layers of Gully Moyeni. Since iron oxides are known to provide structural cementation in soils, this explains why the prismatic RU3 (of KwaThunzi and Moyeni) has such a strong absorption in this range.

A primary amino group (NH$_2$) absorption band is located in the area around R_c(1050 nm) and indicates the presence of amino acids or other derivates of biological origin. Evidence of absorption in this wavelength can be found in all samples from Gully KwaThunzi, whereas the Hazeldene Pedoderm (RU1.2) shows strongest influence and RU1.1 lowest. Also, this reinforces the assumption that the former has been a biologically active soil horizon. However, at KwaGade, all samples except RU1.2 show amino group absorption. At Gully Moyeni, the influence can be described as rather low, with most samples showing no absorption features.

In summary, it can be stated that spectral signatures observed at the gullies KwaThunzi and KwaGade differ from gully Moyeni. Especially the weaker signatures attributed to iron oxide, calcium carbonate and amines seem to be absent or weakly present at the latter. The pattern suggests, that the occurrence of carbonates is connected to the proximity to dolerite, which can be found near KwaThunzi and KwaGade, but not near Moyeni. However, the overall absence of the absorption features at Moyeni, even those of amines, leads to the question if post-depositional leaching processes may have removed traces thereof. In this case, the distinction between the spectral properties cannot be assigned to a contribution of the igneous rocks, but rather local preservation conditions at Gully Moyeni.

Furthermore, the within-layer variability is high and prohibits a direct or even automated classification of allomembers or pedoderms based on their spectral properties. In contrast, the findings of analytical absorption features in different layers and locations indicate, that some geochemical properties are not correlatable over larger areas, since they are (i) induced by external factors, such as proximal carbonaturces, or (ii) the result of post-depositional vertical mobility of particles and solutes across the succession. However, especially the weak absorption bands seem to support observations that were made with the "classical" soil profile analysis and thus represent a suitable supplementary analytical approach.
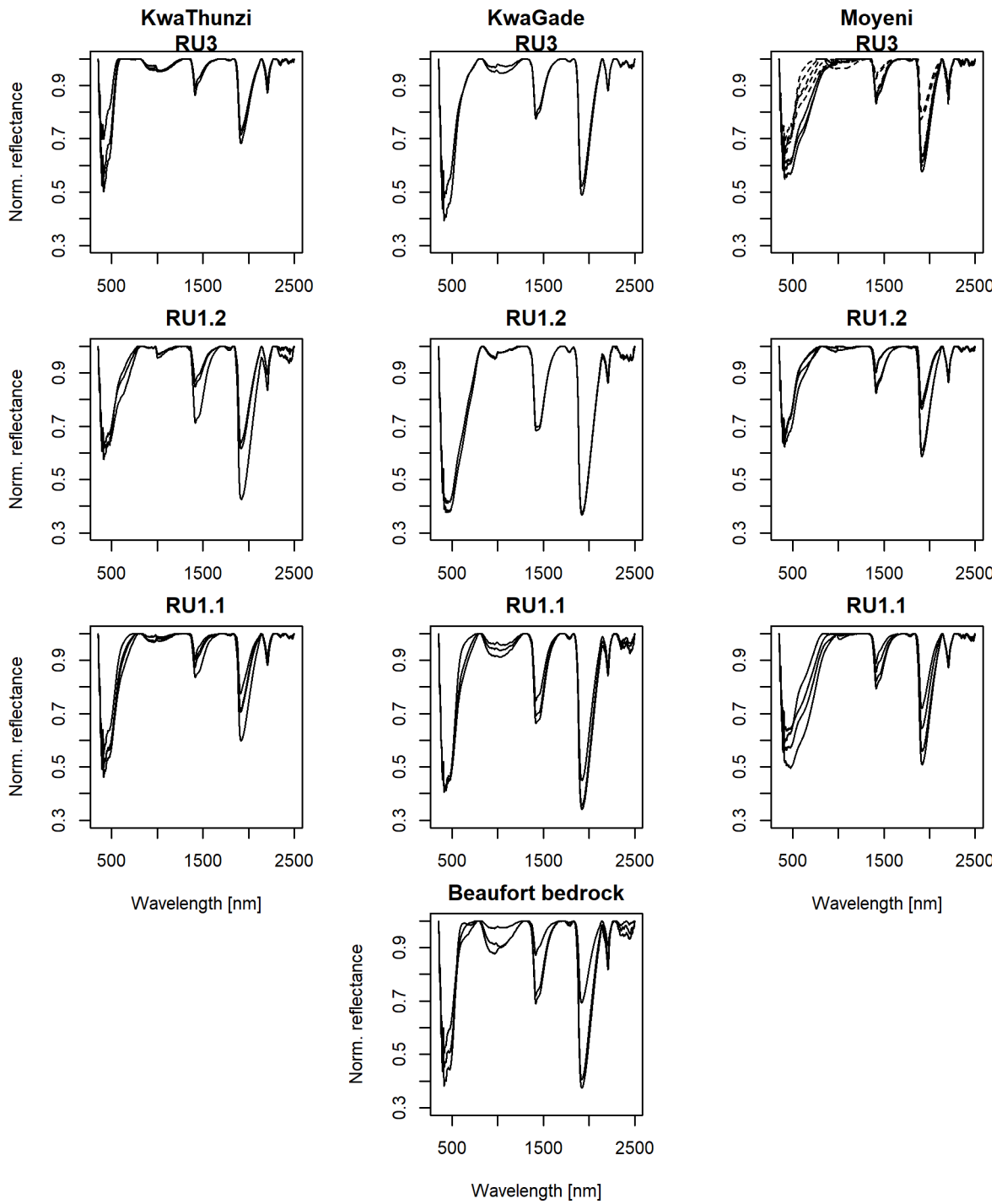
Fig. 6.13: Continuum-removal normalized reflectance of different Masotcheni units in the VIS-NIR region, sampled in three different exposures.

6.4. Discussion

6.4.1. Regional correlation of the Masotcheni Formation

The thickness of the colluvial deposits at KwaThunzi are on average larger than 3 meters, but also more than 9 m were measured from in situ measurements and the UAV-derived 3D model of the gully sidewalls. The same is true for the intact deposits, which have not been affected by gullying yet, as confirmed through non-invasive ERI sounding. While the modern surface of the Masotcheni Fm. slopes gently to the northeast, where not dissected by erosion, the underlying bedrock shows planar but stepped topography. The major step coincides with the thickest colluvial overlay and deepest trench of the gully, at the transition from the middle to the upper gully. It is also where the gully's morphology changes from V-shaped cross-section to the deep and U-shaped type with tens of meters of width. This uneven bedrock topography is likely the result of prior fluvial incision and terrace formation, but also initial gullying pre-dating the Late Pleistocene Masotcheni Fm. can be expected. Situated ~20 m above modern stream level of the Umkomazi, this elevation corresponds with nearby cut-off meanders directly upstream of the site and exposed terraces downstream (Bosino et al., 2020). This interpretation is supported by the presence of amygdules, which testify fluvial transport of this allochthonous material from the Great Escarpment and its deposition at this site. The timing of terrace formation remains unclear, but the presence of Masotcheni colluvia on both lower and higher terraces in this study area, indicates a formation predating the Late Pleistocene, at least.

According to the alloformation-pedoderm system proposed by Botha (1996), four distinct rock units (RU1-4) could be diagnosed at site. These were further differentiated into lower and upper horizons (RU1.1, 3.1 and 4.1 as well as RU1.2,3.2 and 4.2 respectively). These are summarized in table 6.4.

Tab. 6.4: Correlation of the KwaThunzi stratigraphy with the reference by Botha (1996). Layers with absolute OSL dates are indicated by *.

Allostratigraphy (Alloformation / Allomember)		Pedostratigraphy (Pedoderm, Pedocomplex, soil)		KwaThunzi stratigraphy
Batshe		Vumankala soil		RU4.1–4.2(?)
Telezene		NtababomVu		
St Paul's	Malonjeni	Dabekazi Pedokomplex	Matatana	RU 3.1–3.2
	Kwa Vundla		Magongolozi	RU 2*
	Nqutu		Hazeldene	RU 1.1–1.2*
Dingaanstad		Ndhalamadoda		
St Augustine's		Dwarsirivier		

The Masotcheni Fm. is fundamentally different from other geological strata, which, as defined by the South African Committee for Stratigraphy (SACS 1980), are divided primarily on the basis of their lithology. As the Masotcheni Fm. is lithologically homogeneous at a single site, the factors color, texture and structure are used instead for the internal differentiation of the succession. This explains why only two horizons could be divided with the ERI method. The homogeneous source lithology produces uniform electric resistivity, so that only the change in texture and structure between RU1 and RU 2-4 is recognized as a boundary. The lower one (RU1) is characterized by unconsolidated material and shows internal variations that can be explained by

differences in moisture content. The upper one (RU2-4), on the other hand, has a prismatic structure that is interspersed with air-filled fissures and thus increases resistivity. Furthermore, the carbonate crusts seem to exert an influence on the measured values.

The lowermost RU 1 contains a lower horizon (RU 1.1) with stratified sandy clay loam and a upper (RU1.2) horizon featuring a pronounced pedoderm, which stands out by its dark-grey color, fine organic matter and high clay content. Besides the visible color, the spectral analysis showed also a strong reflectance in the region around R_c(1050 nm), which is associated with amino acids. This can be seen as an indicator of former organic activity in this paleosoil layer. The higher clay content in the upper layer is untypical for in-situ soil formation and likely the effect of a reversed profile, where a redistributed A-horizon was overlaid by its subsoil. Due to these characteristics, RU 1 can be correlated to the Nqutu allomember and RU 1.2 to Hazeldene Pedoderm, which is widely distributed throughout eastern South Africa and Swaziland. This attribution is also supported by the results of OSL dating, which estimate the age of deposition to 66.62±7.68 ka for the sample from RU 1.1. This value lies in the expected range of this allomember, which is in other parts of the country in the range between ~52 ka (at St Paul's) and ~68 ka (at Hazeldene type locality) (Botha, 1996, Botha and Fedoroff, 1995).

RU2 overlies RU1 gradually with a smooth to wavy topography, which indicates an erosion phase, that stripped off the top of RU1 prior to the deposition of RU2. The layer's texture graduates from a clay-rich base to a finer clay-loamy top, which is likely caused by lessivation within this paleosoil. The unit is of bright greyish-green color and is characterized by a pronounced columnar structure. These features can be correlated with the Kwa Vundla allomember. At the site of Nqutu, this layer was dated to an age of ~41 ka, which aligns reasonably well with the date of 39.42±5.27 ka, that was sampled in RU2. Taking into consideration, that RU2 is separated from RU3 by a sharp distinction, it becomes obvious that topsoil of the pedoderm was removed through erosion before the deposition of RU3.

RU3 contains, just like RU2, a B-horizon with a prismatic structure, although this appears to be split into two sub-horizons. Such "stacked paleosol horizons", as reported by Botha (1996), are a distinct feature of the Malonjeni allomember, and were described at the study sites of the Masotcheni Formation at St Paul's Mission, Nqutu and Hazeldene. The paleosol B-horizon is topped by the intact clay-rich A-horizon of RU3.1. Apparently, the transition from RU3 to RU4 was not accompanied by as severe erosion as the previous ones. The Malonjeni allomember was not dated at KwaThunzi, but equivalent layers' dates range widely from 10-11 ka at the Hazeldene Gully to 46 ka at St Paul's Mission.

While RU4 is clearly a distinct layer with abrupt boundary, it is not clear if it is just another "stacked horizon" of the Malonjeni allomember/Matatana Pedoderm pedocomplex, or an individual alloformation. RU4.1 displays, just like RU2 and RU3.1 a prismatic-columnar B-horizon. The subsequent unit of the reference sequence would be the Telezeni allomember with the Ntababomvu Pedoderm, however this is just an assumption here, that needs to be verified by absolute OSL dating. The topsoil, RU4.2 is only preserved in some places on the north side of the gully, whereas it is eroded in large parts of the southern side. The units succeeding the Malonjeni allomember most often lie in the second half of the Holocene.

6.4.2 Late Pleistocene colluviation in the temporal context

This chapter puts the relative chronostratigraphy and absolute dates of KwaThunzi in a regional and temporal context. Figure 6.14 displays the most important dates from the region, and the associated sites are presented in fig. 6.4. Furthermore, precession as the orbital driver for regional hydroclimate, insolation and seasonality is displayed alongside the regional precipitation reconstruction and the Fe/K ratio as an indicator for moist conditions. More details about the environmental factors are mentioned in chapter 2.2.

The driving factors of colluviation operated throughout the whole Pleistocene. However, the absence of older colluvial deposits attest an episodical accretion and (in geological terms) short-lived preservation in this geomorphologically active environment (Botha et al., 2016). Considering the fact, that just a minority of such sediments reach ages of up to ~150 ka (Wintle et al., 1995), Clarke et al. (2003) suggested that "during the preceding Interglacial (MIS 5e), the hillslopes were largely stripped of their older colluvial mantle". Thereafter, the same process, that can be observed today, is made responsible for the clearing of sediments during the Last Interglacial: sheet and deep-cut gully erosion.

The late MIS 5 is often mentioned as the inset of widespread colluvial accretion in KZN. Deposits of this age lay the foundation of many deposits in the area, for example the basal layers of the profiles around St. Paul's Mission, known as Dingaanstad alloformation, which are assigned to an age after the peak of the Last Interglacial (Wintle et al., 1995). Analogically, the basal stratum of the Voordrag profile is attributed to the end of the Last Interglacial or the early Last Glacial (Clarke et al., 2003).

The ensuing MIS 4 and MIS 3 display some spatial disparities in the accretion or preservation of the sediments. Clarke et al. (2003) mention continuous colluviation throughout MIS 4 and MIS 2 with increasing intensity, only interrupted by phases of slope stability and pedogenesis. In contrast, Wintle et al. (1995) stress, that there are no remains of MIS 4, until the Nqutu allomember of MIS 3. The same observation was made in this study, where the Nqutu allomember (RU1.1) is the basal layer. Considering that gully erosion processes during MIS 3 were recorded in the stratigraphy, it remains unclear, if the absence of MIS 4 sediments should be attributed to the absence of colluvial processes at that time, or a subsequent removal of possible remains. The oldest deposits from Okhombe Valley, deposited through solifluction, have been dated back to the MIS 3 age of ~42 –29 ka (Temme et al., 2008), which overlaps with the age of the Kwa Vundla allomember (RU2) at KwaThunzi.

MIS 2 with the Last Glacial Maximum is characterized through spatial variability of sedimentation patterns. At the Voordrag profile, this time span is marked by extensive colluviation and strong fluctuations, thus representing the dominant sedimentary sequence with four intermediary pedoderms (Clarke et al., 2003). Also a study by Lyons et al. (2013) report a layer dated to ~23 ka (underlying layers exist, but were not dated). In contrast, evidence of sediments from MIS 2 are absent in the strata of the Okhombe Valley (Temme et al., 2008), due to minimal precipitation and temperature at that time, according to the authors. Wintle et al. (1995) describe organic material of this age in one of their four sites near St. Paul's Mission, but its position between two older strata demands careful interpretation regarding inter-profile contamination. This age was estimated with relative chronology, but not dated, for RU 3 (Malonjeni alloformation) at KwaThunzi.
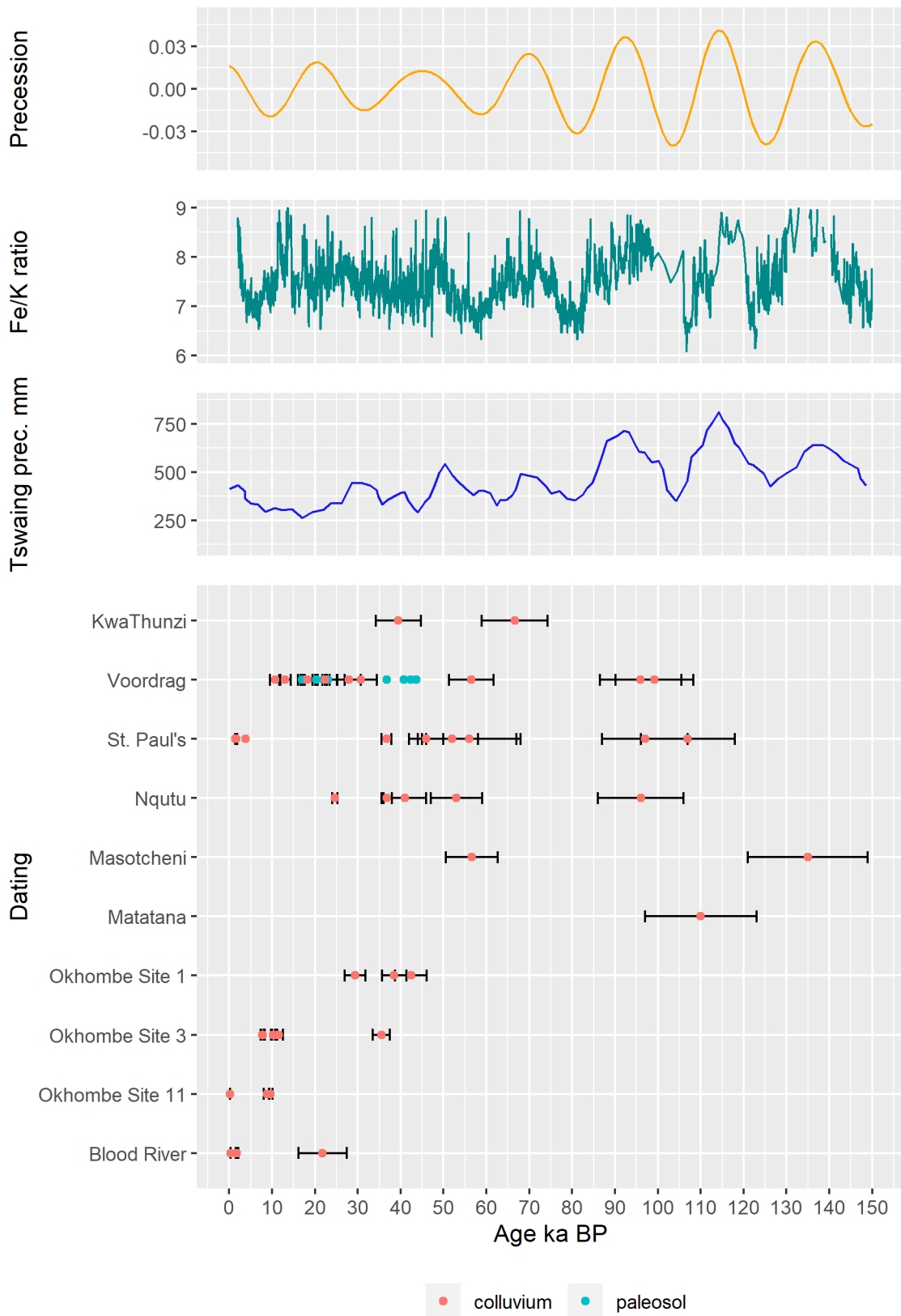
Fig. 6.14: Dates of colluvia and paleosols in KZN (Wintle et al., 1995, Clarke et al., 2003, Temme et al., 2008, Lyons et al., 2013) and paleoenvironmental records (Simon et al., 2015, Partridge et al., 1997).

Early Holocene layers, deposited in multiple phases and containing thin pedoderms, have been reported from St. Paul's Mission (Botha et al., 1994) and Voodrag (Clarke et al., 2003). Late Holocene deposits appear to be widespread, as the results from St. Pauls' Mission, Okhombe Valley and the Blood River catchment show. At Voordrag, two colluvium-pedoderm sequences overlie Early Holocene layers, but have not been dated. The uppermost RU4 falls potentially in this timespan.

6.4.3 Conclusions on landscape stability and environmental factors

First of all, it can be stated that the profile is largely consistent with other investigations of KZN's Masotcheni Fm. in three basic characteristics. First, the remains show that the balance between colluvial deposition and subsequent erosion is shifted towards net accumulation of sediment and secondly, these processes have acted one after the other in alternating ways for multiple times. Thirdly, these processes were temporarily suspended or weakened, promoting relative landscape stability and the formation of paleosoils.

The presence of Masotcheni Fm. as a widespread intact landscape element proves the former. The oldest deposits in KwaThunzi with only 66.62±7.68 ka (MIS 4) are significantly younger than the oldest layers in northern KZN, which reach MIS 5e or are even older (Wintle et al., 1995). Whether the absence of these layers is the result of extreme erosion events before the deposition of the Nqutu member, the locally absent deposition of sediment during earlier times, or the exposed location of KwaThunzi still remains an open question. A deeper insight on the erosive capacity under present-day conditions and potential effectiveness in the past is provided in chapter 7 of this thesis. Thereafter, the lack of materials predating the Nqutu member may well be the result of a short and intensive phase of gully erosion lasting only a few centuries.

The second characteristic, the alternating effectiveness of erosion and deposition, is particularly evident in the RUs and the contact surfaces that separate them. All the RUs in KwaThunzi are the result of colluvial deposition, but there are also layers of fluvial origin preserved, especially at lower elevations like Gully KwaGade close to the Umkomazi. The characteristics, especially the distinctness and topography of the layer boundaries, enable us to draw conclusions about the erosion processes. In the Hazeldene pedoderm, the clay-rich upper horizon was first redistributed along the footslope, resulting in an inverted soil profile. The wavy, undulating topography separating it from the overlying RU2, with partially infilled paleochannels also indicates the subsequent effectiveness of sheet and gully erosion before this surface was buried under the Kwa Vundla sediments. The upper boundaries of the units Kwa Vundla and Telezeni, as well as the stacked profiles within the Malonjeni member with their respective pedoderms, are both marked by a very abrupt distinctness and a planar, smooth topography with few irregularities. From this, and from the non-existence of the topsoils of these RUs, it can be concluded that effective sheet erosion completed the life cycle of these paleosols before they were covered by the subsequent sedimentation. Only the Malonjeni topsoil is still preserved and indicates weaker erosion forces after its burial.

The third characteristic, the formation of soils, not only indicates long lasting phases of landscape stability, but also provides insights into the respective environmental conditions that are responsible for the development of different soils. According to the fundamental works of Jenny (1941), soil formation is considered the result of the major factors regional climate, biota, relief, parent material and time, as well as secondary factors. Given that the relief position

remained unchanged, the parent material is composed of the detritus of the local geology and landscape stability allowed sufficient time for the processes to take effect, it can be assumed, that differences in the paleosoils of KwaThunzi are the response to changed conditions in regional climate and biota. The KwaThunzi paleosoils can be divided into two different soil types.

The development of the Hazeldene pedoderm can be placed between 66.62±7.68 ka and 39.42±5.27 ka due to the OSL dates. With its distinctive dark color and increased concentration of organic matter, it is associated with overall moist conditions. This is supported by a number of regional proxies, which indicate more humid conditions through a peak in the Fe/K ratio (Simon et al., 2015) and increased precipitation in the Tswaing record (Partridge et al., 1997) around ~50 ka (see fig. 6.14). This wet phase is also reconstructed in the Late MSA "OMOD" layer at Sibudu Cave (51.8±2.1 ka, 46.6±2.3 ka), as indicated by various environmental proxies (Wadley, 2004, Plug, 2004, Wadley et al., 2008, Bruch et al., 2012).

The younger pedoderms differ fundamentally from the Hazeldene pedoderm, most visibly by their pronounced columnar or prismatic structure. The Taxonomic System for South Africa, i.e. the regional soil classification, describes such a feature as a distinctive property of the "Estcourt Form" soil type. This consist of an orthic A-horizon on top, eventually an E-horizon and followed by the prismacutanic B-horizon. Thereafter, "this horizon accommodates the classical concept of the solodized solonetz B in which prismatic or columnar structure has" (Soil Classification Working Group, 1991). The Estcourt Form belongs to the family of Duplex soils, which are nowadays "most common in the sub-humid and drier parts of South Africa" (Fey, 2010) and prominent in the southern part of Free State, west of Lesotho. Today, these soils are absent in the Drakensberg Foothills of the Upper Umkomazi. Furthermore, Fey (2010) notes, that these "are not found where extreme chemical weathering has occurred in warm and humid climates", but in environments with sedimentary or siliceous igneous rocks that are affected by "weathering under sub-humid to semi-arid climates". Consequently, a shift to drier conditions after the deposition of the Kwa Vundla allomember can be assumed. Semi-arid conditions with high seasonality are expected in the Southern Outer Tropics at times of high orbital precession, when the summer (wet season) insolation is high and winter (dry season) insolation low, thus increasing summer precipitation and decreasing winter precipitation. After the curve of Berger (1978) depicted in fig 6.14, these orbital conditions reach their maximum around ~20 ka, during the period in question at 39.42±5.27 ka, and the Holocene. Given that the simultaneous global cooling towards the LGM reduced latent heat transfer into the interior and therefore reduced precipitation, these factors are suitable to explain the genesis observed in soil types.

6.4.4 Discussion of conceptual landscape evolution models

The Masotcheni Formation studied in KwaThunzi fits well into the composite model of landscape evolution proposed by Botha (1996). The erosion phases can be correlated by OSL dating with the phases of the net landscape instability phases. The stability phases are characterized by soil formation. Here, the soil properties derived from Hazeldene pedoderm differs from the subsequent pedoderms, indicating a shift from moist to semi-arid conditions between the formation of these soils, which is consistent with regional climate data and proxies from the Sibudu Cave.

The results further show that although the emergence of the Masotcheni Fm. can be correlated over wider areas, the local appearance of the formation may vary. Clarke et al. (2003) concluded from their observations in northern KwaZulu-Natal that temperature had a minor effect on the development because both colluviation and soils were formed in both the cold LGM and the warmer Holocene. Accordingly, the hydroclimate has a primary role, with wetter phases associated with soil formation and drier phases associated with erosion. While the humid phase around ~50 ka is linked with the formation of the Hazeldene pedoderm at KwaThunzi, the subsequent phase with drier climate is not, as expected, accompanied by erosion. Instead, typical soils for this climate with their distinct prismacutanic B-horizons developed. This leads to the assumption, that different climatic thresholds than in northern KwaZulu-Natal are probably at work, and the same climatic change affecting both regions does not lead to erosion in this environment, but to the genesis of a specific type of soil.

This leaves the question of what led to phases of landscape instability on the local scale. One hypothesis relates to changes in the hydrological system that affect hillslope processes. According to this model, stable knickpoints are able to stop the downcutting of streams and thus reduce the up-valley erosion forces that eventually destabilize slopes and promote gullying. After Temme et al. (2008), such a stationary knickpoint can potentially stop erosion and thus stimulate pedogenesis. However, several outcrops of the Masotcheni Fm. can be correlated in the Upper Umkomazi Valley (Bosino 2020), although these are influenced by different knickpoints resulting from steps in lithology and the dissection of the valley by several dikes (fig. 7.17). Because each of these knickpoints represents an independent erosion base level, it is unlikely that the erosion impulses can be synchronized over larger regions, which is necessary to have correlatable layer boundaries. Therefore, this hypothesis arguably plays a minor role in the simultaneous occurrence of erosion events in larger areas.

From the observation of the OSL dating it is evident that the deposition of colluvia takes place temporally after a precession maximum with a declining tendency. Accordingly, the seasonal distribution of insolation and thus of the hydroclimate changes in this phase. With December insolation, water availability also decreases due to reduced latent heat flux in the rainy season. At the same time, June insolation increases, thus amplifying the dry season conditions. In the long term, this leads to a more balanced climate throughout the year, characterized by lower total precipitation, but more evenly distributed throughout the year, because of reduced rainy season precipitation and increased precipitation in the shorter dry season. This aspect is not apparent from the commonly used climate data, i.e. Partridge et al. (1997), since they only reflect the annual totals of precipitation, but not its seasonal distribution. Such transitional phases, which also prevailed during the colluvial deposition in KwaThunzi, are characterized by short-term extreme climatic fluctuations. Later on, towards the LGM, global cooling replaced precession as the primary driving factor accompanied by short termed climatic extreme events. Accordingly, the increased climate variability stimulated by the change in global forcing can be considered as an alternative factor for landscape instability in the Upper Umkomazi catchment.

6.4.5 Relevance for early humans and archaeological research

The underscored value of the Masotcheni Fm. for archaeological science lies in its outsider role. The most important Late Pleistocene sites in the wider region, such as Sibudu Cave, Border Cave, Umhlatuzana Rock Shelter, Umbeli Belli and Rose Cottage Cave, are all, as the name suggests, caves or abris. They offer special conditions for conserving deposits and preserving finds

together with their context. Open air sites often do not offer these advantages because finds are destroyed and displaced by erosion, or surface finds do not offer a geologic horizon that provides important context. The Masotcheni Fm. is an exception to this rule. Its geological layers can be regionally correlated, they allow dating of the finds, and they contain a wealth of environmental proxies. Furthermore, gully erosion exposes the profiles and makes them easily accessible.

The close association of archaeological finds with the Masotcheni Fm. was documented early on. In the first scientific investigations, attempts were made to use lithic artifacts in the manner of index fossils, to derive a cultural chronology of the formation (Lebzelter, 1926, Davies, 1949, Davies, 1951). According to Botha (1996), the spectrum of archaeological finds ranges from the ESA to the LSA. Especially the region north of Nqutu, the Jojosi donga complex, is considered a hotspot for ESA artifacts, where artifacts were found in buried 'knapping floors' with thousands of flakes, as excavated by Dr. A. Mazel of the Natal Museum. Some lithic artefacts were exposed at KwaThunzi and are now to be found in the collection of the Natal Museum.

Furthermore, it is of course intriguing which impact the landscape changes, that are preserved in the Masotcheni Fm. layers, had on early human populations. The phase of landscape instability, that led to the accumulation of the Nqutu allomember overlaps with the age of the Howiesons Poort technocomplex, which is characterized at Klipdrift Shelter (Reynard et al., 2016) and Sibudu Cave (Clark, 2017) by a fluctuating environment with shifts from grazing to browsing herbivores. In the same time span, human diets shifted to small prey animals (Clark and Kandel, 2013) and technological inventions like bow and arrow were made (Wadley, 2015). But also the next phase of landscape instability, responsible for the accretion of the Kwa Vundla alloformation, is associated with a an important archaeological date. Around ~46-43 ka the Early LSA is introduced at Border Cave and is dispersed across the region over the following 25 ka (Bousman and Brink, 2018). This raises the question, if such phases of landscape instability challenged human populations to adapt to changed environment through innovation and increased behavioral flexibility. The link between evolutionary theory and environmental forcing is still a subject of vivid debate in the context of the South African MSA.

Phases of landscape stability, like the one that formed Hazeldene pedoderm presumably in the first half of MIS 3, are marked by growing human occupation, if the regional characteristics of the Southern Cape are left aside (Wadley, 2015). Many assemblages of this time, Klein Kliphuis, Diepkloof, Klasies River, Border Cave, Rose Cottage Cave, Umhlatuzana and Sibudu Cave feature (often unifacially retouched) points (Wurz, 2013, Wurz, 2019). The Upper Umkomazi Valley lies in the middle between the last three of this listing, and thus it can be assumed that the area, with the nearby passes (e.g. Sani Pass) over the Great Escarpment, is part of a transit route that led to the exchange of people and technologies. As finds from Sibudu Cave suggest, this period is marked by demographic continuity and that "innovations from neighboring groups may have spread to the occupants of Sibudu via social and economic interaction" (Conard and Will, 2015).

Chapter 7: Recent Gully Erosion

This chapter addresses Q5: gully erosion phenomena related to the Masotcheni Formation. Since erosion marks the phases of landscape instability in the profile of KwaThunzi, its effectiveness will be further examined here. Therefore, the development of the gully was investigated with two methods in order to be able to draw conclusions about the onset and the velocity of gully erosion as well as possible environmental or anthropogenic drivers (chapter 7.1.1).

The development of the gully was examined on a historical timescale (chapter 7.2.3). For this purpose, 3D models were created from current (2018) and historical (early 1940s) aerial imagery and compared to estimate current growth rates. While the modern models could be processed straight forward (chapter 7.2.1), many solutions had to be found for the historical data to (a) reconstruct the sensor geometry of the no longer existing device and (b) develop customized post-processing algorithms to minimize model errors (chapter 7.2.2.4).

7.1 State of research

7.1.1 Regional conceptual models of gully erosion

Gully or Donga erosion in Southern Africa is widely described in a context with quaternary colluvial mantles and especially with the Masotcheni Formation. Extensive gully erosion is made responsible for the absence of quaternary colluvial material pre-dating the LIG and, as Clarke et al. (2003) suggest, contemporaneous gullying is likely to erase large parts of the recently observable colluvia. During the last glacial period, gullies have repeatedly and episodically eroded the beforehand deposited material (Botha et al., 1994) and thus created hiatuses in these sedimentological archives (Botha et al., 2016). Some sites however show better preservation, e.g. at the Voordrag Gully, where Clarke et al. (2003) stress explicitly, that incision occurred in a single event. Lyons et al. (2013) dated colluvia and fans in the Upper Blood River catchment, which are associated with incising gullies. Their results constitute net accretion of colluvial material until ~1.6 ka, followed by gully erosion initiation and fan deposition from ~0.89 ka onward. Also the evidence of dated wood (170±45 a) in residual gully fills, suggest that erosion emerged mainly "within the past few centuries" (Botha et al., 1994).

Tab. 7.1: Factors affecting gully formation as categorized by the FAO (Geyik, 1986).

	Natural factors		Man-made factors
1	Precipitation	**1**	Improper land use
1a	Monthly distribution	**2**	Forest and grass fires
1b	Intensity and runoff	**3**	Overgrazing
1c	Rapid snowmelts	**4**	Mining
2	Topography	**5**	Road construction
2a	shape of catchment	**6**	Livestock and vehicle trails
2b	size of catchment	**7**	Destructive logging
2c	Length and gradient of slope		
3	Soil Properties		
4	Vegetative cover		

This leads to the question of what provoked the widespread gully erosion we observe today, even in those sites, that apparently have been unaffected by late quaternary incision. These can be of natural or man-made origin. The FAO provides a list (tab. 7.1) with several factors of natural or anthropogenic origin, which promote gully incision (Geyik, 1986). Most of these factors are observable in the field or have been documented in regional scientific publications. This section ought to demonstrate, which factors gave favorable conditions for erosion at different times.

A geological control on gully formation has been observed by Tooth et al. (2004) in the Highveld region. When rivers incise and lower their stream, this affects the whole fluvial system, as the tributaries readjust to the new base level. Local knickpoints migrate headwards through the branches of the network and facilitate gully erosion, especially in areas directly connected to the main stream. In low lying alluvium and colluvium, the desiccation of the former floodplain, coupled with the knickpoint migration, increases erodibility, eventually provoking bank gully erosion (Vandekerckhove et al., 2000). These geologically induced gully mechanics imply spatial and temporal asynchrony of gully initiation. Stream base level lowering is retarded, for example through geomorphological barriers, such as the abundant dolerite dikes in the Drakensberg. Therefore, neighboring catchments may react differently on the same climatic influence by temporarily lagged incision. Furthermore, gullying within one catchment may vary, depending on the position of the knickpoint. This promotes gullying in the lower catchments, downstream of the knickpoint, whereas the upper catchment remains unaffected.

But also climatic factors and especially fluctuations within the last millennium are considered a trigger for the initiation of gully erosion (fig. 7.1). Short termed and abrupt climatic variations are capable of damaging vegetation, that forms the protective cover of the colluvial deposits. Abnormal long dry periods, intense rainfalls or even the combination of both, are capable to destabilize land and thus provoke erosion. Two prominent climatic anomalies fall into the last millennium, that affected hydrology, vegetation and fluvial systems in Southeast Africa or even globally (Holmgren et al., 2003, Lyons et al., 2013). The Medieval Climate Anomaly (MCA) is suspected to originate from indirect variations in solar activity and dominated the beginning of the millennium around (AD 900–1200). It is characterized by high variability of multiple climatic proxies and an increased presence of C4 plants, indicating higher temperatures in the region (Norström et al., 2018). The Little Ice Age (LIA, AD 1300-1800) shows some regional variations with increased moisture in the Lesotho Highlands (Norström et al., 2018) and cooler and drier conditions than present in the coastal lowlands of Mozambique (Ekblom, 2008, Tyson, 1999, Tyson et al., 2000). Considering the impact on hydrological systems, the LIA is attributed with an increased number of large floods with a particularly high frequency in the beginning (AD 1390–1425) and the end (AD 1800–1825) of the millennium. This is explained through changes in the atmospheric circulation pattern (Benito et al., 2011, Zawada et al., 1996, Smith, 1991).

Finally, also anthropogenic influence, or as Botha et al. (1994) coins it, "the escalation of agricultural, pastoral and Iron Age industrial practices during the past 1000 years" is made responsible for gully initiation. Iron age populations are known to have inhabited the region for about 2000 years (Badenhorst, 2010). In the Early Iron Age (AD 200–900), Bantu practiced agriculture in KZN until being replaced by Khoisan pastoralists in the Late Iron Age (AD 1300–1840) (Huffman, 1982, Huffman, 2007). This land use change is contemporaneous with the aforementioned shift from the generally warmer and agriculturally favorable MCA to the moister

and cooler LIA. Lyons et al. (2013) mention a possible impact of overgrazing, which is accompanied by increasing erosion susceptibility and gully incision. Also Marker and Evers (1976) consider Iron Age land use change as triggering or amplifying factor for erosion, alongside increased population density in interaction with environmental factors. Subsequently, Late Iron Age Bantu spread over KZN in the 15th century (Bruton et al., 1980), who cultivated a lifestyle of massive wood consumption for housing, heating, cooking or iron production, thus degrading the natural forests considerably (Neumann et al., 2008, Neumann et al., 2010). By the second half of the 18th century, another shift towards intensive farming brought by European settlers is suspected to have reinforced gullying (Watson, 1996, Hoffman and Todd, 2000, McCarthy et al., 2011, Lyons et al., 2013, Tooth et al., 2013).
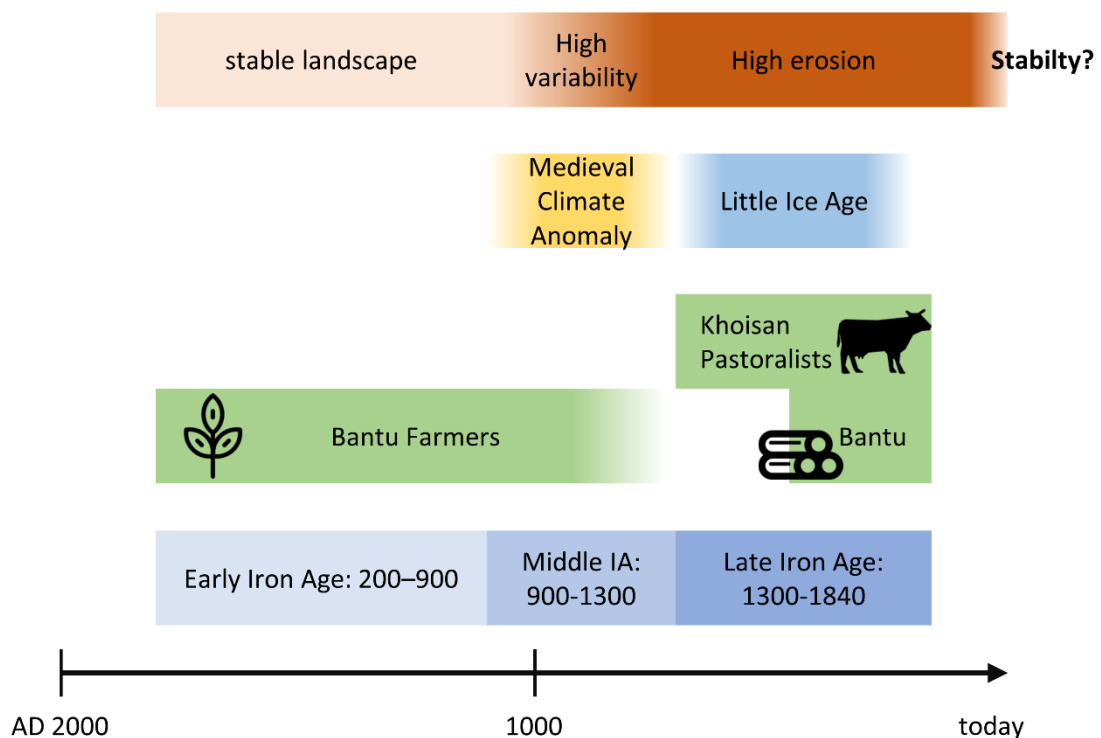
Fig. 7.1: Summary of settlement phases, land use practices, climatic influences and the resulting landscape (in)stability.

Märker (2001) describes another major land use change that affected the region of the Upper Umkomazi basin between the beginning of the 20th century and the 1970s. During this period, the area was managed by cattle farms and used as pasture. By the end of this period, these farms were abandoned and the fields became common pasture. Thereafter, the local population increased numbers of livestock and a change of the composition towards a higher number towards goats. Consequently, this produced overgrazing, so that land use became increasingly unsustainable and intensified erosion.

Another more recent anthropogenic influence that is known to provoke gully erosion is the construction of road cuts (Seutloali and Beckedahl, 2015, Seutloali et al., 2016).

7.2. Methods and Data

Historical aerial and recent UAV-borne imagery was used to create DEMs and orthophotos of gully KwaThunzi and its surroundings with the Structure-From-Motion (SfM) method. However, two different approaches were applied, to get the best possible results of the very diverse raw data.

7.2.1. UAV Mapping

The images were acquired in the field campaign on 2018-01-13 with a custom made unmanned aerial vehicle (UAV) carrying a downward facing Canon PowerShot S110 camera. The camera was modified with a CHDK script, which allows to automate camera actions. The predefined flight route was conducted autonomously and covered the entire subcatchment of the gully at an elevation of ~55 m above ground level. This resulted in an estimated swath width of 79 m by 59 m and a ground pixel resolution of 3.9 cm. Through the definition of parallel flight axes, a mean sidelap of 58.2% was achieved. The camera was triggered in intervals of < 2 s in response to the flight speed, thus generating a mean overlap of 76.0% between images. The camera had a fixed shutter speed of 1/1000 s and the aperture was specified to f/3.2. Accordingly, ISO was adjusted by the internal camera software to the local lighting conditions and ranges between ISO 160 and 400. This setting allowed a reasonable trade-off between flight speed and image quality. The entire flight mission lasted 21 min and produced 464 images.
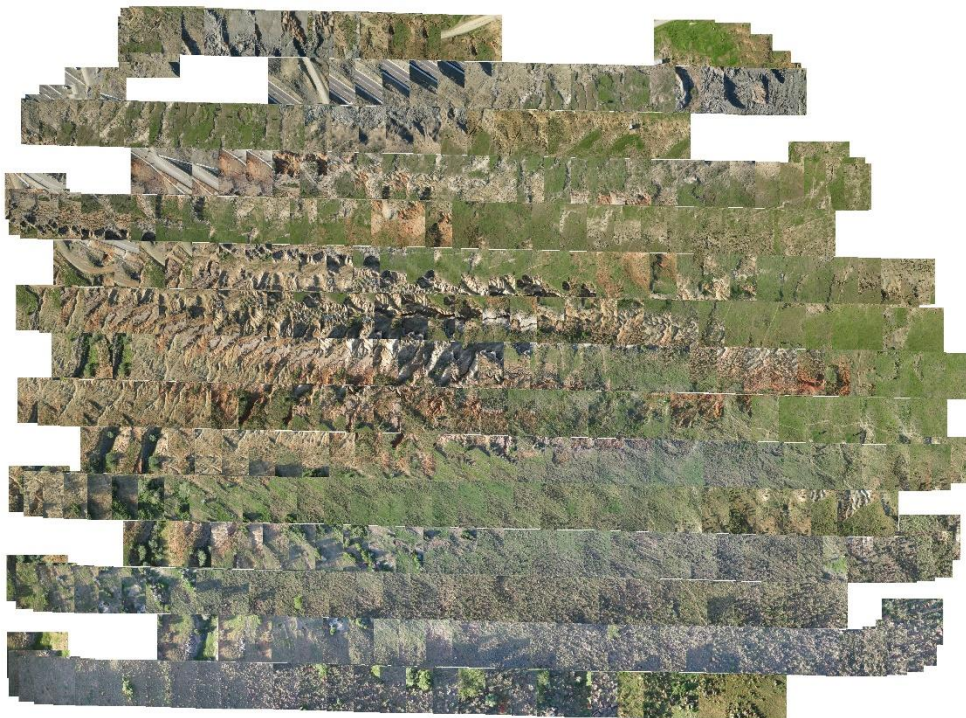
Fig. 7.2: UAV images aligned by image location and orientation.

Pre-processing and 3D processing were conducted with the software "BitMapping" by Mavis (v.17.09.00). First, the images were tagged with the GPS positions of the sensor and inertial navigation system (INS) data of the UAV. Datasets with inapt imaging geometries (yaw, pitch and roll), which resulted from turbulences during flight, were removed through a threshold. With the

image location and orientation information, the datasets were aligned, as shown in figure 7.2. The majority of images has an overlap with 10 or more neighboring images.

Orthomosaic

Digital elevation model
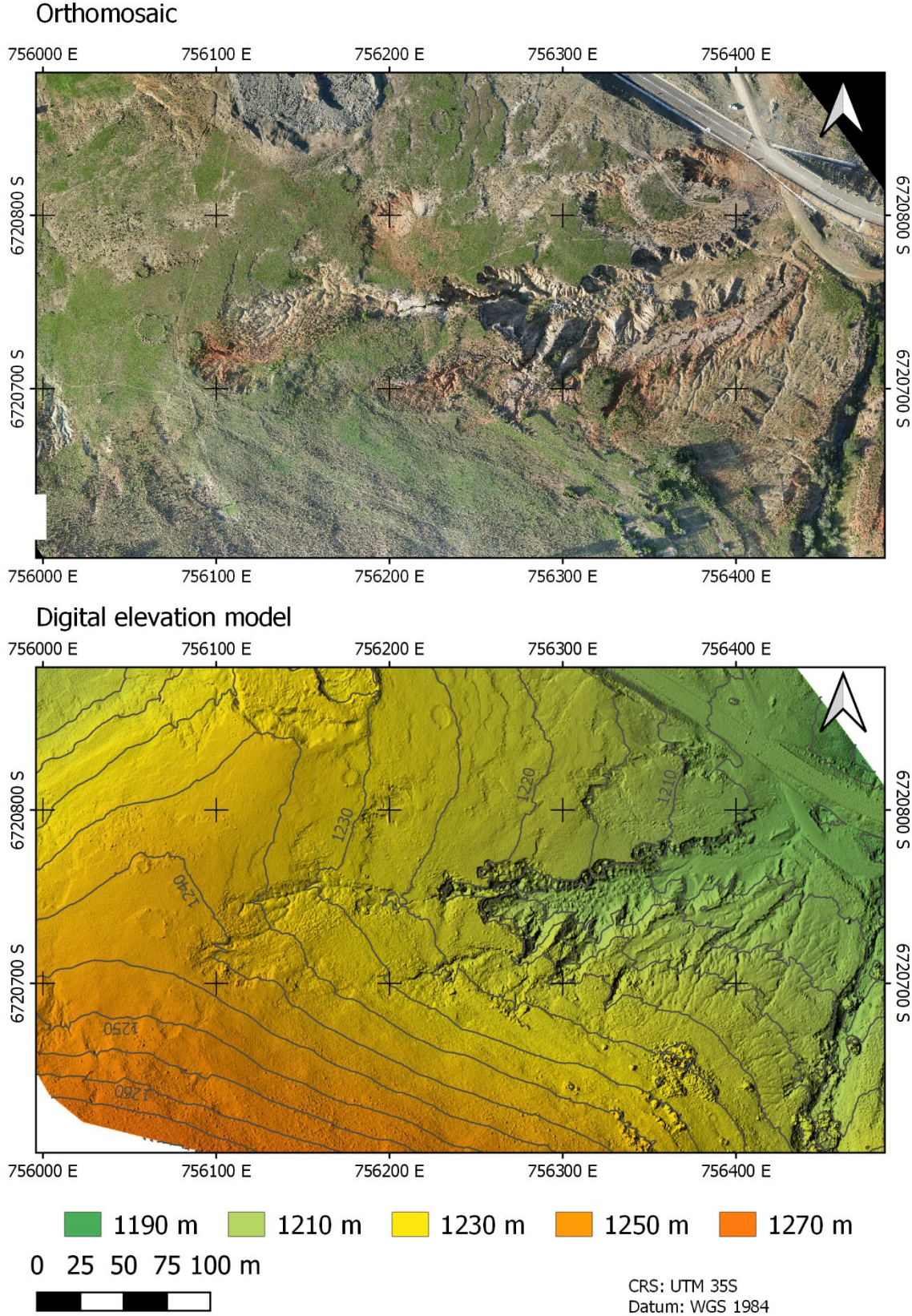
Fig. 7.3: Orthomosaic and DEM of gully KwaThunzi as results of the UAV based 3D mapping.

The 3D processing software by Mavis is based on the photogrammetry software MicMac, which is developed by the French National Geographic Institute (IGN) and the French National School for Geographic Sciences (ENSG) and available under a free and open source license (Rupnik et al., 2017). Besides a range of applications in archaeology and heritage conservation, this method has also been used in the context of landscape processes monitoring, e.g. fluvial morphology (Stumpf et al., 2016), landslide monitoring (Stumpf et al., 2015, Stumpf et al., 2017) and tectonic deformation experiments (Galland et al., 2016). The images were camera-calibrated and a depth map was computed. Thus, a tie point cloud was generated and transformed to a gridded DEM with a resolution of 10 cm. This was also used as basis for the creation of an orthomosaic with a resolution of 5.5 cm. These results are depicted in figure 7.3.

7.2.2 Historical Aerial Images

In order to study past morphological evolution of the Upper Umkomazi, digital reference data from the earliest days of photogrammetric surveying were used as a comparison to the modern topography. An example featuring the position of gully KwaThunzi is presented in figure 7.4. The historical aerial imagery was recorded by the Trig Survey (today: National Geo-spatial Information) on the flight track No. 471 between 1940 and 1945 (NGI, 2019). These are nearly parallel airborne photographs with an overlap of ~60%. The images were obtained from the file record of the Pietermaritzburg Department of the Council for Geoscience. The physical copies were digitized with a resolution of 1200 pixels per inch and a pixel depth of 8 bit greyscale by using a 20-micron image scanner. Images with lower resolution, like those freely available from a digitizing campaign of Chief Surveyor General, showed to be unsuitable for SFM. The image editor software Gimp 2.10.14 was then used to crop the scanned images to the same size at pixel-accuracy (The GIMP Development Team, 2019). Following, the rotation of the images was corrected, so that the upper boundary of the image frame was precisely horizontal. This pre-processing requires careful manual work, but paid off through the considerably increased quality of the sensor calibration.
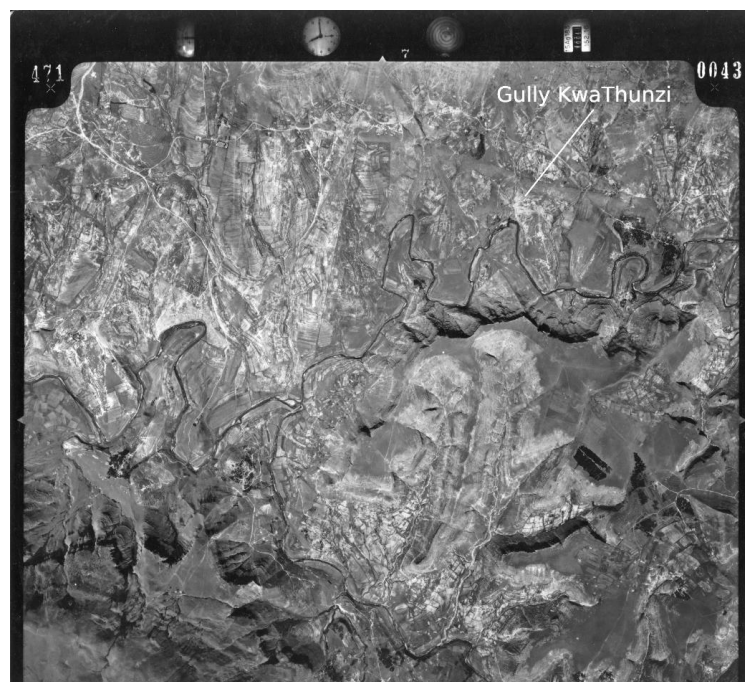
Fig. 7.4: Historical orthophoto from the flight campaign 1940-45. Up is South.

The raw images were aligned with the software "AgiSoft Photoscan" v.1.4.5 (AgiSoft, 2019), which relies on the SIFT algorithm for feature detection (Lowe, 1999). The number of key and tie points was restricted to 40 000 and 4 000 respectively, to reduce the number of unreliable matches between the images. The files were aligned at native resolution, because the images were scanned with an effective resolution of 62 cm, which already includes a gentle upscaling of the 1 m original resolution, thus rendering further upscaling unnecessary. Downscaling was not taken into consideration, since processing time hardly affected the procedure.

7.2.2.1 Sensor calibration

The first two components of the SfM procedure, i.e. reconstruction of 3D scene structure and extrinsic camera calibration (sensor position and orientation), were performed with "AgiSoft Photoscan". The third component, intrinsic sensor calibration, was computed with the tool Lens from the same software package. A sensor's optical properties are represented through the parameters focal length (f), coordinates of principal point (cx, cy), affinity and skew (b), coefficients of radial distortion (k) and tangential distortion (p). Since the original camera is not available, these variables had to be estimated from the residuals of the aligned images with the following procedure.

The focal length of the surveying camera is known to lie at 177.5 mm and the image scale is 1:20000, resulting in a ground resolution of 1 m in the original images (Grellier et al., 2012). With a digitized ground resolution of 62 cm, the focal length can be expressed as f = 0.28629 px. These parameters were fixed and the calibration tool was used to optimize the other parameters. The best results were produced with the principal points at cx=-13.9256 and cy=659.72, where the optical axis of the image intersects the image plane. The radial distortion can be expressed with k1= 0.000196311 and k2= 0.00477415. Skewness was not estimated, because square pixels were assumed (b=0) and also tangential distortion could be discarded (Carrivick et al., 2016). A graphic representation of the reconstructed lens distortion, derived from this equation, is presented in figure 7.5. The residuals lie around 3 px (horizontal: 2.36875 px, vertical: 3.71402 px).

396 pix
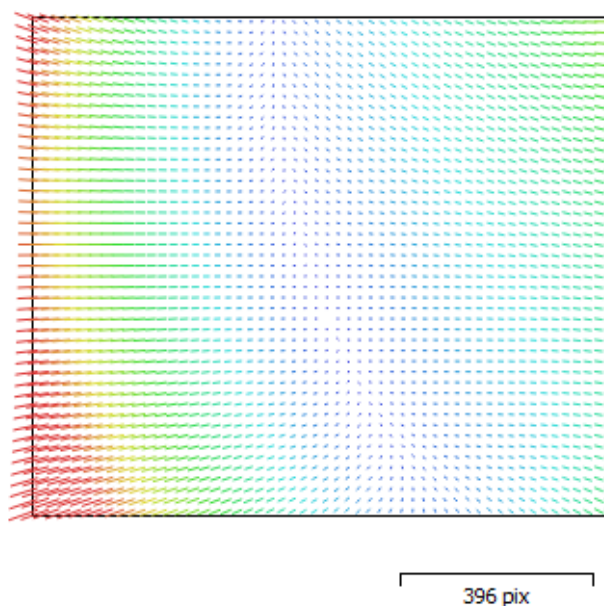
Fig. 7.5: Distortion plot of the lens as calibrated from aligned images.

7.2.2.2 Dense point cloud generation

The calibrated cameras were used to calculate elevation information from the images and combine them to a single dense point cloud. The quality of a resulting point cloud is primarily controlled by the parameters "quality" and "depth filtering mode". The first is a measure of the level of detail of the resulting point cloud and controlled by downscaling of the original images before depth calculation. However, the higher the number of calculated points, the higher is the number of outliers or errors, due to noise, focus or other factors affecting the image. Depth filtering is a method to detect these inapt points and thus, increase quality. Mild filtering preserves detail but also errors, while aggressive filtering reduces errors but also erases details. A number of combinations of these parameters was applied to find the best results, which are displayed in tab. 7.2. The effects of the combinations are irrelevant for the orthomosaic generation. The resolution with Ultra settings (i.e. no downscaling) appears to be highest, however this exceeds the resolution of the physical input data, and is therefore rather an effect of over-matching. After visual interpretation, the combination of High quality (i.e. downscaling factor 2) and aggressive filter produced the best results with lowest image noise.

Tab. 7.2: Results of different parameters of dense point calculation.

Dense cloud quality	Depth filtering	Tie points	Dense points	DEM resolution	Orthomosaic resolution
Medium	Aggressive	4 919	9 089 758	3.35 m/px	83.9 m/px
High	Moderate	4 919	29 788 519	1.68 m/px	83.8 m/px
High	Aggressive	4 919	31 758 633	1.68 m/px	83.9 m/px
Ultra	Aggressive	4 919	103 252 567	84.2 m/px	84.2 m/px

7.2.2.3 Georeferencing

Ground Control Points (GCPs) were collected from georeferenced satellite imagery and D-GPS measurements (fig. 7.6).
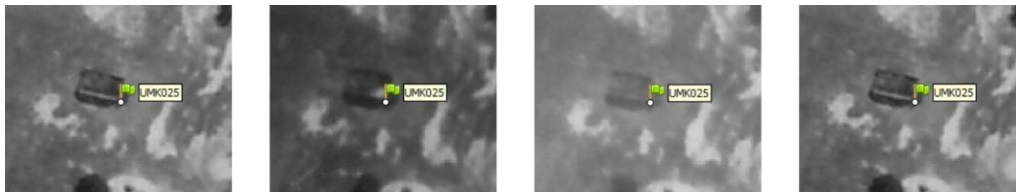
Fig. 7.6: A GCP, located on the corner of an abandoned farmhouse, from four images and perspectives (images 9930, 9931, 9942, 9943).

Although a minimum number of 3 GCPs per image is adequate for photogrammetry and the same number is sufficient for point clouds from SfM, a higher number leads to improved model accuracy in mountainous environments (Javernick et al., 2014, Mölg and Bolch, 2017). Location information for the georeferencing process in this study was provided through 66 GCPs, that were partly collected from D-GPS measurements with a high accuracy of ~20 cm, and GCPs collected from the Google Earth Map Service with considerably lower accuracy. Penalties were inflicted for the more unprecise digitized GCPs, to compensate their weight on the georeferencing model. The selection of GCPs was rather complicated, because persistent markers are sparse in this area: permanent roads did not exist in the 1940s and only few path crossings are still recognizable; Zulu settlements appear to be agile and no stable buildings could be used in these areas; Especially ruins and bridge fundaments outside the growing

municipalities, turned out to serve as adequate markers (fig. 7.6). The stable GCPs are spread evenly across the images and cover the full range of elevations, from valley bottoms to mountain tops (7.7).
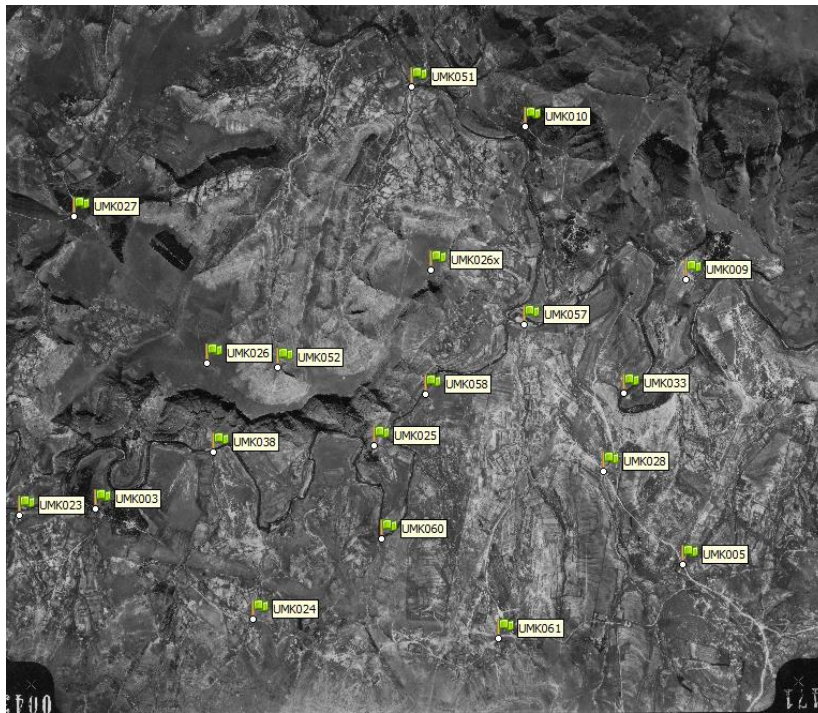
Fig. 7.7: Image with Ground Control Points.

Finally, the georeferenced dense point cloud was clipped to the area of interest and regions with low quality were deleted. After a Delaunay triangulation, a DEM with 1.68 m resolution was exported, as well as the orthophoto with 84 cm resolution.

7.2.2.4 Post-processing

An accuracy assessment of the resulting DEM was carried out with the TanDEM-X DEM, which is known for its high vertical accuracy of ~3 m. The correlation between both datasets was high, however an absolute vertical mean error of 26.24 m was still included. Furthermore, this error was found to follow an altitudinal and spatial pattern.

In order to correct the error in the post-processing, elevation information of both datasets was collected from 2500 randomly distributed sample points. This revealed, that low points, e.g. valley bottoms, were estimated too low, while high points, e.g. mountain tops, were overestimated. After fitting a linear regression with the statistics library CRAN, results show that the altitudinal error includes an offset of 186.8 m and a linear stretching factor of ~0.855, which can be expressed in equation 7.1:

$$Z_{cor} = 0.8553505 \cdot Z_{mod} + 186.8035 + Z_{res} \qquad\qquad \text{eq. 7.1}$$

with
Z_{cor} = corrected elevation
Z_{mod} = uncorrected, modelled elevation
Z_{res} = residuals of elevation

The remaining residuals showed an additional spatial trend, with underestimation in larger parts of the northern DEM, and an overestimation of elevations in the South. The central DEM had lowest residuals.
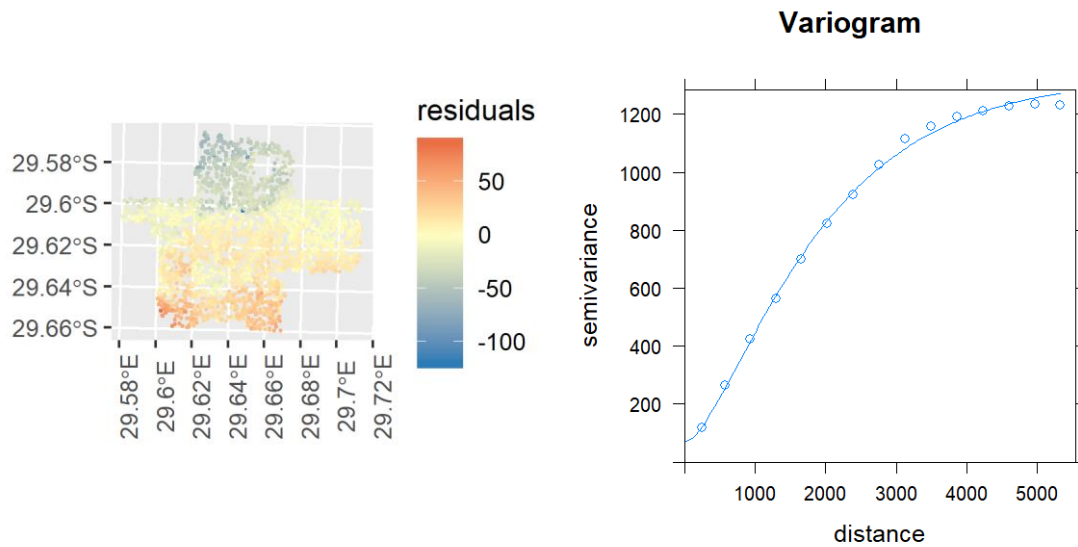
Fig. 7.8: Residuals of the vertical error after the linear correction follow a spatial trend. Left: Spatial distribution of the residuals with a latitudinal gradient. Right: Spatial autocorrelation of the residuals expressed in a semi-variogram (Model: Bessel, nugget: 69.4, sill: 1257.7, range: 1286.6).

A correction surface was constructed to compensate this error distribution with the geostatistical tools in the "gstat" package of the CRAN library (Pebesma, 2004). With the semi-variogram, shown in figure 7.8, an ellipsoidal function of the Bessel form could be derived, which allows to produce such a function using Kriging (fig. 7.9). Note that the high variance in the corners of the prediction in figure 7.9 is meaningless, because the modelled DEM does not cover these areas.
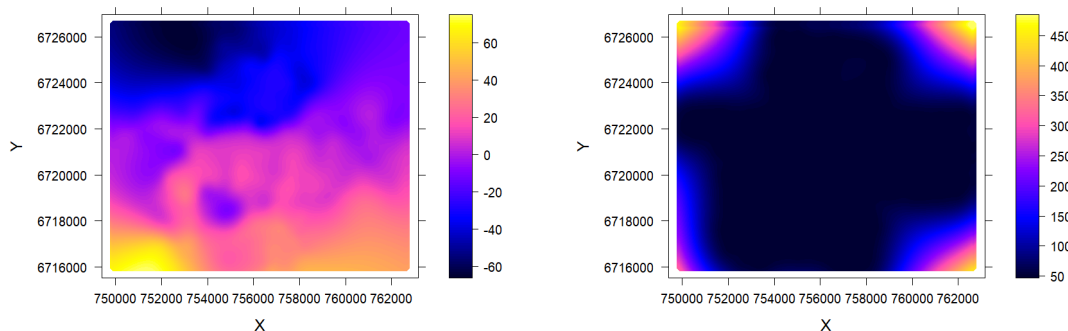
Fig. 7.9: A correction function through Kriging to minimize the spatially autocorrelated residuals. Left: Predicted correction surface, which is later subtracted from the SfM model. Right: Variance of the prediction.

By applying both the function for linear altitudinal correction and the subtraction of the residual surface, the model vertical accuracy could be improved. Figure 7.10 displays the overshoot and undershoot of the uncorrected model, as well as the higher vertical accuracy in the corrected data.
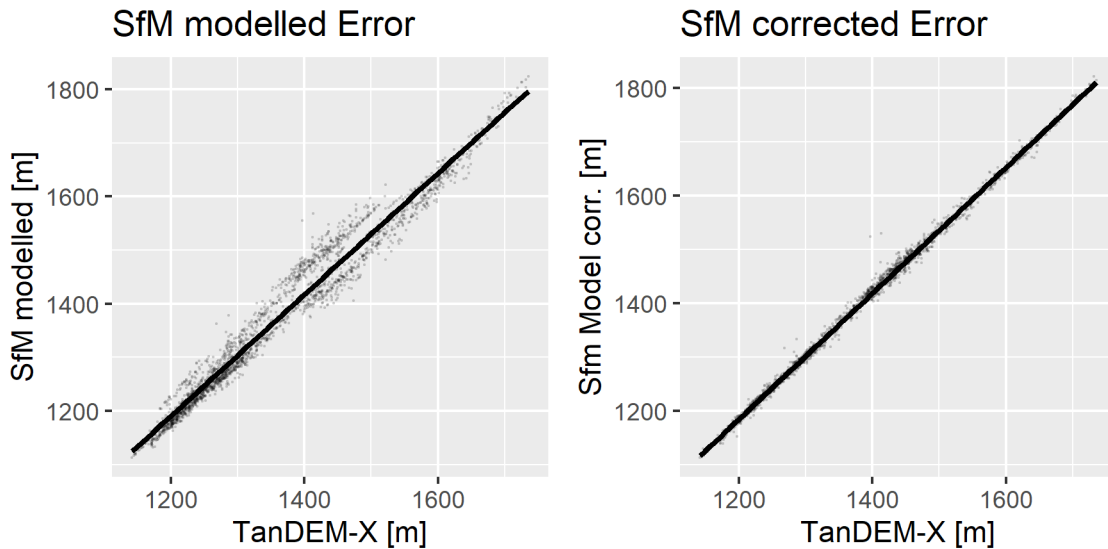
Fig. 7.10: Elevation error with the reference TanDEM-X on the x-axis and the modelled (left diagram) and corrected (right diagram) elevations on the y-axis. The diagonal line indicates a perfect matching of the model with the reference. The smaller residuals in the right diagram indicate a lower vertical error.

While the original SfM model featured a mean absolute error of 26.24 m, the correction through linear regression improved the model to 18.57 m. The additional correction through the kriged residual surface lowered the vertical error to 3.68 m, which is in the range of the vertical error of TanDEM-X. The reduction of elevation errors through these stages is presented in the histograms in figure 7.11.
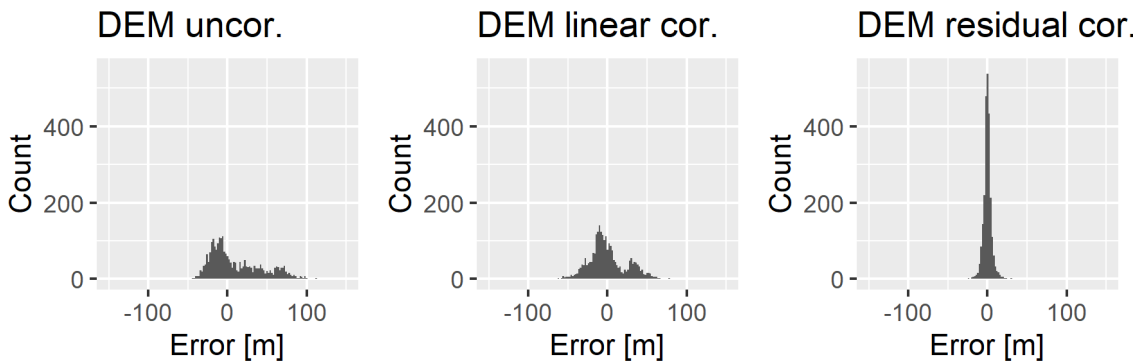
Fig. 7.11 The reduction of vertical errors, compared to Tandem-X, through the correction steps. Left: Vertical error of the uncorrected DEM. Middle: Vertical Error after the linear correction. Right: Vertical error after the application of the kriged correction surface.

Consequently, the corrected DEM combines the high vertical accuracy of the TanDEM-X DEM with the high spatial detail of the photogrammetric model. The results are presented in figure 7.12.
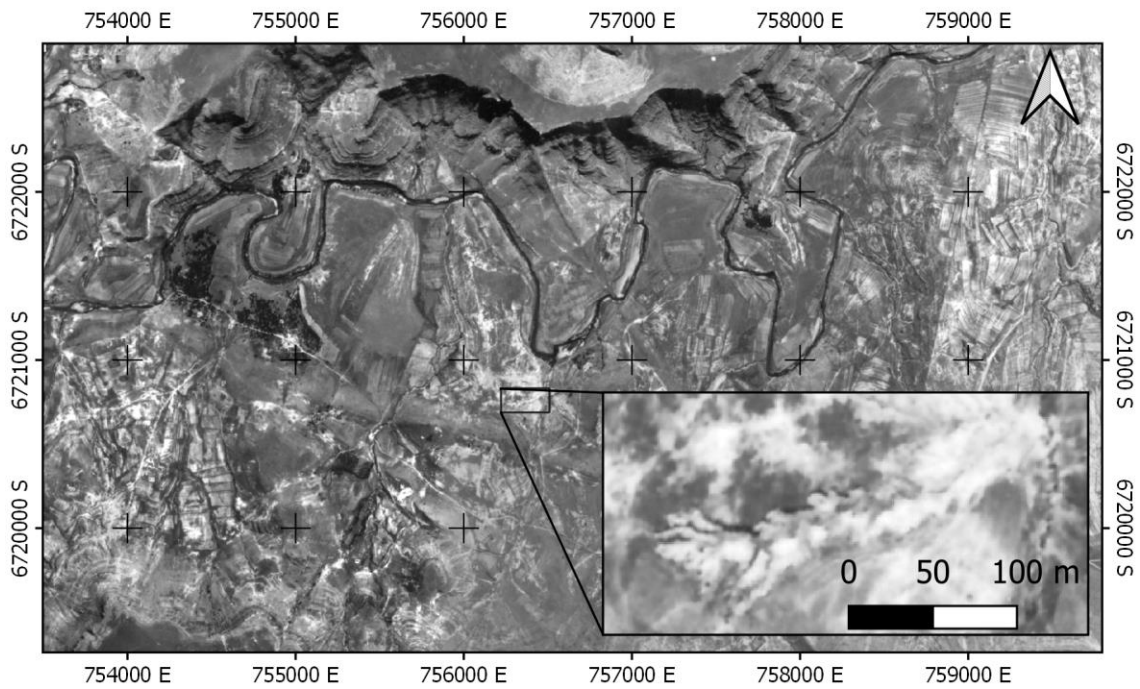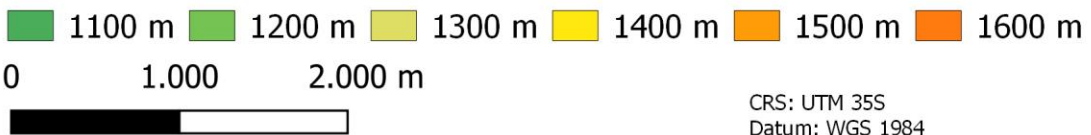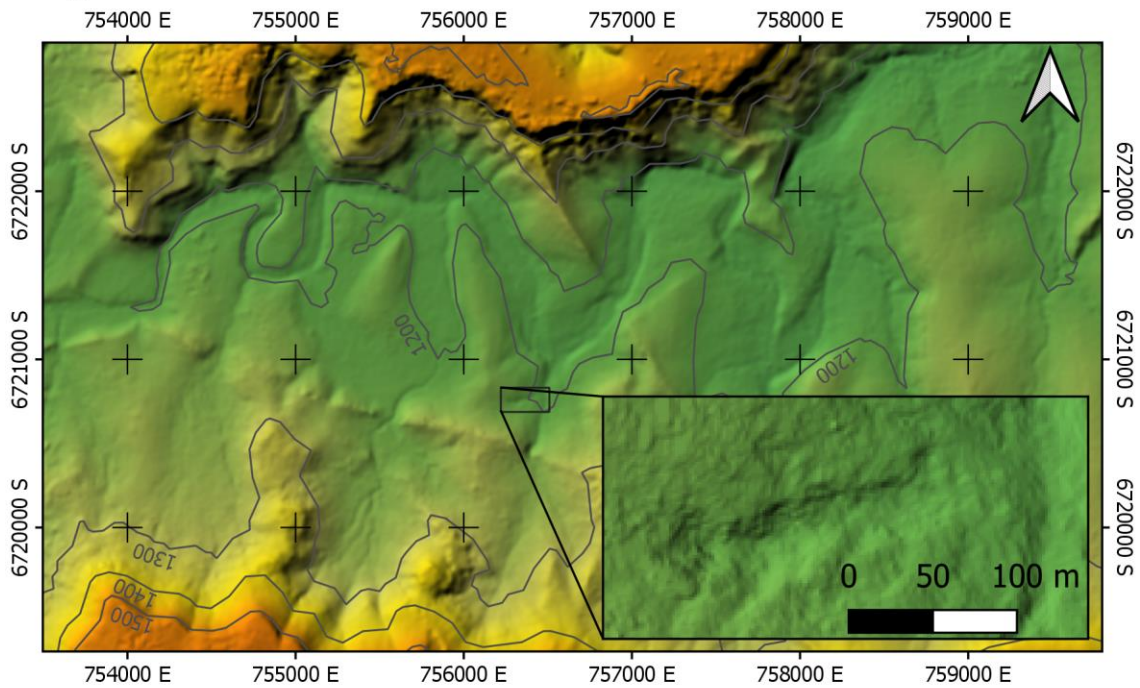
Fig. 7.12: Results of the 3D modelling of historical aerial images of the Umkomazi with a detail view of Gully KwaThunzi.

7.3. Results

7.3.1 Gully classification

Three classification systems for gully erosion are utilized by the FAO, which are based on the characteristics size, shape and continuation. Following the classification system based on size parameters (tab. 7.3) by Schwab et al. (2002), the values for gully depth and drainage area were derived from the UAV DEM with 10 cm resolution (chapter 7.2.1).

Tab. 7.3: FAO gully classification based on size (Geyik, 1986, Schwab et al., 2002)

Gully class	Gully depth [m]	Gully drainage area [ha]
Small gully	<1	<2
Medium gully	1–5	2–20
Large gully	>5	>20
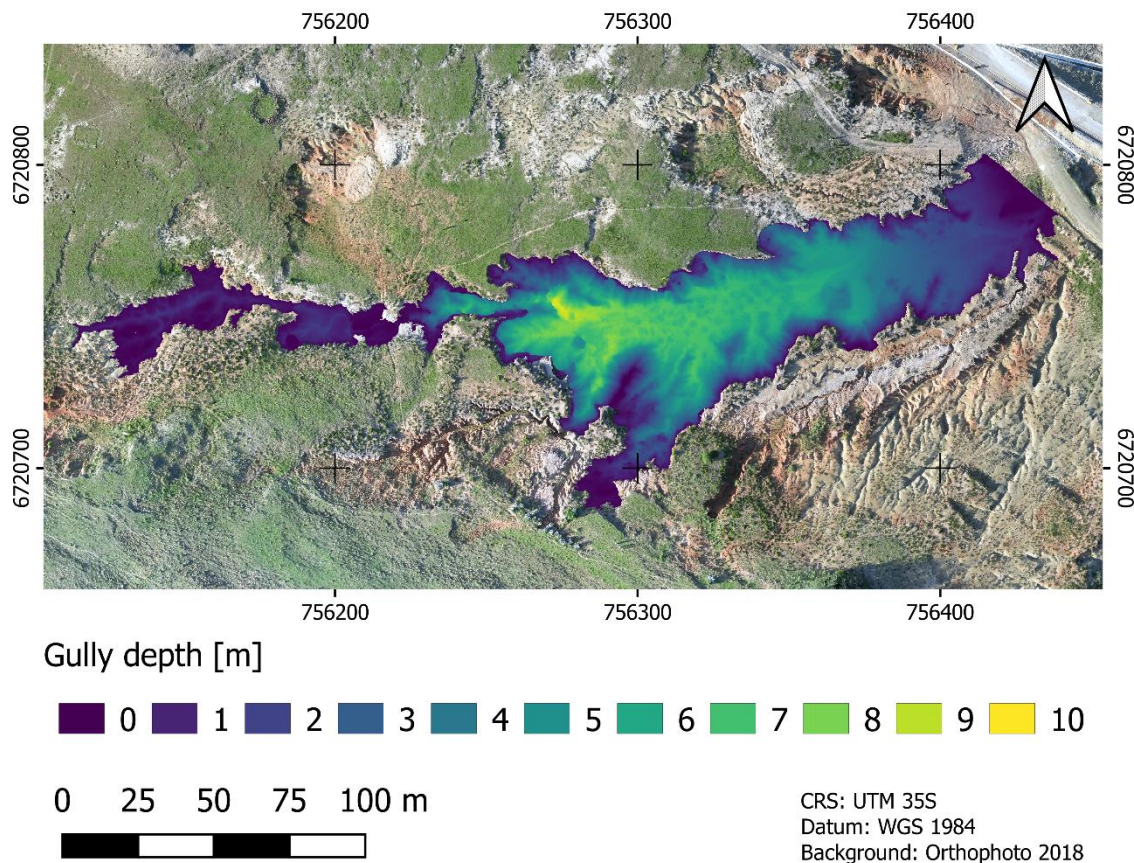
Fig. 7.13: Depth of Gully KwaThunzi derived from a differential infilled DEM (10cm) from 2018.

Drainage area (fig. 7.15) was calculated with the "Terrain Analysis Toolbox" in "SAGA GIS" (Conrad et al., 2015). The depth values were estimated by calculating a differential DEM, through the division of the actual gully DEM with a virtually filled counterpart, where the unaffected gully margins were interpolated. The resulting gully depth is depicted in figure 7.13. Following the classification, Gully KwaThunzi can be described as a *medium gully*, since its mean depth lies around 3.2 m and the area of its drainage system covers ~9.3 ha. If only the lower, well developed part is considered, the gully depth, reaching more to 9 m, can also be labelled as large (tab. 7.4).

Tab. 7.4: Size properties of Gully KwaThunzi derived from the DEM and differential DEM

Catchment area	83 161 m^2
Gully area	9 396 m^2
Mean depth	3.24 m
Standard deviation of depth	2.31 m
Maximal depth	9.58 m
Gully volume	30 355.56 m^3

The second FAO classification method relies on the shape of the gully cross-section, as first proposed by Weidelt (1976), and differentiates between

- U-shaped gullies with nearly vertical side walls, which form, where the erosion resistance of topsoil and subsoil is homogeneous.
- V-shaped gullies (the most common form), where the subsoil is more resistant than the topsoil.
- Trapezoidal gullies, where topsoil and subsoil is underlain by a very resistant stratum.

Photographs of the erosion features at KwaThunzi are displayed in figure 7.16. Again, the upper and lower part of gully KwaThunzi show different characteristics. The smaller upper section of the gully displays clearly the type of a V-shaped gully, mainly incising the recent top- and subsoil. The FAO class of U-shaped branches incise in the underlying paleosols, where recent top and subsoil has been stripped off. These indicate a more homogeneous erodibility than the recent soil strata, or even a reversed erodibility sequence where the overlying stratum is more resistant, which is not considered in the FAO classification.
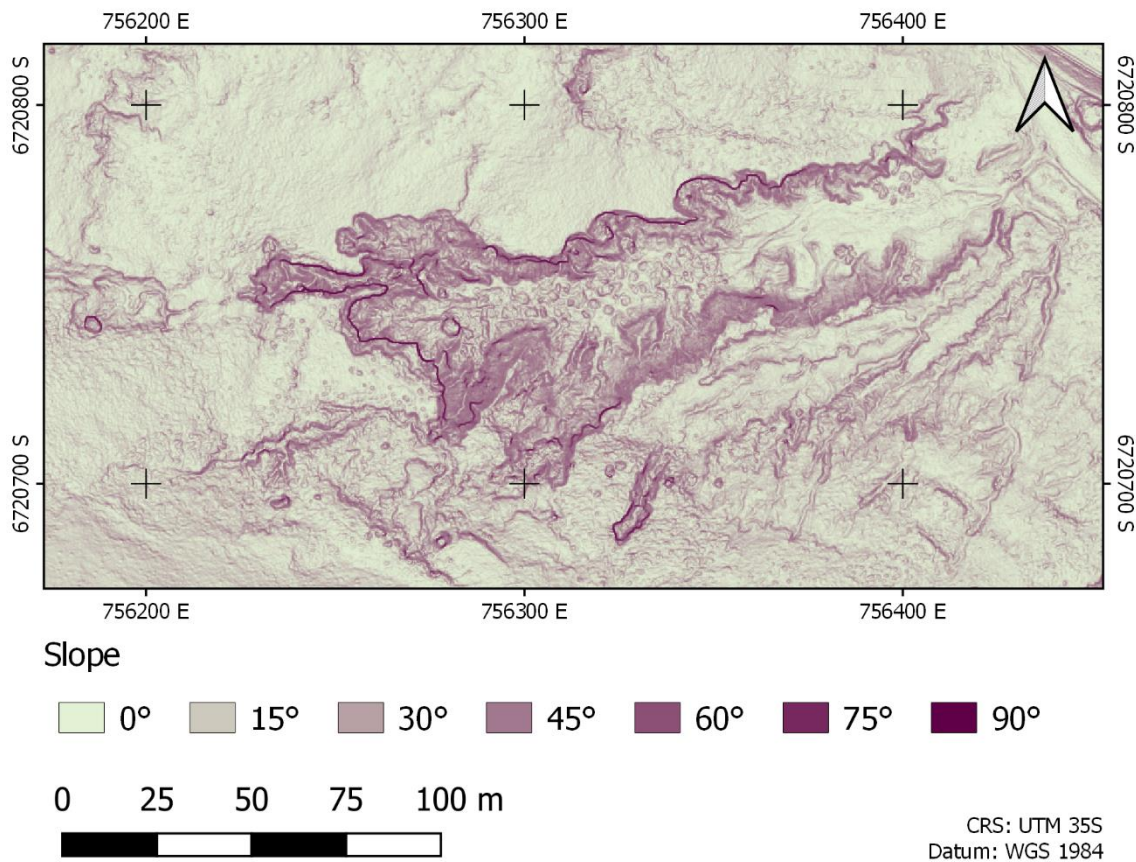
Fig. 7.14: Slopes of Gully KwaThunzi.
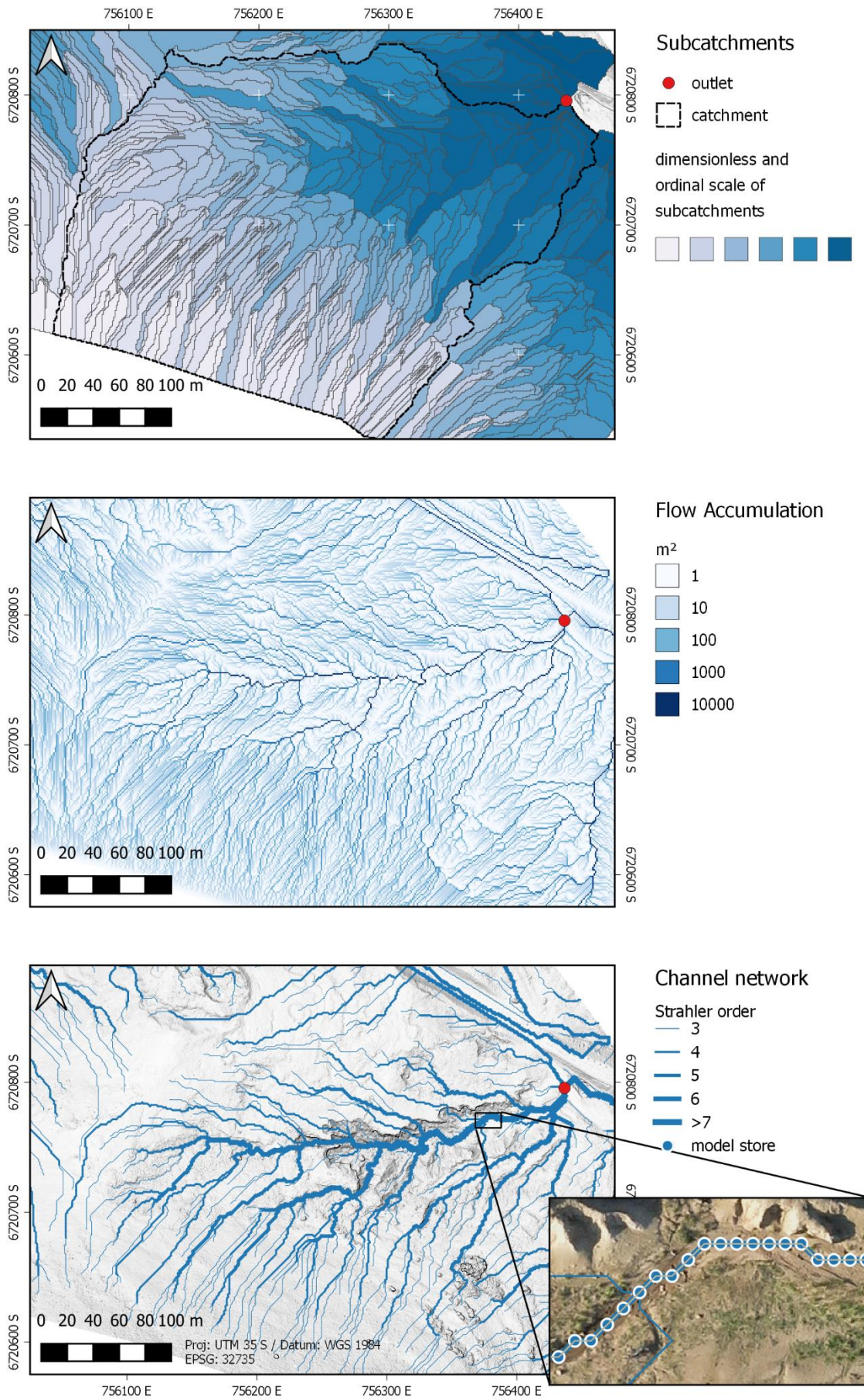
Fig 7.15: Subcatchments, flow accumulation and channel network of Gully KwaThunzi.

147
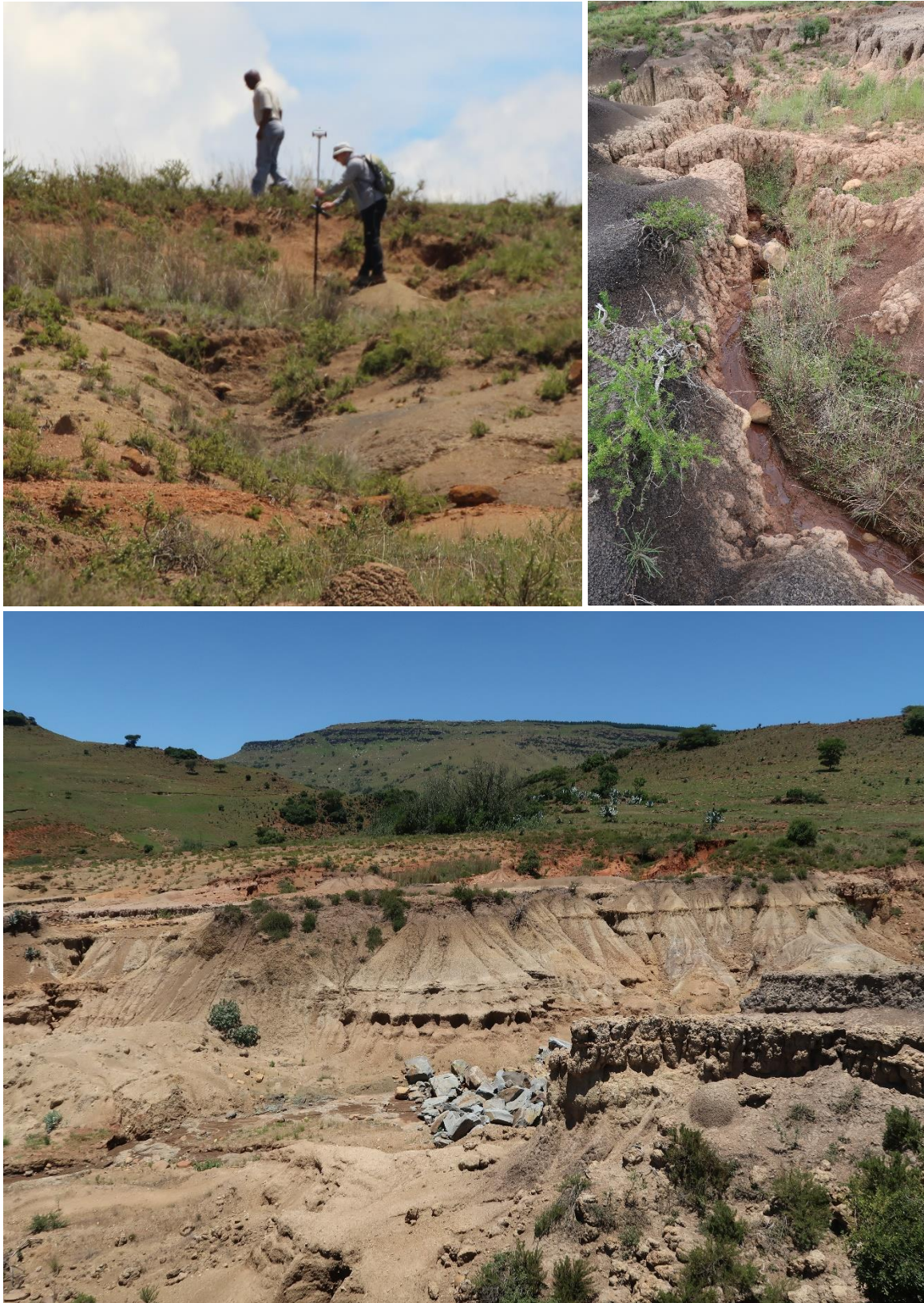
Fig. 7.16: Gully KwaThunzi displays multiple shapes of gully erosion. Upper left: V-shaped profile of the rather shallow upper gully. Upper right: U-shaped, canyon-like incision, where the upper layer (hard paleo B-horizon) is more resistant than the lower. Lower: Trapezoidal shape of the lower gully. Photos: C. Sommer.

The lower section of the gully, in contrast, is eroded to the stable shalestone bedrock, resulting in steep gully walls (fig. 7.14). These are typical attributes of a trapezoidal gullies and represent the majority of gully KwaThunzi. Taking into consideration, that the hard paleo B-horizon layers, which are responsible for the V-type of the upper gully crop out in the profile of the walls of the lower section, it can be deduced that the entire gully belonged to the V-type in earlier stages, until the Masotcheni sequence was excavated to the bottom, thus changing to a trapezoidal type.

The third FAO classification system distinguishes between continuous and discontinuous gullies. Gully KwaThunzi is a mature branch of a continuous gully system, which is connected to the Umkomazi river and whose length exceeds 1800 m (fig. 7.17). Gully KwaThunzi is situated in the lower part of this system, ~200 m from the outlet into the river and it is the most severely degraded branch of this network. Most recently, gully KwaThunzi, just as the majority of the network, have been disconnected from the outlet through the construction of the tarred "Stepmore Road", which crosses the main channel. The gully network dissected two Late Jurassic dolerite dikes and captured nearly the whole subcatchment. The middle part between the dikes is characterized by settlement structure with degraded surrounding pastures. Most of the branch gullies therein show (traces of) conservational treatment, like contour ploughing, however with limited success.
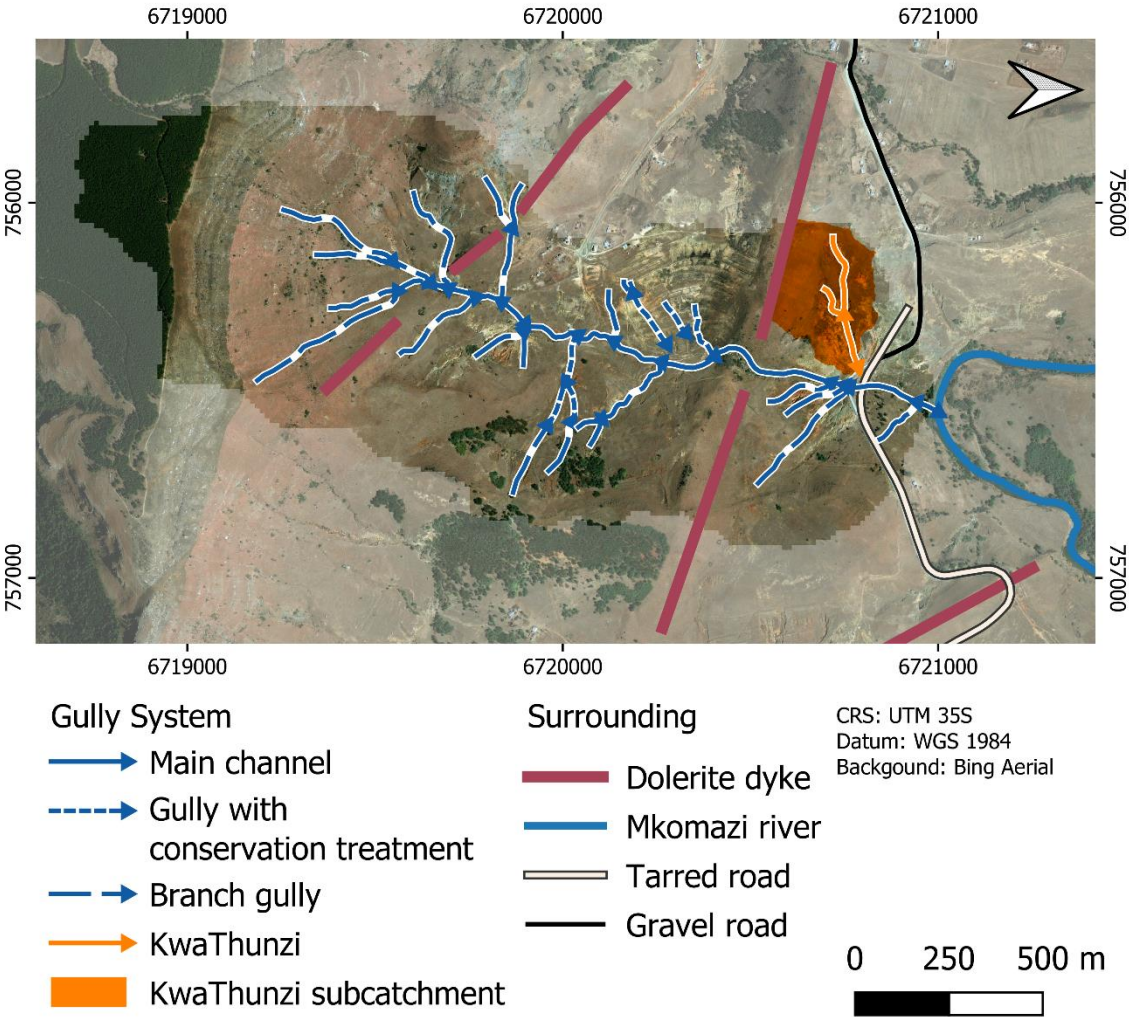
Fig 7.17: The gully network of KwaThunzi.

7.3.2 Soils

14 surface soil samples have been taken from the surroundings of gully KwaThunzi and were analyzed at the CEDARA Department for Agricultural and Rural Development of KwaZulu-Natal. Soil texture was tested according to the USDA Classification, with fine analyses for the surface samples.
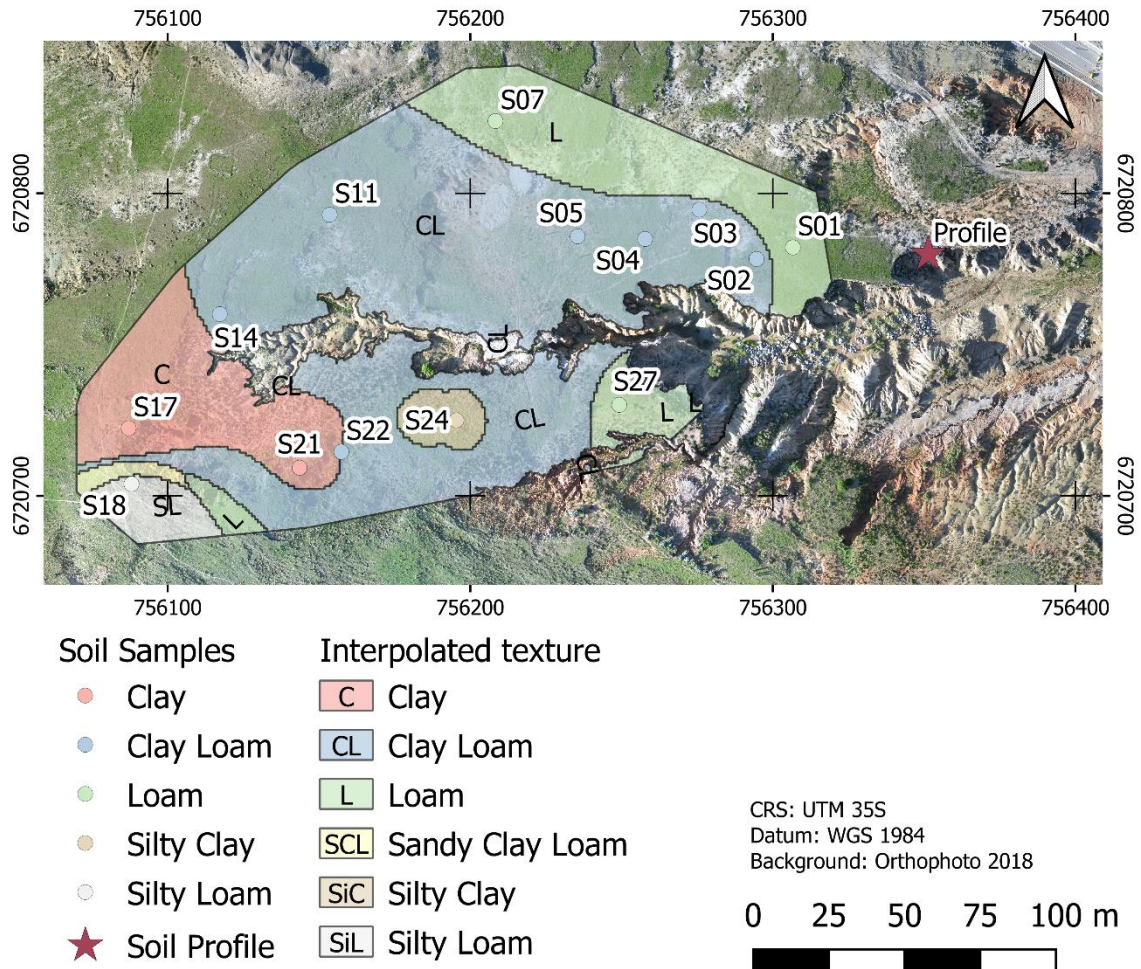
Fig. 7.18: Surface soil samples, interpolated textures and the profile from figure 6.6.

Figure 7.18 shows the distribution of surface samples around the gully and their respective texture class. The composition of the single samples is presented in the texture triangle in figure 7.19. The samples have been regionalized through a spline interpolation of the individual soil class fractions and subsequently classified with the tool "Soil Texture Classification" in the SAGA GIS 7.3.0 software package (Conrad et al., 2015). The spatial distribution shows a general trend from clays in the high-lying and level parts of the subcatchment (western part), through clay loams in the steeper middle part, representing the majority of samples, towards the lower catchment (eastern part), which is characterized by loams. This top-down transition is developed on both sides of the gully. This general topo-hydrological pattern differs, where the stable, vegetated surface has been eroded and underlying layers were exposed (i.e. samples S18, S24).
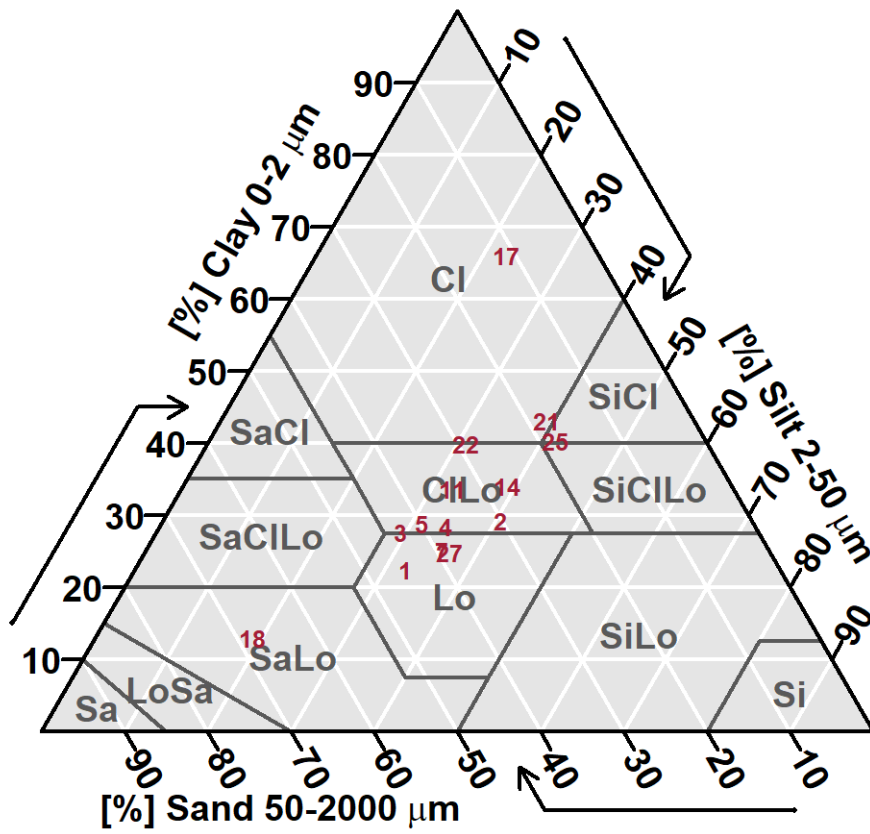
Figure 7.19: USDA soil texture triangle with surface soil samples surrounding the gully.

7.3.3 Historic gully erosion

According to Kosov et al. (1978), the development of a gully over time can be described with the variables length, depth, area and volume. To be able to understand the development of the KwaThunzi gully, the results of the 3D modelling (i.e. DEM and orthomosaic) of the years 1944 and 2018 were compared. Unfortunately, it was not possible to compare the two variables depth and volume, as the DEM from 1944 turned out to be too coarse to make meaningful volumetric measurements. Even if the spatial resolution of the 2018 UAV DEM is downscaled to the resolution of the historical DEM, the results were not comparable with a satisfying quality. Also, the use of DEMs with milder depth filtering methods or more aggressive dense point generation did not bring any improvement. It is possible that the object is simply too small on the original images (<2 cm, 200x50 pixels), which makes the surface unsuitable to perform SfM depth mapping correctly.
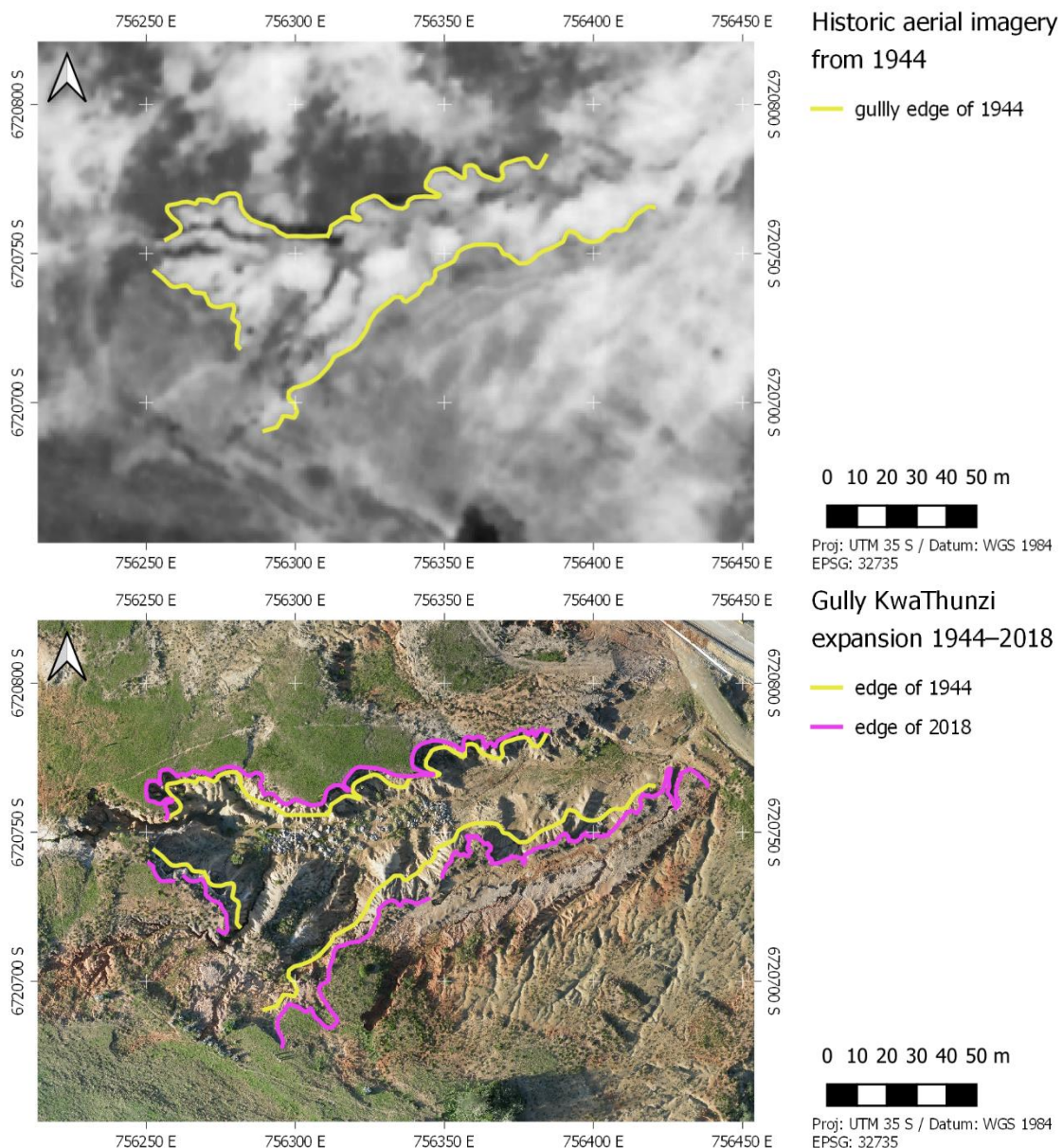
Fig. 7.20: Gully edge in the historical (upper) and modern (lower) imagery.

However, the reconstruction of the two variable lengths and area, both obtained from the orthophoto, worked reasonably well. The outlines of the gully were digitized from the 1944 orthomosaic. The sharp brightness difference between the darker grass cover and the brighter eroded soils served as an appropriate marker (fig. 7.20). The modern state of the gully outline was digitized from the UAV orthomosaic without any restraints, due to its high resolution. Then the shortest Euclidean distance between the two lines was calculated, which represents gully growth. Thus, the edge displacement can be reconstructed for each point (fig. 7.21). The mean change is 4.20 m, with values varying between 0 and 13.56 m (tab. 7.5).

Tab. 7.5: Gully edge erosion between 1944 and 2018.

	Total retreat [m]	Annual retreat [cm a^{-1}]
Mean	4.20	5.7
Median	4.00	5.4
Min	0	0
Max	13.56	18.3
25% Quantile	2.58	3.5
75% Quantile	5.42	7.3
Variance	4.73	8.6

The mean annual edge retreat rate could be determined from the absolute displacement values and the time span of 74 years, that lies between the images. The rate is 5.7 cm a^{-1} on average, with a maximum value of 18.3 cm a^{-1} (fig. 7.22). Moreover, there are apparently a few stable areas where no erosion was detected (fig. 7.21). It should be noted that this linear estimate is only valid for the analysis of long timescales. In shorter timescales, it can be assumed that the edge retreat will not be gradual, but will occur in response to short and intense events.
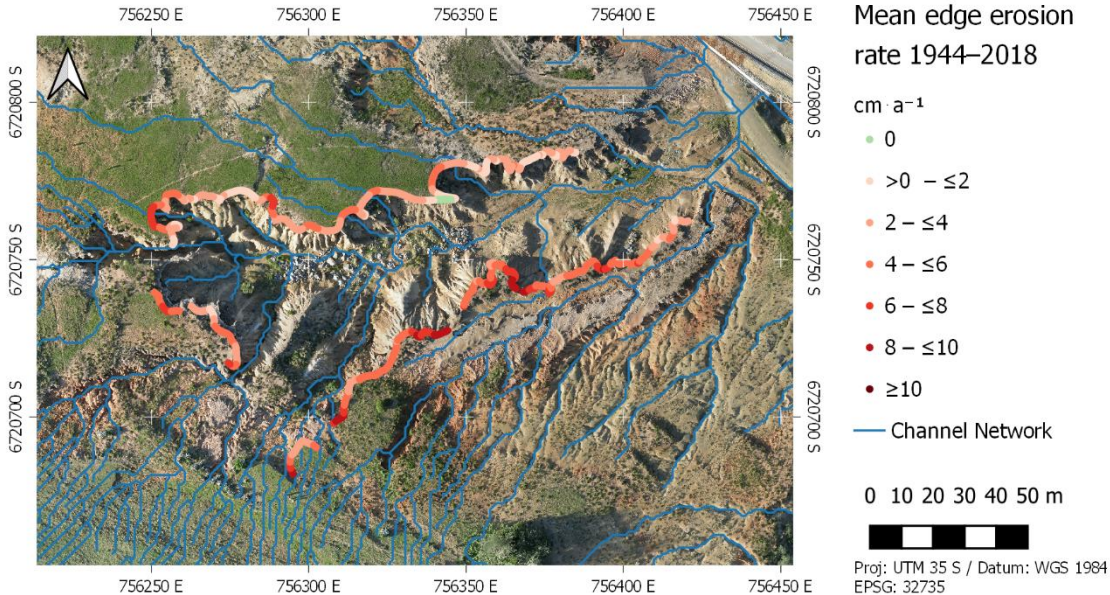
Fig. 7.21: Growth of Gully KwaThunzi between 1944 and 2018.
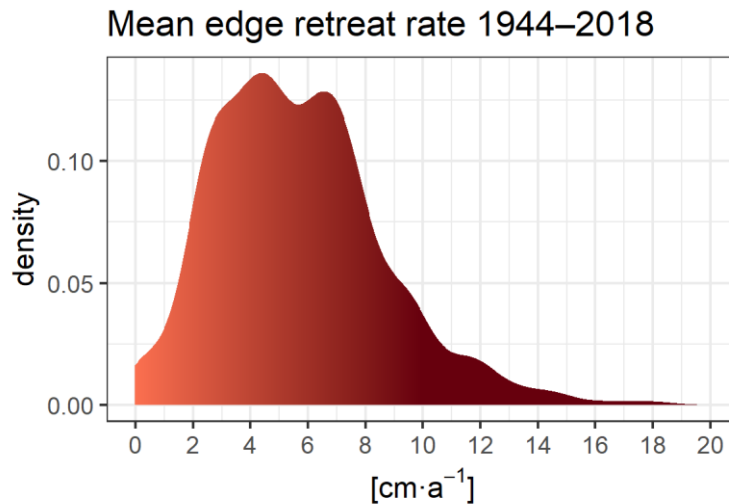
Fig. 7.22: Density distribution of retreat rates of the gully edge.

While there has been no detectable change of the length of main stream, the average side stream grew by 5.97 m since 1944 (variance: 6.23 m). This is a growth of an average 27% (variance: 2%) since 1944 or, in other words, 21% (variance: 0.8%) of the modern side stream length was added in the last 74 years, if the junction with the main stream is used as reference point. The growth relative to the gully outlet is on average 3% (variance 0.04%). This measure is only relevant for the computational gully model, but has little meaning in the real world, since it emphasizes streams closer to the outlet.

The area of the active lower part of the gully grew by 1570 m², which equals a growth of 25% since 1944, or in other words, 20% of the gully's area, as of today, were added in the last 74 years.

Fig. 7.23: Rock mushrooms and channels indicate recent erosion on the southern gully side.

This shows that Gully KwaThunzi is still an active gully system, however in the late stage of its evolution. It is characterized mainly by head erosion of side streams, and lateral erosion of the side walls. Although much of the erosion appears to be on the sides, the majority is due to the still active side channels of the network, whose location is associated with the highest edge retreat rates (fig. 7.21). The analysis of the northern and southern side shows differences: On the

northern side the overlap of side channel with peak erosion can be observed. On the southern side, and especially in the lower part, the channel network seems to bypass the gully and reach the main stream just before the outlet. Nevertheless, erosion seems to have significantly displaced the gully edge here as well. This contradiction can best be explained by a reorganization of the channel network at a unknown point in time after 1944. Field observations showed that larger amounts of the uppermost soil layer have been removed in the south in recent times. Erosion forms, such as rock mushrooms or small trees and shrubs, that protect the remains of this soil layer and former surface, can still be found (fig. 7.23). The southern channel network, which was previously presumably still flowing directly into the gully side, has provided enough flow accumulation due to its relatively large subcatchment to sustain erosion. With the later removal of the upper soil layer and a general restructuring of the network, the channels were redirected and now flow parallel the gully.

7.4. Discussion

7.4.1 The age of the gully

Several potential drivers are made responsible for gully erosion in the region, as explained in chapter 7.1.1. These can be summarized as geological, climatic and anthropogenic factors. Now the question of the cause or causes at KwaThunzi is to be addressed. Of course, there can be no clear answer to this question, since some are active at the same time and overlap or condition each other (fig. 7.1). For this reason, this discussion focuses on what causes are plausible and how the timing of the initiation can be narrowed down in time.

The results in chapter 7.3.1. show that Gully KwaThunzi is part of a larger continuous gully system. This spreads over various lithologies, including resistant dolerite dikes as well as metamorphic shalestones. As a result, the single parts of the system are affected by different erosional base levels, and are thus disconnected from the direct influence of Umkomazi incision. Therefore, a lowering of the base level can be ruled out as initiating event.

This shifts the focus to climatic and anthropogenic causes. However, these show large temporal variations and changes over the last 2 millennia, so that the timing of the initial phase of gully erosion must be estimated. The method presented in chapter 7.2 made it possible to reconstruct the development of the existing gullies in the period 1944-2018. Since the gully hardly shows any longitudinal growth at this late stage and gully depth evolution is restricted by the basal bedrock, the area growth is approximated as a proxy for overall gully evolution. This parameter was also found to be more reliable than gully volume, which was impaired by the lower spatial resolution of the historical 3D model.

According to the results of chapter 7.3.3, the gully grew strongest by edge retreat with a rate of 5.7 cm a^{-1}, which resulted in a growth of 4.2 meters in the observed timespan. In the still active lower gully, this led to an increase of the area by about 25%, from 6300 m^2 to 7900 m^2 in a time span of 74 years. If linear growth is assumed, this growth rate can be extrapolated, an age of roughly 370 years can be approximated. Thereafter, the gully erosion would have been initiated in the middle of the 17th century. This is associated with the Little Ice Age (AD 1300-1800), that appears to have affected South African climate in various ways. While the majority of the coastal evidence suggest colder and drier conditions (Tyson, 1999, Tyson et al., 2000, Ekblom, 2008, Holmgren et al., 2012, Sitoe et al., 2015, du Plessis et al., 2020), rare data from eastern Lesotho reveal "relatively higher available moisture during LIA, tentatively as a result of less evaporative water loss under a regionally cooler climate situation and/or a shift in rainfall seasonality resulting in more precipitation during winters" (Norström et al., 2018). At the same time, however, Late Iron Age populations are made responsible for overgrazing and soil degradation in the area (Badenhorst, 2010, Lyons et al., 2013). This shows a coexistence of multiple possible drivers, that cannot be resolved here.

Furthermore, this estimation should be treated with caution, since gullies are known not to grow linearly. According to experiments by Kosov et al. (1978), gully morphological properties, comprising length, depth, area and volume, are known to grow dynamically in the first stage of gully erosion. Ergo, the estimated initiation in the middle 17th century should be considered as older margin, and the gully might actually be younger. Furthermore, climate fluctuations might have varied erosion rates, just as anthropogenic factors, like the land use change brought into the discussion by Märker (2001), which renders a linear extrapolation problematic.

While these results are just approximations of the age of the gully, the observed historical gully growth proves that gully erosion is highly effective under recent climatic conditions. Accordingly, the time required to remove colluvial sediments of the Masotcheni Fm. type can be estimated to be a few centuries. This explains why remains of the Masotcheni Fm. predating the MIS 5e with comparable conditions as today, are extremely rare.

8 Synthesis

The geomorphic evolution of the Tongati Valley occurred throughout the Cenozoic and was controlled by multiple cycles lasting millions of years, which resulted in landforms, whose elevation levels could be correlated over large distances. From the reconstructed African, Post-African I, and Post-African II Surfaces, it was possible to estimate the uplift and tilting of these paleo surfaces, which are consistent with results of Partridge and Maud (1987). Only the last one, dating to the Plio-Pleistocene, appears to be lower, which is likely due to the distance to the center of uplift. The evolution of the valley comprises these stages:

- The catchment with its present borders was created with the termination of the African Surface, when substantial uplift caused the Nsuze River to cut between the Ozwatini Plateau, the highest part of the valley, and the neighboring Noodsberg.
- Consequently, the former planation surface was dissected, so that only some plateaus and mesas remain today. This resulted in a second level, the Post-African I, which is found in the mountain tops and ranges of the upper valley and the Sibudu-Sinembe hills of the lower valley.
- Further uplift caused the initiation of the Post-African II cycle and incision cut deep gorges especially in the middle valley, where confined meanders exist. This uplift also raised a former coastal plain to an elevation of up to 100 m, which today forms the Maputaland Fm. in the lower Tongati Valley.
- With the much lower uplift rates of the Pleistocene, sea level fluctuations gained influence on valley evolution. However, the geological circumstances created a complex river long profile, where the middle catchment was continuously in a transient state due to resistant lithology, while the lower catchment adapted to the sea level baseline. This resulted in three levels of terraces, whereas level T2 could be correlated with a MIS 5 standstill. The lower valley was infilled with alluvium after the LGM lowstand, so that the lower part reached its modern floodplain elevation in the beginning of the Holocene, as a date of T1 suggests.

This last erosion cycle also produced the rock shelter of Sibudu Cave. Its origin could not be clarified unambiguously, because it lies directly at the boundary between the transient middle channel with slow incision rates and the lower channel with faster rates. Nevertheless, based on the lithology, a slower incision can be favored, suggesting that the formation of the rock shelter continued throughout the Pleistocene.

in addition to the incision of the Tongati, the Pleistocene sea level fluctuations also caused shifts of the coastline. Due to the wide and flat topography of Natal Bight, regressions have exposed up to 5500 km^2 shelf area and the shore distance of the Sibudu Cave has increased from 11 km, as of today, to over 30 km at maximal lowstands. This supports the interpretation that shells found in SB, HP and late MSA layers of Sibudu Cave were not collected for consumption or tools, but rather suggest symbolic traditions (d'Errico et al., 2008, Vanhaeren et al., 2019). In Umbeli Belli, these expansions were less pronounced because of a narrower shelf. There are reasons to assume that this area was similar to today's Coastal Plain and the Maputaland Fm., but larger wetlands and back barrier dune systems are also plausible. This opens the possibility of an expanded niche that could be populated and exploited by the occupants of Sibudu, which would indicate high mobility, range and behavioral flexibility.

The study of the Masotcheni Fm. at KwaThunzi showed that, based on absolute dating and index horizons, they can be correlated with the occurrence of these Late Pleistocene colluvia in northern KZN.

The lowermost layer with an age of 66.62±7.68 ka was correlated with the Nqutu allomember topped by a Hazeldene pedoderm, and the following layer with an age of 39.42±5.27 could be correlated with the KwaVundla allomember. Multiple younger layers were found as well. This profile reflects the landscape stability cycles coined by Botha (1996), in which unstable phases are initially characterized by erosion and subsequent deposition of detritus, while stable phases are characterized by soil formation.

The use of electromagnetic field spectroscopy showed, that (i) the spectral properties of the Masotcheni Fm. feature a spectral curve that is typical for soils rather than minerals, and (ii) the analysis of minor absorption bands reveals soil properties of the layers, such as iron oxides, carbonates, organic matter and amino acids. Organic matter and amino acids are interpreted as indicators of vegetation and therefore moister conditions, while iron oxides point at structural cementation in soils, which is the case in the upper, prismatic B-horizons. Carbonate was only detected at sites proximal to dolerite dikes, which refers to an origin in intrusive rock. However, the signature of carbonate can be disturbed by the presence of organic matter, which leads to misclassification. Furthermore, the spectral signatures indicate post-depositional mobility of particles and solutes in the profile.

The Hazeldene pedoderm indicates a stable phase of moist conditions in late MIS4 or early MIS 3, whereas the multiple stacked prismatic B-horizons of the layers postdating the middle of MIS 3 are comparable to the modern "Estcourt Form" soil type. This is related to sub-humid to sub-arid conditions, that are found today in the southern Free State, but not in the Drakensberg foothills. Ergo, conditions were likely drier than today. This observation was not consistent with the interpretation from northern KZN that wet phases were related to soil formation and dry phases to erosion. Therefore, an alternative hypothesis was proposed that in stable phases both moist and dry climates produce the respective soils, while in unstable phases climatic fluctuations cause erosion instead.

A phase of landscape instability in MIS 4 was found contemporaneous with fluctuating environments from the archaeological record of the HP at Sibudu Cave and Klipdrift Shelter (Reynard et al., 2016, Clark, 2017), which is associated with a change in human diet and technological inventions (Wadley, 2015, Kandel et al., 2016). Another phase of landscape instability overlaps with the inset of the Early LSA (Bousman and Brink, 2018). This can be interpreted as increased behavioral flexibility in context of the environmental forcing theory. The late MIS 4 / early MIS 3 phase of stability discovered at KwaThunzi in contrast is associated with increased population and connectivity all over Southern Africa. Summarizing, the layers of the Masotcheni Fm. reflect (supra-)regional landscape cycles and provide an open-air archive with chronometric control, lithic artefacts and environmental proxies.

The gully erosion rates at KwaThunzi were estimated from historic aerial imagery and present-day UAV-borne imagery. A possible age of 370 years was extrapolated, which points at the middle 17th century, a time characterized by climatic variability of the LIA and changes in population and land use. This shows, that erosion under modern-day interglacial conditions is

highly effective and helps to understand, why only few remains of the Masotcheni Fm. predate the MIS 5e.

9. Conclusion

The aim of this thesis was to reconstruct the landscape, its landforms and processes in southern KwaZulu-Natal following the five key research question formulated in chapter 1.2. based on the results of a mixture of geographical methods, i.e. GIS, remote sensing and geomorphological techniques, it can be concluded that the Late Pleistocene was characterized by high spatial and temporal variability that resulted in multiple landscape phases, while substantial changes occurred within millennia. Several drivers, e.g. tectonics, climate and sea level fluctuations, acted simultaneously, but their effect differed regionally, as different susceptibilities arose from local framework conditions. This results in a variety of geomorphic processes and resulting landforms in a narrow space. For this reason, regional and local studies such as this one are important in order to be able to assess on site the effects of supra-regional environmental developments, which are described by increasingly better paleoenvironmental data time series, such as climate models or sea level reconstructions.

The results show that the high flexibility and methodological range of GIS and remote sensing allows to produce tailored solutions to investigate the various landscape features. This ranges from the adaption of rather classical approaches, like interpolation (e.g. of planation surfaces), to customized simulations, like the shoreline retreat relative to Sibudu Cave. The spatial approach was especially helpful to delineate geomorphic domains, where distinct primary drivers dominate, and to find their margins. The methodology was complemented by geomorphological terrain work, the use of which goes beyond mere ground truthing. By combining the advantages of the individual methods, a coherent overall picture could be created, as can be seen in the example of the river terraces: The OBIA approach allowed to predict potential fluvial terraces, but failed to separate these from raised marine terraces and was furthermore not able to detect buried terraces. This downside could be compensated through the use of classic geomorphological mapping and electric resistivity imaging. However, both methods were not capable to differentiate between the two types of terrace control, those affected by geology and those responding to sea level, as could be demonstrated by the analysis of the fluvial morphometry.

Added value was also provided through the use of innovative methos, such as the analysis of the physio-chemical properties of the Masotcheni Fm. using spectrometry, the application of ERI for the non-invasive study of colluvium and alluvium, or the study of erosion rates using SfM based on historical data.

The findings also affect the archaeological research of the region. The differentiation of the ages and the longevity of landforms in the Tongati catchment and the Drakensberg foothills helps to understand the availability of natural resources in the landscape for early Humans, but gives also insights to the taphonomic properties of landforms. Thus, the results address specific issues such as the use of marine resources over time in Sibudu Cave or the use of space in a changing coastal habitat. However, supraregional observations can also be made, such as the correlation of the emergence of lithic industries with large-scale landscape cycles or climate changes, as preserved in the Masotcheni Fm. This provides the opportunity to look at cultural development in the context of common hypotheses such as the adaption to abiotic forcing or social dynamics affected by the spatial connectivity of groups. However, further interdisciplinary research is

needed to make robust and detailed statements about paleoenvironmental conditions, such as the analysis of the colluvia from the perspectives of micromorphology, paleobiology, etc.

References

Literature

ADAMIEC, G., BAILEY, R. M., WANG, X. L. & WINTLE, A. G. 2008. The mechanism of thermally transferred optically stimulated luminescence in quartz. *Journal of Physics D: Applied Physics,* 41**,** 135503. DOI:10.1088/0022-3727/41/13/135503.

AHNERT, F. 2015. *Einführung in die Geomorphologie,* 5 ed*,* Stuttgart, Eugen Ulmer Verlag, 458 p. ISBN:3825286279.

BACHOFER, F. 2016. *Assessment of Paleo-Landscape Features using Advanced Remote Sensing Techniques, Modelling and GIS Methods in the Lake Manyara Basin, Northern Tanzania.* Dissertation, University of Tübingen.

BADENHORST, S. 2010. Descent of Iron Age Farmers in Southern Africa During the Last 2000 Years. *African Archaeological Review,* 27**,** 87-106. DOI:10.1007/s10437-010-9073-1.

BARD, E., ROSTEK, F. & SONZOGNI, C. 1997. Interhemispheric synchrony of the last deglaciation inferred from alkenone palaeothermometry. *Nature,* 385**,** 707-710. DOI:10.1038/385707a0.

BARKER, R. D. 1997. Electrical imaging and its application in engineering investigations. *Geological Society, London, Engineering Geology Special Publications,* 12**,** 37-43. DOI:10.1144/gsl.eng.1997.012.01.02.

BENITO, G., THORNDYCRAFT, V. R., RICO, M. T., SÁNCHEZ-MOYA, Y., SOPEÑA, A., BOTERO, B. A., MACHADO, M. J., DAVIS, M. & PÉREZ-GONZÁLEZ, A. 2011. Hydrological response of a dryland ephemeral river to southern African climatic variability during the last millennium. *Quaternary Research,* 75**,** 471-482. DOI:10.1016/j.yqres.2011.01.004.

BERGER, A. 1978. Long-Term Variations of Daily Insolation and Quaternary Climatic Changes. *Journal of the Atmospheric Sciences,* 35**,** 2362-2367. DOI:10.1175/1520-0469(1978)035<2362:ltvodi>2.0.co;2.

BERLIN, M. M. & ANDERSON, R. S. 2007. Modeling of knickpoint retreat on the Roan Plateau, western Colorado. *Journal of Geophysical Research: Earth Surface,* 112. DOI:10.1029/2006JF000553.

BINTANJA, R., VAN DE WAL, R. S. W. & OERLEMANS, J. 2005. Modelled atmospheric temperatures and global sea levels over the past million years. *Nature,* 437**,** 125. DOI:10.1038/nature03975.

BIRCH, G. F. 1982. Sedimentological and geophysical investigations of a major sediment exit point on the south-east African continental margin (vicinity of Port St Johns). *South African Journal of Geology,* 85**,** 91-103.

BLASCHKE, T. 2010. Object based image analysis for remote sensing. *ISPRS Journal of Photogrammetry and Remote Sensing,* 65**,** 2-16. DOI:10.1016/j.isprsjprs.2009.06.004.

BLASCHKE, T., HAY, G. J., KELLY, M., LANG, S., HOFMANN, P., ADDINK, E., QUEIROZ FEITOSA, R., VAN DER MEER, F., VAN DER WERFF, H., VAN COILLIE, F. & TIEDE, D. 2014. Geographic Object-Based Image Analysis – Towards a new paradigm. *ISPRS Journal of Photogrammetry and Remote Sensing,* 87**,** 180-191. DOI:10.1016/j.isprsjprs.2013.09.014.

BLIGHT, G. E. 1994. The master profile for hydraulic fill tailings beaches. *Proceedings of the Institution of Civil Engineers - Geotechnical Engineering,* 107**,** 27-40. DOI:10.1680/igeng.1994.25718.

BOISSONNAT, J.-D. & CAZALS, F. 2002. Smooth surface reconstruction via natural neighbour interpolation of distance functions. *Computational Geometry,* 22**,** 185-203. DOI:10.1016/S0925-7721(01)00048-7.

BOSINO, A., BERNINI, A., BOTHA, G. A., BONACINA, G., PELLEGRINI, L., OMRAN, A., HOCHSCHILD, V., SOMMER, C. & MAERKER, M. 2020. Geomorphology of the upper Mkhomazi River basin, KwaZulu-Natal, South Africa, with emphasis on late Pleistocene colluvial deposits. *Journal of Maps***,** 1-12. DOI:10.1080/17445647.2020.1790435.

BOSMAN, C., UKEN, R. & OVECHKINA, M. N. 2007. The Aliwal Shoal revisited: New age constraints from nannofossil assemblages. *South African Journal of Geology,* 110**,** 647-653. DOI:10.2113/gssajg.110.4.647.

BOSMAN, C., UKEN, R. & SMITH, A. M. 2005. The bathymetry of the Aliwal Shoal, Scottburgh, South Africa : research letter. *South African Journal of Science,* 101**,** 255-257.

BOTHA, G. & PORAT, N. 2007. Soil chronosequence development in dunes on the southeast African coastal plain, Maputaland, South Africa. *Quaternary International,* 162-163**,** 111-132. DOI:10.1016/j.quaint.2006.10.028.

BOTHA, G. A. 1996. *The geology and palaeopedology of late Quaternary colluvial sediments in northern KwaZulu-Natal, South Africa,* Pretoria, Council for Geoscience, 165 p. ISBN:1875061363.

BOTHA, G. A. 2000. Paleosols and Duricruts. *In:* PARTRIDGE, T. C. & MAUD, R. R. (eds.) *The Cenozoic of Southern Africa.* New York: Oxford University Press, p. 131-145. ISBN:0195125304.

BOTHA, G. A. 2018. Lithostratigraphy of the late Cenozoic Maputaland Group. *South African Journal of Geology,* 121**,** 95-108. DOI:10.25131/sajg.121.0007.

BOTHA, G. A. & FEDOROFF, N. 1995. Palaeosols in Late Quaternary colluvium, northern KwaZulu-Natal, South Africa. *Journal of African Earth Sciences,* 21**,** 291-311. DOI:10.1016/0899-5362(95)00072-2.

BOTHA, G. A., SCOTT, L., VOGEL, J. C. & VON BRUNN, V. 1992. Palaeosols and palaeoenvironments during the Late Pleistocene Hypothermal in nothern Natal. *South African Journal of Science,* 88**,** 508-512.

BOTHA, G. A., TEMME, A. J. A. M. & SINGH, R. G. 2016. Colluvial deposits and slope instability. *In:* KNIGHT, J. & GRAB, S. W. (eds.) *Quaternary Environmental Change in Southern Africa: Physical and Human Dimensions.* Cambridge: Cambridge University Press, p. 137-152. ISBN:9781107055797. DOI:DOI: 10.1017/CBO9781107295483.009.

BOTHA, G. A., WINTLE, A. G. & VOGEL, J. C. 1994. Episodic late quaternary palaeogully erosion in northern KwaZulu-Natal, South Africa. *CATENA,* 23**,** 327-340. DOI:10.1016/0341-8162(94)90076-0.

BØTTER-JENSEN, L., MCKEEVER, S. W. & WINTLE, A. G. 2003. *Optically stimulated luminescence dosimetry,* 1 ed*,* Amsterdam, Elsevier, 335 p. ISBN:0444506845.

BOUSMAN, C. B. & BRINK, J. S. 2018. The emergence, spread, and termination of the Early Later Stone Age event in South Africa and southern Namibia. *Quaternary International,* 495**,** 116-135. DOI:10.1016/j.quaint.2017.11.033.

BOWERS, S. A. & HANKS, R. J. 1965. Reflection of radiant energy from soils. *Soil Science,* 100**,** 130-138.

BREWER, R., CROOK, K. A. W. & SPEIGHT, J. G. 1970. Proposal for Soil-Stratigraphic units in the Australian Stratigraphic code. *Journal of the Geological Society of Australia,* 17**,** 103-111. DOI:10.1080/00167617008728728.

BRIDGLAND, D. & WESTAWAY, R. 2008. Climatically controlled river terrace staircases: A worldwide Quaternary phenomenon. *Geomorphology,* 98**,** 285-315. DOI:10.1016/j.geomorph.2006.12.032.

BRIDGLAND, D. R. & WESTAWAY, R. 2014. Quaternary fluvial archives and landscape evolution: a global synthesis. *Proceedings of the Geologists' Association,* 125**,** 600-629. DOI:10.1016/j.pgeola.2014.10.009.

BRIERLEY, G. J. & FRYIRS, K. 2005. *Geomorphology and River Management: Applications of the River Styles Framework,* Oxford, UK, Blackwell Publishing. ISBN:9781405115162. DOI:10.1002/9780470751367.

BROAD, D. S., JUNGSLAGER, E. H. A., MCLACHLAN, I. R., ROUX, J. & VAN DER SPUY, D. 2012. 15 - South Africa's offshore Mesozoic basins. *In:* ROBERTS, D. G. & BALLY, A. W. (eds.) *Regional Geology and Tectonics: Phanerozoic Passive Margins, Cratonic Basins and Global Tectonic Maps.* Boston: Elsevier, p. 534-564. ISBN:978-0-444-56357-6. DOI:10.1016/B978-0-444-56357-6.00014-7.

BROCCOLI, A. J., DAHL, K. A. & STOUFFER, R. J. 2006. Response of the ITCZ to Northern Hemisphere cooling. *Geophysical Research Letters,* 33. DOI:10.1029/2005gl024546.

BROWN, R. W., SUMMERFIELD, M. A. & GLEADOW, A. J. W. 2002. Denudational history along a transect across the Drakensberg Escarpment of southern Africa derived from apatite fission track thermochronology. *Journal of Geophysical Research: Solid Earth,* 107**,** 10-1-10-18. DOI:10.1029/2001jb000745.

BRUCH, A., SIEVERS, C. & WADLEY, L. 2012. Quantification of climate and vegetation from southern African Middle Stone Age sites – an application using Late Pleistocene plant material from Sibudu, South Africa. 45**,** 7-17. DOI:10.1016/j.quascirev.2012.04.005.

BRUTON, M. N., SMITH, M. & TAYLOR, R. H. 1980. A brief history of human evolvement in Maputaland. *In:* BRUTON, M. N. & COOPER, K. H. (eds.) *Studies on the Ecology of Maputaland.* Durban, South Africa: Rhodes University and the Natal Branch of the Wildlife Society of Southern Africa, p. 432–459. ISBN:0868100358.

BURKE, K. & GUNNELL, Y. 2008. The African Erosion Surface: A Continental-Scale Synthesis of Geomorphology, Tectonics, and Environmental Change over the Past 180 Million Years. *Memoir 201: The African Erosion Surface: A Continental-Scale Synthesis of Geomorphology, Tectonics, and Environmental Change over the Past 180 Million Years.* p. 1-66. ISBN:978-0-8137-1201-7. DOI:10.1130/2008.1201.

BURKE, K. & WILKINSON, M. J. 2016. Landscape evolution in Africa during the Cenozoic and Quaternary—the legacy and limitations of Lester C. King. *Canadian Journal of Earth Sciences,* 53**,** 1089-1102. DOI:10.1139/cjes-2016-0099.

CAMARGO, L. A., MARQUES, J., BARRÓN, V., ALLEONI, L. R. F., PEREIRA, G. T., TEIXEIRA, D. D. B. & BAHIA, A. S. R. D. S. 2018. Predicting potentially toxic elements in tropical soils from iron oxides, magnetic susceptibility and diffuse reflectance spectra. *CATENA,* 165**,** 503-515. DOI:10.1016/j.catena.2018.02.030.

CAMPFORTS, B., SCHWANGHART, W. & GOVERS, G. 2017. Accurate simulation of transient landscape evolution by eliminating numerical diffusion: the TTLEM 1.0 model. *Earth Surf. Dynam.,* 5**,** 47-66. DOI:10.5194/esurf-5-47-2017.

CARR, A. S., CHASE, B. M. & MACKAY, A. 2016. Mid to Late Quaternary Landscape and Environmental Dynamics in the Middle Stone Age of Southern South Africa. *In:* JONES, S. C. & STEWART, B. A. (eds.) *Africa from MIS 6-2: Population Dynamics and Paleoenvironments.* Dordrecht: Springer Netherlands, p. 23-47. ISBN:978-94-017-7520-5. DOI:10.1007/978-94-017-7520-5_2.

CARRIVICK, J. L., SMITH, M. W. & QUINCEY, D. J. 2016. *Structure from Motion in the Geosciences*, John Wiley & Sons, Ltd, 197 p. ISBN:9781118895849. DOI:10.1002/9781118895818.

CASTAÑEDA, I. S., WERNE, J. P. & JOHNSON, T. C. 2007. Wet and arid phases in the southeast African tropics since the Last Glacial Maximum. *Geology,* 35**,** 823-826. DOI:10.1130/g23916a.1.

CAWTHRA, H. C., NEUMANN, F. H., UKEN, R., SMITH, A. M., GUASTELLA, L. A. & YATES, A. 2012a. Sedimentation on the narrow (8km wide), oceanic current-influenced continental shelf off Durban, Kwazulu-Natal, South Africa. *Marine Geology,* 323-325**,** 107-122. DOI:10.1016/j.margeo.2012.08.001.

CAWTHRA, H. C., UKEN, R. & OVECHKINA, M. N. 2012b. New insights into the geological evolution of the Durban Bluff and adjacent Blood Reef, South Africa. *South African Journal of Geology,* 115**,** 291-308. DOI:10.2113/gssajg.115.3.291.

CHASE, B. M. 2010. South African palaeoenvironments during marine oxygen isotope stage 4: a context for the Howiesons Poort and Still Bay industries. *Journal of Archaeological Science,* 37**,** 1359-1366. DOI:10.1016/j.jas.2009.12.040.

CHASE, B. M., LIM, S., CHEVALIER, M., BOOM, A., CARR, A. S., MEADOWS, M. E. & REIMER, P. J. 2015. Influence of tropical easterlies in southern Africa's winter rainfall zone during the Holocene. *Quaternary Science Reviews,* 107**,** 138-148. DOI:10.1016/j.quascirev.2014.10.011.

CHASE, B. M. & MEADOWS, M. E. 2007. Late Quaternary dynamics of southern Africa's winter rainfall zone. *Earth-Science Reviews,* 84**,** 103-138. DOI:10.1016/j.earscirev.2007.06.002.

CHEVALIER, M. & CHASE, B. M. 2015. Southeast African records reveal a coherent shift from high- to low-latitude forcing mechanisms along the east African margin across last glacial–interglacial transition. *Quaternary Science Reviews,* 125**,** 117-130. DOI:10.1016/j.quascirev.2015.07.009.

CLARK, J. L. 2017. The Howieson's Poort fauna from Sibudu Cave: Documenting continuity and change within Middle Stone Age industries. *Journal of Human Evolution,* 107**,** 49-70. DOI:10.1016/j.jhevol.2017.03.002.

CLARK, J. L. & KANDEL, A. W. 2013. The Evolutionary Implications of Variation in Human Hunting Strategies and Diet Breadth during the Middle Stone Age of Southern Africa. *Current Anthropology,* 54**,** S269-S287. DOI:10.1086/673386.

CLARK, R. N., KING, T. V. V., KLEJWA, M., SWAYZE, G. A. & VERGO, N. 1990. High spectral resolution reflectance spectroscopy of minerals. *Journal of Geophysical Research: Solid Earth,* 95**,** 12653-12680. DOI:10.1029/JB095iB08p12653.

CLARK, R. N. & ROUSH, T. L. 1984. Reflectance spectroscopy: Quantitative analysis techniques for remote sensing applications. *Journal of Geophysical Research: Solid Earth,* 89**,** 6329-6340. DOI:10.1029/JB089iB07p06329.

CLARKE, B. M., SCHIEMAN, P. & KOTA, M. W. 2007. *The Geology of the Verulam Area,* Pretoria, Council for Geosciences, 94 p. ISBN:978-1-919908-29-8.

CLARKE, M. L., VOGEL, J. C., BOTHA, G. A. & WINTLE, A. G. 2003. Late Quaternary hillslope evolution recorded in eastern South African colluvial badlands. *Palaeogeography, Palaeoclimatology, Palaeoecology,* 197**,** 199-212. DOI:10.1016/S0031-0182(03)00461-9.

COLLINS, J. A., SCHEFUß, E., GOVIN, A., MULITZA, S. & TIEDEMANN, R. 2014. Insolation and glacial–interglacial control on southwestern African hydroclimate over the past 140 000 years. *Earth and Planetary Science Letters,* 398**,** 1-10. DOI:10.1016/j.epsl.2014.04.034.

CONACHER, A. J. & DARLYMPLE, J. B. 1977. The nine unit landsurface model and pedogeomorphic research. *Geoderma,* 18**,** 127-144. DOI:10.1016/0016-7061(77)90087-8.

CONARD, N. J. & WILL, M. 2015. Examining the Causes and Consequences of Short-Term Behavioral Change during the Middle Stone Age at Sibudu, South Africa. *PLOS ONE,* 10**,** e0130001. DOI:10.1371/journal.pone.0130001.

CONRADIE, D. C. U. South Africa's Climatic Zones: today, Tomorrow. International Green Building Conference and Exhibition, July 25-26 2012 2012 Sandton, South Africa.

COOK, K. L., TUROWSKI, J. M. & HOVIUS, N. 2013. A demonstration of the importance of bedload transport for fluvial bedrock erosion and knickpoint propagation. *Earth Surface Processes and Landforms,* 38**,** 683-695. DOI:10.1002/esp.3313.

COOK, K. L., TUROWSKI, J. M. & HOVIUS, N. 2014. River gorge eradication by downstream sweep erosion. *Nature Geoscience,* 7**,** 682-686. DOI:10.1038/ngeo2224.

COOPER, A. 1986. *Sedimentation in the Mgeni Estuary, Natal, South Africa.* M.Sc., University of Natal.

COOPER, J. A. G. 1993. Sedimentation in a river dominated estuary. *Sedimentology,* 40**,** 979-1017. DOI:10.1111/j.1365-3091.1993.tb01372.x.

COOPER, J. A. G. 1994. Sedimentary processes in the river-dominated Mvoti estuary, South Africa. *Geomorphology,* 9**,** 271-300. DOI:10.1016/0169-555X(94)90050-7.

COOPER, J. A. G. 2001. Geomorphological variability among microtidal estuaries from the wave-dominated South African coast. *Geomorphology,* 40**,** 99-122. DOI:10.1016/S0169-555X(01)00039-3.

COOPER, J. A. G. & FLORES, R. M. 1991. Shoreline deposits and diagenesis resulting from two Late Pleistocene highstands near +5 and +6 metres, Durban, South Africa. *Marine Geology,* 97**,** 325-343. DOI:10.1016/0025-3227(91)90124-M.

COOPER, J. A. G., GREEN, A. N. & COMPTON, J. S. 2018. Sea-level change in southern Africa since the Last Glacial Maximum. *Quaternary Science Reviews,* 201**,** 303-318. DOI:10.1016/j.quascirev.2018.10.013.

CRUZ, F. W., BURNS, S. J., KARMANN, I., SHARP, W. D., VUILLE, M., CARDOSO, A. O., FERRARI, J. A., SILVA DIAS, P. L. & VIANA, O. 2005. Insolation-driven changes in atmospheric circulation over the past 116,000 years in subtropical Brazil. *Nature,* 434**,** 63-66. DOI:10.1038/nature03365.

D'ERRICO, F., HENSHILWOOD, C., VANHAEREN, M. & VAN NIEKERK, K. 2005. Nassarius kraussianus shell beads from Blombos Cave: evidence for symbolic behaviour in the Middle Stone Age. *Journal of Human Evolution,* 48**,** 3-24. DOI:10.1016/j.jhevol.2004.09.002.

D'ERRICO, F., VANHAEREN, M. & WADLEY, L. 2008. Possible shell beads from the Middle Stone Age layers of Sibudu Cave, South Africa. *Journal of Archaeological Science,* 35**,** 2675-2685. DOI:10.1016/j.jas.2008.04.023.

D'ERRICO, F., BACKWELL, L., VILLA, P., DEGANO, I., LUCEJKO, J. J., BAMFORD, M. K., HIGHAM, T. F. G., COLOMBINI, M. P. & BEAUMONT, P. B. 2012. Early evidence of San material culture represented by organic artifacts from Border Cave, South Africa. *Proceedings of the National Academy of Sciences,* 109**,** 13214-13219. DOI:10.1073/pnas.1204213109.

DAVIES, O. 1949. Notes from Natal. *South African Archaeological Bulletin,* 4**,** 87-94.

DAVIES, O. 1951. *Archaeology of Natal: Natal Regional Survey*, Oxford University Press.

DAVIES, O. 1976. The older coastal dunes in Natal and Zululand and their relation to former shorelines. *Annals of the South African Museum,* 71**,** 19-32.

DAVIS, W. M. 1899. The Geographical Cycle. *The Geographical Journal,* 14**,** 481-504. DOI:10.2307/1774538.

DE LECEA, A. M., GREEN, A. N. & COOPER, J. A. G. 2016. Environmental change during the Pleistocene and Holocene: Estuaries and lagoons of southern Africa. *In:* KNIGHT, J. & GRAB, S. W. (eds.) *Quaternary Environmental Change in Southern Africa: Physical and Human Dimensions.* Cambridge: Cambridge University Press, p. 219-233. ISBN:9781107055797. DOI:10.1017/CBO9781107295483.014.

DE WET, W. M. 2013. *Bathymetry of the South African Continental Shelf.* Ph.D., University of Cape Town.

DEMOULIN, A. 1998. Testing the tectonic significance of some parameters of longitudinal river profiles: the case of the Ardenne (Belgium, NW Europe). *Geomorphology,* 24**,** 189-208. DOI:10.1016/S0169-555X(98)00016-6.

DEMOULIN, A., BECKERS, A. & HUBERT-FERRARI, A. 2015. Patterns of Quaternary uplift of the Corinth rift southern border (N Peloponnese, Greece) revealed by fluvial landscape morphometry. *Geomorphology,* 246**,** 188-204. DOI:10.1016/j.geomorph.2015.05.032.

DEMOULIN, A., BOVY, B., RIXHON, G. & CORNET, Y. 2007. An automated method to extract fluvial terraces from digital elevation models: The Vesdre valley, a case study in eastern Belgium. *Geomorphology,* 91**,** 51-64. DOI:10.1016/j.geomorph.2007.01.020.

DEMOULIN, A., MATHER, A. & WHITTAKER, A. 2017. Fluvial archives, a valuable record of vertical crustal deformation. *Quaternary Science Reviews,* 166**,** 10-37. DOI:10.1016/j.quascirev.2016.11.011.

DEMOULIN, A., SCHIATTARELLA, M. & PEDERSEN, V. K. 2018. Geomorphic response to active tectonics: Numerical and field-based approaches. *Earth Surface Processes and Landforms,* 43**,** 2666-2668. DOI:10.1002/esp.4397.

DIBIASE, R. A., WHIPPLE, K. X., HEIMSATH, A. M. & OUIMET, W. B. 2010. Landscape form and millennial erosion rates in the San Gabriel Mountains, CA. *Earth and Planetary Science Letters,* 289**,** 134-144. DOI:10.1016/j.epsl.2009.10.036.

DIKAU, R. 1989. The application of a digital relief model to landform analysis. *In:* RAPER, J. F. (ed.) *Three dimensional applications in Geographical Information Systems.* London: Taylor and Francis, p. 51-77. ISBN:9780850667769.

DLADLA, N. N. 2013. *Seismic-stratigraphic models for late Pleistocene/Holocene incised valley systems on the Durban continental shelf.* Master of Science, University of KwaZulu-Natal.

DOLLAR, L. H., DOLLAR, E. S. J. & MOOLMAN, J. 2006. Development of an automated desktop procedure for defining macro-reaches for river longitudinal profiles. *Water SA,* 32**,** 395–402.

DRĂGUŢ, L. & BLASCHKE, T. 2006. Automated classification of landform elements using object-based image analysis. *Geomorphology,* 81**,** 330-344. DOI:10.1016/j.geomorph.2006.04.013.

DU PLESSIS, N., CHASE, B. M., QUICK, L. J., HABERZETTL, T., KASPER, T. & MEADOWS, M. E. 2020. Vegetation and climate change during the Medieval Climate Anomaly and the Little Ice Age

on the southern Cape coast of South Africa: Pollen evidence from Bo Langvlei. *The Holocene,* 30**,** 1716-1727. DOI:10.1177/0959683620950444.

DU TOIT, A. L. 1954. *The geology of South Africa,* Edinburgh; London, Oliver and Boyd.

DULLER, G. A. T. 2004. Luminescence dating of quaternary sediments: recent advances. *Journal of Quaternary Science,* 19**,** 183-192. DOI:10.1002/jqs.809.

DUPONT, L. M., CALEY, T., KIM, J. H., CASTAÑEDA, I., MALAIZÉ, B. & GIRAUDEAU, J. 2011. Glacial-interglacial vegetation dynamics in South Eastern Africa coupled to sea surface temperature variations in the Western Indian Ocean. *Clim. Past,* 7**,** 1209-1224. DOI:10.5194/cp-7-1209-2011.

DWYER, G. S. & CHANDLER, M. A. 2009. Mid-Pliocene sea level and continental ice volume based on coupled benthic Mg/Ca palaeotemperatures and oxygen isotopes. *Philosophical Transactions of the Royal Society A: Mathematical, Physical and Engineering Sciences,* 367**,** 157-168. DOI:10.1098/rsta.2008.0222.

EERKENS, J. W. & LIPO, C. P. 2005. Cultural transmission, copying errors, and the generation of variation in material culture and the archaeological record. *Journal of Anthropological Archaeology,* 24**,** 316-334. DOI:10.1016/j.jaa.2005.08.001.

EKBLOM, A. 2008. Forest–savanna dynamics in the coastal lowland of southern Mozambique since c. AD 1400. *The Holocene,* 18**,** 1247-1257. DOI:10.1177/0959683608096599.

EPSTEIN, S., BUCHSBAUM, R., LOWENSTAM, H. A. & UREY, H. C. 1953. REVISED CARBONATE-WATER ISOTOPIC TEMPERATURE SCALE. *GSA Bulletin,* 64**,** 1315-1326. DOI:10.1130/0016-7606(1953)64[1315:rcits]2.0.co;2.

ERKENS, G., DAMBECK, R., VOLLEBERG, K. P., BOUMAN, M. T. I. J., BOS, J. A. A., COHEN, K. M., WALLINGA, J. & HOEK, W. Z. 2009. Fluvial terrace formation in the northern Upper Rhine Graben during the last 20000 years as a result of allogenic controls and autogenic evolution. *Geomorphology,* 103**,** 476-495. DOI:10.1016/j.geomorph.2008.07.021.

ERLANGER, E. D., GRANGER, D. E. & RYAN, J. G. 2012. Rock uplift rates in South Africa from isochron burial dating of fluvial and marine terraces. *Geology,* 40**,** 1019-1022. DOI:10.1130/G33172.1.

EVANS, M. 2019-06-18 2019. *RE: E-mail communication about OSL datings.* Type to SOMMER, C.

EVENSTAR, L. A., MATHER, A. E. & HARTLEY, A. J. 2020. Using spatial patterns of fluvial incision to constrain continental-scale uplift in the Andes. *Global and Planetary Change,* 186**,** 103119. DOI:10.1016/j.gloplacha.2020.103119.

FAVRE, A., HEWITSON, B., LENNARD, C., CEREZO-MOTA, R. & TADROSS, M. 2013. Cut-off Lows in the South Africa region and their contribution to precipitation. *Climate Dynamics,* 41**,** 2331-2351. DOI:10.1007/s00382-012-1579-6.

FEY, M. 2010. *Soils of South Africa,* Cambridge, Cambridge University Press, 288 p. ISBN:9781107000506. DOI:DOI: 10.1017/CBO9780511782183.

FINNEGAN, N. J. 2013. Interpretation and downstream correlation of bedrock river terrace treads created from propagating knickpoints. *Journal of Geophysical Research: Earth Surface,* 118**,** 54-64. DOI:10.1029/2012jf002534.

FISHER, E. C., BAR-MATTHEWS, M., JERARDINO, A. & MAREAN, C. W. 2010. Middle and Late Pleistocene paleoscape modeling along the southern coast of South Africa. *Quaternary Science Reviews,* 29**,** 1382-1398. DOI:10.1016/j.quascirev.2010.01.015.

FITCHETT, J. M. & GRAB, S. W. 2014. A 66-year tropical cyclone record for south-east Africa: temporal trends in a global context. *International Journal of Climatology,* 34**,** 3604-3615. DOI:10.1002/joc.3932.

FLEMMING, B. W. 1978. Underwater sand dunes along the southeast African continental margin — Observations and implications. *Marine Geology,* 26**,** 177-198. DOI:10.1016/0025-3227(78)90059-2.

FLEMMING, B. W. 1980. Sand transport and bedform patterns on the continental shelf between Durban and Port Elizabeth (southeast African continental margin). *Sedimentary Geology,* 26**,** 179-205. DOI:10.1016/0037-0738(80)90011-1.

FLEMMING, B. W. 1981. Factors controlling shelf sediment dispersal along the southeast African continental margin. *Marine Geology,* 42**,** 259-277. DOI:10.1016/0025-3227(81)90166-3.

FLEMMING, B. W. & HAY, E. R. 1988. Sediment Distribution And Dynamics On The Natal Continental Shelf. *In:* SCHUMANN, E. (ed.) *Coastal Ocean Studies off Natal, South Africa.* New York: Springer, p. 47-80. DOI:10.1029/LN026p0047.

FLINT, J. J. 1974. Stream gradient as a function of order, magnitude, and discharge. *Water Resources Research,* 10**,** 969-973. DOI:10.1029/WR010i005p00969.

FORGY, E. 1965. Cluster Analysis of Multivariate Data: Efficiency versus Interpretability of Classifications. *Biometrics***,** 768-780.

FRYIRS, K. A., BRIERLEY, G. J., PRESTON, N. J. & KASAI, M. 2007. Buffers, barriers and blankets: The (dis)connectivity of catchment-scale sediment cascades. *CATENA,* 70**,** 49-67. DOI:10.1016/j.catena.2006.07.007.

FUCHS, M. & LANG, A. 2009. Luminescence dating of hillslope deposits—A review. *Geomorphology,* 109**,** 17-26. DOI:10.1016/j.geomorph.2008.08.025.

GALBRAITH, R. F., ROBERTS, R. G., LASLETT, G. M., YOSHIDA, H. & OLLEY, J. M. 1999. Optical dating of single and multiple grains of quartz from Jinmium rock shelter, northern Australia: Part I, Experimental design and statistical models. *Archaeometry,* 41**,** 339-364. DOI:10.1111/j.1475-4754.1999.tb00987.x.

GALLAND, O., BERTELSEN, H. S., GULDSTRAND, F., GIROD, L., JOHANNESSEN, R. F., BJUGGER, F., BURCHARDT, S. & MAIR, K. 2016. Application of open-source photogrammetric software MicMac for monitoring surface deformation in laboratory models. *Journal of Geophysical Research: Solid Earth,* 121**,** 2852-2872. DOI:10.1002/2015JB012564.

GEACH, M. R., VIVEEN, W., MATHER, A. E., TELFER, M. W., FLETCHER, W. J., STOKES, M. & PEYRON, O. 2015. An integrated field and numerical modelling study of controls on Late Quaternary fluvial landscape development (Tabernas, southeast Spain). *Earth Surface Processes and Landforms,* 40**,** 1907-1926. DOI:10.1002/esp.3768.

GEYIK, M. P. 1986. *FAO watershed management field manual: Gully control,* Rome, Food and Agriculture Organization of the United Nations.

GOLDBERG, P., MILLER, C. E., SCHIEGL, S., LIGOUIS, B., BERNA, F., CONARD, N. J. & WADLEY, L. 2009. Bedding, hearths, and site maintenance in the Middle Stone Age of Sibudu Cave, KwaZulu-Natal, South Africa. *Archaeological and Anthropological Sciences,* 1**,** 95-122. DOI:10.1007/s12520-009-0008-1.

GOLDRICK, G. & BISHOP, P. 2007. Regional analysis of bedrock stream long profiles: evaluation of Hack's SL form, and formulation and assessment of an alternative (the DS form). *Earth Surface Processes and Landforms,* 32**,** 649-671. DOI:10.1002/esp.1413.

GOODLAD, S. W. 1986. *Tectonic and sedimentary history of the Mid-Natal Valley (S.W. Indian Ocean).* Ph.D., University of Cape Town.

GOUDIE, A. S. 1998. *Geomorphologie: ein Methodenhandbuch für Studium und Praxis,* Berlin, Springer, 645 p. ISBN:354062905X.

GOVIN, A., HOLZWARTH, U., HESLOP, D., FORD KEELING, L., ZABEL, M., MULITZA, S., COLLINS, J. A. & CHIESSI, C. M. 2012. Distribution of major elements in Atlantic surface sediments (36°N–49°S): Imprint of terrigenous input and continental weathering. *Geochemistry, Geophysics, Geosystems,* 13. DOI:10.1029/2011gc003785.

GOVIN, A., MICHEL, E., LABEYRIE, L., WAELBROECK, C., DEWILDE, F. & JANSEN, E. 2009. Evidence for northward expansion of Antarctic Bottom Water mass in the Southern Ocean during the last glacial inception. *Paleoceanography,* 24. DOI:10.1029/2008pa001603.

GRAB, S. W., MILLS, S. C. & CARR, S. J. 2012. Periglacial and Glacial Geomorphology. *In:* HOLMES, P. & MEADOWS, M. E. (eds.) *Southern African Geomorphology. Recent Trend and New Directions.* 1 ed. Bloemfontein: Sun Media, p. 231-266. ISBN:9781920382025.

GREEN, A. 2011. The late Cretaceous to Holocene sequence stratigraphy of a sheared passive upper continental margin, northern KwaZulu-Natal, South Africa. *Marine Geology,* 289**,** 17-28. DOI:10.1016/j.margeo.2011.09.001.

GREEN, A. N. 2009a. *The marine geology of the Northern KwaZulu-Natal continental shelf, South Africa.* Ph.D., University of KwaZulu-Natal.

GREEN, A. N. 2009b. Palaeo-drainage, incised valley fills and transgressive systems tract sedimentation of the northern KwaZulu-Natal continental shelf, South Africa, SW Indian Ocean. *Marine Geology,* 263**,** 46-63. DOI:10.1016/j.margeo.2009.03.017.

GREEN, A. N., COOPER, J. A. G., LEUCI, R. & THACKERAY, Z. 2013a. Formation and preservation of an overstepped segmented lagoon complex on a high-energy continental shelf. *Sedimentology,* 60**,** 1755-1768. DOI:10.1111/sed.12054.

GREEN, A. N., COOPER, J. A. G. & SALZMANN, L. 2017. The role of shelf morphology and antecedent setting in the preservation of palaeo-shoreline (beachrock and aeolianite) sequences: the SE African shelf. *Geo-Mar Lett,* 38**,** 5-18. DOI:10.1007/s00367-017-0512-8.

GREEN, A. N., DLADLA, N. & GARLICK, G. L. 2013b. Spatial and temporal variations in incised valley systems from the Durban continental shelf, KwaZulu-Natal, South Africa. *Marine Geology,* 335**,** 148-161. DOI:10.1016/j.margeo.2012.11.002.

GREEN, A. N. & GARLICK, L. G. 2011. A sequence stratigraphic framework for a narrow, current-swept continental shelf: The Durban Bight, central KwaZulu-Natal, South Africa. *Journal of African Earth Sciences,* 60**,** 303-314. DOI:10.1016/j.jafrearsci.2011.03.007.

GRELLIER, S., KEMP, J., JANEAU, J.-L., FLORSCH, N., WARD, D., BAROT, S., PODWOJEWSKI, P., LORENTZ, S. & VALENTIN, C. 2012. The indirect impact of encroaching trees on gully extension: A 64year study in a sub-humid grassland of South Africa. *CATENA,* 98**,** 110-119. DOI:10.1016/j.catena.2012.07.002.

GRENFELL, M. C., ELLERY, W. & GRENFELL, S. E. 2008. Tributary valley impoundment by trunk river floodplain development: a case study from the KwaZulu-Natal Drakensberg foothills, eastern South Africa. *Earth Surface Processes and Landforms,* 33**,** 2029-2044. DOI:10.1002/esp.1652.

GRENFELL, M. C., ELLERY, W. N. & GRENFELL, S. E. 2009. Valley morphology and sediment cascades within a wetland system in the KwaZulu-Natal Drakensberg Foothills, Eastern South Africa. *CATENA,* 78**,** 20-35. DOI:10.1016/j.catena.2009.02.004.

GRENFELL, S. E., GRENFELL, M. C., ROWNTREE, K. M. & ELLERY, W. N. 2014. Fluvial connectivity and climate: A comparison of channel pattern and process in two climatically contrasting fluvial sedimentary systems in South Africa. *Geomorphology,* 205**,** 142-154. DOI:10.1016/j.geomorph.2012.05.010.

GROUP, S. C. W. 1991. *Soil Classification - A taxonomic system for South Africa,* 2 ed*,* Republic of South Africa, Department of Agricultural Development 257 p. ISBN:0621107840.

GUISAN, A., WEISS, S. B. & WEISS, A. D. 1999. GLM versus CCA spatial modeling of plant species distribution. *Plant Ecology,* 143**,** 107-122. DOI:10.1023/A:1009841519580.

GUPTA, R. P. 2018. *Remote Sensing Geology,* Berlin, Heidelberg, Springer-Verlag GmbH Germany, 428 p. ISBN:978-3-662-55874-4. DOI:10.1007/978-3-662-55876-8.

HACK, J. T. 1957. *Studies of longitudinal stream profiles in Virginia and Maryland*, US Government Printing Office, 91 p.

HACK, J. T. 1973. Stream-profile analysis and stream-gradient index. *Journal of Research of the U.S. Geological Survey,* 1**,** 421-429.

HAIDLE, M. N., BOLUS, M., BRUCH, A. A., HERTLER, C., KANDEL, A., MÄRKER, M., CONARD, N. J., HOCHSCHILD, V., SCHRENK, F. & MOSBRUGGER, V. 2010. The role of culture in early expansions of humans – A new research center. *Quaternary International,* 223-224**,** 429-430. DOI:10.1016/j.quaint.2009.07.011.

HALL, K. & MEIKLEJOHN, I. 2011. Chapter 78 - Glaciation in Southern Africa and in the Sub-Antarctic. *In:* EHLERS, J., GIBBARD, P. L. & HUGHES, P. D. (eds.) *Developments in Quaternary Sciences.* Elsevier, p. 1081-1085. ISBN:1571-0866. DOI:10.1016/B978-0-444-53447-7.00078-7.

HANSON, E. K., MOORE, J. M., BORDY, E. M., MARSH, J. S., HOWARTH, G. & ROBEY, J. V. A. 2009. CRETACEOUS EROSION IN CENTRAL SOUTH AFRICA: EVIDENCE FROM UPPER-CRUSTAL XENOLITHS IN KIMBERLITE DIATREMES. *South African Journal of Geology,* 112**,** 125-140. DOI:10.2113/gssajg.112.2.125.

HAREL, M. A., MUDD, S. M. & ATTAL, M. 2016. Global analysis of the stream power law parameters based on worldwide 10Be denudation rates. *Geomorphology,* 268**,** 184-196. DOI:10.1016/j.geomorph.2016.05.035.

HARRIS, I., JONES, P. D., OSBORN, T. J. & LISTER, D. H. 2014. Updated high-resolution grids of monthly climatic observations – the CRU TS3.10 Dataset. *International Journal of Climatology,* 34**,** 623-642. DOI:10.1002/joc.3711.

HART, N. C. G., REASON, C. J. C. & FAUCHEREAU, N. 2013. Cloud bands over southern Africa: seasonality, contribution to rainfall variability and modulation by the MJO. *Climate Dynamics,* 41**,** 1199-1212. DOI:10.1007/s00382-012-1589-4.

HENSHILWOOD, C., D'ERRICO, F., VANHAEREN, M., VAN NIEKERK, K. & JACOBS, Z. 2004. Middle Stone Age Shell Beads from South Africa. *Science,* 304**,** 404-404. DOI:10.1126/science.1095905.

HOBDAY, D. K. 1982. The Southeast African Margin. *In:* NAIRN, A. E. M. & STEHLI, F. G. (eds.) *The Ocean Basins and Margins: The Indian Ocean.* Boston, MA: Springer US, p. 149-183. ISBN:978-1-4615-8038-6. DOI:10.1007/978-1-4615-8038-6_3.

HOCHSCHILD, V., MÄRKER, M., RODOLFI, G. & STAUDENRAUSCH, H. 2003. Delineation of erosion classes in semi-arid southern African grasslands using vegetation indices from optical remote sensing data. *Hydrological Processes,* 17**,** 917-928. DOI:10.1002/hyp.1170.

HOFFMAN, M. T. & TODD, S. 2000. A National Review of Land Degradation in South Africa: The Influence of Biophysical and Socio-economic Factors. *Journal of Southern African Studies,* 26**,** 743-758. DOI:10.1080/713683611.

HOLBROOK, J. & SCHUMM, S. A. 1999. Geomorphic and sedimentary response of rivers to tectonic deformation: a brief review and critique of a tool for recognizing subtle epeirogenic deformation in modern and ancient settings. *Tectonophysics,* 305**,** 287-306. DOI:10.1016/S0040-1951(99)00011-6.

HOLMGREN, K., LEE-THORP, J. A., COOPER, G. R. J., LUNDBLAD, K., PARTRIDGE, T. C., SCOTT, L., SITHALDEEN, R., SIEP TALMA, A. & TYSON, P. D. 2003. Persistent millennial-scale climatic variability over the past 25,000 years in Southern Africa. *Quaternary Science Reviews,* 22**,** 2311-2326. DOI:10.1016/S0277-3791(03)00204-X.

HOLMGREN, K., RISBERG, J., FREUDENDAHL, J., ACHIMO, M., EKBLOM, A., MUGABE, J., NORSTRÖM, E. & SITOE, S. 2012. Water-level variations in Lake Nhauhache, Mozambique, during the last 2,300 years. *Journal of Paleolimnology,* 48**,** 311-322. DOI:10.1007/s10933-012-9596-3.

HUFFMAN, T. N. 1982. Archaeology and Ethnohistory of the African Iron Age. *Annual Review of Anthropology,* 11**,** 133-150. DOI:10.1146/annurev.an.11.100182.001025.

HUFFMAN, T. N. 2007. *Handbook to the Iron Age: the archaeology of pre-colonial farming societies in Southern Africa,* Scottsville, South Africa, University of KwaZulu-Natal Press, 504 p. ISBN:1869141083.

HUGHES, G. 1974. The sea turtles of South-east Africa. 2. The biology of the Tongaland loggerhead turtle Caretta caretta L. with comments on the leatherback turtle Dermochelys coriacea L. and the green turtle Chelonia mydas L. in the study region. *Invest. Rep. Oceanogr. Res. Inst. Durban***,** 96.

HUNT, G. R. 1979. Near-infrared (1.3–2.4) μm spectra of alteration minerals—Potential for use in remote sensing. *GEOPHYSICS,* 44**,** 1974-1986. DOI:10.1190/1.1440951.

HUYBERS, P. 2011. Combined obliquity and precession pacing of late Pleistocene deglaciations. *Nature,* 480**,** 229. DOI:10.1038/nature10626.

JACKSON, D. W. T., COOPER, J. A. G. & GREEN, A. N. 2014. A preliminary classification of coastal sand dunes of KwaZulu-Natal. *Journal of Coastal Research,* 70**,** 718-722. DOI:10.2112/si70-121.1.

JACOBS, Z. 2010. An OSL chronology for the sedimentary deposits from Pinnacle Point Cave 13B—A punctuated presence. *Journal of Human Evolution,* 59**,** 289-305. DOI:10.1016/j.jhevol.2010.07.010.

JACOBS, Z. & ROBERTS, D. L. 2009. Last Interglacial Age for aeolian and marine deposits and the Nahoon fossil human footprints, Southeast Coast of South Africa. *Quaternary Geochronology,* 4**,** 160-169. DOI:10.1016/j.quageo.2008.09.002.

JACOBS, Z., ROBERTS, R. G., LACHLAN, T. J., KARKANAS, P., MAREAN, C. W. & ROBERTS, D. L. 2011. Development of the SAR TT-OSL procedure for dating Middle Pleistocene dune and shallow marine deposits along the southern Cape coast of South Africa. *Quaternary Geochronology,* 6**,** 491-513. DOI:10.1016/j.quageo.2011.04.003.

JAVERNICK, L., BRASINGTON, J. & CARUSO, B. 2014. Modeling the topography of shallow braided rivers using Structure-from-Motion photogrammetry. *Geomorphology,* 213**,** 166-182. DOI:10.1016/j.geomorph.2014.01.006.

JENNY, H. 1941. *Factors of soil formation: a system of quantitative pedology,* New York, McGraw-Hill, 281 p. ISBN:0486681289.

JOHNSON, T. C., BROWN, E. T., MCMANUS, J., BARRY, S., BARKER, P. & GASSE, F. 2002. A High-Resolution Paleoclimate Record Spanning the Past 25,000 Years in Southern East Africa. *Science,* 296**,** 113-132. DOI:10.1126/science.1070057.

KANDEL, A. W., BOLUS, M., BRETZKE, K., BRUCH, A. A., HAIDLE, M. N., HERTLER, C. & MÄRKER, M. 2016. Increasing Behavioral Flexibility? An Integrative Macro-Scale Approach to Understanding the Middle Stone Age of Southern Africa. *Journal of Archaeological Method and Theory,* 23**,** 623-668. DOI:10.1007/s10816-015-9254-y.

KARKANAS, P. & GOLDBERG, P. 2010. Site formation processes at Pinnacle Point Cave 13B (Mossel Bay, Western Cape Province, South Africa): resolving stratigraphic and depositional complexities with micromorphology. *Journal of Human Evolution,* 59**,** 256-273. DOI:10.1016/j.jhevol.2010.07.001.

KEAREY, P., BROOKS, M. & HILL, I. 2002. *An Introduction to Geophysical Exploration,* 3 ed*,* Oxford, Blackwell Science, 272 p. ISBN:ISBN 0-632-04929-4.

KEEN-ZEBERT, A., TOOTH, S., RODNIGHT, H., DULLER, G. A. T., ROBERTS, H. M. & GRENFELL, M. 2013. Late Quaternary floodplain reworking and the preservation of alluvial sedimentary archives in unconfined and confined river valleys in the eastern interior of South Africa. *Geomorphology,* 185**,** 54-66. DOI:10.1016/j.geomorph.2012.12.004.

KING, L. C. 1948. On The ages of African land-surfaces. *Quarterly Journal of the Geological Society,* 104**,** 439. DOI:10.1144/GSL.JGS.1948.104.01-04.20.

KING, L. C. & FAIR, T. J. D. 1944. Hill-slopes and dongas. *Transactions, Geological Society of South Africa***,** 1–4.

KING, L. C. & KING, L. A. 1959. A Reappraisal of the Natal Monocline. *South African Geographical Journal,* 41**,** 15-30. DOI:10.1080/03736245.1959.10559341.

KING, L. J. 1973. Pliocene marine fossils from the Alexandria Formation in the Patterson District, Eastern Cape Province, and their geomorphic significance. *Transactions of the Geological Society of South Africa,* 75**,** 159-160.

KING, L. J. & MAUD, R. R. 1964. The geology of Durban and environs. *Bulletin of the Geological Survey South Africa,* 42.

KIRBY, E. & OUIMET, W. 2011. Tectonic geomorphology along the eastern margin of Tibet: insights into the pattern and processes of active deformation adjacent to the Sichuan Basin. *Geological Society, London, Special Publications,* 353**,** 165. DOI:10.1144/SP353.9.

KIRBY, E. & WHIPPLE, K. 2001. Quantifying differential rock-uplift rates via stream profile analysis. *Geology,* 29**,** 415-418. DOI:10.1130/0091-7613(2001)029<0415:qdrurv>2.0.co;2.

KIRBY, E. & WHIPPLE, K. X. 2012. Expression of active tectonics in erosional landscapes. *Journal of Structural Geology,* 44**,** 54-75. DOI:10.1016/j.jsg.2012.07.009.

KLEYNHANS, C. J., THIRION, C. & MOOLMAN, J. 2005. A Level I River Ecoregion classification System for South Africa, Lesotho and Swaziland. Pretoria, South Africa: Department of Water Affairs and Forestry.

KNIGHT, J. 2019. The Making of the South African Landscape. *In:* KNIGHT, J. & ROGERSON, C. (eds.) *The Geography of South Africa. Contemporary Changes and New Directions.* 1 ed.: Springer International Publishing, p. 7-14. ISBN:978-3-319-94973-4. DOI:10.1007/978-3-319-94974-1.

KNIGHT, J. & GRAB, S. W. 2018. Drainage network morphometry and evolution in the eastern Lesotho highlands, southern Africa. *Quaternary International,* 470**,** 4-17. DOI:10.1016/j.quaint.2017.07.024.

KNOX, J. C. 1972. Valley alluviation in southwestern Wisconsin. *Annals of the Association of American Geographers,* 62**,** 401-410. DOI:10.1111/j.1467-8306.1972.tb00872.x.

KOSOV, B., NIKOL'SKAYA, I. & ZORINA, Y. F. 1978. Eksperimental'nyye issledovaniya ovragoobrazovaniya. *Eksperimental'naya geomorfologiya,* 3**,** 113-140.

KRIGE, L. J. 1932. The geology of Durban. *Transactions of the Royal Society of South Africa,* 35**,** 37-67.

KULONGOSKI, J. T., HILTON, D. R. & SELAOLO, E. T. 2004. Climate variability in the Botswana Kalahari from the late Pleistocene to the present day. *Geophysical Research Letters,* 31. DOI:10.1029/2003gl019238.

LAMBECK , K., WOODROFFE, C. D., ANTONIOLI, F., ANZIDEI, M., GEHRELS, W. R., LABOREL, J. & WRIGHT, A. J. 2010. Paleoenvironmental Records, Geophysical Modeling, and Reconstruction of Sea-Level Trends and Variability on Centennial and Longer Timescales. *In:* CHURCH, J. A., WOODWORTH, P. L., AARUP, T. & WILSON, W. S. (eds.) *Understanding Sea-Level Rise and Variability.* Oxford: Wiley-Blackwell, p. 61-121. DOI:10.1002/9781444323276.ch4.

LARKIN, Z. T., RALPH, T. J., TOOTH, S. & MCCARTHY, T. S. 2017. The interplay between extrinsic and intrinsic controls in determining floodplain wetland characteristics in the South African drylands. *Earth Surface Processes and Landforms,* 42**,** 1092-1109. DOI:10.1002/esp.4075.

LAUER, T., WEISS, M., BERNHARDT, W., HEINRICH, S., RAPPSILBER, I., STAHLSCHMIDT, M. C., VON SUCHODOLETZ, H. & WANSA, S. 2020. The Middle Pleistocene fluvial sequence at Uichteritz, central Germany: Chronological framework, paleoenvironmental history and early human presence during MIS 11. *Geomorphology,* 354**,** 107016. DOI:10.1016/j.geomorph.2019.107016.

LEBZELTER, V. 1926. Eine Expedition zur umfassenden Erforschung des Buschmänner in Südafrika. *Anthropes,* 21**,** 954-957.

LEDOUX, H. & GOLD, C. An Efficient Natural Neighbour Interpolation Algorithm for Geoscientific Modelling. *In:* FISHER, P. F., ed. Developments in Spatial Data Handling, 2005// 2005 Berlin, Heidelberg. Springer Berlin Heidelberg, 97-108.

LENNARD, C. 2019. Multi-Scale Drivers of the South African Weather and Climate. *In:* KNIGHT, J. & ROGERSON, C. M. (eds.) *The Geography of South Africa : Contemporary Changes and New Directions.* Cham: Springer International Publishing, p. 81-89. ISBN:978-3-319-94974-1. DOI:10.1007/978-3-319-94974-1_9.

LI, H., CHEN, L., WANG, Z. & YU, Z. 2019. Mapping of River Terraces with Low-Cost UAS Based Structure-from-Motion Photogrammetry in a Complex Terrain Setting. *Remote Sensing,* 11**,** 464. DOI:10.3390/rs11040464.

LINDESAY, J. A. 1988. South African rainfall, the Southern Oscillation and a Southern Hemisphere semi-annual cycle. *Journal of Climatology,* 8**,** 17-30. DOI:10.1002/joc.3370080103.

LISIECKI, L. E. & RAYMO, M. E. 2005. A Pliocene-Pleistocene stack of 57 globally distributed benthic δ18O records. *Paleoceanography,* 20. DOI:10.1029/2004PA001071.

LOKE, M. H. 2000. Topographic Modelling in Electrical Imaging Inversion. *62nd European Association of Geoscientists & Engineers.* Glascog, Scotland: European Association of Geoscientists & Engineers.

LOKE, M. H. 2011. Electrical Resistivity Surveys and Data Interpretation. *In:* GUPTA, H. K. (ed.) *Encyclopedia of Solid Earth Geophysics.* Dordrecht: Springer Netherlands, p. 276-283. ISBN:978-90-481-8702-7. DOI:10.1007/978-90-481-8702-7_46.

LOMBARD, M. 2012. Thinking through the Middle Stone Age of sub-Saharan Africa. *Quaternary International,* 270**,** 140-155. DOI:10.1016/j.quaint.2012.02.033.

LOWE, D. G. Object recognition from local scale-invariant features. Proceedings of the Seventh IEEE International Conference on Computer Vision, 20-27 Sept. 1999 1999. 1150-1157 vol.2. DOI:10.1109/ICCV.1999.790410.

LUTJEHARMS, J. R. E., VALENTINE, H. R. & VAN BALLEGOOYEN, R. C. 2000. The hydrography and water masses of the Natal Bight, South Africa. *Continental Shelf Research,* 20**,** 1907-1939. DOI:10.1016/S0278-4343(00)00053-4.

LYONS, R., TOOTH, S. & DULLER, G. A. T. 2013. Chronology and controls of donga (gully) formation in the upper Blood River catchment, KwaZulu-Natal, South Africa: Evidence for a climatic driver of erosion. *The Holocene,* 23**,** 1875-1887. DOI:10.1177/0959683613508157.

MACKIN, H. J. 1948. Concept of the graded river. *GSA Bulletin,* 59**,** 463-512. DOI:10.1130/0016-7606(1948).

MAREAN, C. W., COWLING, R. M. & FRANKLIN, J. 2020. The Palaeo-Agulhas Plain: Temporal and spatial variation in an extraordinary extinct ecosystem of the Pleistocene of the Cape Floristic Region. *Quaternary Science Reviews,* 235**,** 106161. DOI:10.1016/j.quascirev.2019.106161.

MÄRKER, M. 2001. *Regionale Erosionsmodellierung unter Verwendung des Konzepts der Erosion Response Units (ERU) am Beispiel zweier Flusseinzugsgebiete im südlichen Afrika.* Dr. rer. nat., Friedrich-Schiller-Universität Jena.

MÄRKER, M. & SIDORCHUK, A. Assessment of gully erosion process dynamics for water resources management in a semiarid catchment of Swaziland (Southern Africa). Erosion Prediction in Ungauged Basins: Integrating Methods and Techniques, 2003 Sapporo. 188-198.

MARKER, M. E. 1987. A note on marine benches of the southern Cape. *South African Journal of Geology,* 90**,** 120-123.

MARKER, M. E. & EVERS, T. M. 1976. Iron Age Settlement and Soil Erosion in the Eastern Transvaal, South Africa. *The South African Archaeological Bulletin,* 31**,** 153-165. DOI:10.2307/3887737.

MARTIN, A. K. & FLEMMING, B. W. 1988. Physiography, Structure Add Geological Evolution of The Natal Continental Shelf. *In:* SCHUMANN, E. (ed.) *Coastal Ocean Studies off Natal, South Africa.* Berlin: Springer, p. 11-46. DOI:10.1029/LN026p0011.

MARTIN, K. 1987. Comparison of sedimentation rates in the Natal Valley, south-west Indian Ocean, with modern sediment yields in east coast rivers of Southern Africa. *South African Journal of Science,* 83**,** 716-724.

MARTIN, K. & FLEMMING, B. W. 1986. The Holocene shelf sediment wedge off the south and east coast of South Africa. *In:* KNIGHT, R. J. & MCLEAN, J. R. (eds.) *Shelf Sands and Sandstones. Memoir of the Canadian Society for Petroleum Geology.* p. 27-44.

MATHER, A. E., STOKES, M. & WHITFIELD, E. 2017. River terraces and alluvial fans: The case for an integrated Quaternary fluvial archive. *Quaternary Science Reviews,* 166**,** 74-90. DOI:10.1016/j.quascirev.2016.09.022.

MAUD, R. R. 1968. Quaternary geomorphology and soil formation in coastal Natal. *Annals Geomorphology***,** 155-199.

MAUD, R. R. 2000. Estuarine Deposits. *In:* PARTRIDGE, T. C. & MAUD, R. R. (eds.) *The Cenozoic of Southern Africa.* New York: Oxford University Press, p. 162-172. ISBN:0-19-512530-4.

MAUD, R. R. 2012. Macroscale Geomorphic Evolution. *In:* HOLMES, P. & MEADOWS, M. E. (eds.) *Southern African Geomorphology. Recent Trends and New Directions.* 1 ed. Bloemfontein, ZA: Sun Media, p. 5-22. ISBN:978-1-920382-02-5.

MAUD, R. R. & BOTHA, G. A. 2000. Deposits of the south-eastern and southern coasts. *In:* PARTRIDGE, T. C. & MAUD, R. R. (eds.) *The cenozoic of Southern Africa.* Oxford: Oxford University Press, p. 19-32. ISBN:0195125304.

MCCALL, G. S. 2007. Behavioral ecological models of lithic technological change during the later Middle Stone Age of South Africa. *Journal of Archaeological Science,* 34**,** 1738-1751. DOI:10.1016/j.jas.2006.12.015.

MCCARTHY, M. J. 1967. Stratigraphical and sedimentological evidence from the Durban region of major sea-level movements since the late tertiary. *South African Journal of Geology,* 70**,** 135-165.

MCCARTHY, T. S., TOOTH, S., JACOBS, Z., ROWBERRY, M. D., THOMPSON, M., BRANDT, D., HANCOX, P. J., MARREN, P. M., WOODBORNE, S. & ELLERY, W. N. 2011. The origin and development of the Nyl River floodplain wetland, Limpopo Province, South Africa: trunk–tributary river

interactions in a dryland setting. *South African Geographical Journal,* 93**,** 172-190. DOI:10.1080/03736245.2011.619324.

MCMILLAN, I. K. 2003. Foraminiferally defined biostratigraphic episodes and sedimentation pattern of the Cretaceous drift succession (Early Barremian to Late Maastrichtian) in seven basins on the South African and southern Namibian continental margin : research article. *South African Journal of Science,* 99**,** 537-576.

MCNEILL, J. D. 1980. *Electrical conductivity of soils and rocks,* Ontario, Canada, Geonics Ltd., 20 p.

MECKLER, A. N., CLARKSON, M. O., COBB, K. M., SODEMANN, H. & ADKINS, J. F. 2012. Interglacial Hydroclimate in the Tropical West Pacific Through the Late Pleistocene. *Science,* 336**,** 1301-1304. DOI:10.1126/science.1218340.

MERRITTS, D. J., VINCENT, K. R. & WOHL, E. E. 1994. Long river profiles, tectonism, and eustasy: A guide to interpreting fluvial terraces. *Journal of Geophysical Research: Solid Earth,* 99**,** 14031-14050. DOI:10.1029/94JB00857.

MILANKOVIC, M. 1941. *Kanon der Erdbestrahlung und seine Anwendung auf das Eiszeitenproblem,* Belgrade, Mihaila Curcica.

MILLER, C., FINCH, J., HILL, T., PETERSE, F., HUMPHRIES, M., ZABEL, M. & SCHEFUß, E. 2019. Late Quaternary climate variability at Mfabeni peatland, eastern South Africa. *Clim. Past,* 15**,** 1153-1170. DOI:10.5194/cp-15-1153-2019.

MILLER, K. G., KOMINZ, M. A., BROWNING, J. V., WRIGHT, J. D., MOUNTAIN, G. S., KATZ, M. E., SUGARMAN, P. J., CRAMER, B. S., CHRISTIE-BLICK, N. & PEKAR, S. F. 2005. The Phanerozoic Record of Global Sea-Level Change. *Science,* 310**,** 1293. DOI:10.1126/science.1116412.

MILLS, S. C., BARROWS, T. T., TELFER, M. W. & FIFIELD, L. K. 2017. The cold climate geomorphology of the Eastern Cape Drakensberg: A reevaluation of past climatic conditions during the last glacial cycle in Southern Africa. *Geomorphology,* 278**,** 184-194. DOI:10.1016/j.geomorph.2016.11.011.

MILLS, S. C., GRAB, S. W. & CARR, S. J. 2009. Recognition and palaeoclimatic implications of late Quaternary niche glaciation in eastern Lesotho. *Journal of Quaternary Science,* 24**,** 647-663. DOI:10.1002/jqs.1247.

MILLS, S. C., GRAB, S. W., REA, B. R., CARR, S. J. & FARROW, A. 2012. Shifting westerlies and precipitation patterns during the Late Pleistocene in southern Africa determined using glacier reconstruction and mass balance modelling. *Quaternary Science Reviews,* 55**,** 145-159. DOI:10.1016/j.quascirev.2012.08.012.

MILSOM, J. & ASGER, E. 2011. *Field Geophysics,* Chichester, Wiley, 287 p. ISBN:978-0-470-74984-5. DOI:10.1002/9780470972311.

MÖLG, N. & BOLCH, T. 2017. Structure-from-Motion Using Historical Aerial Images to Analyse Changes in Glacier Surface Elevation. *Remote Sensing,* 9. DOI:10.3390/rs9101021.

MOORE, A. E., BLENKINSOP, T. & COTTERIL, F. P. D. 2012. Dynamic evolution of the Zambezi-Limpopo watershed, central Zimbabwe. *South African Journal of Geology,* 115**,** 551-560. DOI:10.2113/gssajg.115.4.551.

MOORE, A. E. & LARKIN, P. A. 2001. Drainage evolution in south-central Africa since the breakup of Gondwana. *South African Journal of Geology,* 104**,** 47-68. DOI:10.2113/104.1.47.

MORTIMORE, J. L., MARSHALL, L.-J. R., ALMOND, M. J., HOLLINS, P. & MATTHEWS, W. 2004. Analysis of red and yellow ochre samples from Clearwell Caves and Çatalhöyük by vibrational spectroscopy and other techniques. *Spectrochimica Acta Part A: Molecular and Biomolecular Spectroscopy,* 60**,** 1179-1188. DOI:

10.1016/j.saa.2003.08.002.

MUDD, S. M., CLUBB, F. J., GAILLETON, B. & HURST, M. D. 2018. How concave are river channels? *Earth Surf. Dynam.,* 6**,** 505-523. DOI:10.5194/esurf-6-505-2018.

NASH, D. J. 2012. Duricrusts. *In:* HOLMES, P. & MEADOWS, M. E. (eds.) *Southern African Geomorphology. Recent Trends and New Directions.* 1 ed. Bloemfontein, ZA: Sun Media, p. 193-229. ISBN:978-1-920382-02-5.

NASH, D. J. & ULLYOTT, J. S. 2007. Silcrete. *In:* NASH, D. J. & MCLAREN, S. J. (eds.) *Geochemical Sediments and Landscapes.* Blackwell, p. 95-143. ISBN:9781405125192. DOI:10.1002/9780470712917.ch4.

NEUMANN, F. H., SCOTT, L., BOUSMAN, C. B. & VAN AS, L. 2010. A Holocene sequence of vegetation change at Lake Eteza, coastal KwaZulu-Natal, South Africa. *Review of Palaeobotany and Palynology,* 162**,** 39-53. DOI:10.1016/j.revpalbo.2010.05.001.

NEUMANN, F. H., STAGER, J. C., SCOTT, L., VENTER, H. J. T. & WEYHENMEYER, C. 2008. Holocene vegetation and climate records from Lake Sibaya, KwaZulu-Natal (South Africa). *Review of Palaeobotany and Palynology,* 152**,** 113-128. DOI:10.1016/j.revpalbo.2008.04.006.

NORSTRÖM, E., BRINGENSPARR, C., FITCHETT, J. M., GRAB, S. W., RYDBERG, J. & KYLANDER, M. 2018. Late-Holocene climate and vegetation dynamics in eastern Lesotho highlands. *The Holocene,* 28**,** 1483-1494. DOI:10.1177/0959683618777054.

OLDKNOW, C. J. & HOOKE, J. M. 2017. Alluvial terrace development and changing landscape connectivity in the Great Karoo, South Africa. Insights from the Wilgerbosch River catchment, Sneeuberg. *Geomorphology,* 288**,** 12-38. DOI:10.1016/j.geomorph.2017.03.009.

OLSZAK, J. 2017. Climatically controlled terrace staircases in uplifting mountainous areas. *Global and Planetary Change,* 156**,** 13-23. DOI:10.1016/j.gloplacha.2017.07.013.

ORIEL, S., GABRIELSE, HAY, W., KOTTLOWSKI, F., PATTON, J. & VITO, S. 1983. North American Stratigraphic Code. *AAPG Bulletin,* 67**,** 841-875.

OTTO-BLIESNER, B. L., RUSSELL, J. M., CLARK, P. U., LIU, Z., OVERPECK, J. T., KONECKY, B., DEMENOCAL, P., NICHOLSON, S. E., HE, F. & LU, Z. 2014. Coherent changes of southeastern equatorial and northern African rainfall during the last deglaciation. *Science,* 346, 1223-1227. DOI:10.1126/science.1259531.

OUIMET, W. B., WHIPPLE, K. X. & GRANGER, D. E. 2009. Beyond threshold hillslopes: Channel adjustment to base-level fall in tectonically active mountain ranges. *Geology,* 37**,** 579-582. DOI:10.1130/g30013a.1.

PALACKY, G. 1988. Resistivity characteristics of geologic targets. *In:* NABIGHIAN, M. N. (ed.) *Electromagnetic methods in applied geophysics.* Tulsa, USA: Society of Exploration Geophysicists, p. 53-129. ISBN:978-1-56080-069-9.

PARTRIDGE, T. C. 1997. Cainozoic environmental change in southern Africa, with special emphasis on the last 200 000 years. *Progress in Physical Geography: Earth and Environment,* 21**,** 3-22. DOI:10.1177/030913339702100102.

PARTRIDGE, T. C. 1998. Of diamonds, dinosaurs and diastrophism : 150 million years of landscape evolution in southern Africa. *South African Journal of Geology,* 101**,** 167-184.

PARTRIDGE, T. C., BOTHA, G. A. & HADDON, I. G. 2006. Cenozoic deposits of the interior. *In:* JOHNSON, M. R., ANHAEUSSER, C. R. & THOMAS, R. J. (eds.) *The Geology of South Africa.* Johannesburg/Pretoria: GSSA/Council for Geoscience, p. 585–604.

PARTRIDGE, T. C., DEMENOCAL, P. B., LORENTZ, S. A., PAIKER, M. J. & VOGEL, J. C. 1997. Orbital forcing of climate over South Africa: A 200,000-year rainfall record from the pretoria saltpan. *Quaternary Science Reviews,* 16**,** 1125-1133. DOI:10.1016/S0277-3791(97)00005-X.

PARTRIDGE, T. C., DOLLAR, E. S. J., MOOLMAN, J. & DOLLAR, L. H. 2010. The geomorphic provinces of South Africa, Lesotho and Swaziland: A physiographic subdivision for earth and environmental scientists. *Transactions of the Royal Society of South Africa,* 65**,** 1-47. DOI:10.1080/00359191003652033.

PARTRIDGE, T. C., KERR, S. J., METCALFE, S. E., SCOTT, L., TALMA, A. S. & VOGEL, J. C. 1993. The Pretoria Saltpan: a 200,000 year Southern African lacustrine sequence. *Palaeogeography, Palaeoclimatology, Palaeoecology,* 101**,** 317-337. DOI:10.1016/0031-0182(93)90022-B.

PARTRIDGE, T. C. & MAUD, R. R. 1987. Geomorphic evolution of southern Africa since the Mesozoic. *South African Journal of Geology,* 90**,** 179-208.

PARTRIDGE, T. C. & MAUD, R. R. 1989. The end-Cretaceous event: new evidence from the southern hemisphere. *South African Journal of Science,* 85**,** 428-430.

PARTRIDGE, T. C. & MAUD, R. R. 2000. Macro-scale geomorphic evolution of southern Africa. *In:* PARTRIDGE, T. C. & MAUD, R. R. (eds.) *The Cenozoic ofcSouthern Africa.* Oxford: Oxford University Press, p. 3-18.

PEBESMA, E. J. 2004. Multivariable geostatistics in S: the gstat package. *Computers & Geosciences,* 30**,** 683-691. DOI:10.1016/j.cageo.2004.03.012.

PÉREZ-PEÑA, J. V., AZAÑÓN, J. M., AZOR, A., DELGADO, J. & GONZÁLEZ-LODEIRO, F. 2009. Spatial analysis of stream power using GIS: SLk anomaly maps. *Earth Surface Processes and Landforms,* 34**,** 16-25. DOI:10.1002/esp.1684.

PÉREZ-PEÑA, J. V., AZOR, A., AZAÑÓN, J. M. & KELLER, E. A. 2010. Active tectonics in the Sierra Nevada (Betic Cordillera, SE Spain): Insights from geomorphic indexes and drainage pattern analysis. *Geomorphology,* 119**,** 74-87. DOI:10.1016/j.geomorph.2010.02.020.

PILLANS, B. & NAISH, T. 2004. Defining the Quaternary. *Quaternary Science Reviews,* 23**,** 2271-2282. DOI:10.1016/j.quascirev.2004.07.006.

PLANET TEAM 2017. Planet Application Program Interface: In Space for Life on Earth. San Francisco, CA.

PLUG, I. 2004. Resource exploitation: Animal use during the Middle Stone Age at Sibudu Cave, KwaZulu-Natal. *South African Journal of Science,* 100**,** 151-158.

PLUG, I. 2006. Aquatic animals and their associates from the Middle Stone Age levels at Sibudu. *Southern African Humanities,* 18**,** 289-299.

POHL, B., FAUCHEREAU, N., REASON, C. J. C. & ROUAULT, M. 2010. Relationships between the Antarctic Oscillation, the Madden–Julian Oscillation, and ENSO, and Consequences for Rainfall Analysis. *Journal of Climate,* 23**,** 238-254. DOI:10.1175/2009JCLI2443.1.

PORAT, N. & BOTHA, G. 2008. The luminescence chronology of dune development on the Maputaland coastal plain, southeast Africa. *Quaternary Science Reviews,* 27**,** 1024-1046. DOI:10.1016/j.quascirev.2008.01.017.

POWELL, A., SHENNAN, S. & THOMAS, M. G. 2009. Late Pleistocene Demography and the Appearance of Modern Human Behavior. *Science,* 324**,** 1298. DOI:10.1126/science.1170165.

QUÉNÉHERVÉ, G. S. 2018. *Assessment of Landscape Processes, Forms and Features in the Lake Manyara Region, East African Rift Valley.* Dissertation, University of Tübingen.

RAMSAY, P., SMITH, A., LEE-THORP, J., VOGEL, J., TYLDSLEY, M. & KIDWELL, W. 1993. 130000-year-old fossil elephant found near Durban, South-Africa: preliminary-report. *South african Journal of Science,* 89**,** 165.

RAMSAY, P. J. 1991. *Sedimentology, Coral Reef Zonation, and Late Pleistocene Coastline Models of the Sodwana Bay Continental Shelf, Northern Zululand.* Doctor of Philosophy, University of Natal.

RAMSAY, P. J. 1994. Marine geology of the Sodwana Bay shelf, southeast Africa. *Marine Geology,* 120**,** 225-247. DOI:10.1016/0025-3227(94)90060-4.

RAMSAY, P. J. Holocene sea-level changes. *In:* BOTHA, G. A., ed. Maputaland focus on the Quaternary evolution of the south-east African coastal plain, 1997 International Union for Quaternary Research. Private Bag X112, Pretoria, South Africa: Council for Geoscience, 56-57.

RAMSAY, P. J. & , M., T.R. 1990. Development of a Type Zoning Model for Zululand Coral Reefs, Sodwana Bay, South Africa. *Journal of Coastal Research,* 6**,** 829-852.

RAMSAY, P. J. & COOPER, J. A. G. 2002. Late Quaternary Sea-Level Change in South Africa. *Quaternary Research,* 57**,** 82-90. DOI:10.1006/qres.2001.2290.

RAPER, P. E., MÖLLER, L. A. & DU PLESSIS, T. 1989. *Dictionary of Southern African place names,* Johannesburg, Jonathan Ball Publishers. ISBN:0947464042.

REASON, C. J. C., ALLAN, R. J., LINDESAY, J. A. & ANSELL, T. J. 2000. ENSO and climatic signals across the Indian Ocean Basin in the global context: part I, interannual composite patterns. *International Journal of Climatology,* 20**,** 1285-1327. DOI:10.1002/1097-0088(200009)20:11<1285::aid-joc536>3.0.co;2-r.

REASON, C. J. C. & MULENGA, H. 1999. Relationships between South African rainfall and SST anomalies in the Southwest Indian Ocean. *International Journal of Climatology,* 19**,** 1651-1673. DOI:10.1002/(sici)1097-0088(199912)19:15<1651::aid-joc439>3.0.co;2-u.

REASON, C. J. C. & ROUAULT, M. 2005. Links between the Antarctic Oscillation and winter rainfall over western South Africa. *Geophysical Research Letters,* 32. DOI:10.1029/2005gl022419.

REYNARD, J. P., DISCAMPS, E., WURZ, S., VAN NIEKERK, K. L., BADENHORST, S. & HENSHILWOOD, C. S. 2016. Occupational intensity and environmental changes during the Howiesons Poort at Klipdrift Shelter, southern Cape, South Africa. *Palaeogeography, Palaeoclimatology, Palaeoecology,* 449**,** 349-364. DOI:10.1016/j.palaeo.2016.02.035.

ROBERTS, D. L., KARKANAS, P., JACOBS, Z., MAREAN, C. W. & ROBERTS, R. G. 2012. Melting ice sheets 400,000 yr ago raised sea level by 13m: Past analogue for future trends. *Earth and Planetary Science Letters,* 357-358**,** 226-237. DOI:10.1016/j.epsl.2012.09.006.

ROBERTS, G. G. & WHITE, N. 2010. Estimating uplift rate histories from river profiles using African examples. *Journal of Geophysical Research: Solid Earth,* 115**,** n/a-n/a. DOI:10.1029/2009JB006692.

RØNNING, J. S., LAURITSEN, T. & MAURING, E. 1995. Locating bedrock fractures beneath alluvium using various geophysical methods. *Journal of Applied Geophysics,* 34**,** 158.

ROSGEN, D. L. & SILVEY, H. L. 1996. *Applied river morphology,* 2 ed*,* Pagosa Springs, Colorado, Wildland Hydrology, 378 p. ISBN:0965328902.

ROVERE, A., RAYMO, M. E., VACCHI, M., LORSCHEID, T., STOCCHI, P., GÓMEZ-PUJOL, L., HARRIS, D. L., CASELLA, E., O'LEARY, M. J. & HEARTY, P. J. 2016. The analysis of Last Interglacial (MIS 5e) relative sea-level indicators: Reconstructing sea-level in a warmer world. *Earth-Science Reviews,* 159**,** 404-427. DOI:10.1016/j.earscirev.2016.06.006.

RUBIN, J. 1967. Optimal classification into groups: An approach for solving the taxonomy problem. *Journal of Theoretical Biology,* 15**,** 103-144. DOI:10.1016/0022-5193(67)90046-X.

S.C., M., GRAB, S. W. & CARR, S. J. 2009. Late Quaternary moraines along the Sekhokong Range, Eastern Lesotho: Contrasting the geomorphic history of north- and south-facing slopes. *Geografiska Annaler: Series A, Physical Geography,* 91**,** 121-140. DOI:10.1111/j.1468-0459.2009.00359.x.

SALZMAN, L. 2013. *Submerged shoreline sequences on the KwaZulu-Natal shelf: A comparison between two morphological settings.* Master of Science, University of KwaZulu-Natal.

SALZMAN, L., GREEN, A. & COOPER, A. 2013. Submerged barrier shoreline sequences on a high energy, steep and narrow shelf. *Marine Geology,* 346**,** 366–374. DOI:10.1016/j.margeo.2013.10.003.

SASAKI, Y. 1992. Resolution of resistivity tomography inferred from numerical simulation. *Geophysical Prospecting,* 40**,** 453-463. DOI:10.1111/j.1365-2478.1992.tb00536.x.

SCHEFUß, E., KUHLMANN, H., MOLLENHAUER, G., PRANGE, M. & PÄTZOLD, J. 2011. Forcing of wet phases in southeast Africa over the past 17,000 years. *Nature,* 480**,** 509. DOI:10.1038/nature10685.

SCHILDGEN, T. F., EHLERS, T. A., WHIPP JR, D. M., VAN SOEST, M. C., WHIPPLE, K. X. & HODGES, K. V. 2009. Quantifying canyon incision and Andean Plateau surface uplift, southwest Peru: A thermochronometer and numerical modeling approach. *Journal of Geophysical Research: Earth Surface,* 114. DOI:10.1029/2009JF001305.

SCHMID, V. C., PORRAZ, G., ZEIDI, M. & CONARD, N. J. 2019. Blade Technology Characterizing the MIS 5 D-A Layers of Sibudu Cave, South Africa. *Lithic Technology,* 44**,** 199-236. DOI:10.1080/01977261.2019.1637627.

SCHMIDT, G. A. 1999. Forward modeling of carbonate proxy data from planktonic foraminifera using oxygen isotope tracers in a global ocean model. *Paleoceanography,* 14**,** 482-497. DOI:10.1029/1999pa900025.

SCHROTT, L., OTTO, J. C., GÖTZ, J. & GEILHAUSEN, M. 2013. 14.2 Fundamental Classic and Modern Field Techniques in Geomorphology: An Overview A2 - Shroder, John F. *Treatise on*

Geomorphology. San Diego: Academic Press, p. 6-21. ISBN:978-0-08-088522-3. DOI:10.1016/B978-0-12-374739-6.00369-9.

SCHUMM, S. A. 1985. Patterns of alluvial rivers. *Annual Review of Earth and Planetary Sciences,* 13**,** 5-27.

SCHUMM, S. A. 1993. River Response to Baselevel Change: Implications for Sequence Stratigraphy. *The Journal of Geology,* 101**,** 279-294. DOI:10.1086/648221.

SCHUMM, S. A., SCHUMM, S. A., DUMONT, J. F. & HOLBROOK, J. M. 2002. *Active tectonics and alluvial rivers,* Cambridge, UK, Cambridge University Press, 199 p. ISBN:0521890586.

SCHWAB, G. O., FANGMEIER, D. D. & ELLIOT, W. J. 2002. *Soil and water conservation engineering,* 3 ed*,* New York, John Wiley & Sons, 507 p. ISBN:9788126521081.

SCHWANGHART, W. & SCHERLER, D. 2014. Short Communication: TopoToolbox 2 – MATLAB-based software for topographic analysis and modeling in Earth surface sciences. *Earth Surf. Dynam.,* 2**,** 1-7. DOI:10.5194/esurf-2-1-2014.

SCOTT, L. 1982. A late quaternary pollen record from the Transvaal bushveld, South Africa. *Quaternary Research,* 17**,** 339-370. DOI:10.1016/0033-5894(82)90028-X.

SEUTLOALI, K. E. & BECKEDAHL, H. R. 2015. Understanding the factors influencing rill erosion on roadcuts in the south eastern region of South Africa. *Solid Earth,* 6**,** 633-641. DOI:10.5194/se-6-633-2015.

SEUTLOALI, K. E., BECKEDAHL, H. R., DUBE, T. & SIBANDA, M. 2016. An assessment of gully erosion along major armoured roads in south-eastern region of South Africa: a remote sensing and GIS approach. *Geocarto International,* 31**,** 225-239. DOI:10.1080/10106049.2015.1047412.

SHARMA, S. P. & BARANWAL, V. C. 2005. Delineation of groundwater-bearing fracture zones in a hard rock area integrating very low frequency electromagnetic and resistivity data. *Journal of Applied Geophysics,* 57**,** 155-166. DOI:10.1016/j.jappgeo.2004.10.003.

SHI, X., YANG, Z., DONG, Y., QU, H., ZHOU, B. & CHENG, B. 2020. Geomorphic indices and longitudinal profile of the Daba Shan, northeastern Sichuan Basin: Evidence for the late Cenozoic eastward growth of the Tibetan Plateau. *Geomorphology,* 353**,** 107031. DOI:10.1016/j.geomorph.2020.107031.

SIBSON, R. 1981. A Brief Description of Natural Neighbor Interpolation. *In:* BARNET, V. (ed.) *Interpreting Multivariate Data.* Chichester: Wiley, p. 21-36.

SIMON, M. H., ZIEGLER, M., BOSMANS, J., BARKER, S., REASON, C. J. C. & HALL, I. R. 2015. Eastern South African hydroclimate over the past 270,000 years. *Scientific Reports,* 5**,** 18153. DOI:10.1038/srep18153.

SINGLETON, A. T. & REASON, C. J. C. 2007. Variability in the characteristics of cut-off low pressure systems over subtropical southern Africa. *International Journal of Climatology,* 27**,** 295-310. DOI:10.1002/joc.1399.

SITOE, S. R., RISBERG, J., NORSTRÖM, E., SNOWBALL, I., HOLMGREN, K., ACHIMO, M. & MUGABE, J. 2015. Paleo-environment and flooding of the Limpopo River-plain, Mozambique, between c. AD 1200–2000. *CATENA,* 126**,** 105-116. DOI:10.1016/j.catena.2014.10.038.

SMITH, A. M. 1991. Extreme palaeofloods: Their climatic significance and the chances of floods of similar magnitude recurring. *South African Journal of Science,* 87**,** 219–220.

SNYDER, N. P., WHIPPLE, K. X., TUCKER, G. E. & MERRITTS, D. J. 2000. Landscape response to tectonic forcing: Digital elevation model analysis of stream profiles in the Mendocino triple junction region, northern California. *GSA Bulletin,* 112**,** 1250-1263. DOI:10.1130/0016-7606(2000)112<1250:lrttfd>2.0.co;2.

SONZOGNI, C., BARD, E. & ROSTEK, F. 1998. Tropical sea surface temperatures durig the last glacial period: A view based on alkenones in Indian Ocean sediments. *Quaternary Science Reviews,* 17**,** 1185-1201. DOI:10.1016/S0277-3791(97)00099-1.

SORIA-JÁUREGUI, Á., GONZÁLEZ-AMUCHÁSTEGUI, M. J., MAUZ, B. & LANG, A. 2016. Dynamics of Mediterranean late Quaternary fluvial activity: An example from the River Ebro (north Iberian Peninsula). *Geomorphology,* 268**,** 110-122. DOI:10.1016/j.geomorph.2016.06.006.

STENBERG, B. & ROSSEL, R. A. V. 2010. Diffuse Reflectance Spectroscopy for High-Resolution Soil Sensing. *In:* VISCARRA ROSSEL, R. A., MCBRATNEY, A. B. & MINASNY, B. (eds.) *Proximal Soil Sensing.* Dordrecht: Springer Netherlands, p. 29-47. ISBN:978-90-481-8859-8. DOI:10.1007/978-90-481-8859-8_3.

STUMPF, A., AUGEREAU, E., DELACOURT, C. & BONNIER, J. 2016. Photogrammetric discharge monitoring of small tropical mountain rivers: A case study at Rivière des Pluies, Réunion Island. *Water Resources Research,* 52**,** 4550-4570. DOI:10.1002/2015WR018292.

STUMPF, A., MALET, J.-P. & DELACOURT, C. 2017. Correlation of satellite image time-series for the detection and monitoring of slow-moving landslides. *Remote Sensing of Environment,* 189**,** 40-55. DOI:10.1016/j.rse.2016.11.007.

STUMPF, A., MALET, J. P., ALLEMAND, P., PIERROT-DESEILLIGNY, M. & SKUPINSKI, G. 2015. Ground-based multi-view photogrammetry for the monitoring of landslide deformation and erosion. *Geomorphology,* 231**,** 130-145. DOI:10.1016/j.geomorph.2014.10.039.

STUUT, J.-B. W., CROSTA, X., VAN DER BORG, K. & SCHNEIDER, R. 2004. Relationship between Antarctic sea ice and southwest African climate during the late Quaternary. *Geology,* 32**,** 909-912. DOI:10.1130/g20709.1.

SYDOW, C. J. 1988. *Stratigraphic control of slumping and canyon development on the continental margin, East Coast, South Africa.* B.Sc. Hons, University of Cape Town.

TANKARD, A. J. 1976. Pleistocene history and coastal morphology of the Ysterfontein-Elands Bay area, Cape Province. 69**,** 73-119.

TANKARD, A. J., JACKSON, M., ERIKSSON, K. A., HOBDAY, D. K., HUNTER, D. R. & MINTER, W. E. L. 1982a. *Crustal Evolution of Southern Africa,* 1 ed*,* New York, Springer, 523 p. ISBN:978-1-4613-8149-5. DOI:10.1007/978-1-4613-8147-1.

TANKARD, A. J., JACKSON, M. P. A., ERIKSSON, K. A., HOBDAY, D. K., HUNTER, D. R. & MINTER, W. E. L. 1982b. Fragmentation and Mesozoic Paleogeography. *In:* TANKARD, A. J., JACKSON, M. P. A., ERIKSSON, K. A., HOBDAY, D. K., HUNTER, D. R. & MINTER, W. E. L. (eds.) *Crustal Evolution of Southern Africa. 3.8 Billion Years of Earth History.* New York: Springer, p. 407-423. ISBN:978-1-4613-8149-5. DOI:10.1007/978-1-4613-8147-1.

TEMME, A. J. A. M., BAARTMAN, J. E. M., BOTHA, G. A., VELDKAMP, A., JONGMANS, A. G. & WALLINGA, J. 2008. Climate controls on late Pleistocene landscape evolution of the Okhombe valley, KwaZulu-Natal, South Africa. *Geomorphology,* 99**,** 280-295. DOI:10.1016/j.geomorph.2007.11.006.

THOMPSON, D. W. J. & WALLACE, J. M. 2000. Annular Modes in the Extratropical Circulation. Part I: Month-to-Month Variability. *Journal of Climate,* 13**,** 1000-1016. DOI:10.1175/1520-0442.

TOOTH, S., BRANDT, D., HANCOX, P. J. & MCCARTHY, T. S. 2004. Geological controls on alluvial river behaviour: a comparative study of three rivers on the South African Highveld. *Journal of African Earth Sciences,* 38**,** 79-97. DOI:10.1016/j.jafrearsci.2003.08.003.

TOOTH, S., HANCOX, P. J., BRANDT, D., MCCARTHY, T. S., JACOBS, Z. & WOODBORNE, S. 2013. Controls On the Genesis, Sedimentary Architecture, and Preservation Potential of Dryland Alluvial Successions In Stable Continental Interiors: Insights from the Incising Modder River, South Africa. *Journal of Sedimentary Research,* 83**,** 541-561. DOI:10.2110/jsr.2013.46.

TOOTH, S., RODNIGHT, H., DULLER, G. A. T., MCCARTHY, T. S., MARREN, P. M. & BRANDT, D. 2007. Chronology and controls of avulsion along a mixed bedrock-alluvial river. *GSA Bulletin,* 119**,** 452-461. DOI:10.1130/b26032.1.

TRUC, L., CHEVALIER, M., FAVIER, C., CHEDDADI, R., MEADOWS, M. E., SCOTT, L., CARR, A. S., SMITH, G. F. & CHASE, B. M. 2013. Quantification of climate change for the last 20,000years from Wonderkrater, South Africa: Implications for the long-term dynamics of the Intertropical Convergence Zone. *Palaeogeography, Palaeoclimatology, Palaeoecology,* 386**,** 575-587. DOI:10.1016/j.palaeo.2013.06.024.

TWIDALE, C. R. 1988. The missing link: planation surfaces and etch forms in southern Africa. *In:* DARDIS, G. F. & MOON, P. B. (eds.) *Geomorphological studies in Southern Africa.* Johannesburg, p. 31-46. ISBN:1868120724.

TYSON, P., KARLÉN, W., HOLMGREN, K. & HEISS, G. 2000. The Little Ice Age and medieval warming in South Africa. *South African Journal of Science,* 96**,** 121-126.

TYSON, P. D. 1999. Late-Quaternary and Holocene palaeoclimates of southern Africa : a synthesis. *South African Journal of Geology,* 102**,** 335-349.

VAN HEERDEN, J., TERBLANCHE, D. E. & SCHULZE, G. C. 1988. The southern oscillation and South African summer rainfall. *Journal of Climatology,* 8**,** 577-597. DOI:10.1002/joc.3370080603.

VAN NIEKERK, H. S., GUTZMER, J., BEUKES, N., PHILLIPS, D. & KIVIETS GNOINSKI, G. 1999. An 40Ar/39Ar age of supergene K-Mn oxyhydroxides in a post-Gondwana soil profile on the Highveld of South Africa. *South African Journal of Science,* 95**,** 450-454.

VANDEKERCKHOVE, L., POESEN, J., OOSTWOUD WIJDENES, D., GYSSELS, G., BEUSELINCK, L. & DE LUNA, E. 2000. Characteristics and controlling factors of bank gullies in two semi-arid mediterranean environments. *Geomorphology,* 33**,** 37-58. DOI:10.1016/S0169-555X(99)00109-9.

VANDENBERGHE, J. 2015. River terraces as a response to climatic forcing: Formation processes, sedimentary characteristics and sites for human occupation. *Quaternary International,* 370**,** 3-11. DOI:10.1016/j.quaint.2014.05.046.

VANHAEREN, M., WADLEY, L. & D'ERRICO, F. 2019. Variability in Middle Stone Age symbolic traditions: The marine shell beads from Sibudu Cave, South Africa. *Journal of Archaeological Science: Reports,* 27**,** 101893. DOI:10.1016/j.jasrep.2019.101893.

VISCARRA ROSSEL, R. A., BEHRENS, T., BEN-DOR, E., BROWN, D. J., DEMATTÊ, J. A. M., SHEPHERD, K. D., SHI, Z., STENBERG, B., STEVENS, A., ADAMCHUK, V., AÏCHI, H., BARTHÈS, B. G., BARTHOLOMEUS, H. M., BAYER, A. D., BERNOUX, M., BÖTTCHER, K., BRODSKÝ, L., DU, C. W., CHAPPELL, A., FOUAD, Y., GENOT, V., GOMEZ, C., GRUNWALD, S., GUBLER, A., GUERRERO, C., HEDLEY, C. B., KNADEL, M., MORRÁS, H. J. M., NOCITA, M., RAMIREZ-LOPEZ, L., ROUDIER, P., CAMPOS, E. M. R., SANBORN, P., SELLITTO, V. M., SUDDUTH, K. A., RAWLINS, B. G., WALTER, C., WINOWIECKI, L. A., HONG, S. Y. & JI, W. 2016. A global spectral library to characterize the world's soil. *Earth-Science Reviews,* 155**,** 198-230. DOI:10.1016/j.earscirev.2016.01.012.

VOGEL, J. C. & VISSER, E. 1981. Pretoria radiocarbon dates. *Radiocarbon,* 23. DOI:10.1017/S003382220002018X.

VOGEL, S. & MÄRKER, M. 2010. Reconstructing the Roman topography and environmental features of the Sarno River Plain (Italy) before the AD 79 eruption of Somma–Vesuvius. *Geomorphology,* 115**,** 67-77. DOI:10.1016/j.geomorph.2009.09.031.

VOGEL, S., MÄRKER, M., RELLINI, I., HOELZMANN, P., WULF, S., ROBINSON, M., STEINHÜBEL, L., DI MAIO, G., IMPERATORE, C., KASTENMEIER, P., LIEBMANN, L., ESPOSITO, D. & SEILER, F. 2016. From a stratigraphic sequence to a landscape evolution model: Late Pleistocene and Holocene volcanism, soil formation and land use in the shade of Mount Vesuvius (Italy). *Quaternary International,* 394**,** 155-179. DOI:10.1016/j.quaint.2015.02.033.

WADLEY, L. 2004. Vegetation changes between 61 500 and 26 000 years ago: the evidence from seeds in Sibudu Cave, KwaZulu-Natal. *South African Journal of Science,* 100**,** 167-173.

WADLEY, L. 2015. Those marvellous millennia: the Middle Stone Age of Southern Africa. *Azania: Archaeological Research in Africa,* 50**,** 155-226. DOI:10.1080/0067270X.2015.1039236.

WADLEY, L., PLUG, I. & CLARK, J. 2008. The contribution of Sibudu fauna to an understanding of KwaZulu-Natal environments at ~60 ka, ~50 ka and ~37 ka. *In:* BADENHORST, S., MITCHELL, P. & DRIVER, C. D. (eds.) *Animals and People: Archaeozoological Papers in Honour of Ina Plug.* Oxford: Archaeopress, p. 34-45. ISBN:9781407303369.

WADLEY, L., SIEVERS, C., BAMFORD, M., GOLDBERG, P., BERNA, F. & MILLER, C. 2011. Middle Stone Age Bedding Construction and Settlement Patterns at Sibudu, South Africa. *Science,* 334**,** 1388. DOI:10.1126/science.1213317.

WAELBROECK, C., LABEYRIE, L., MICHEL, E., DUPLESSY, J. C., MCMANUS, J. F., LAMBECK, K., BALBON, E. & LABRACHERIE, M. 2002. Sea-level and deep water temperature changes derived from benthic foraminifera isotopic records. *Quaternary Science Reviews,* 21**,** 295-305. DOI:10.1016/S0277-3791(01)00101-9.

WALKER, P. H., BECKMANN, G. G. & BREWER, R. 1984. Definition and use of the term 'pedoderm'. *Journal of Soil Science,* 35**,** 505-510. DOI:10.1111/j.1365-2389.1984.tb00307.x.

WANG, Y., CHENG, H., EDWARDS, R. L., KONG, X., SHAO, X., CHEN, S., WU, J., JIANG, X., WANG, X. & AN, Z. 2008. Millennial- and orbital-scale changes in the East Asian monsoon over the past 224,000 years. *Nature,* 451**,** 1090. DOI:10.1038/nature06692.

WATSON, A., PRICE-WILLIAMS, D. & GOUDIE, A. S. 1984. The palaeoenvironmental interpretation of colluvial sediments and palaeosols of the late pleistocene hypothermal in Southern Africa. *Palaeogeography, Palaeoclimatology, Palaeoecology,* 45**,** 225-249. DOI:10.1016/0031-0182(84)90008-7.

WATSON, D. 1999. The natural neighbor series manuals and source codes. *Computers & Geosciences,* 25**,** 463-466. DOI:10.1016/S0098-3004(98)00150-2.

WATSON, H. K. 1996. Short and long term influence on soil erosion of settlement by peasant farmers in KwaZulu-Natal. *South African Geographical Journal,* 78**,** 1-6. DOI:10.1080/03736245.1996.9713600.

WEATHERALL, P., MARKS, K. M., JAKOBSSON, M., SCHMITT, T., TANI, S., ARNDT, J. E., ROVERE, M., CHAYES, D., FERRINI, V. & WIGLEY, R. 2015. A new digital bathymetric model of the world's oceans. *Earth and Space Science,* 2**,** 331-345. DOI:10.1002/2015ea000107.

WEIDELT, H. J. 1976. *Manual of reforestation and erosion control for the Philippines,* Eschborn, German Agency for Technical Cooperation (GTZ), 569 p. ISBN:3880850208.

WEIDONG, L., BARET, F., XINGFA, G., QINGXI, T., LANFEN, Z. & BING, Z. 2002. Relating soil surface moisture to reflectance. *Remote Sensing of Environment,* 81**,** 238-246. DOI:10.1016/S0034-4257(01)00347-9.

WEISS, A. D. 2001. Topographic Position and Landforms Analysis. *ESRI User Conference.*

WELDON, D. & REASON, C. J. C. 2014. Variability of rainfall characteristics over the South Coast region of South Africa. *Theoretical and Applied Climatology,* 115**,** 177-185. DOI:10.1007/s00704-013-0882-4.

WESTAWAY, R. 2007. Late Cenozoic uplift of the eastern United States revealed by fluvial sequences of the Susquehanna and Ohio systems: coupling between surface processes and lower-crustal flow. *Quaternary Science Reviews,* 26**,** 2823-2843. DOI:10.1016/j.quascirev.2007.06.031.

WESTAWAY, R., MADDY, D. & BRIDGLAND, D. 2002. Flow in the lower continental crust as a mechanism for the Quaternary uplift of south-east England: constraints from the Thames terrace record. *Quaternary Science Reviews,* 21**,** 559-603. DOI:10.1016/S0277-3791(01)00040-3.

WHIPPLE, K. X. 2001. Fluvial Landscape Response Time: How Plausible Is Steady-State Denudation? *American Journal of Science,* 301**,** 313-325. DOI:10.2475/ajs.301.4-5.313.

WHIPPLE, K. X. & TUCKER, G. E. 1999. Dynamics of the stream-power river incision model: Implications for height limits of mountain ranges, landscape response timescales, and research needs. *Journal of Geophysical Research: Solid Earth,* 104**,** 17661-17674. DOI:10.1029/1999jb900120.

WHITTAKER, A. C. & BOULTON, S. J. 2012. Tectonic and climatic controls on knickpoint retreat rates and landscape response times. *Journal of Geophysical Research: Earth Surface,* 117. DOI:10.1029/2011jf002157.

WIDDOWSON 2007. Laterite and Ferricrete. *In:* NASH, D. J. & MCLAREN, S. J. (eds.) *Geochemical Sediments and Landscapes.* Blackwell, p. 45-94. ISBN:9781405125192. DOI:10.1002/9780470712917.ch3.

WILL, M., CONARD, N. & TRYON, C. 2019a. Timing and trajectory of cultural evolution on the African continent 200,000-30,000 years ago. p. 25-72. ISBN:978-3-935751-30-8.

WILL, M., KANDEL, A. W. & CONARD, N. J. 2019b. Midden or Molehill: The Role of Coastal Adaptations in Human Evolution and Dispersal. *Journal of World Prehistory*. DOI:10.1007/s10963-018-09127-4.

WILLETT, S. D. & BRANDON, M. T. 2002. On steady states in mountain belts. *Geology,* 30**,** 175-178. DOI:10.1130/0091-7613(2002)030<0175:ossimb>2.0.co;2.

WILSON, J. P. & GALLANT, J. C. 2000. Primary Topographic Attributes. *In:* WILSON, J. P. & GALLANT, J. C. (eds.) *Terrain Analysis: Principles and Applications.* John Wiley & Sons, p. 51-85. ISBN:978-0-471-32188-0.

WINTLE, A. G., BOTHA, G. A., LI, S. H. & VOGEL, J. C. 1995. A chronological framework for colluviation during the last 110 kyr in KwaZulu/Natal. *South African Journal of Science,* 91**,** 134-139.

WORKMAN, J. 2001. *The Handbook of Organic Compounds: NIR, IR, Raman, and UV-Vis Spectra Featuring Polymers and Surfactants*, Academic Press, 1493 p. ISBN:978-0-12-763560-6

DOI:10.1016/B978-0-12-763560-6.X5000-4.

WORSLEY, T. R., NANCE, D. & MOODY, J. B. 1984. Global tectonics and eustasy for the past 2 billion years. *Marine Geology,* 58**,** 373-400. DOI:10.1016/0025-3227(84)90209-3.

WURZ, S. 2013. Technological Trends in the Middle Stone Age of South Africa between MIS 7 and MIS 3. *Current Anthropology,* 54**,** S305-S319. DOI:10.1086/673283.

WURZ, S. 2019. Human Evolution, Archaeology and the South African Stone Age Landscape During the Last 100,000 Years. *In:* KNIGHT, J. & ROGERSON, C. M. (eds.) *The Geography of South Africa : Contemporary Changes and New Directions.* Cham: Springer International Publishing, p. 125-132. ISBN:978-3-319-94974-1. DOI:10.1007/978-3-319-94974-1_13.

YADAV, G. S. & SINGH, S. K. 2007. Integrated resistivity surveys for delineation of fractures for ground water exploration in hard rock areas. *Journal of Applied Geophysics,* 62**,** 301-312. DOI:10.1016/j.jappgeo.2007.01.003.

YOSHINO, T. 2011. Electrical Properties of Rocks. *In:* GUPTA, H. K. (ed.) *Encyclopedia of Solid Earth Geophysics.* Dordrecht: Springer Netherlands, p. 270-276. ISBN:978-90-481-8702-7. DOI:10.1007/978-90-481-8702-7_45.

ZAWADA, P. K., HATTINGH, J. & VAN BLADEREN, D. 1996. *Paleoflood hydrological analysis of selected South African rivers,* Pretoria, Water Research Commission, 239 p. ISBN:1868452409.

ZIEGLER, M., SIMON, M. H., HALL, I. R., BARKER, S., STRINGER, C. & ZAHN, R. 2013. Development of Middle Stone Age innovation linked to rapid climate change. *Nature Communications,* 4**,** 1905. DOI:10.1038/ncomms2897.

Software

AGISOFT, 2019. *AgiSoft PhotoScan Professional* v. 1.4.5. Available: http://www.agisoft.com/downloads/installer/.

CONRAD, O., BECHTEL, B., BOCK, M., DIETRICH, H., FISCHER, E., GERLITZ, L., WEHBERG, J., WICHMANN, V. & BÖHNER, J. 2015. System for Automated Geoscientific Analyses (SAGA) v. 2.1.4. *Geosci. Model Dev.,* 8**,** 1991-2007. DOI:10.5194/gmd-8-1991-2015.

HIJMANS, R. J., 2019. *geosphere: Spherical Trigonometry* v. 1.5-10. Available: https://CRAN.R-project.org/package=geosphere.

LOKE, M. H., 2017. *RES2DINV - 2D Geophysical Inversion Software for Resistivity and Induced Polarization data* v. 4.07.16. Geotomo Software. Available: www.geotomosoft.com.

MATLAB, 2019. v. R2019b. Natick, Massachusetts: The MathWorks Inc.

MEIRELES, J. E., SCHWEIGER, A. K. & CAVENDER-BARES, J., 2018. *spectrolab: Class and Methods for Hyperspectral Data* v. 0.0.8. Available: https://github.com/meireles/spectrolab.

NGI. 2019. *National Aerial Photography and Imagery Programme* [Online]. National Geo-spatial Information. Available: http://www.ngi.gov.za/index.php/what-we-do/aerial-photography-and-imagery [Accessed 2019-07-13 2019].

QGIS DEVELOPMENT TEAM, 2020. *QGIS Geographic Information System* v. 3.16. Open Source Geospatial Foundation. Available: http://qgis.org.

R CORE TEAM, 2019. *R: A language and environment for statistical computing* v. 3.5.3. Vienna, Austria: R Foundation for Statistical Computing. Available: https://www.R-project.org/.

RUPNIK, E., DAAKIR, M. & PIERROT DESEILLIGNY, M. 2017. MicMac – a free, open-source solution for photogrammetry. *Open Geospatial Data, Software and Standards,* 2**,** 14. DOI:10.1186/s40965-017-0027-2.

SCHWANGHART, W. & KUHN, N. J. 2010. TopoToolbox: A set of Matlab functions for topographic analysis. *Environmental Modelling & Software,* 25**,** 770-781. DOI:10.1016/j.envsoft.2009.12.002.

STEVENS, A. & RAMIREZ-LOPEZ, L., 2014. *prospectr: Miscellaneous functions for processing and sample selection of vis-NIR diffuse reflectance data* v. v. 0.1.3. Available: https://github.com/antoinestevens/prospectr.

STOUT, J. C. & BELMONT, P. 2014. TerEx Toolbox for semi-automated selection of fluvial terrace and floodplain features from lidar. *Earth Surface Processes and Landforms,* 39**,** 569-580. DOI:10.1002/esp.3464.

THE GIMP DEVELOPMENT TEAM, 2019. *GIMP* v. 2.10. Available: https://www.gimp.org.

WEYER, L. & LO, S. C. 2002. Spectra– Structure Correlations in the Near-Infrared. *In:* GRIFFITHS, P. & CHALMERS, J. M. (eds.) *Handbook of Vibrational Spectroscopy.* Wiley, p. 1817-1837. DOI:10.1002/0470027320.s4102.